**DOKUZ EYLÜL UNIVERSITY**
**GRADUATE SCHOOL OF NATURAL AND APPLIED SCIENCES**

# NUMERICAL AND EXPERIMENTAL INVESTIGATION OF EJECTOR USE AS THE EXPANDER IN THE VAPOR-COMPRESSION REFRIGERATION CYCLE OPERATING WITH A NEW GENERATION REFRIGERANT

**by**
**Ayşe Uğurcan ATMACA**

**March, 2020**
**İZMİR**

# NUMERICAL AND EXPERIMENTAL INVESTIGATION OF EJECTOR USE AS THE EXPANDER IN THE VAPOR-COMPRESSION REFRIGERATION CYCLE OPERATING WITH A NEW GENERATION REFRIGERANT

**A Thesis Submitted to the**
**Graduate School of Natural and Applied Sciences of Dokuz Eylül University**
**In Partial Fulfillment of the Requirements for the Degree of Doctor of Philosophy in Mechanical Engineering, Thermodynamics Program**

**by**
**Ayşe Uğurcan ATMACA**

**March, 2020**
**İZMİR**

**Ph.D. THESIS EXAMINATION RESULT FORM**

We have read the thesis entitled **"NUMERICAL AND EXPERIMENTAL INVESTIGATION OF EJECTOR USE AS THE EXPANDER IN THE VAPOR-COMPRESSION REFRIGERATION CYCLE OPERATING WITH A NEW GENERATION REFRIGERANT"** completed by **AYŞE UĞURCAN ATMACA** under supervision of **PROF.DR. AYTUNÇ EREK** and we certify that in our opinion it is fully adequate, in scope and in quality, as a thesis for the degree of Doctor of Philosophy.

Prof. Dr. Aytunç EREK

Supervisor

Prof. Dr. Can Özgür ÇOLPAN

Thesis Committee Member

Assoc. Prof. Dr. Orhan EKREN

Thesis Committee Member

Assoc. Prof. Dr. Erdal ÇETKİN

Examining Committee Member

Assoc. Prof. Dr. M. Turhan ÇOBAN

Examining Committee Member

Prof. Dr. Kadriye ERTEKİN
Director
Graduate School of Natural and Applied Science

## ACKNOWLEDGMENT

When I turn back and think about the last decade in terms of my personal and academic progress, it is one of my biggest chance in my life to meet my advisor Prof. Dr. Aytunç Erek. I really can't express my deepest gratitude for his endless assistance, support, patience, motivations, and guidance. Besides, I would like to acknowledge the support of the Scientific and Technological Research Council of Turkey (TÜBİTAK) for our project directly related my Ph.D. thesis and entitled as "Design improvement and numerical and experimental performance investigation of the ejectors used in the vapor compression refrigeration cycle" under grant number of 116M367.

Secondly, I would like to express my special thanks of gratitude to Assoc. Prof. Dr. Orhan Ekren for his invaluable helps, suggestions, and contributions to both my thesis and the aforecited project. My sincere thanks also go to Prof. Dr. Can Özgür Çolpan for his valuable comments throughout the thesis progress meetings. Next, I am so grateful to Assoc. Prof. Dr. Mustafa Turhan Çoban for his suggestions concerned with the numerical studies. One of the biggest thanks is for Mr. Nihat Ege from Işık Soğutma Endüstriyel Soğutma Sistemleri for the construction of the ejector expansion refrigeration cycle experimental test rig. Moreover, I want to thank Mr. Alim Zorluol, technician of Thermodynamics and Heat Transfer Laboratory at DEU, for all his significant helps with the experimental works and M.Sc. student Okan Gök for the technical drawings of the ejector assembly.

Special thanks are also to my beloved family for their endless support in my entire life. As the last statement, life always has shown me that there is a way if you really want it. Most of us are struggling among various troubles while catching our ambitions. Thank goodness, however strong the obstacles are I could make real my childhood's dream which is having a profession in a research field and contributing to science in this way.

Ayşe Uğurcan ATMACA

**NUMERICAL AND EXPERIMENTAL INVESTIGATION OF EJECTOR USE AS THE EXPANDER IN THE VAPOR-COMPRESSION REFRIGERATION CYCLE OPERATING WITH A NEW GENERATION REFRIGERANT**

## ABSTRACT


The subject of this thesis is related to ejector expansion refrigeration cycle (EERC). EERC is the modification of the conventional vapor-compression refrigeration cycle (VCRC) with the use of the ejector instead of the expansion valve of the classical cycle and implementation of a liquid-vapor separator to increase cycle performance. The main objective of the thesis is to investigate the performance of the EERC numerically and experimentally.

Main working fluids of this thesis are R134a and R1234yf. It is experimentally and numerically shown in the literature that performance of R1234yf is lower than R134a in the conventional cycle. Hence, R1234yf which is an appropriate refrigerant alternative according to F-gas Regulation needs performance improvement in the classical cycle.

Firstly, zero-dimensional (0D) comprehensive thermodynamic models are established for constant area and constant pressure mixing ejector theories. Moreover, one-dimensional (1D) model of the motive nozzle is constructed to obtain the pressure and velocity distributions throughout the nozzle. Hence, semi-1D model of the EERC is established after combining 0D thermodynamic models and 1D model of the motive nozzle.

Solution algorithm of the mathematical models are built in MATLAB® and properties of the refrigerants are obtained using REFPROP. EERC/VCRC test rig is established to conduct the experimental performance evaluations and to experimentally validate the numerical results obtained from the semi-1D model.

Maximum differences between the performance improvement percentages of the semi-1D model and the thermodynamic model are calculated as 14 percent and 20 percent for R134a and R1234yf, respectively. Therefore, it is shown that semi-1D modelling approach is required for more realistic performance evaluations. Results of the experiments declare that sensitivity of the ejector design according to operating conditions and liquid-vapor separator efficiency is critical for the cycle performance. The comparison between the experimental data and numerical results obtained from the semi-1D model of the EERC yields a good agreement in terms of the cycle coefficient of performance (COP), secondary fluid mass flow rate, and entrainment ratio.

**Keywords:** Ejector expansion refrigeration cycle, two-phase ejector, constant area mixing ejector, constant pressure mixing ejector, thermodynamic modelling, experimental analysis, new generation refrigerants, hydrofluoroolefin (HFO) refrigerants, F-gas Regulation

**YENİ NESİL BİR SOĞUTUCU AKIŞKANLA ÇALIŞAN BUHAR SIKIŞTIRMALI SOĞUTMA ÇEVRİMİNDE GENLEŞTİRİCİ OLARAK EJEKTÖR KULLANIMININ SAYISAL VE DENEYSEL OLARAK İNCELENMESİ**

# ÖZ

Bu tezin konusu ejektör genleştiricili soğutma çevrimi (EGSÇ) ile ilgilidir. EGSÇ, performans iyileştirmesi sağlamak amacıyla klasik çevrimdeki genleşme vanası yerine ejektör kullanılması ve çevrime sıvı-buhar ayırıcı eklenmesi ile geleneksel buhar sıkıştırmalı soğutma çevrimi (BSSÇ) değiştirilerek oluşturulmuştur. Bu tezin temel amacı EGSÇ üstüne sayısal ve deneysel incelemeler yapmaktır.

Bu tezin temel akışkanları R134a ve R1234yf'dir. R1234yf soğutkanının geleneksel çevrimde R134a soğutkanından daha düşük bir performans sergilediği deneysel ve sayısal olarak literatürde gösterilmiştir. Böylece, F-gaz yönetmeliğine göre uygun bir soğutkan alternatifi olan R1234yf klasik çevrimde bir performans iyileştirmesine ihtiyaç duymaktadır.

Öncelikle sıfır boyutlu (0B) kapsamlı termodinamik modeller sabit alanda ve sabit basınçta karışımlı ejektör teorileri için kurulmuştur. Ayrıca lüle boyunca oluşan basınç ve hız dağılımını hesaplayabilmek için birincil lülenin bir boyutlu (1B) modeli kurulmuştur. Böylece termodinamik modeller ve birincil lülenin 1B modeli birleştirilerek EGSÇ'nin yarı-1B modeli elde edilmiştir.

Matematik modellerin çözüm algoritmaları MATLAB® ortamında kurulmuştur ve soğutkanların özellikleri REFPROP'tan elde edilmiştir. Deneysel performans analizlerini yapabilmek ve yarı-1B modelden elde edilen sayısal sonuçları denelysel olarak doğrulamak için EGSÇ/BSSÇ test düzeneği kurulmuştur.

Yarı-1B model ve termodinamik modellerin performans iyileştirme yüzdeleri arasındaki maksimum fark R134a ve R1234yf için sırası ile yüzde 14 ve yüzde 20 olarak hesaplanmıştır. Böylece, yarı-1B modelleme yaklaşımının daha gerçekçi performans değerlendirmeleri için gerekli olduğu gösterilmiştir. Deneylerin sonuçları ortaya koymaktadır ki çalışma koşullarına göre ejektör tasarımının hassasiyeti ve sıvı-buhar ayırıcı verimliliği çevrim performansı açısından kritiktir. Deneysel verilerin ve EGSÇ'nin yarı-1B modelinden elde edilen sayısal sonuçların karşılaştırması çevrim performans katsayısı (COP), ikincil akışkan kütlesel debisi ve akışkanların karışma oranı açısından iyi bir uyum ile sonuçlanmıştır.

**Anahtar Kelimeler:** Ejektör genleştiricili soğutma çevrimi, iki fazlı ejektör, sabit alanda karışımlı ejektör, sabit basınçta karışımlı ejektör, termodinamik modelleme, deneysel analiz, yeni nesil soğutkanlar, hidrofloroolefin (HFO) soğutkanlar, F-gaz Yönetmeliği

**CONTENTS**

## LIST OF FIGURES

**Page**

## LIST OF TABLES

# CHAPTER ONE
# INTRODUCTION

The aim of air-conditioning, heat pumping, and refrigeration is to move heat in the opposite of the natural heat flow direction making use of the thermodynamic cycles. Heat naturally flows from higher temperature environment to lower temperature space and the target of the refrigeration cycle is therefore removing heat from a cooler space. The working fluid of these kinds of cycles is called as refrigerant. In the thermodynamic cycles such as classical vapor-compression refrigeration cycle (VCRC), the refrigerant removes heat from a cooler space while evaporating at low pressure and rejects heat condensing at high pressure, hence accomplish the heat flow from the cold environment to the hot environment. The subject of this thesis is the modification of the classical VCRC to decrease the throttling losses occurred in the expansion device. The resulting cycle is called ejector expansion refrigeration cycle (EERC). The content of the thesis is comprised of both numerical and experimental investigations made on the EERC. Firstly, this chapter briefly introduces the ejector and EERC concept. Secondly, the objectives of the thesis are presented and later on methodology of the studies and motivations are given. Lastly, outline of the thesis is summarized in this chapter.

## 1.1 Ejectors and EERC

There are four basic thermodynamic losses concerned with the conventional VCRC causing the reduction in the coefficient of performance (COP) of the cycle when compared to the COP of the Carnot refrigerator and heat pump. In other words, the sources of the thermodynamic losses are categorized as follows; (i) heat transfer across a temperature difference between the refrigerant and cold/hot environment in the evaporator and condenser, respectively, (ii) inefficient compressor, (iii) heat transfer from the refrigerant in superheated vapor state at the compressor outlet, and (iv) throttling losses in the expansion device. The first and second of these losses caused by the evaporator, condenser, and compressor are concerned with the selected components to establish the cycle. On the other hand, the third and fourth of the losses exist inevitably as one of the basic characteristics of the VCRC concept. Although first two losses are eliminated in the ideal VCRC, last two losses remain and decrease the cycle performance. The influence of these last two losses depends on the type and properties of the refrigerants.

This thesis focuses on one of the ways to decrease the throttling losses which is the ejector expansion technology. Actually, the expansion valve in the VCRC could be replaced with a kind of work-producing device, i.e. turbine, in order to increase the cycle performance. However, these kinds of devices would be expensive and could be easily damaged by the two-phase flow conditions. Hence, an ejector low in cost and durable to multi-phase flow is an advantageous option instead of a work-producing device to improve the cycle performance.

Ejector is typically a simple device including four basic sections, namely motive (primary) nozzle, suction (secondary) nozzle (chamber), mixing section (chamber), and diffuser. The internal energy and pressure related flow work of the motive fluid having high pressure is converted into the kinetic energy while passing through the motive nozzle. Hence the pressure of the motive fluid decreases at the outlet of the motive nozzle and the low pressure secondary fluid could be sucked into the ejector. As a result of the momentum transfer between the primary and secondary fluid streams, the total fluid leaves the ejector with a higher pressure when compared to the pressure of the secondary stream.

The basic idea of ejector use instead of the expander in the VCRC is converting the isenthalpic process throughout the expansion valve to the isentropic one in order to increase the COP. In the EERC, the high pressure primary fluid comes from the condenser and the refrigerant is in compressed liquid or saturated liquid state; whereas the low pressure secondary fluid is refrigerant coming from the evaporator and it is in superheated vapor or saturated vapor state. Using an ejector instead of an expansion valve improves the cycle COP since it increases the evaporation capacity, the pressure of the refrigerant entering the compressor, and therefore the compressor efficiency. To sum up, EERC is the modification of the VCRC by replacing the expansion valve with a two-phase ejector and adding a liquid-vapor separator.

## 1.2 Thesis Objectives

EERC configuration is commonly studied in the transcritical $CO_2$ (R744) concept since these kinds of high-pressure refrigerants experience very high expansion losses. Therefore, experimental and numerical studies about the EERC considering the low-pressure refrigerants are less in number when compared to transcritical $CO_2$ EERC investigations. Low-pressure refrigerants as well have improvement potentials in the EERC. Moreover, new alternative working fluids are required to be discovered instead of the widely used refrigerant, R134a which is about to be phased out by the F-gas Regulation (Regulation (EU) No 517/2014, 2014), the European Directive 2006/40/EC (Directive 2006/40/EC, 2006), and Kigali Amendment (The Kigali Amendment to the Montreal Protocol: HFC Phase-down, 2016).

Two of the hydrofluoroolefins (HFOs), namely R1234yf and R1234ze(E), are the promising alternatives since they are appropriate with respect to the strict limitations on the global warming potential (GWP) of the refrigerants. However, R1234yf results in lower performance in the conventional cycle when compared to R134a (Atmaca, Erek, & Ekren, 2019a). When Total Equivalent Warming Impact (TEWI) is the issue, not only GWP value of the refrigerants, but also the efficiency of the cycle is to be considered. Thus, cycle performance improvement is required when R1234yf is selected as the refrigerant. Percentage expansion loss calculations show that R1234yf is a suitable candidate in terms of the performance improvement in the EERC. Therefore, all objectives are determined based on the comparative analyses of mainly R134a and R1234yf and other environmentally-friendly refrigerant alternatives. The objectives of this thesis are as follows;

- Analyzing the refrigerants compatible with the GWP requirements of the environmental legislation in terms of the performance.

- Presenting the second-law (exergy) efficiency of the VCRC for the potential working fluids to highlight the refrigerants needing performance improvement.
- Calculating percentage expansion losses in the VCRC to define the most appropriate working fluid candidates for the rest of the comprehensive experimental and numerical EERC investigations.
- Establishing zero-dimensional (0D) thermodynamic models of the EERC with respect to the constant area mixing (CAM) and constant pressure mixing (CPM) ejector theories and making comparisons according to the most essential modelling assumptions, i.e. suction nozzle pressure.
- Analyzing the effect of suction nozzle pressure drop assumption on the performance.
- Investigating the performance improvement ratio, entrainment ratio, and area ratio in detail at the optimum suction nozzle pressure drop.
- Analyzing percentage expansion losses and performance improvement ratio for a couple of high pressure refrigerants and the most appropriate low-pressure natural refrigerant alternatives making use of these thermodynamic models.
- Investigating the performance improvement of the EERC under the reversible ejector assumption.
- Widening the content of the thermodynamic models with the implementation of the ejector mixing section efficiency and liquid-vapor separator efficiency when compared to the previously established models including only the efficiency of the motive nozzle, suction nozzle, and diffuser.
- Comparing the influence of the ejector component efficiencies on the performance improvement ratio in the subcritical and transcritical EERC for a typical operating condition.
- Investigating the effects of the ejector component and liquid-vapor separator efficiencies on the overall performance improvement ratio with respect to the various operating conditions.
- Displaying the characteristic behaviors of CAM and CPM ejector theories independent of the selected refrigerants.

- Constructing a preliminary design model for the ejector to be used in the EERC according to the defined cooling capacity and optimum suction nozzle pressure based on the thermodynamic modelling approach.
- Building one-dimensional (1D) model of the motive nozzle to obtain pressure and velocity distribution of the primary fluid.
- Combining the 0D thermodynamic model of the EERC and 1D model of the motive nozzle to present a semi-1D model of the EERC and expand the content of the preliminary design tool.
- Comparing the results of the 0D thermodynamic and semi-1D modelling approaches for the critical performance parameters, i.e. performance improvement ratio, entrainment ratio, area ratio, etc.
- Manufacture of the two-phase ejector with respect to the proposed design metrics with reference to the semi-1D modelling approach.
- Constructing an VCRC/EERC experimental set-up and conducting the performance tests of the manufactured ejector.
- Defining critical aspects for the performance of the EERC based on the experimental investigations.
- Comparing the experimental results for the conventional cycle analyses of R134a and R1234yf.
- Investigating experimentally the performance of R134a in the EERC.
- Making comparison between the experimental data and numerical results obtained from the semi-1D model of the EERC for R134a in order to show the practical use of the semi-1D model for the performance evaluations of the EERC.

### 1.3 Methodology

The content of this thesis includes both numerical and experimental analyses. Numerical analyses are comprised of 0D thermodynamic modelling of the EERC and 1D modelling of the motive nozzle. Most of the numerical analyses are presented for R134a, R1234yf, and R1234ze(E) although the target refrigerant of the thesis is R1234yf and R134a. R1234ze(E) and some other environmentally-friendly refrigerant alternatives are added to the comparisons to widen the thesis content. R134a is one of the widely used refrigerant and it is about to be phased out by the environmental legislation. Experimental results are only valid for R1234yf and R134a. Solution algorithms of the 0D thermodynamic models and 1D model are built in MATLAB®. The thermodynamic and thermophysical properties of the refrigerants are obtained from REFPROP version 9.1 (Lemmon, Huber, & McLinden, 2013) and version 10.0 (Lemmon, Bell, Huber, & McLinden, 2018).

Under 0D modelling approach, conservation of mass, momentum, and energy equations are applied between the inlets and outlets of all ejector and refrigeration cycle components. Moreover, 1D model of the motive nozzle is established by applying conservation of mass, momentum, and energy equations with the equation of state to the computational flow domain divided previously into a number of control volumes. Total derivatives of pressure, velocity, specific enthalpy, and density are the unknowns of the equation set of the 1D model and they are solved implicitly.

For the experimental investigations, VCRC/EERC test rig is constructed. Temperature and pressure measurements are to be collected from various critical points to define the state of the refrigerant and make elaborate thermodynamic analyses based on the experimental data. The test rig has two operation options, namely VCRC and EERC modes. Consumed energy of the compressor and evaporator electrical heater is measured as well by energy analyzers. The secondary heat transfer fluid (SHTF) is water at the evaporator and condenser sides. With the adjustment of temperature and flow rate of the secondary heat transfer fluids (water) at the evaporator and condenser, various operation condition arrangements are created. Mass flow rates of the refrigerant flows, namely primary and secondary fluids (EERC operation mode), are determined from the consumed energy of the compressor per unit time and evaporation capacity.

## 1.4 Motivations of the Thesis

Starting from the Montreal Protocol (1987) and Kyoto Protocol (1997) to the European Directive 2006/40/EC (2006), EU Regulation No 517/2014 (2014), Paris

Agreement (2015), and Kigali Amendment (2016), environmental legislation always brings challenging targets about the ozone layer and global warming and this affects the refrigeration industry. Therefore, the working fluids to be used in the refrigeration systems are required to be environmentally-friendly. Although the refrigerant transition is the issue of the 90 years, it is more noticeable for the recent 25-30 years. These transitions not only bring about big changes in the selection criteria, but also essential developments in the refrigeration technology. Finding zero ozone depletion potential (ODP) and low-GWP refrigerant alternatives is of vital importance to the manufacturers of the refrigeration, heat pump, and air-conditioning industry.

The fourth generation refrigerants include zero or near-zero ODP and very low or ultra-low GWP candidates. However, low-GWP refrigerants could affect the efficiency of the VCRC adversely. Hence, it is possible to divide the effects of the working fluids into two categories as direct and indirect. Energy use of the refrigerants is indirect effect when compared to the refrigerant leakages or releases to the atmosphere. More comprehensive analyses such as Net Warming Impact (NWI), TEWI, and Life-Cycle Climate Performance (LCCP) declare that greenhouse gas (GHG) emissions resulted from the cycle energy consumption is higher than direct release of the refrigerants to the atmosphere. Thus, efficiency of the cycle is one of primary aspects for the refrigerant selection.

Especially R1234yf has lower COP in the conventional cycle when compared to the widely used refrigerant R134a which has a high GWP value and about to be phased out by the environmental legislation. Thus, replacement for R134a is obligatory and R1234yf is one of the most appropriate alternatives. Lower efficiency problem of R1234yf when compared to R134a could be solved decreasing the high throttling losses of R1234yf with the ejector expansion technology. To sum up, the need for high-efficiency cycles and environmentally-friendly refrigerant alternatives leads to the necessity of the elaborate numerical and experimental analyses regarding both the ejector and the overall cycle utilizing R1234yf as the working fluid.

The other driving forces to conduct this research is the need to increase the sensitivity of the thermodynamic models. The thermodynamic models in the literature generally include the efficiency of the motive nozzle, suction nozzle, and the diffuser in addition the compressor isentropic efficiency. Our investigations started from the same viewpoint as well. In the subsequent analyses ejector mixing section efficiency and liquid-vapor separator efficiency are added to the models. Not only entrainment ratio, area ratio, and performance improvement ratio; but also velocity and density ratio of the secondary stream to the primary stream are discussed.

The importance order of the efficiency parameters is also determined for the subcritical and transcritical EERC. Moreover, effects of the ejector component and liquid-vapor separator efficiencies are discussed based on the operating conditions by means of thermodynamic modelling approach for the first time. The primary finding for the literature contribution is that ejector design is more important than the appropriate operating conditions.

Furthermore, to define the highest performance improvement limits, the reversible ejector model is implemented into the EERC model and the constructed overall performance evaluation model under this assumption is new for the literature. The influence of the liquid-vapor separator efficiency on the ejector design is discussed for the first time. Characteristic behavior of the ejector is displayed for the CAM and CPM ejectors and the declarations of the refrigerant-independent behavior is unique to this thesis.

More realistic results could be calculated from the thermodynamic models when some of the assumptions, i.e. suction nozzle pressure drop, are replaced by the actual values. Suction nozzle pressure drop could not be calculated directly with reference to the thermodynamic modelling approach including no geometrical inputs. Hence it is to be defined based on the assumptions according to the pressure of the secondary fluid to be sucked into the ejector. The investigation on this assumption is not available in the literature. The current approaches to define this pressure are discussed in detail as the literature contribution of this thesis. Moreover, 1D model of the motive nozzle is implemented into the thermodynamic models, hence the pressure is calculated accurately with reference to the nozzle geometry and the operating conditions.

Two preliminary design models for the two-phase ejector of the EERC are established as the numerical outcomes of this thesis. One of them is fully based on the 0D thermodynamic models; whereas the other combines 1D model of the motive nozzle and 0D thermodynamic model of the EERC constituting a semi-1D modelling approach which is unique to this thesis. Experimentally validated semi-1D model is proposed as a useful preliminary performance and design evaluation tool for the EERC investigations.

## 1.5 Thesis Outline

This thesis is comprised of nine chapters as follows;

- In the first section titled "Introduction", the main points about the ejector and ejector expansion technology are summarized. Thesis objectives, motivations, and methodology are explained in the first introductory chapter. A brief summary of the thesis chapters is also given.
- The second chapter gives detailed information relative to the basics of the ejector operation and presents a comprehensive review of the previous studies about the various ejector refrigeration cycles, environmentally-friendly refrigerant alternatives, thermodynamic modelling, multidimensional ejector modelling, and experimental analyses.
- The third chapter declares the refrigerant alternatives compatible with the environmental regulations and the thermodynamic assessments on these candidate working fluids to make a reasonable selection among them. COP, second-law efficiency, and percentage exergy destruction in the expansion valve are compared for the alternative working fluids in the conventional VCRC.
- Chapter four describes thermodynamic models of the EERC with reference to constant area and constant pressure mixing ejector theories. Thermodynamic

model of the EERC is also established under reversible ejector assumption. Various refrigerant groups, i.e. refrigerants to be operated in the transcritical EERC and appropriate natural refrigerant candidates for the ejector expansion technology, are analyzed in this chapter although the target refrigerants are R1234yf and R134a.

- A preliminary design model based on the thermodynamic model of the constant area mixing ejector is constructed in Chapter five. The preliminary design model in this chapter is established according to optimum suction nozzle pressure drop assumption.
- Chapter six presents the flow analyses throughout the motive nozzle to calculate the properties of the refrigerants at the motive nozzle outlet with respect to the actual operating conditions and the nozzle design. Subcooling temperature difference, motive nozzle mass flow rate, inlet pressure, and motive nozzle outlet diameter are investigated parametrically in this section.
- Chapter seven introduces the semi-1D model combining 1D model of the motive nozzle and 0D thermodynamic model of the EERC. Hence, a modified preliminary design model is established based on this semi-1D modelling approach. The geometrical dimensions of a two-phase ejector are determined with the help of this preliminary design model. Furthermore, comparisons of the performance evaluation between the thermodynamic modelling approach and the semi-1D modelling approach are presented in this chapter.
- The construction of the EERC test rig is given in Chapter eight. Experimental performance analyses of R1234yf and R134a in the VCRC are displayed in this chapter. EERC tests are conducted for only R134a. Critical aspects having influence on the performance parameters of the EERC are discussed based on the experiments. Experiments of R134a in the EERC are used to validate the semi-1D model. Conventional cycle tests of R1234yf as well presented in this chapter to highlight the performance reduction when this new generation refrigerant is used instead of R134a.
- Chapter nine summarizes the main aspects of the thesis, concluding remarks, literature contributions, and potential future research targets.

- The technical drawings are given in Appendix-1. The proposed geometrical dimensions obtained from the semi-1D model are provided in this section for all ejector components.
- In Appendix-2, example calibration curves of the J-type thermocouples are given. Coefficients of the linearly fitted calibration curves for all thermocouples used in the set-up are tabulated in this section.
- In Appendix-3, the experiments for checking the repeatability of the set-up are given in detail.
- In Appendix-4, nomenclature is given.

# CHAPTER TWO

# THE BASICS OF THE EJECTOR AND LITERATURE REVIEW

Ejectors are not only used in refrigeration applications but also in many fields, e.g., nuclear reactors to supply emergency cooling water, chemical industry to pump hazardous substances, high energy chemical lasers, direct contact evaporative cooling, and aircraft propulsion systems for increasing the thrust. The first ejector dates back to 1858 and it is actually condensing-type injector invented by Henry Giffard. It was used to provide with the liquid water to refill the reservoir of the steam engine boilers. Mechanical pumps were not very reliable and they required the steam engine for their operation in order to supply water to the boiler. Therefore, the invention of Giffard solved the problem with the help of the condensing ejector since the motive steam which was the driving fluid to pump the liquid water was available as well during the standstill. The only disadvantage was about the configuration of the motive nozzle geometry for Giffard and other early ejector designers (Elbel & Hrnjak, 2008a).

Ejectors have been used in various applications after this first invention. In 1901, Parsons used the ejector to remove the non-condensable gasses from steam condensers for the first time making use of the vacuum capability of the ejector devices (Elbel & Hrnjak, 2008a). In this thesis, the target is focusing on the air-conditioning and refrigeration applications as hereinafter provided, hence further details are presented based on this viewpoint.

There are very important review studies on the experimental and numerical studies of the ejectors, different kinds of ejector refrigeration cycles, historical developments, and latest industrial applications, e.g. Chunnanond & Aphornratana (2004); Elbel & Hrnjak (2008a); Elbel (2011); Elbel & Lawrence (2016); Sarkar (2012); Sumeru, Nasution, & Ani (2012); Tashtoush, Al-Nimr, & Khasawneh (2019).

In this chapter, firstly the working principle of an ejector is explained in detail. Secondly, various ejector refrigeration cycle configurations are presented and the EERC concept is shown in detail with the governing *P-h* diagrams. The previous studies of the literature concerned with the refrigerants, thermodynamic modelling approaches, multi-dimensional ejector modelling, and lastly experimental analyses of the EERC are given in this section.

### 2.1 Fundamentals of the Ejector

Ejectors are preferred in various applications due to lack of moving parts, their simple construction, low cost, durability under multi-phase flow conditions, low maintenance cost, and long service life (Ersoy & Sag, 2014; Kornhauser, 1990; Liu, 2014). There are two kinds of ejector mixing theories as constant pressure and constant area mixing. The four basic sections of the ejector, namely motive nozzle, suction nozzle, mixing section, and diffuser, are shown in Figure 2.1 (a) and (b) displaying the schematic views of the constant pressure and the constant area mixing ejector theories, respectively with reference to Sumeru et al. (2012).

Motive nozzle is a typical converging-diverging nozzle in order to produce high-speed supersonic jet at the nozzle outlet. The condition is supposed to be supersonic at the motive nozzle outlet. However, motive nozzle had the converging form only for the early ejector applications and the flow reaches the sonic conditions at which the Mach number is equal to unity. The converging-diverging motive nozzle was invented in 1869 by an engineer named Schau. Actually, it was earlier than the de Laval's works which are the first experiments of the supersonic steam nozzles in 1890 (Elbel & Hrnjak, 2008a).

While the high-pressure primary fluid is passing through the motive nozzle, the velocity of the primary fluid increases and its pressure decreases. Hence the secondary fluid flow having relatively low pressure is sucked into the suction chamber. In other words, the flow of the suction fluid is induced by the primary fluid having low pressure at the primary nozzle exit. The interaction between the high-speed primary fluid and the secondary fluid starts in the suction chamber. The sucked fluid starts to be accelerated by the momentum transfer from the high-speed motive flow. The velocity of the total flow is still high at the exit of the mixing section and the diffuser is used to recover part of the kinetic energy in favor of pressure rise (Elbel & Hrnjak, 2008a).

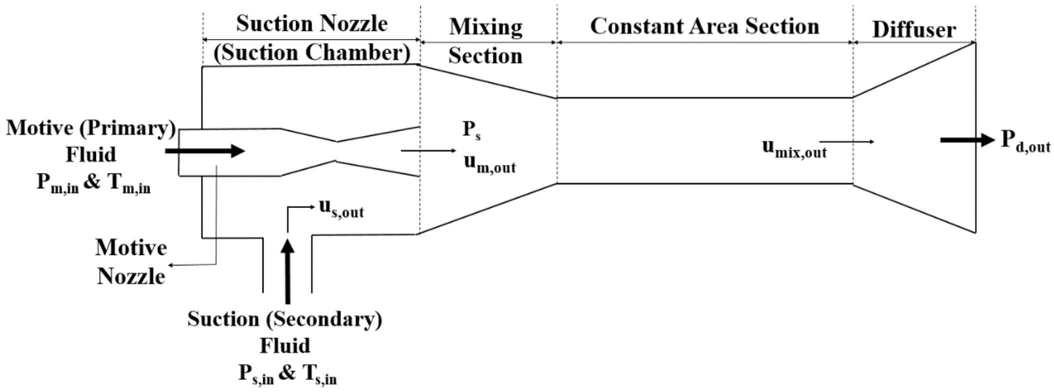


**(a)**

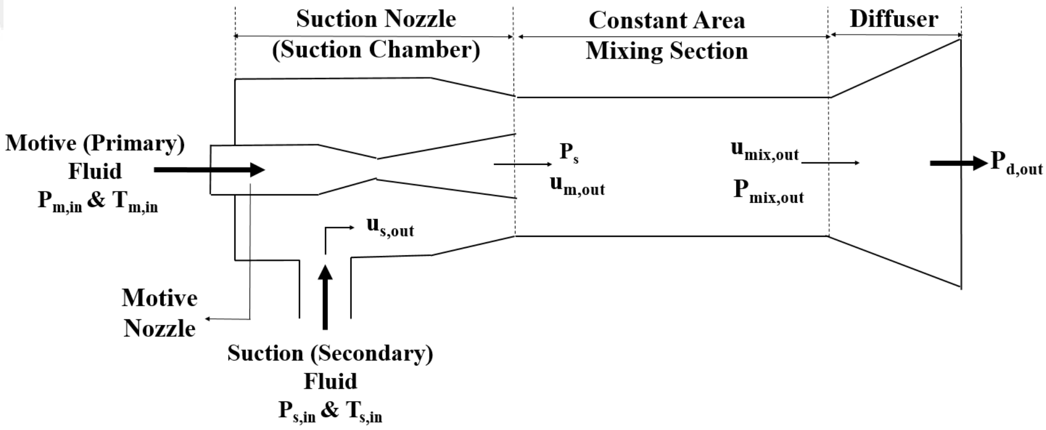


**(b)**

Figure 2.1 Schematic diagrams of (a) the CPM and (b) the CAM ejectors (Sumeru et al., 2012)

The mixing section has a constant cross-sectional area and generally the inlet of this section is tapered. CAM and CPM ejector theories arise from the modelling simplifications and assumptions (Elbel & Hrnjak, 2008a). As shown in Figure 2.1 (a) and (b), the ejector mixing section has a kind of cross-sectional geometry enabling constant pressure mixing process under the CPM ejector theory; whereas the primary and secondary refrigerant fluid flows directly meet at the inlet of the constant area mixing section through the CAM ejector theory. In CAM ejector theory, mixing process completely occurs in the constant area mixing section. When compared to CPM assumption, the pressure of the total flow increases at the outlet of the mixing section with respect to the CAM approach.

Ejectors investigated numerically and experimentally based on the realistic designs for the refrigeration applications in the literature are typically represented by the CAM ejector theory (Banasiak & Hafner, 2011; Ersoy & Sag, 2014; Palacz et al., 2016; etc.). There may be a pre-mixing chamber (the tapered inlet) as well before the constant area mixing section in some of the actual designs (Elbel & Hrnjak, 2008a). However, proposing designs based on the CPM approach as in the study of Sherif, Lear, Steadham, Hunt, & Holladay (2000) is also appropriate.

Sherif et al. (2000) selected CPM theory assuming that the mixing section outlet pressure was equal to the pressure of the secondary fluid at the exit of the secondary flow tube (the pressure along the slanted sides) since it yielded a bit higher compression ratios in the jet pump when compared to CAM approach. The schematic diagram of the CPM ejector proposed by Sherif et al. (2000) and given in Figure 2.2 is different than the schematic view established by Sumeru et al. (2012). The CPM ejector (jet pump) in Figure 2.2 includes the design details and the notation is directly the same as the original paper. All symbols are explained in the figure since the notation of this thesis is different from the figure. The CAM and CPM ejector mixing theories are evaluated for the performance analyses, but only CAM approach is considered for the rest of design issues of this thesis since ejector design based on the CPM requires a series of design points according to the operating conditions in order to satisfy the mixing process at the constant pressure.

All in all, the ejector could be thought as a fluid pump driven by the motive fluid flow in order to increase the pressure of the sucked (entrained) flow. Two essential performance parameters, namely the entrainment ratio and the suction pressure ratio (pressure lift ratio), are expected to be as high as possible for a well-designed ejector. Entrainment ratio is the ratio of the secondary fluid mass flow rate to the primary fluid mass flow rate; whereas suction pressure ratio is the ratio of the diffuser outlet pressure to the secondary fluid pressure to be sucked into the ejector (Elbel & Hrnjak, 2008a). Entrainment ratio (w) and suction pressure ratio ($P_{lr}$) is respectively formulated below as follows;

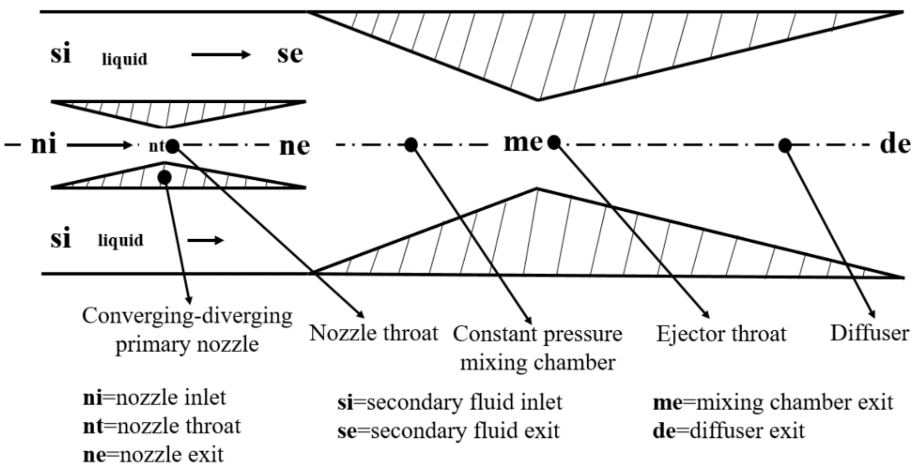


Figure 2.2 Schematic view of the constant pressure ejector (Sherif et al., 2000)

$$w = \frac{\dot{m}_s}{\dot{m}_m} \tag{2.1}$$

$$P_{lr} = \frac{P_{d,out}}{P_{s,in}} \tag{2.2}$$

The term *injector* sometimes could be used instead of the term *ejector* according to the range of the diffuser outlet pressure. For an ejector, the diffuser outlet pressure is closer to the suction fluid pressure when compared to the pressure of the motive fluid. The injector is used for the applications having diffuser outlet pressure close to the motive fluid pressure rather than the pressure of the suction fluid. There are some more definitions as well to be used instead of the ejector such as *eductor*, *diffusion pump*, *aspirator*, and *jet pump* (Elbel & Hrnjak, 2008a).

Lastly, classification of the ejectors according to motive and suction fluids having the same chemical composition (single component) is presented in Table 2.1 by Elbel & Hrnjak (2008a). In the vapor jet ejector, both of the motive and suction fluids are vapor and the exit flow as well is vapor. Two-phase flow can occur and formation of the shock waves is possible in the vapor jet ejectors. Motive and suction fluids and the total fluid at the ejector exit are all in liquid state in the liquid jet ejector. Single-phase flow without shock waves is observed in this type ejectors. Condensing ejectors include driving flow in vapor phase, driven flow in liquid phase, and total flow in liquid phase. Strong shock waves occur and two-phase flow is observed due to the condensation of driving vapor. The two-phase ejector which is used as the throttling device in the EERC has motive fluid in liquid phase, suction flow in vapor phase, and the total flow in two-phase. Shock waves are also possible.

Table 2.1 Classification of the single-component flow ejectors (Elbel & Hrnjak, 2008a)

| | **Driving flow** | **Driven flow** | **Exit flow** |
|---|---|---|---|
| **Vapor jet ejector** | Vapor | Vapor | Vapor |
| **Liquid jet ejector** | Liquid | Liquid | Liquid |
| **Condensing ejector** | Vapor | Liquid | Liquid |
| **Two-phase ejector** | Liquid | Vapor | Two-phase |

## 2.2 Overview of the Ejector Refrigeration Cycles and EERC

There are two basic ejector refrigeration cycle concepts as heat-driven ejector refrigeration cycle and EERC. Heat-driven ejector refrigeration cycle uses a vapor jet ejector and the refrigeration effect is produced making use of low-grade energy, i.e., renewable energy resources or waste energy. This concept was introduced by Leblanc in 1910. The latter configuration is introduced for the first time by Gay in 1931 (Gay, 1931) conceptually in order to explain the use of the two-phase ejectors in the refrigeration cycles to decrease the expansion losses (Elbel & Hrnjak, 2008a). The proposed cycle by Gay is accepted as the standard two-phase EERC by the literature (Lawrence, 2012). Kemper et al. (1966) patented a new and improved multiple-phase ejector refrigeration cycle minimizing the inefficiencies resulting from the heat and momentum transfer. Additional achievements concerned with the controls of the cycle yielded two more patents by Newton (1972a, 1972b) (Kornhauser, 1990).

As seen from the chronological order of the advances in the EERC technology, although some more patented works related to the modified versions of the standard two-phase EERC followed the patent of Gay, the modifications in question could not be tested and adapted widely. The reason for this situation is the need for understanding the standard EERC comprehensively as the primary step (Lawrence, 2012). All in all, after brief historical background of the two widely-known ejector refrigeration cycles, the details of both cycles are given comprehensively in this section. Moreover, two different ejector refrigeration cycle concepts as well are introduced although they are out of the scope of this thesis.

### *2.2.1 Heat-driven Ejector Refrigeration Cycle*

Heat-driven ejector refrigeration cycle or vapor jet refrigeration cycle is used to harness low-grade heat resources or renewable energy resources such as solar heat. When this configuration was first proposed by Leblanc in 1910, it started to be preferred in the air-conditioning of large buildings and railroad cars due to the availability of the steam. The schematic view of the heat-driven ejector refrigeration cycle concept is given in Figure 2.3 with reference to Yapıcı & Ersoy (2005). Vapor-jet ejector is used in this cycle as the name implies.

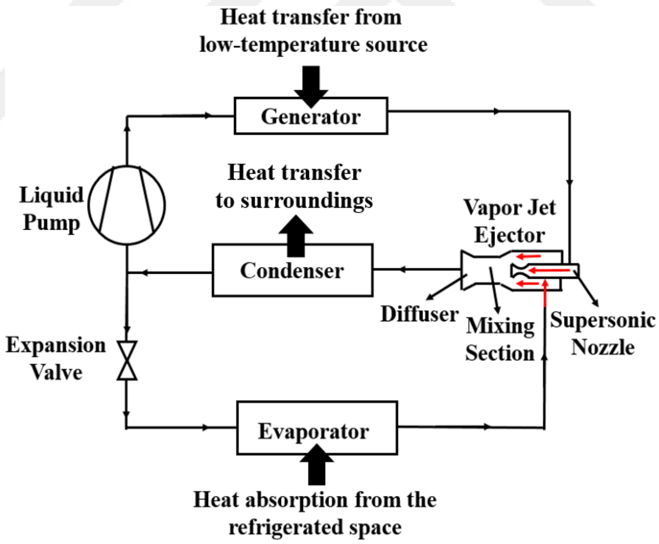


Figure 2.3 Schematic display of the heat-driven ejector refrigeration cycle (vapor jet refrigeration cycle for utilization of a low-grade energy source) (Yapıcı & Ersoy, 2005)

Some part of the refrigerant coming from the condenser goes through the liquid pump in order to have a higher pressure before entering the generator. This portion sending to the generator is the motive fluid of the cycle. The low-grade energy source is used in the generator to heat the motive fluid isobarically. The refrigerant is vaporized in the generator and it enters the motive nozzle in vapor state. The vapor refrigerant expands while passing through the motive nozzle. Therefore, the refrigerant has a high velocity at the outlet of the motive nozzle thereby creating a low-pressure region. The refrigerant even be in two-phase state at the outlet of the motive nozzle according to its temperature at the outlet of the generator exit.

The secondary flow coming from the evaporator is in vapor state and sucked into the suction chamber. Due to the momentum transfer between the motive and suction fluid flows, the suction fluid is accelerated. After the mixing section, the pressure of the total flow is increased more in the diffuser. After the total flow leaves the ejector, it is condensed at constant pressure. Some portion of this total flow again goes through the pump, and the rest is sent to expansion valve to decrease its pressure to the evaporator pressure. Hence this secondary fluid stream is called as the suction fluid and it absorbs heat from the refrigerated space while flowing through the evaporator. After exiting from the evaporator, the suction fluid is entrained into the ejector and completes its own cycle.

There are both advantages and disadvantages concerned with this concept. According to Ouzzane & Aidoun (2003), an ejector, a liquid pump, and a vapor generator could be used instead of the compressor in the vapor jet ejector refrigeration cycle concept. This cycle utilizes the waste heat or renewable energy resources as the low-grade energy sources. Less work is required for a liquid pump in comparison with the compressor work for the same pressure range. There is no need for the lubrication since compressor is replaced with the pump, hence all negative effects relative to lubrication are eliminated. However, the COP of the vapor jet refrigeration cycle is comparatively low (Elbel & Hrnjak, 2008a).

### *2.2.2 Ejector Expansion Refrigeration Cycle*

The environmental characteristics of the refrigerants such as their ODP and GWP are considered owing to the requirements of the officially compelling regulation while selecting a working fluid for a refrigeration system. Therefore, the new working fluid alternatives are sought. Carbon dioxide (R744 or $CO_2$) seems a very good solution to this problem; and implementing an ejector into the refrigeration cycle to improve the efficiency of the transcritical $CO_2$ cycle by decreasing the throttling losses started to be considered after the transcritical $CO_2$ systems have become widespread in the late 1980s (Elbel & Hrnjak, 2008a).

As seen from Figure 2.4 (b), the compressed liquid or saturated liquid coming from the condenser is the motive fluid and the superheated vapor or saturated vapor coming from the evaporator is the suction fluid. Since the motive fluid is in liquid phase and the suction fluid is in vapor phase, two-phase ejector is used in the EERC. Figure 2.4 displays the comparison of the classical VCRC and the EERC. The first advantage of the ejector in the EERC compared to VCRC is the reduction in the compressor work due to the increase in the compressor inlet pressure. The reduction in the pressure ratio of the compressor increases the isentropic efficiency as well. Secondly, the increment in the volumetric cooling capacity (VCC) of the evaporator is the other aspect improving the overall performance of the cycle.

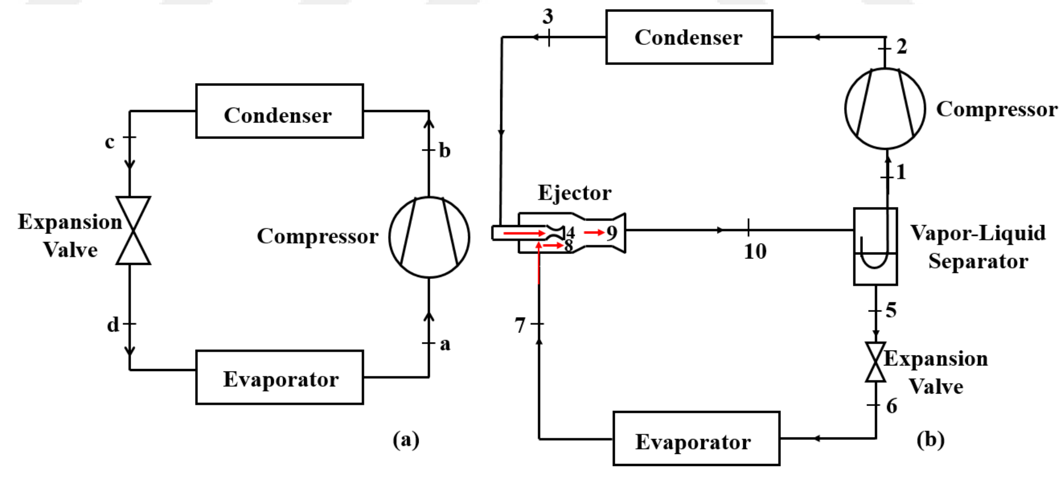


Figure 2.4 Comparison of (a) the VCRC and (b) the EERC (Kornhauser, 1990)

The motive fluid flows through the motive nozzle after the heat removal at the condenser. Using the pressure related energy and internal energy of the high-pressure condenser fluid, the pressure of the evaporator fluid is increased to some degree. After the entrainment of the secondary fluid and the mixing process, the total flow velocity is still fairly high. As it is seen also from the schematic views of the CAM and CPM ejectors in Figure 2.1 (a) and (b), a diffuser is used to recover the rest of the kinetic energy to provide more pressure rise.

The total flow, which is saturated vapor-liquid mixture, goes through the liquid-vapor separator. Vapor and liquid portions of the two-phase total flow are separated and sent to compressor and evaporator, respectively. Actually, the separation capability of the liquid-vapor separator depends on the efficiency of the separator and this issue would be investigated comprehensively in the subsequent sections. For a liquid-vapor separator having 100% liquid and vapor separation efficiencies, the saturated vapor refrigerant and the saturated liquid refrigerant leave the separator and then enter the compressor and the evaporator, respectively.

Since the total fluid at the outlet of the diffuser has a higher pressure than the evaporator pressure, the suction fluid, which is in saturated liquid phase, firstly passes through a small-scale expansion valve. Hence, the saturated liquid at the outlet of the separator is throttled to the evaporation pressure. The suction fluid absorbs heat from the refrigerated space while passing through the evaporator and it is entrained into the ejector completing its cycle. Similarly, the motive fluid which is in saturated vapor is compressed to the condensation pressure. After heat removal process at the condenser, the motive fluid enters the motive nozzle closing its loop.

All the steps and processes are summarized in the *P-h* diagrams given in Figure 2.5 (a) and (b) (Atmaca et al., 2019a). The mixing processes are also distinguished in the *P-h* diagrams (Klein, 2017) for the EERC using R1234yf as the working fluid. Figure 2.5 (a) and (b) shows the CPM and CAM processes, respectively. The notation in Figure 2.4 and Figure 2.5 is the same for the VCRC and the EERC. Therefore, the mixing processes are denoted from points 4 (state of the motive flow) and 8 (state of the suction flow) to the point 9 (the state of the total flow). In Figure 2.5 (a), the pressure does not change during the mixing process; whereas in Figure 2.5 (b) the mixing of the refrigerants is accompanied by a pressure increase (Atmaca et al., 2019a).

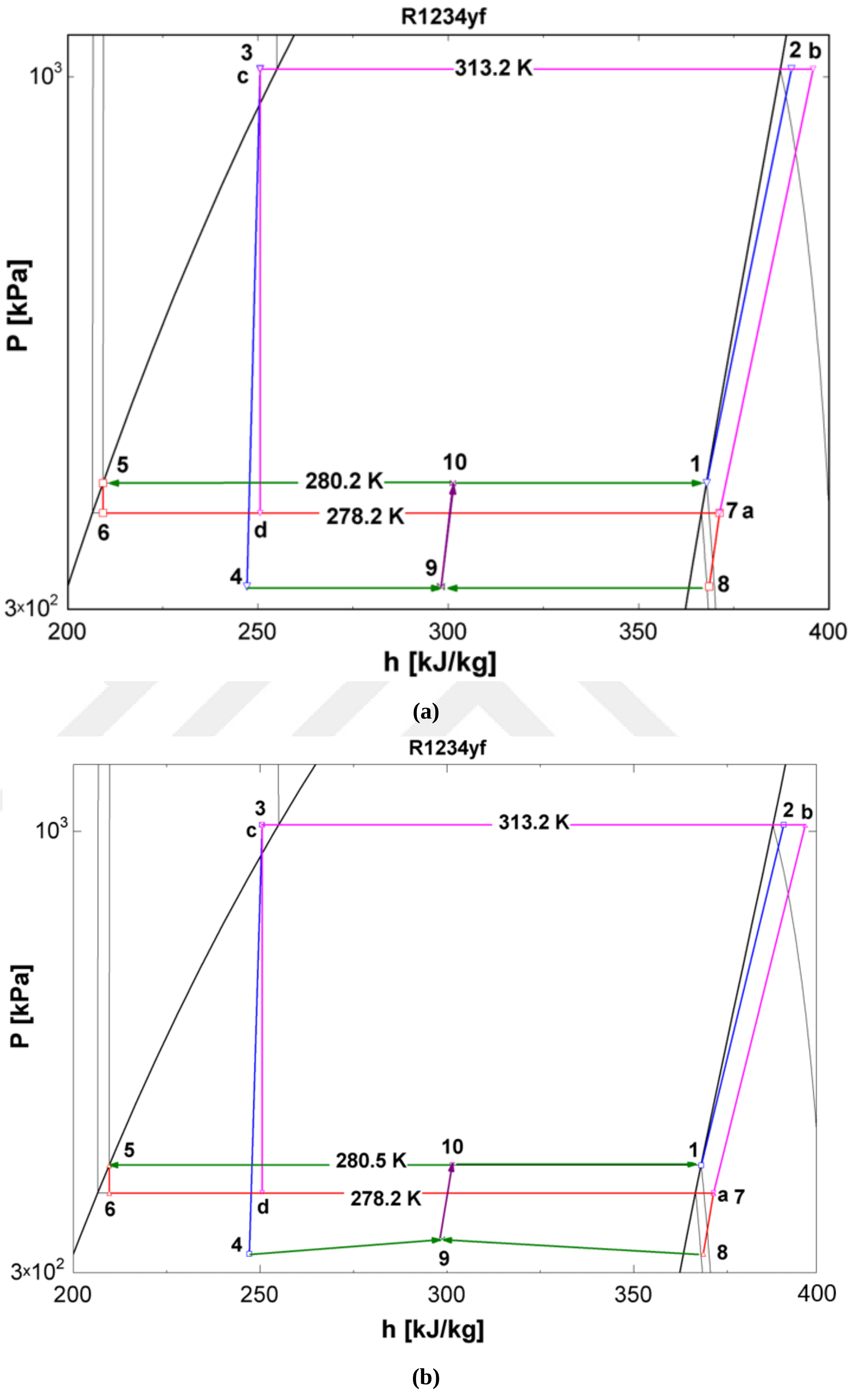


**(a)**



**(b)**

Figure 2.5 *P*-*h* diagrams of the EERC utilizing R1234yf with reference to (a) CPM and (b) CAM ejectors (Atmaca et al. 2019a)

*2.2.2.1 Expansion of the Motive and Suction Fluid Flows*

Constant enthalpy lines are nearly parallel to the lines of constant entropy in the low-quality two-phase region, while the slope of the constant entropy lines and constant enthalpy lines are completely different from each other in the high-quality two-phase region (Kornhauser, 1990). It is obvious from the *P-h* diagrams of R134a and R1234yf (Klein, 2019) given in Figure 2.6 (a) and (b), respectively. When the constant entropy lines are followed both in the low-quality and the high-quality two-phase regions from the given example *P-h* diagrams, it could be understood that expansion through an isentropic nozzle between the same pressure range yields larger enthalpy difference, and hence greater velocity change for a high quality fluid when compared to a low quality fluid. When the application of the two-phase ejector in the EERC is considered, the motive fluid which is in the saturated liquid or compressed liquid phase expands between a large pressure difference; whereas the suction fluid in saturated vapor or superheated vapor phase expands across a small pressure range.

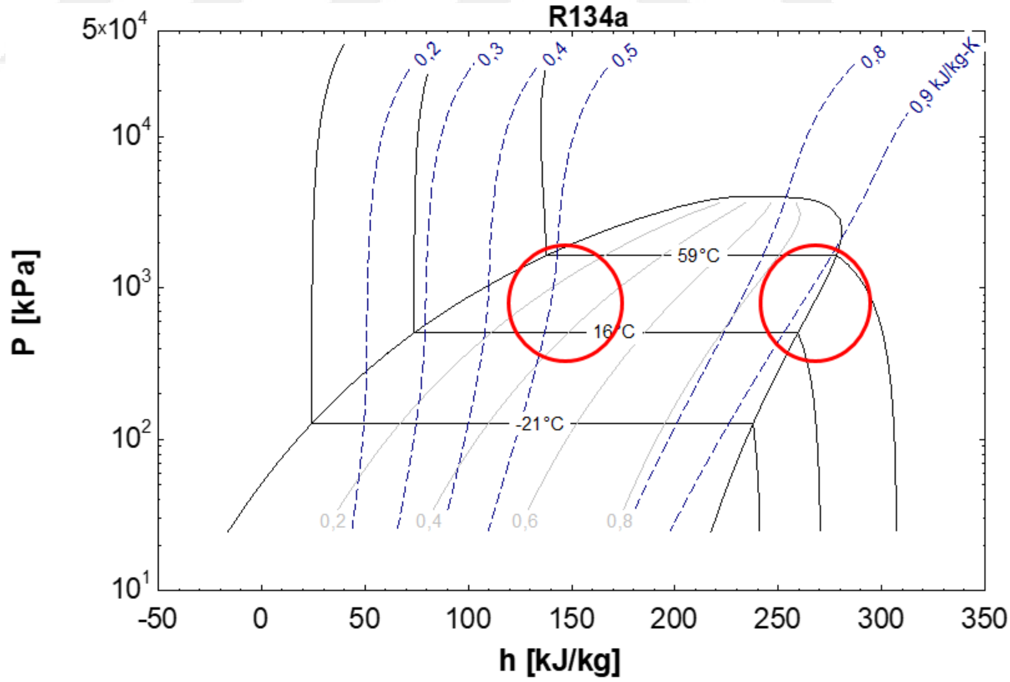


**(a)**

Figure 2.6 Characteristics of the expansion processes at the high quality and low quality two-phase regions for (a) R134a and (b) R1234yf

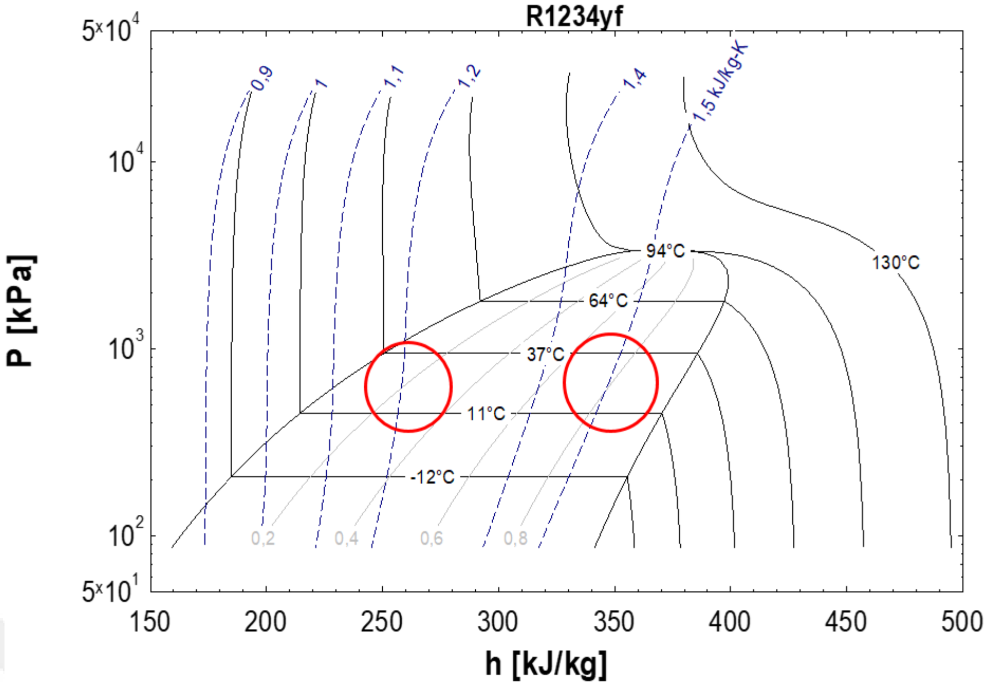


**(b)**

Figure 2.6 continues

The efficiencies of the expansion processes are introduced into the thermodynamic models as constant values and it would be expressed in detail in the following chapters. Figure 2.7 displays the comparison between the isentropic and actual expansion processes. Hence, the efficiency of the motive and suction nozzles are defined clearly. Mollier diagram (*h-s* diagram) for the isentropic and actual expansion processes in Figure 2.7 is given for R1234yf. It is obvious that the enthalpy difference as a result of the isentropic expansion is larger than that of an actual expansion for the same pressure range. Thus, the efficiency formulations of the motive and suction nozzles based on the negligible inlet velocity are defined as follows (Dixon, 1998);

$$\eta_m = \frac{h_{m,in} - h_{m,out}}{h_{m,in} - h_{m,out,isen}} \tag{2.3}$$

$$\eta_s = \frac{h_{s,in} - h_{s,out}}{h_{s,in} - h_{s,out,isen}} \tag{2.4}$$

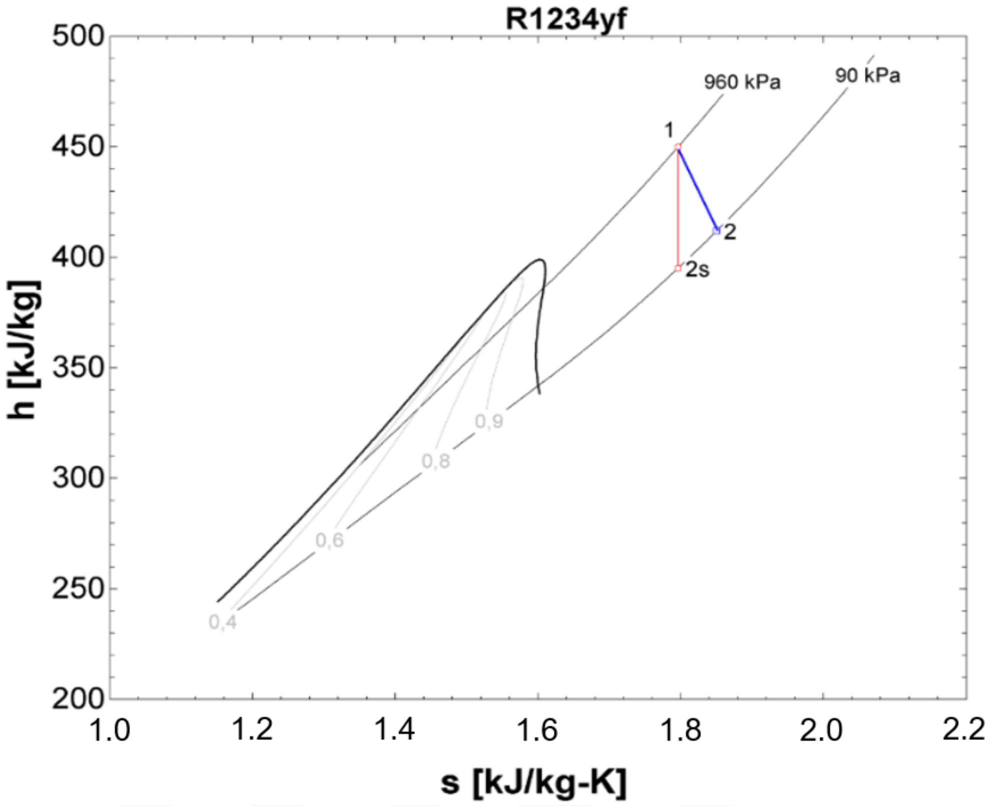


Figure 2.7 Actual and isentropic expansions through a nozzle operating between 960 kPa and 90 kPa for R1234yf

### *2.2.2.2 Compression of the Total Mixed Flow throughout the Diffuser*

The *h-s* diagram of R1234yf is provided in Figure 2.8 in order to exemplify the isentropic and actual compressions of the total mixed flow throughout the diffuser. Therefore, the diffuser efficiency is defined accordingly (Dixon, 1998).

$$\eta_d = \frac{h_{d,out,isen} - h_{d,in(mix,out)}}{h_{d,out} - h_{d,in(mix,out)}} \tag{2.5}$$

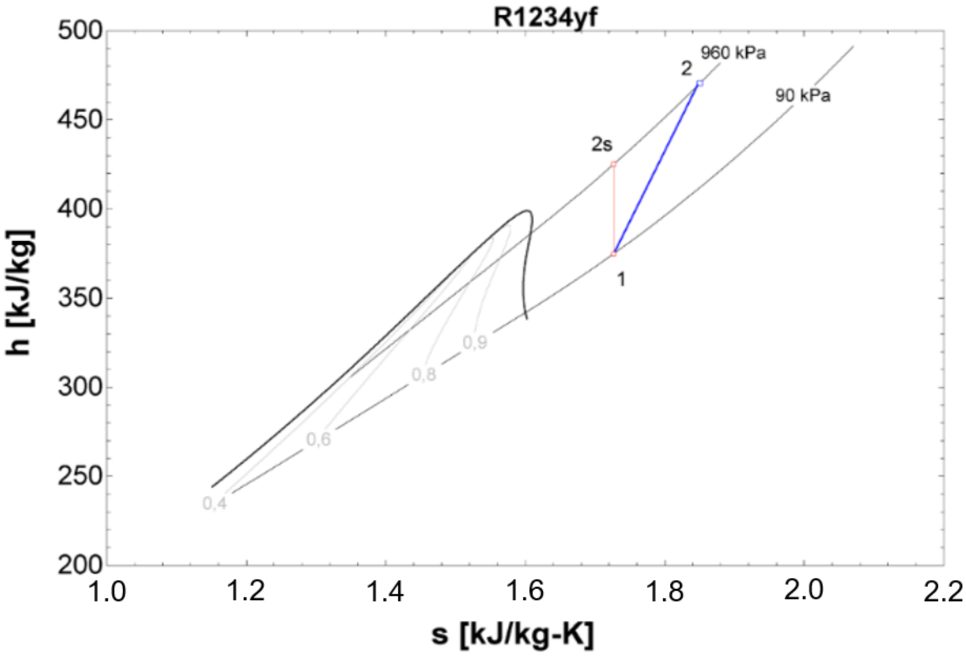


Figure 2.8 Comparison of the actual and isentropic compressions in terms of inlet and outlet enthalpy differences through a diffuser operating between the same pressure range of the expansion case

### *2.2.3 Alternative Ejector Refrigeration Cycle Configurations to Eliminate Liquid-Vapor Separator*

Two alternative cycles including the two-phase ejector to decrease the throttling losses were patented by Oshitani et al. (2005) and Burk et al. (2006) with reference to Lawrence (2012). The cycle proposed by Oshitani et al. (2005) is named as condenser outlet split (COS) ejector refrigeration cycle and the schematic of the cycle is shown in Figure 2.9. As the name implies, the liquid refrigerant at the outlet of the condenser is diverged into two branches. The first refrigerant stream is sent to the ejector as the motive fluid of the cycle and it expands isentropically. The second stream is throttled isenthalpically by an expansion valve to a lower pressure. After the second stream leaves the low-temperature evaporator, it is sucked into the ejector as the secondary fluid of the ejector refrigeration cycle. Hence, primary and secondary refrigerant flows are mixed inside the ejector. The two-phase refrigerant flow at the outlet of the diffuser passes through a second evaporator having a higher pressure when compared to the firstly mentioned one through which the secondary fluid of the cycle flows. Later on, it is compressed to the condenser pressure and enters the ejector after the heat removal occurred in the condenser. As a result, both the motive and suction fluid flows complete their loops.

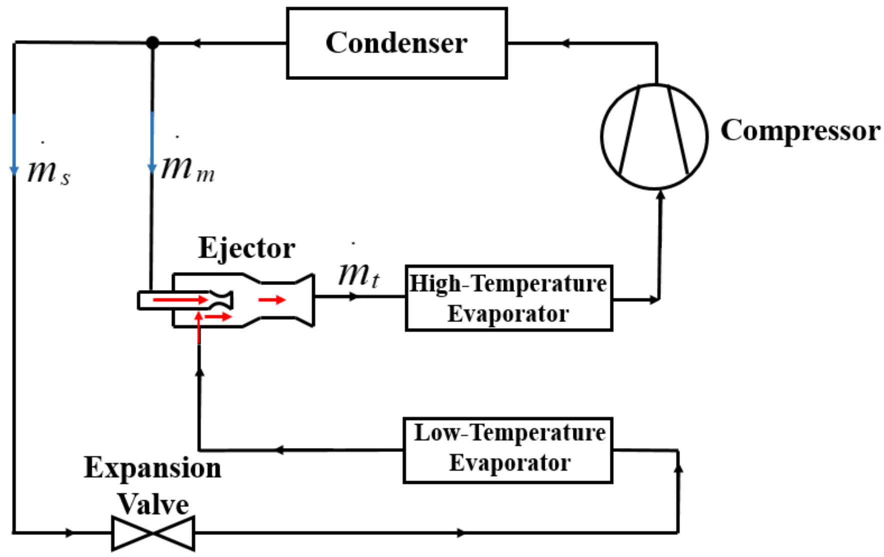


Figure 2.9 Schematic view of the COS ejector refrigeration cycle (Oshitani et al., 2005)

Since the two-phase flow at the outlet of the ejector directly enters the high-temperature evaporator before the compressor, there is no need to use a liquid-vapor separator. Since the pressure of the total flow at the outlet of the ejector is higher than the sucked fluid (suction side), this cycle configuration requires the implementation of two separate evaporators operating at low and high pressures.

The cycle proposed by Burk et al. (2006) is named as diffuser outlet split (DOS) ejector refrigeration cycle as shown in Figure 2.10. This time two-phase refrigerant flow is divided into two streams at the outlet of the diffuser. The first stream which is the motive fluid of the cycle directly enters an evaporator and compressed to the condenser pressure. After heat removal process at the condenser, it flows through the motive nozzle.  The second stream is the suction fluid of the cycle and throttled to slightly a lower temperature and pressure. Hence, it passes through a lower-temperature evaporator and after the heat absorption process throughout the evaporator, it is sucked into the ejector completing its own loop. Similar to previously defined COS cycle concept, the DOS ejector refrigeration cycle does not need a liquid-vapor separator and it includes two evaporators operating at different pressures.

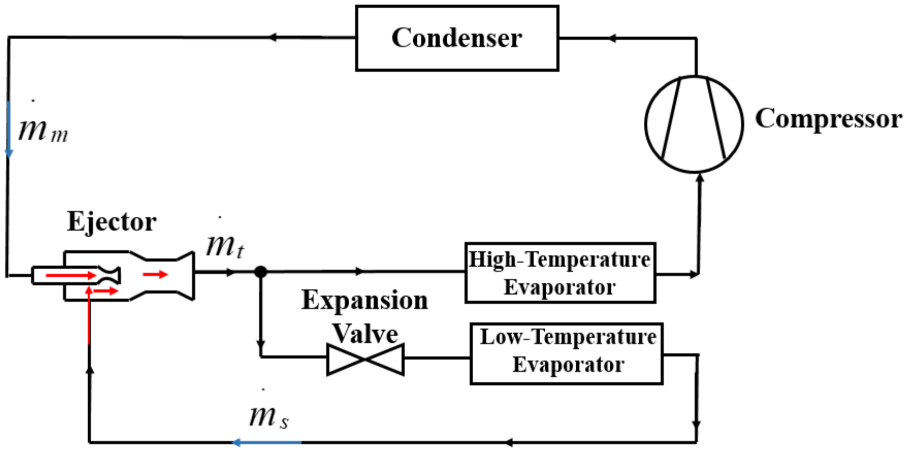


Figure 2.10 Schematic view of the DOS ejector refrigeration cycle (Burk et al., 2006)

Vapor and liquid separation efficiencies affect both the ejector and overall cycle performances as hereinafter described in detail. All in all, after taking all details into consideration with respect to both COS and DOS ejector refrigeration cycle concepts, they are advantageous since the efficiency of the liquid-vapor separator is eliminated (Lawrence, 2012; Lawrence & Elbel, 2013).

## 2.3 Refrigerants

Montreal Protocol approved in 1987, the Kyoto Protocol signed in 1997, the European Directive 2006/40/EC (Directive 2006/40/EC, 2006), EU Regulation No 517/2014 (Regulation (EU) No 517/2014, 2014), Paris Agreement accepted in 2015, and Kigali Amendment entering into force from the beginning of 2019 have promoted the developments of the environmentally-friendly refrigerants having zero ODP and low GWP. In this section, the previous analyses from the literature relative to the refrigerants are summarized.

Based on the limitations of the EU Regulation No 517/2014, Mota-Babiloni, Navarro-Esbrí, Barragán-Cervera, Molés, & Peris (2015) analyzed theoretically alternative refrigerant mixtures of the Air-Conditioning, Heating, and Refrigeration Institute (AHRI) comprising of hydrofluorocarbons (HFCs) (R32, R125, R152a and R134a) and HFOs (R1234yf and R1234ze(E)). They showed that the analyzed HFCs performed better than most of the proposed HFC/HFO mixtures. Moreover, most of the proposed mixtures still could not fulfill the GWP requirement of the European legislation and some of them had the flammability problems as well. Mota-Babiloni et al. (2016) investigated the literature studies associated with one of the HFO refrigerants, R1234ze(E). The review of this promising refrigerant included thermophysical and compatibility properties, heat transfer and pressure drop characteristics, and vapor-compression system performance.

Pigani, Boscolo, & Pagan (2016) investigated theoretically ammonia ($NH_3$), carbon dioxide ($CO_2$), R1234yf, and R1234ze(E) as a substitute for R407F in existing marine refrigeration plants. They concluded that none of the refrigerants in question are satisfactory in terms of safety, efficiency, volumetric capacity and TEWI. As far as the present authors are concerned, not only GWP, but also TEWI must be considered selecting the refrigerants. Motta, Bercerra, & Spatz (2010) investigated R1234yf and R1234ze having atmospheric lifetimes of 11 and 18 days, and subsequently low GWP values of 4 and 6, respectively in small refrigeration equipment, i.e., vending systems. Corresponding atmospheric lifetime of 12 years and GWP values of 1410 for R134a show the necessity of using these HFO group refrigerants. They showed that HFO fluids could be applied such kind of small systems utilizing R134a without significant system modification.

Pham & Rajendran (2012) investigated R32 and HFO blends both theoretically and experimentally as the potential replacement for R410A. It was stated in their research that pure R1234yf and R1234ze could not be an efficient substitute for R410A since a redesign process including larger compressor, piping and heat exchangers, and added cost to compensate for the high pressure drop would be required. According to their preliminary test results of HFO blends, they were not superior to R32. Jarall (2012) also conducted an experimental and theoretical study on a refrigeration system with a hermetic rotary compressor employing R1234yf as the working fluid by means of a comparative approach with R134a. The authors also showed that subcooling or superheating had a more powerful effect on the cycle using R1234yf than the system with R134a.

Zilio, Brown, Schiochet, & Cavallini (2011) showed experimentally that the performance of the refrigeration systems employing R1234yf was lower than the ones having R134a. Therefore, they investigated numerically the effects of the required modifications to catch the performance levels of R134a systems for a given cooling capacity. They emphasized that R1234yf is a potential substitute for R134a in the automotive applications. McLinden, Kazakov, Brown, & Domanski (2014) presented 62 candidate refrigerants by means of their thermodynamic properties, their stability, toxicity, flammability, and environmental characteristics. The results were not promising since each fluid has its own advantages and disadvantages. Two HFOs, namely R1234yf and R1234ze(E), having low toxicity and mild flammability, were also highlighted as the promising candidates.

Musser & Hrnjak (2014) worked with the refrigerants R744 and R445A (simulated as R134a and R744 blend) and highlighted the importance of the system control and optimization to achieve the maximum performance. Bivens & Minor (1998) investigated fluorinated ethers, alcohols, amines, silicon, and sulfur compounds utilizing the literature findings in terms of toxicity, flammability, stability, atmospheric lifetime, refrigeration performance, and manufacturing issues and the cost of the fluids to propose zero ODP alternatives to the HFCs. Wu, Liang, Tu, & Zhuang (2012) analyzed theoretically the performance of the thermodynamic cycle utilizing R161 as the working fluid of an air-conditioner to make comparison among R161, R22, and R290 for a wide range of operation conditions. Moreover, R22 and R161 were analyzed experimentally under various operation conditions. Aprea, Greco, & Maiorino (2016) conducted experiments to compare the energy performance of a domestic refrigerator utilizing R134a and its drop-in replacement, R1234yf. Yataganbaba, Kilicarslan, & Kurtbaş (2015) carried out an exergy analyses on the components of a two evaporator vapor-compression refrigeration system for R134a, R1234yf, and R1234ze to make analyses basically regarding the effects of the operation conditions on the system losses and to propose alternative refrigerants to R134a.

Mota-Babiloni, Navarro-Esbrí, Barragán, Molés, & Peris (2014) investigated experimentally the energy performance of R1234yf, R1234ze(E), and R134a for various combinations of condensation and evaporation temperatures and with/without internal heat exchanger configurations. The effects of the parameters on the volumetric efficiency, cooling capacity, and COP were displayed to compare the HFOs with R134a in main. Navarro-Esbrí, Mendoza-Miranda, Mota-Babiloni, Barragán-Cervera, & Belman-Flores (2013) carried out experiments to investigate the energy performance of the refrigerants R134a and R1234yf on a comparative basis considering the effects of the condensation and evaporation temperatures, the superheating degree, the compressor speed, and the internal heat exchanger use. Molés, Navarro-Esbrí, Peris, Mota-Babiloni, & Barragán-Cervera (2014) investigated six various single stage vapor-compression refrigeration cycle configurations to compensate for the performance decrease of R1234yf and R1234ze(E) when compared to the performance of the R134a in the conventional cycle.

As for the high pressure refrigerant alternatives, R41 and $CO_2$ are similar to each other in terms of the physical properties and they have nearly the same normal boiling points (NBP) (Wang, Lu, & Tao, 2017); whereas R170 and $CO_2$ have very close critical temperatures. Lorentzen (1995) highlighted the superiority of $CO_2$ when compared to the other natural refrigerants such as ammonia, isobutane, etc. owing to its good environmental characteristics, non-toxicity, non-flammability, and excellent thermophysical properties. However, another hindrance of the systems utilizing $CO_2$ is the huge throttling losses resulting in decrease in the cycle performance (Dai, Dang, Li, Tian, & Ma, 2015). Wang, Lu et al. (2017) analyzed the application of the azeotropic refrigerant mixture of $CO_2$ and R41 in different systems, namely a refrigerated cabinet, a water-source and air-source heat pump water heaters under various operation conditions. One of the problem of the pure $CO_2$ is the high operation pressures; whereas the limitation of pure R41 is the flammability. Wang, Lu et al. (2017) stated that the reason for making blends of them is proposing a refrigerant mixture having lower flammability and lower operation pressures in comparison with the pure working fluids.

As seen from the summarized literature, there are plenty of studies focusing on the performance analyses of R1234yf, R1234ze(E), and R134a. In this thesis, R1234yf and R1234ze(E) from the HFOs are selected intentionally due to the GWP restrictions concerned with the fluorinated gases. However, R134a, one of the widely used refrigerants before F-gas Regulation, is analyzed to create a comparative base though it is about to be phased out by the environmental legislation. Benefiting from this literature review related to working fluids, a candidate refrigerant list is proposed in the next chapter. All in all, the most appropriate refrigerants for the EERC concept are chosen according to energy and exergy analyses of these working fluids in the conventional VCRC. The comprehensive further analyses are conducted considering the core refrigerants defined according to the results of those energy and exergy analyses. Additionally, R744, R170, and R41 are selected for the transcritical VCRC and EERC investigations to widen the scope of the thesis due to the lack and necessity of the comparisons between these three refrigerants in the literature.

### 2.4 Thermodynamic Modelling of the EERC for the Performance and Design Evaluation

The literature review concerned with the thermodynamic models consist of three sections as follows; (i) thermodynamic analyses of the EERC for performance evaluations, (ii) reversible ejector approaches, and (iii) thermodynamic models for both performance and design analyses. Firstly, studies from the literature are summarized and then the investigations completed within the content of this thesis are presented.

Thermodynamic analyses are the crucial part of this thesis, hence a comprehensive review is given to highlight the contributions of this thesis to the literature. To present performance analyses of the EERC, 0D thermodynamic modelling is one of the options and they are established with reference to different mixing assumptions, i.e., CPM and

CAM. CPM assumption was first used by Kornhauser (1990) and CAM approach was established for the first time by Li & Groll (2005) while creating the model of the EERC (Elbel & Lawrence, 2016).

Kornhauser (1990) analyzed the performance improvement potential of various refrigerants, e.g., R11, R12, R22, and R113, in the EERC with respect to CPM assumption. Efficiency of the motive nozzle, suction nozzle, diffuser, and compressor were assumed as the constant values, and hence the irreversibilities within the system are taken into account by means of these specified values. The mixing efficiency was assumed to be equal to unity. The effects of the ejector component efficiencies were investigated as well. Li & Groll (2005) made analyses on the transcritical $CO_2$ EERC assuming that the mixing process occurred completely in the constant-area mixing section. Moreover, they proposed a new EERC configuration to establish a compromise between the entrainment ratio and the quality of the total flow at the diffuser outlet. The influence of the operating parameters, namely gas cooler pressure, gas cooler outlet temperature, evaporator temperature, evaporator outlet superheat temperature difference with respect to evaporation temperature ($\Delta T_{sh}$) on the performance improvement were displayed for various entrainment ratio values.

Bilir & Ersoy (2009) made thermodynamic investigations on the two-phase ejector for R134a according to CAM ejector assumption. Their model was established with reference to the model of Li & Groll (2005). They analyzed the effect of the suction nozzle pressure drop on the COP and diffuser outlet pressure. Variations of the optimum area ratio (ratio of the cross-sectional area of the constant-area mixing section to the cross-sectional area of the motive nozzle outlet), optimum suction nozzle pressure drop, entrainment ratio, and performance improvement were displayed according at various operating conditions. Moreover, some of the results were presented at the off-design conditions and they concluded that EERC performs better than the conventional cycle even out of the optimum operating point.

Nehdi, Kairouani, & Bouzaina (2007) constructed a thermodynamic model to investigate the effect of a geometrical parameter defined as the area ratio of the cross-sectional area of the constant area mixing section to the cross-sectional area of the primary nozzle outlet and the refrigerant type on the performance. According to their essential outcomes, R141b from the pure working fluids and R408a from the refrigerant mixtures displayed the highest COP at the optimum geometrical parameter and the specified operating conditions. Wang, Li, & Zhou (2016) established the thermodynamic analyses of the EERC assuming that the mixing process occurs in the constant area mixing section. They defined the mixing pressure according to optimum operating conditions. The working fluid used in the analyses was R141b and analyses at off-design conditions were presented as well. Lawrence & Elbel (2012) and Lawrence (2012) analyzed the effects of the liquid-vapor separator efficiency on the performance making use of the thermodynamic models. They presented COP ratio of the EERC to the base cycle according to condenser temperatures for R1234yf and R134a and investigated the vapor and liquid separation efficiencies for the fixed condensation temperature of 45 °C.

Comparison of the CAM and CPM ejector theories is essential and hence it is investigated in some of the studies. Yapıcı & Ersoy (2005) compared the ejector mixing theories via the thermodynamic models constructed for the single-phase ejector (vapor-jet ejector) to be used in the heat-driven ejector refrigeration cycle. They established their thermodynamic model with reference to CAM assumption and compared their results with the CPM model of Sun & Eames (1996). Yapıcı & Ersoy (2005) stated that COP and area ratio calculated under CAM assumption were greater than the values determined with respect to CPM approach. Since the equations of the thermodynamic models, the basic assumptions upon which the models are established, and the whole cycle components for the EERC utilizing two-phase ejector and heat-driven ejector cycle including single-phase ejector are completely different, comparing the impact of the mixing assumptions for a two-phase ejector proposed to be used in the EERC is as well required.

Moreover, Seckin (2017) compared the performance of the CAM and CPM ejectors in the EERC for R134a, but the inputs of the model included motive nozzle and suction nozzle exit areas and total refrigerant mass flow rate when compared to the thermodynamic model presented in this thesis. Hence the mass flow rates and the pressures of the refrigerants in the suction nozzle (chamber) could be calculated in the study of Seckin (2017). CPM was assumed when both of the refrigerants had the same pressure before mixing; whereas CAM approach was defined as the case of refrigerants when they had different pressures before mixing at the inlet of the constant area section in that study. Lastly, the author stated that COP and pressure lift factor calculated according to CPM ejector assumption were higher than the values defined with reference to CAM approach.

Investigations on the ejector component efficiencies are of critical importance. Therefore, effect of the ejector section efficiencies is investigated previously in the literature. Ersoy & Bilir (2010) compared only the efficiency of the motive nozzle, suction nozzle, and diffuser. Li, Cao, Bu, Wang, & Wang (2014) added the mixing section efficiency to the other component efficiencies and defined the efficiency of the mixing section in the same way as Yu, Ren, Chen, & Li (2007).

Theoretically, independent of the selected refrigerant, any ejector could accomplish 100% power recovery efficiency. However, the efficiency of the $CO_2$ ejectors varied from 30% to 20%; whereas R134a ejectors had efficiency values less than 20% since R134a ejectors were more dependent on the optimum design with respect to the operating conditions than $CO_2$ (Lawrence & Elbel, 2015). Originating from this idea, R744, R170, and R41 having low critical temperatures are investigated in this thesis to make comparisons in the transcritical refrigeration cycle and the modified cycle configuration with the ejector expansion. Furthermore, their performance is evaluated within a specific gas cooler pressure range that the working fluids could exhibit their maximum COP.

It is shown in this thesis that under the same operation conditions, the refrigerants react similarly to the typical amount of the pressure drops determined with reference to the evaporator temperature for each mixing assumption. Performance improvement is analyzed under both of the optimum pressure drop and a specific pressure drop approaches of the suction nozzle for each mixing assumption. Optimum suction nozzle pressure drop assumption brings evaluations at the design conditions; whereas the constant value pressure drop approach results in the analyses out of the design conditions. The discrepancy of the performance improvement ratios obtained according to both pressure drop assumptions is expressed using the pressure drop profiles within the same operation ranges. The geometrical parameter, area ratio ($\phi$) is analyzed under both of the mixing assumptions and the variation of the area ratios are explained interpreting the density ratio and velocity ratio of the secondary flow to the primary (motive) flow at the mixing section inlet.

Effect of the efficiency definitions for each ejector section (component) on the overall performance improvement is studied in this thesis to determine the most important parameter based on the optimum operation conditions. The performance improvement potential of R1234yf and R1234ze(E) in the EERC with respect to the efficiency of all ejector components and liquid-vapor separator for an air-conditioning application is investigated to widen the content of the thermodynamic models. The density ratio and the velocity ratio of the refrigerants in the suction nozzle with respect to the mixing assumptions and the operating conditions are analyzed deeply. Originating from the performance and flow analyses of the refrigerants, the characteristic variations of the typical parameters such as density and velocity ratios of the secondary and primary fluid flows are explained as the general behavior of the working fluids according to the ejector mixing theories.

Effect of the ejector component efficiencies are analyzed also in the transcritical EERC for R744 in this thesis. Ejector component efficiencies on the transcritical $CO_2$ EERC are investigated at various gas cooler pressures and outlet temperatures through medium of the thermodynamic models under CPM approach. Additionally, the influence of the liquid-vapor separator efficiency at various evaporator and condenser temperatures for R1234yf, R1234ze(E), and R134a are displayed. The main conclusion of this thesis from these investigations based on the operating conditions is that if the component efficiencies are not high, in other words if the ejector is not designed well enough, changing the operating conditions for the ranges at which the ejector performs best does not provide advantages.

Chen, Havtun, & Palm (2015) conducted an elaborate exergy analyses on the heat-driven ejector refrigeration system and concluded that half of the total exergy destruction occured in the ejector. Therefore, the ejector had the highest importance for the performance improvement of that cycle configuration. Bai, Yu, & Yan (2016) made comprehensive exergy analyses on the transcritical ejector expansion refrigeration cycle operating with $CO_2$. With respect to the results of their paper, ejector had the second highest priority from the viewpoint of improvement potentials after the compressor having the largest avoidable endogenous exergy destruction. The highest theoretical performance limit of the EERC could be calculated under the reversible ejector assumption eliminating the above-mentioned exergy destructions. This maximum achievable limit lead better design considerations concerned with the ejector.

Lawrence (2012) evaluated the reversible ejector assuming that the motive nozzle, suction nozzle, and diffuser have efficiency equal to unity and the mixing occurs at the optimum pressure of minimum losses. McGovern, Narayan, & Lienhard V (2012) defined the process of the reversible ejector as the sum of two processes in order to establish both mechanical and thermal equilibrium. Chunnanond & Aphornratana (2004) gave the definition of the reversible ejector conceptually in their review study. Their reversible ejector assumption eliminates all irreversibilities arisen from the mixing process and shock waves and the reversible ejector was established as an isentropic turbine-compressor assembly under this assumption. Thermodynamic model of the EERC under reversible ejector assumption is constructed within this thesis.

Sherif et al. (2000) analyzed the flow of a jet pump operating with refrigerant R134a and having a saturated two-phase mixture as the primary fluid and secondary fluid in the subcooled or saturated liquid phase. Inputs were comprised of the inlet conditions of the primary and secondary fluid flows, entrainment ratio, and pump geometry other than the outlet cross-sectional area of the mixing section. Constant pressure mixing theory assuming that the mixing section outlet pressure was equal to the pressure of the secondary fluid at the exit of the secondary flow tube was used since it yielded a bit higher compression ratios in the jet pump when compared to constant area mixing approach. Modelling approach of Sherif et al. (2000) is used while calculating the critical dimensions for the ejector design based on the thermodynamic modelling approach in this thesis, but in the reverse order. Sherif et al. (2000) used the idea that if the geometry was known, the outlet pressures of the ejector sections could be determined. In the model established in Chapter Five, the outlet pressures of the motive and suction nozzles are assumed to be known in a way that the geometry of the ejector which is the main issue is calculated.

Lastly, there are some more thermodynamic models established for geometrical parameter determinations in addition to performance evaluations. Hassanain, Elgendy, & Fatouh (2015) calculated the main diameters of a two-phase ejector, namely motive nozzle throat, motive nozzle exit, suction nozzle exit, and mixing section, to be used in the EERC with reference to constant area mixing assumption for R134a. They established a simulation program through Engineering Equation Solver (EES) software to analyze both performance and design according to various operation conditions and ejector section efficiencies. They cited the study of Yapıcı and Ersoy (2005) claiming that constant area mixing ejector performed better in comparison with the constant pressure mixing ejector for the same operating conditions and they constructed their model with respect to the CAM ejector theory. Ma, Bao, & Roskilly (2017) established a thermodynamic model including both geometry and operation parameters as the inputs to propose an empirical correlations of the hypothetical throat area of the secondary fluid which would be beneficial for the subsequent performance evaluations.

A thermodynamic model similar to Hassanain et al. (2015) is established under the scopes of this thesis to compare the dimensions of a two-phase ejector to be used in an experimental system having 5 kW cooling capacity for R1234yf, R1234ze(E), and R134a. These dimensions are the diameters of the motive nozzle throat, motive nozzle exit, and suction nozzle outlet which is the same as the mixing section diameter under the modelling approaches.

In conclusion, thermodynamic modelling is an important part of this thesis, and hence the literature review concerned with this section is presented in detail. Performance analyses and design calculations with the elaborately explained mathematical equations are declared according to the thermodynamic modelling approaches in the subsequent chapters. The effects of the ejector components and liquid-vapor separator efficiencies on the geometrical parameter definition of the two-phase ejectors are displayed for further investigations as the future targets.

### 2.5 Multi-dimensional Models of the Ejector and Ejector Components

Performance of an EERC or the ejector could be analyzed making use of various modelling approaches, i.e., 0D thermodynamic models (Kornhauser, 1990; Li & Groll, 2005; Bilir & Ersoy, 2009; Lawrence, 2012; Li et al., 2014; Wang et al., 2016; Atmaca et al., 2019a), 1D or multi-dimensional ejector models based on the computational fluid dynamics (CFD) (Banasiak & Hafner, 2011; Ruangtrakoon, Thongtip, Aphornratana, & Sriveerakul, 2013; Palacz, Smolka, Nowak, Banasiak, & Hafner, 2017; Wang, Yan, Wang, & Li, 2017), and semi-empirical models (Balamurugan, Gaikar, & Patwardhan, 2006). Thermodynamic modelling approach is widely used for the overall performance analyses of the EERC. However, this modelling approach offers very limited results due to the critical assumptions including the suction nozzle pressure and the ejector component efficiencies. All these aspects related to these assumptions are strongly dependent on the ejector design parameters and operating conditions, hence definition of these parameters without proper calculations may be misleading.

Although thermodynamic models are simple and quick, they cannot provide with the elaborate results since they only consider inlets and outlets of the ejector sections and refrigeration system components. The factors influencing the EERC performance are the refrigerant type, the ejector design, and the operation conditions. The effects of the refrigerant selection and operation conditions could be tested by means of the 0D thermodynamic models. However, the geometrical parameters concerned with the design of the ejector could not be checked via these models. The effect of the geometry and the other irreversibilities are regarded with the constant efficiency values defined for the motive nozzle, suction nozzle, mixing section, and the diffuser sections of the ejector. They are among the model inputs, but it is misleading to define these critical parameters as constant values since they vary in accordance with the refrigerants, ejector design, and the operation conditions.

Under thermodynamic modelling approach with no geometrical inputs, suction nozzle pressure is the same as the motive nozzle outlet pressure or the mixing section inlet pressure. Kornhauser (1990) made initial calculations assuming that suction nozzle pressure is equal to the evaporator pressure and consequently stated that there is an optimum value for this pressure according to the inlet conditions and assumed ejector component efficiencies. Wang et al. (2016) divided the suction nozzle pressure assumptions into three categories. Firstly, the suction nozzle pressure could be evaluated as the evaporator pressure as in the example study of Deng, Jiang, Lu, & Lu (2007). Secondly, a constant pressure drop could be assumed according to evaporator pressure (Li & Groll, 2005). Lastly, the optimum suction nozzle pressure could be used in order to obtain maximum performance (Bilir & Ersoy, 2009; Li et al., 2014). Although these aforecited assumptions are widely accepted in the previous studies, best approach is calculating the pressure distribution throughout the motive nozzle and determining the component efficiency of the motive nozzle in this way with respect to the motive nozzle geometry and operating conditions.

Hence, 1D ejector models, motive nozzle models, and various multi-dimesional CFD models taking the geometry and operation parameters into account to display the flow characteristics inside the ejector are started to be constructed commonly. Banasiak & Hafner (2011) presented 1D model of the two-phase $CO_2$ ejector to be utilized in the EERC. A system of ordinary differential equations composed of conservation equations of mass, momentum, and energy and the equation of state was established as the mathematical model. The thermodynamic state of the two-phase fluid in the motive and suction nozzles was evaluated with respect to the delayed equilibrium model (DEM), whereas homogeneous equilibrium model (HEM) was used in the mixer and diffuser for the definition of the thermodynamic states of the two-phase fluid. The turbulence effects were taken into account by the introduction of the friction factor and non-isothermal duct assumption was made.

Angielczyk, Bartosiewicz, Butrymowicz, & Seynhaeve (2010) developed a mathematical model using the homogeneous relaxation model (HRM) for the motive nozzle of the two-phase $CO_2$ ejector. Tsuru, Ueno, Kinoue, & Shiomi (2014) analyzed numerically and experimentally the $CO_2$ flow through the motive nozzle of the two-phase ejector. They constructed 1D model of the convergent-divergent motive nozzle under steady-state, adiabatic, frictionless flow assumptions with the equilibrium condition. Moreover, their modelling equations indicated that the convergent section of the nozzle included only single-phase liquid flow; whereas the flow through the divergent part was two-phase. Geng, Liu, & Wei (2019) numerically analyzed the converging-diverging nozzle for the subcritical refrigerant, R134a by means of CFD technique. The critical mass fluxes and the effects of the geometrical parameters on the flow characteristics were displayed as the outcomes of their study. To sum up, Tsuru et al. (2014), Angielczyk et al. (2010), and Geng et al. (2019) focused only on the convergent-divergent two-phase nozzle as being different from the purpose of Banasiak & Hafner (2011), but their motivations which were the deep investigations to improve the two-phase ejector to be used in the EERC were the same.

The effects of the motive nozzle geometry on the ejector performance is so important that there are numerous experimental and numerical investigations on the motive nozzle of the ejectors. Palacz et al. (2017) made a shape optimization on the two-phase $CO_2$ ejector with the help of CFD analyses. They analyzed the effects of the six geometrical parameters, namely the mixing section length, mixing section diameter, pre-mixing chamber length, motive nozzle outlet diameter, motive nozzle diverging angle, and suction nozzle converging angle and concluded that both mixing section and motive nozzle shape optimizations were required in order to design high efficiency ejectors.

More specifically, Wang et al. (2017) conducted an optimization study on the primary nozzle of the ejector making use of CFD analyses. They used R134a as the working fluid and concluded that the throat length, diverging angle, and diverging section length of the primary nozzle had more influence on the performance when compared to converging angle, converging section length, and surface roughness of these three sections. Ruangtrakoon et al. (2013) made investigations on the eight primary nozzle geometries of an ejector to be used in the steam jet refrigeration cycle. The working fluid which was the water vapor was modelled as an ideal gas. As a result of their CFD analyses, the optimum primary nozzle throat diameter and exit Mach number were specified for a typical boiler and evaporator temperature.

There are also CFD analyses focusing on the different geometrical parameters of the ejectors. Metin, Gök, Atmaca, & Erek (2019) investigated the influence of the primary nozzle position and converging angle of the mixing section making use of the CFD method for a vapor-jet ejector proposed to be implemented into the heat-driven refrigeration cycles. They discussed the effective area of the secondary flow and shadowgraph technique as well was used to display the shock series occurred within the ejector. According to their conclusions, entrainment ratio could be increased about 6% and more than 9% with the help of the changes in the primary nozzle position and mixing section converging angle, respectively. Palacz et al. (2016) optimized the mixing section with the help of the two optimization algorithms, namely genetic algorithm and evolutionary algorithm, in addition to a CFD model constructed with reference to the HEM. They showed that the established methodology could provide the appropriate results for the optimization of the $CO_2$ ejector geometry within only a limited operational range. Therefore, more advanced mathematical models are required to improve the optimization methodology.

In this thesis, 1D model of the motive nozzle is established under steady flow, equilibrium, and adiabatic nozzle assumptions. The main objective of such a modelling study is calculating the motive nozzle outlet pressure and motive nozzle efficiency exactly in the thermodynamic analyses. Because of this reason the previous studies relative to motive nozzle models are deeply discussed in this section in addition to 1D and multi-dimensional ejector models. 1D model of the motive nozzle is implemented into 0D thermodynamic models to construct a semi-1D model. Hence, the EERC performance is evaluated in a more realistic way. The content of the semi-1D modelling approach is increased with the addition of various nozzle geometries and operating conditions as for the future research targets.

## 2.6 Experimental Analyses of the Ejector Refrigeration Cycles

There are numerous experimental works related to the ejector refrigeration cycles. Experimental analyses concerned with not only the performance analyses of the EERC, but also the motive nozzle of the ejector to highlight its importance are presented in this section. Hence, the content of the previous experimental studies is narrowed according to the scope of the thesis.

Disawas & Wongwises (2004) conducted experiments on the two-phase ejector refrigeration cycle. The effect of the heat sink and heat source temperatures were discussed through the comparisons between the conventional refrigeration cycle at the same external conditions. They concluded that COP of the EERC is superior to that of the VCRC within the whole investigated range. Wongwises & Disawas (2005) concluded that little performance improvement was observed at low inlet temperatures of cold water which is the heat transfer fluid of the condenser. However, the heat transfer fluid of the evaporator (hot water) was of more critical importance for the performance of the cycle. They used R134a as the working fluid.

Chaiwongsa & Wongwises (2007) investigated experimentally the influence of the motive nozzle throat diameter in main on the performance, primary and secondary mass flow rates, cooling capacity, recirculation ratio, average evaporator pressure, compressor pressure ratio, and discharge temperature for R134a based on the operating conditions. Motive nozzle having diameter of 0.8 mm yielded the highest COP when compared to the other investigated designs, i.e., throat diameters of 0.9 mm and 1.0 mm. Motive nozzle of 0.8 mm diameter resulted in a low primary mass flow rate and high cooling capacity and vaporized mass flow rate. Chaiwongsa & Wongwises (2008) aimed to understand the effects of the external operating parameters and motive nozzle outlet diameter on the system performance as a part of their experimental analyses series. Similar to their previous experimental investigations, COP, mass flow rates of the primary and secondary fluids, recirculation ratio, average evaporator pressure, compressor ratio, discharge temperature, and cooling capacity were discussed based on the operating conditions (heat source and heat sink temperatures) and design of the ejector, i.e., motive nozzle outlet diameter. The motive nozzle outlet diameter was varied between 2.0 mm-3.0 mm and the effect of this geometrical parameter on the performance was found to be negligible.

There are various experimental studies focusing on the transcritical $CO_2$ EERC. Smolka et al. (2013) established a CFD model to investigate the flow of $CO_2$ in the heat pump ejector using enthalpy-based energy equation instead of the temperature-based designation. They conducted experiments on the transcritical $CO_2$ EERC to validate their model for the two-phase flow of $CO_2$. They measured the mass flow rates of the primary and secondary fluids and pressures at various locations of the mixing section and diffuser. Liu, Groll, & Li (2012) analyzed the component efficiencies of a two-phase ejector and the performance of the transcritical $CO_2$ EERC. Similar to previous mentioned investigation, experimental data was used to validate the established model. The two-phase ejector in this study could be controlled from viewpoint of two aspects, namely the throat area control by a needle and the motive nozzle exit position via a thread mechanism. The pressures, temperatures and mass flow rates at the inlets of the motive and suction nozzles and ejector discharge pressure were measured at each test trial. The efficiencies of the motive nozzle, suction nozzle, and mixing section were determined making use of the experimental data and the constructed models.

Liu, Li, & Groll (2012) experimentally analyzed the effects of the operational parameters, compressor frequency, and design parameters in order to define the high performance cases of the transcritical $CO_2$ EERC for an air-conditioning application. Increase in the outdoor air temperature and decrease in the compressor frequency and motive nozzle throat diameter positively affected the performance. Lastly, making the distance between the motive nozzle outlet and constant area mixing section inlet three times of the constant area mixing section diameter yielded the highest COP. Liu, Groll,

& Ren (2016) experimentally studied the cooling and heating performance of the transcritical $CO_2$ ejector expansion cycle elaborately under various operating conditions. The controllable $CO_2$ ejector and variable speed compressor was used in the cycle. The authors presented empirical correlations according to operating conditions, design parameters, and compressor frequency.

Ersoy & Sag (2014) experimentally obtained 6.2-14.5% performance improvement of the EERC over the conventional cycle for R134a. The agreement between the experimental measurements and the results of the thermodynamic models under appropriate ejector component efficiency assumptions was found satisfactory within an acceptable error range of 10%. Sag & Ersoy (2016) experimentally analyzed the effects of the motive nozzle throat diameter and location of the motive nozzle on the performance of the EERC using R134a according to various condenser water inlet temperatures. As for the primary outcomes, the throat diameter of 2.3 mm yielded maximum COP and the performance improvement was calculated between 5–13% based on this optimum throat diameter. However, the authors stated that the influence of the motive nozzle position on the performance was estimated less than 1%.

Lawrence & Elbel (2014) made comparison between the conventional cycles with the expansion valve and the two-phase ejector refrigeration cycle which is of COS type for the low pressure refrigerants, i.e., R134a and R1234yf. The experimental performance improvement percentages of the COS ejector refrigeration cycle were presented according to the conventional cycle with single evaporation temperature and two evaporation temperatures. Maximum percentage performance improvements when compared to the conventional cycle with two evaporation temperatures were declared as 12% and 8% for R1234yf and R134a, respectively; whereas maximum COP improvements in comparison with the conventional cycle with single evaporation temperatures were 6% for R1234yf and 5% for R134a.

The effect of the liquid-vapor separator has been studied experimentally for so long. Comprehensive experimental investigations of Elbel, Reichle, Bowers, & Hrnjak (2012) according to the effects of various separator designs on the transcritical $CO_2$

ejector expansion cycle performance showed that vapor separation efficiency was generally close to unity, but liquid separation efficiency varied between unity and about 0.7. Nakagawa, Marasigan, & Matsukawa (2011) investigated the effects of the internal heat exchanger on the performance of the transcritical ejector cycle using $CO_2$ and stated that they could prevent an important amount of the liquid at the vapor port of the separator from flowing through the compressor with the implementation of the heat exchanger at issue.

Lin et al. (2019) designed four different separators to analyze the separation process through medium of visualization and heat balance method using R290 as the working fluid. The first separator had the two-phase flow inlet and gas outlet at the top and liquid refrigerant outlet to the evaporator at the bottom. There was a baffle at the top of the separator between the two-phase refrigerant inlet and gas outlet. The primary fluid expanded making approximately 40º expansion angle thereby sucking the secondary fluid. Hence, liquid refrigerant could easily go to the suction side of the compressor. Moreover, the flow pattern in the first separator could not be defined clearly due to the strong turbulence and dynamic balance was hard to be reached. The second separator design had the gas outlet at the top and liquid outlet at the bottom. Two-phase fluid entered the separator with an angle. Even in this separator design, there was still some liquid refrigerant at the top outlet open to the compressor inlet. Dynamically balanced flow pattern was observed. The second separator displayed better performance than the first one. An O-ring baffle was set in the third separator. The general structure of the third separator was similar to the second separator. The problem concerned with this design was the stuck liquid flow in the small cylindrical volume over the ring baffle. The position of the top outlet was changed in the fourth separator design when compared to the second separator design. It was estimated that there was a region including less liquid in the center of the pipe and the top outlet was placed in this region. Therefore, the liquid flow going into the compressor suction could be stopped. As a result, the fourth separator had the best performance with the cooling capacity of 244 W and COP of 1.42; whereas the worst design was the first one with the cooling capacity and COP values of 131 W and 0.76, respectively.

Critical details relative to the EERC have been recently discussed in the studies. Li & Yu (2019) made experimental analyses on the effects of the motive nozzle throat diameter and refrigerant charge amount using R290 as the refrigerant. The nozzle throat diameter had influence on the variation of the evaporation temperature. When compared to the nozzle throat diameter, capillary tube length had weaker influence on the variations of the evaporation temperature. The mass flow rate of the secondary fluid could be kept within an appropriate range with the adjustments made to the refrigerant charge amount when the throat diameter and capillary tube length were varied in a specific range. Lastly, the authors stated that these kinds of results would be fruitful to serve practical guidelines.

Thongtip & Aphornratana (2017) made as well experimental investigations on the six primary nozzle geometrical configurations of the ejector utilizing R141b as the working fluid. They tested all nozzles with one fixed geometry ejector creating variations in the operating conditions. Their reference cycle at which the ejector was proposed to be used was the heat-driven ejector refrigeration cycle. They concluded that the design of the motive nozzle seriously affected the ejector performance. Nakagawa, Berena, & Kishine (2009) investigated experimentally decompression phenomena of the rectangular converging-diverging nozzles with respect to the diverging angle. Their two-phase $CO_2$ nozzle as well was proposed to be a part of an ejector to be used in the refrigeration cycle as a secondary compressor. An assessment was made on the appropriate operational range of Isentropic Homogeneous Equilibrium (IHE) theory.

As seen from the summarized literature, experimental analyses are sometimes used for the validation of the mathematical models or directly used for the investigations of the design and operational parameters. In this thesis, thermodynamic models are validated using the experimental data from the literature.  There are two reasons for the use of the experimental analyses from the literature. Firstly, during the numerical analysis phase of this thesis, the EERC test rig planned to be constructed within the scope of this thesis has not been built yet. Secondly, the measurements from the built EERC test rig of this thesis are limited. However, only semi-1D model is validated making use of the experiments conducted for the performance evaluations of this thesis. Hence, the test rig under question is just used for the experimental performance investigation of R134a and R1234yf in the conventional cycle and the experimental performance evaluation of R134a in the EERC. EERC experiments for R134a are used to validate the semi-1D model and to understand the critical operational characteristics of the EERC.

# CHAPTER THREE
# REFRIGERANT SELECTION

Environmental aspects are one of the main constraints in the technological advances and the refrigerants to be used in the refrigeration systems transferring heat from a low-temperature environment to the warm-temperature one are no exception. There are various refrigerant alternatives and making a choice among them is a compromise since there are various selection criteria. When historical developments of the refrigerants are investigated, it is seen that a group of refrigerant is always trying to be phased out due to environmental concerns and a better group is proposed to replace the previous ones within regular periods. In this chapter, firstly, historical developments relative to environmental regulations are summarized. Secondly, governing environmental legislation are explained in detail. As a result of these regulations, a candidate refrigerant list is presented. Thermodynamic modelling equations of the VCRC are expressed. Energy and exergy analyses are displayed to compare the candidate refrigerants with reference to Atmaca et al. (2019a) and Atmaca, Erek, & Ekren (2016).

## 3.1 Historical Developments of the Environmental Regulations

Montreal Protocol approved in 1987 decided to eliminate chlorofluorocarbons (CFCs) owing to their ODP. The protocol in question was revised considering the industrial and scientific developments and each revision was named as the city where the committee was gathered. In the second revision held in Copenhagen in 1992, the use of CFCs was certainly decided to be phased out gradually and hydrochlorofluorocarbons (HCFCs) as well were planned to be controlled for the first time. Turkey signed this protocol on December 19, 1991 and accepted all requirements (Alarko Carrier Technical Bulletin, 2005; Türkiye Cumhuriyeti Çevre ve Şehircilik Bakanlığı, Sözleşme ve Protololler, Montreal Protokolü, n.d.). Hence, the use of these products was banned by the legislation in developed countries by 1996, and developing countries would phase out these products by 2010 according to this protocol (Calm, 2008). The Kyoto Protocol signed in 1997 aimed to reduce the emissions of the greenhouse gases. Although third generation HFCs have zero ODP, they are evaluated as greenhouse gases directly because of their high GWP; thus they are required to be phased out (Mota-Babiloni et al., 2015).

The last environmental regulations having stronger limitations are focusing on eliminating these high GWP refrigerants. The first one is the European Directive 2006/40/EC (Directive 2006/40/EC, 2006) stating that refrigerants having GWP values more than 150 cannot be used in mobile air-conditioning systems by 2017. The second essential one is EU Regulation No 517/2014 (F-gas Regulation) (Regulation (EU) No 517/2014, 2014) putting limitations on the refrigerants according to types of the refrigeration and air-conditioning applications. Some more details regarding the prohibition dates versus limit GWP values of the refrigerants and the gradual quantities to be phased out according to years are displayed in the next sections. In 2015, Paris Agreement is accepted to keep the increase in the global average temperature to well below 2 °C (Paris Agreement - UNFCCC, 2015). Lastly, the Kigali Amendment to the Montreal Protocol came into force from the beginning of January, 2019 to reduce the use of HFCs. Hence with respect to this agreement, the target for this century is preventing global warming by up to 0.4°C (Kigali Amendment Enters into Force, Bringing Promise of Reduced Global Warming, n.d & The Kigali Amendment to the Montreal Protocol: HFC Phase-down, 2016). As shown in Figure 3.1., refrigeration technology is affected by the regulations willy-nilly nearly each 10-year time duration.

There are limited alternatives such as natural refrigerants, HFOs containing at least one carbon-carbon double bond, some of the low GWP HFCs, and HFO/HFC mixtures to commonly used high GWP refrigerants. All refrigerant groups have their own characteristics and there would be always a compromise while selecting a refrigerant.

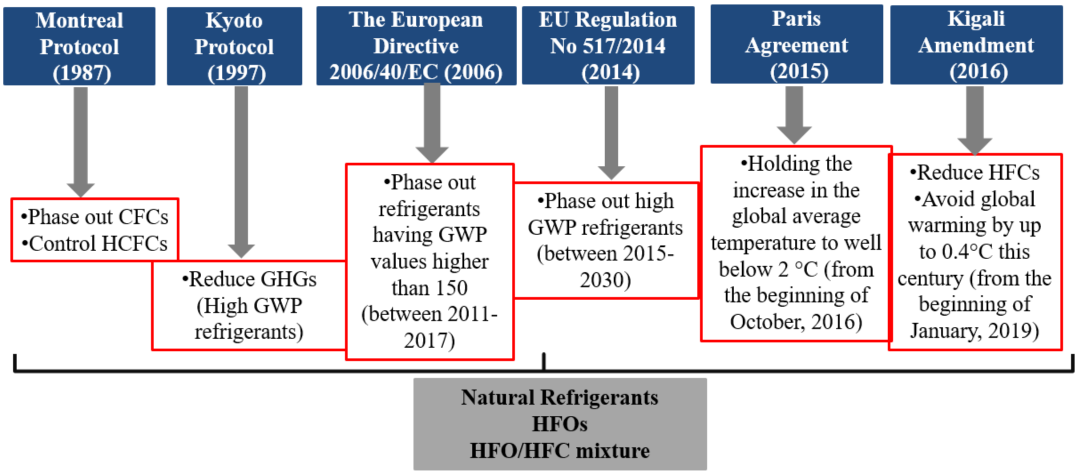


Figure 3.1 Summary of the main environmental regulations and resultant solutions

## 3.2 Aspects of the EU Regulation No 517/2014 (Regulation (EU) No 517/2014, 2014) and the European Directive 2006/40/EC (Directive 2006/40/EC, 2006)

Strict GWP limitations and deadlines imposed by the regulations show that there is a challenge in the refrigeration area. Prohibition date is the beginning of 2015 for domestic refrigerators and freezers containing HFCs with GWP of 150 or more. However, it is the beginning of 2020 and 2022 for the commercial freezers and the refrigerators employing HFCs with GWP of 2500 or more and HFCs with GWP of 150 or more, respectively. Moreover, fluorinated greenhouse gases with GWP of 750 or more will be banned for the single split air-conditioning systems containing fluorinated greenhouse gases less than 3 kg by the beginning of 2025; whereas HFCs with GWP of 150 or more will be prohibited for the movable room air-conditioning equipment by January 1, 2020. The critical prohibition dates as to air-conditioning systems of all motor vehicles is January 1, 2017 and by this due date fluorinated greenhouse gases having GWP values higher than 150 cannot be used. All other deadlines stated by the European normative are given in Table 3.1.

Another respect forcing the countries to take serious precautions related to refrigerants are the allowed quotas determined according to the yearly defined percentages as shown in Table 3.2. The deadlines at issue show that some immediate solutions are required in terms of low GWP refrigerants. Proposing the best refrigerant is a challenging issue since there is no perfect working fluid in all regards. With reference to EU Regulation No 517/2014 (Regulation (EU) No 517/20, 2014), Table 3.2 shows that the amount of the HFCs in 2030 must be decreased to 21% of the total amount in 2015.

Table 3.1 Some of the prohibition dates of the HFC group refrigerants according to the refrigeration and air-conditioning applications (Directive 2006/40/EC, 2006; Regulation (EU) No 517/2014, 2014)

<table>
<tr><th colspan="2">Refrigeration application</th><th>Date of prohibition</th></tr>
<tr><td colspan="2">Domestic refrigerators and freezers that contain HFCs with GWP of 150 or more</td><td>1 January 2015</td></tr>
<tr><td rowspan="2">Refrigerators and freezers for commercial use<br>(hermetically sealed equipment)</td><td>that contain HFCs with GWP of 2500 or more</td><td>1 January 2020</td></tr>
<tr><td>that contain HFCs with GWP of 150 or more</td><td>1 January 2022</td></tr>
<tr><td colspan="2">Movable room air-conditioning equipment that contain HFCs with GWP of 150 or more</td><td>1 January 2020</td></tr>
<tr><td colspan="2">Single split air-conditioning systems containing less than 3 kg of fluorinated greenhouse gases with GWP of 750 or more</td><td>1 January 2025</td></tr>
<tr><td colspan="2">Multipack centralised refrigeration systems for commercial use with a rated capacity of 40 kW or more that contain fluorinated greenhouse gases with GWP of 150 or more, except in the primary refrigerant circuit of cascade systems where fluorinated greenhouse gases with a GWP of less than 1500 may be used</td><td>1 January 2022</td></tr>
<tr><td colspan="2">Refrigerants to be used in the air-conditioners of the motor vehicles with GWP higher than 150</td><td>1 January 2017</td></tr>
</table>

Table 3.2 Years versus percentages to determine the maximum allowed quantities of HFCs (Regulation (EU) No 517/2014, 2014)

| Years | Percentages to calculate the maximum allowed quantities |
|---|---|
| 2015 | 100% |
| 2016-17 | 93% |
| 2018-20 | 63% |
| 2021-23 | 45% |
| 2024-26 | 31% |
| 2027-29 | 24% |
| **2030** | **21%** |

## 3.3 Working Fluids and Potential Refrigerants

The European Directive 2006/40/EC and EU Regulation No 517/2014 put so strict limits on the refrigerants in terms of the GWP values. 150, 750, and 2500 are the critical limits stated by the legislation for the GWP values. These limits are also placed in Figure 3.2 by lines 1, 2, and 3 for 2500, 750, and 150, respectively to emphasize the restricted number of the refrigerants. Along with the F-gas Regulation (Regulation (EU) No 517/2014, 2014) and the European Directive 2006/40/EC (Directive 2006/40/EC, 2006), prohibition date is the beginning of 2015 for domestic refrigerators and freezers containing HFCs with GWP of 150 or more and the beginning of 2017 is the another critical deadline to stop using fluorinated greenhouse gases having GWP values higher than 150 in the air-conditioning systems of all motor vehicles. Therefore, there are only restricted refrigerant alternatives obeying the aforecited limits as shown in Figure 3.2.

Figure 3.2 is mostly comprised of the commercially available pure refrigerants or refrigerant mixtures to show the limited numbers of the working fluids below and above the critical GWP values. Fluorinated ethers and alcohols are also added since every possibility could be investigated since the sector is in great demand to find the most appropriate substitutes for the commonly used high-GWP working fluids, e.g., R134a, in terms of thermodynamic, environmental, efficiency, and safety characteristics. Table 3.3 presents a group of refrigerants for the deep analyses.

Evaluating the properties of the refrigerants in Figure 3.2, nine pure refrigerants are chosen for the investigation of a typical air-conditioning application ($T_e$=5 ˚C and $T_c$=40 ˚C). While refrigerants are chosen, the convenience of the NBP of the refrigerants is considered and parametric range is defined according to NBP. As given in Table 3.3, the target group consists of natural refrigerants, HFOs, and low-GWP HFCs.

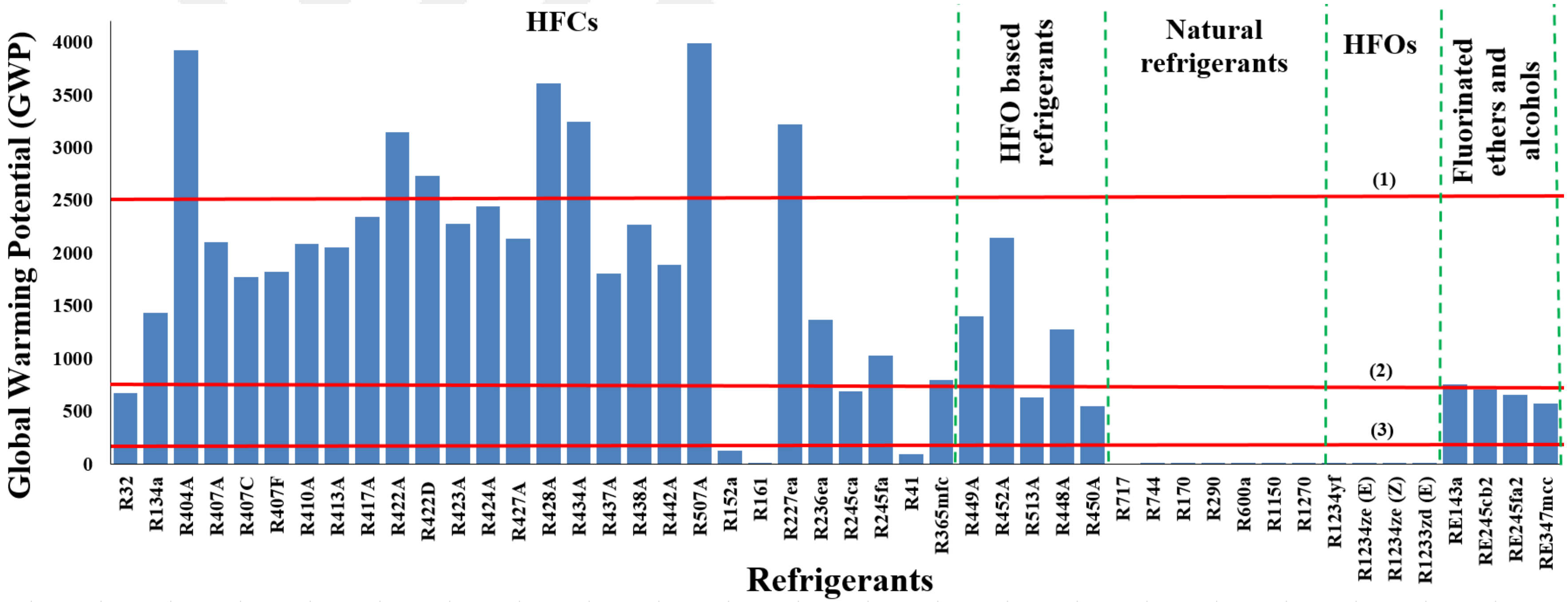


Figure 3.2 GWP values of the widely used refrigerants (The Linde Group (n.d.); The Chemours Company (n.d.); Honeywell International Inc. (n.d.); Regulation (EU) No 517/2014, 2014; Bivens & Minor, 1997)

Table 3.3 Thermodynamic and environmental properties of the investigated refrigerants with safety classes (a:The Linde Group (n.d.); b:Wu et al., 2012; c:ANSI/ASHRAE Standard 34, 2010; d:Regulation (EU) No 517/2014, 2014; e:Lemmon et al., 2013)

| Refrigerants | ASHRAE Safety Group[a,b,c] | | GWP [a,d] | ODP[a,b] | Critical Pressure (MPa)[e] | Critical Temperature (°C)[e] | Normal Boiling Point (°C)[e] |
|---|---|---|---|---|---|---|---|
| R134a | A1 | No flame propagation<br>Lower toxicity | 1430 | 0 | 4.06 | 101.06 | -26.07 |
| R600a | A3 | Higher flammability<br>Lower toxicity | 3 | 0 | 3.63 | 134.66 | -11.75 |
| R717 | B2L | Lower flammability (Max. burning velocity≤10 cm/s)<br>Higher toxicity | 0 | 0 | 11.33 | 132.25 | -33.33 |
| R290 | A3 | Higher flammability<br>Lower toxicity | 3 | 0 | 4.25 | 96.74 | -42.11 |
| R32 | A2 | Lower flammability<br>Lower toxicity | 675 | 0 | 5.78 | 78.11 | -51.65 |
| R152a | A2 | Lower flammability<br>Lower toxicity | 124 | 0 | 4.52 | 113.26 | -24.02 |
| R161 | A3 | Higher flammability<br>Lower toxicity | 12 | 0 | 5.01 | 102.1 | -37.55 |
| R1234yf | A2L | Lower flammability (Max. burning velocity≤10 cm/s)<br>Lower toxicity | 4 | 0 | 3.38 | 94.7 | -29.45 |
| R1234ze(E) | A2L | Lower flammability (Max. burning velocity≤10 cm/s)<br>Lower toxicity | 7 | 0 | 3.63 | 109.36 | -18.97 |

## 3.4 Thermodynamic Modelling Equations of the VCRC

In this section, the equations for the first and second law analyses of the VCRC are given. The process is isenthalpic throughout the expansion valve in the VCRC. Conservation equations are applied to all components of the VCRC in Figure 2.4 (a). Kinetic and potential energy terms are ignored in the cycle analyses. The first law analyses are used to calculate the COP of the cycles for various working fluids. Work input to the adiabatic compressor, the heat rejected from the condenser, and heat gain of the evaporator on a unit-mass basis are as follows;

$$w_{in} = (h_{out} - h_{in})_{comp} \tag{3.1}$$

$$q_H = (h_{in} - h_{out})_c \tag{3.2}$$

$$q_L = (h_{out} - h_{in})_e \tag{3.3}$$

$w_{in}$, $q_H$, and $q_L$ are all formulated above as positive quantities. Second-law analysis is used to calculate the exergy efficiency and the percentage exergy destruction in the expansion valve of the VCRC. Flow (or stream) exergy by neglecting kinetic and potential energy terms is given by (Çengel & Boles, 2007)

$$\psi = h - h_0 - T_0(s - s_0) \tag{3.4}$$

The thermodynamic dead state is taken as 25 °C and 1 atm. The rate form of the general exergy balance for a steady-flow process and the exergy balance for a single stream on a unit-mass basis are expressed as

$$\dot{X}_{dest} = \sum \dot{Q}_k (1 - \frac{T_0}{T_k}) - \dot{W}_{net} + \sum \dot{m}_{in}\psi_{in} - \sum \dot{m}_{out}\psi_{out} \tag{3.5}$$

$$x_{dest} = \sum q_k (1 - \frac{T_0}{T_k}) - w_{net} + \psi_{in} - \psi_{out} \tag{3.6}$$

The temperature $T_k$ is determined considering the evaporation and condensation temperatures that $T_L$ is 10 °C higher than the evaporator temperature and $T_H$ is 10 °C lower than the condenser temperature (Lawrence, 2012) in the following equations. Exergy destruction equations on a unit-mass basis are given for each component of the VCRC as

$$x_{dest,comp} = T_0(s_{out} - s_{in})_{comp} \tag{3.7}$$

$$x_{dest,c} = q_H (T_0 / T_H) + T_0(s_{out} - s_{in})_c \tag{3.8}$$

$$x_{dest,\exp v} = T_0 (s_{out} - s_{in})_{\exp v} \tag{3.9}$$

$$x_{dest,e} = T_0 (s_{out} - s_{in})_e - q_L (T_0 / T_L) \tag{3.10}$$

Second-law (exergy) efficiency of the VCRC is calculated for a realistic performance measure of the refrigerants as (Dinçer & Kanoğlu, 2010)

$$\eta_{\mathrm{II}} = \frac{COP_{VCRC}}{COP_{Carnot}} \tag{3.11}$$

The maximum COP with respect to Carnot refrigeration cycle operating between the limits of the high and low temperature environments, $T_H$ and $T_L$, respectively is expressed as

$$COP_{Carnot} = \frac{1}{\frac{T_H}{T_L} - 1} \tag{3.12}$$

### 3.5 COP, Second-law Efficiency, and the Exergy Destruction Comparisons of the Refrigerants in the VCRC

Theoretical VCRC model is established in Matlab® and thermodynamic states of the refrigerants are obtained using REFPROP version 9.1 (Lemmon et al., 2013). COP, second-law efficiency, and percentage exergy destruction of the expansion valve are compared for the candidate refrigerant list according to the established operating conditions in Table 3.4. Evaporation and condensation temperatures are investigated parametrically around the values described for the air-conditioning applications in Table 3.4.

Generally speaking, R152a, R600a, and R717 display better performance when compared to the others as given in Figure 3.3 (a) and (b). R32 and R1234yf has the lowest *COP* over the investigated ranges. Second-law (exergy) efficiency of the VCRC is presented in Figure 3.4 (a) and (b). R1234yf and R32 has the lowest exergy efficiency within the same investigation range. Second-law efficiency of the cycle increases when condenser temperature is increased; whereas it decreases when evaporator temperature is increased.

Table 3.4 Operation conditions for a typical air-conditioning application

| **Parameters** | **Values** |
|---|---|
| Evaporator temperature ($T_e$) | 5 ˚C |
| Evaporator outlet superheat temperature difference ($\Delta T_{sh}$) | 5 K |
| Condenser Temperature ($T_c$) | 40 ˚C |
| Condenser outlet subcooling temperature difference ($\Delta T_{sc}$) | 3 K |
| Compressor efficiency ($\eta_{comp}$) | 0.75 |

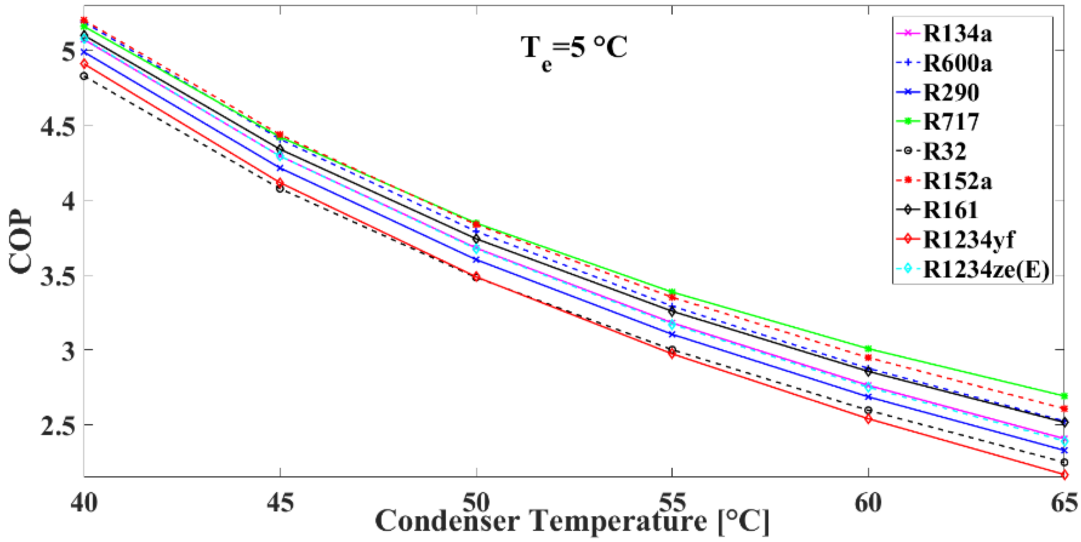


**(a)**

Figure 3.3 Performance comparison of the refrigerants under various (a) condenser and (b) evaporator temperatures

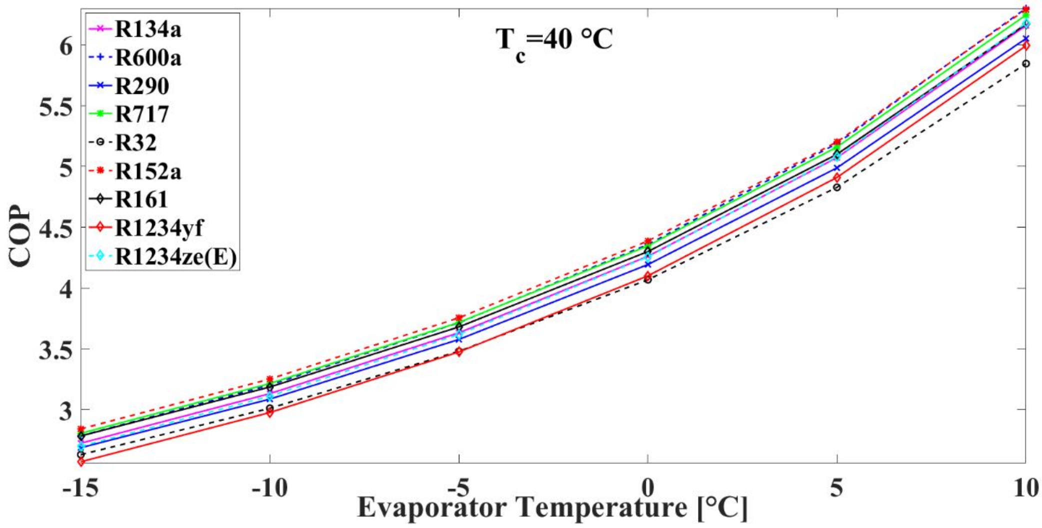


**(b)**

Figure 3.3 continues

The low second-law efficiency shows the necessity of the cycle improvement in order to minimize the irreversibilities. As might be surmised even from the literature, R1234yf and R1234ze(E) become prominent when safety is also considered although these two refrigerants, especially R1234yf, need performance improvement.

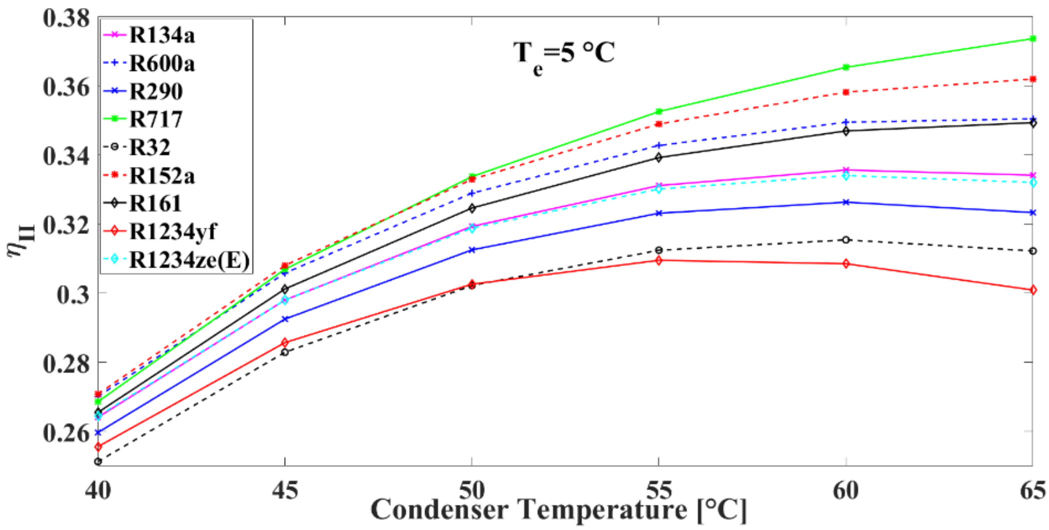


**(a)**

Figure 3.4 Comparison of the second-law efficiency of the refrigerants at various (a) condenser and (b) evaporator temperatures

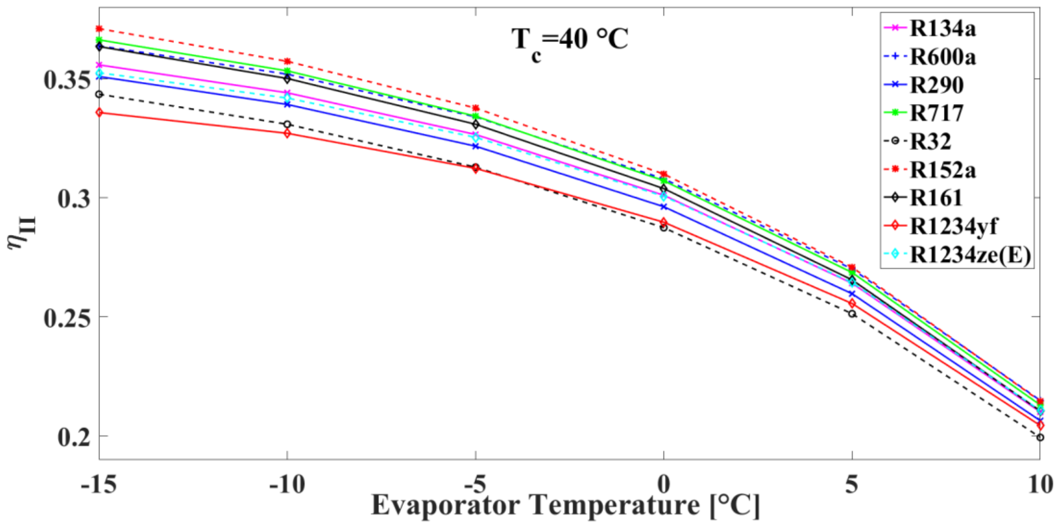


**(b)**

Figure 3.4 continues

Since this study aims to touch on the improvement potential of these new generation working fluids through medium of EERC, percentage expansion losses when compared to the other losses in the VCRC are further discussed as in Figure 3.5 (a) and (b). R1234yf experiences the highest percentage exergy destruction throughout the expansion valve and the maximum value is around 40% all over the investigated ranges. R1234ze(E) as well is a noticeable candidate for the EERC having percentage expansion losses as much as 35% within the investigated ranges. R1234yf and sometimes R1234ze(E) are used in the elaborate investigations of the EERC because of not only lower performance, but also higher percentage expansion losses in the VCRC making them attractive candidates to be analyzed in the EERC.

As a result of the performance analyses of a group of environmentally friendly refrigerants, R1234yf diplays the lowest performance and second-law efficiency accompanied by the highest percentage expansion losses in the VCRC. Due to the highest percentage expansion losses resulting in the best performance improvement potential in the EERC, R1234yf is used in the elaborate investigations of the cycle at issue. For some of the declarations R1234ze(E) as well is used because of the same reason. R134a is analyzed as well since it is one of the mostly used pure refrigerants and about to be phased out by the F-gas Regulation.

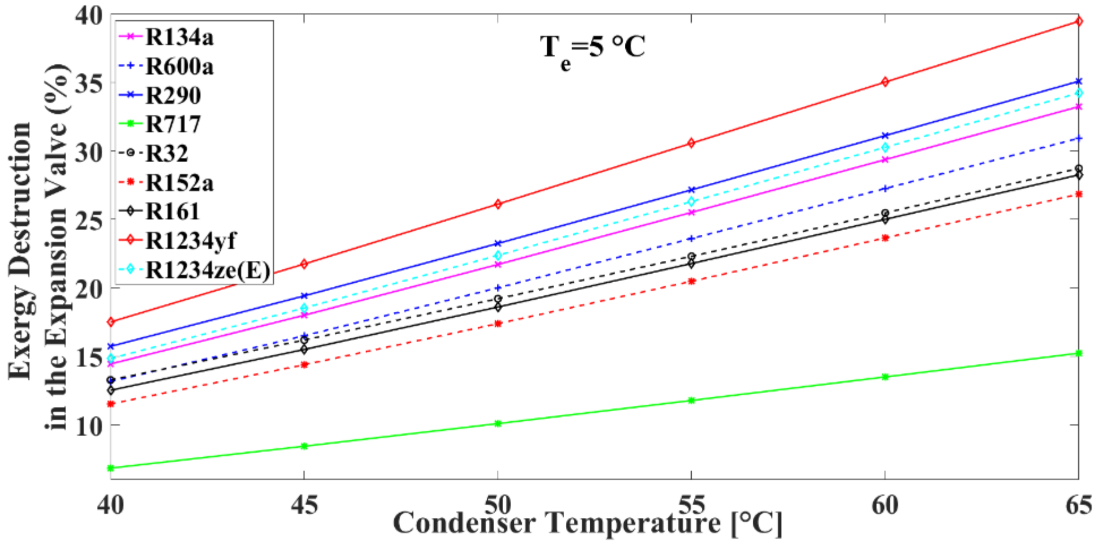


(a)

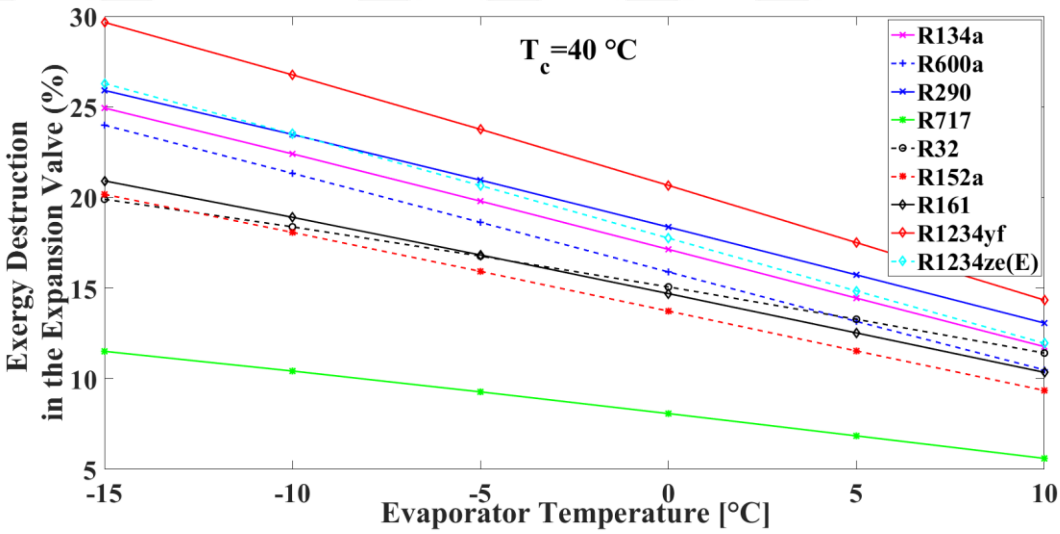


(b)

Figure 3.5 Comparison of the percentage exergy destruction in the expansion valve for various (a) condenser and (b) evaporator temperatures

In the subsequent chapter, some analyses are given for R600a and R290 in order to express some of the flow characteristics within the ejector. Moreover, transcritical EERC analyses as well are given to highlight the advantage of the high-pressure refrigerants in the ejector expansion technology. To sum up, although various refrigerants are used in the performance analyses, the main working fluids of this thesis in the experimental and numerical analyses are R134a and R1234yf.

# CHAPTER FOUR
# THERMODYNAMIC ANALYSES OF THE EJECTOR EXPANSION REFRIGERATION CYCLE

Thermodynamic modelling is a valuable approach to establish the performance evaluation of the cycles based on various design configurations (design and off-design), operating conditions, and different working fluids. This chapter is divided into seven main sections. First of all, mathematical modelling equations of the EERC are presented according to CPM and CAM ejector theories. Solution algorithm for the theoretical model and experimental validation making use of the experimental data from the literature are given. Performance improvement through medium of the EERC concept is displayed according to the mixing approaches and effect of the critical modelling assumptions are investigated. The velocity and density ratio of the secondary and primary fluid flows are investigated focusing on the variation of the area ratio with respect to the operating conditions. The performance improvement potential of the transcritical EERC as well is presented for a couple of high pressure refrigerants. The thermodynamic modelling equations of the EERC is extended for the CPM in order to include the efficiencies of the liquid-vapor separator and the ejector mixing section. Hence, the model is improved step by step. Reversible ejector is modelled to calculate the highest theoretical performance limit of the EERC. Lastly, the effects of the ejector component efficiencies and liquid-vapor separator efficiency based on the operating conditions are discussed.

## 4.1 Thermodynamic Model of the EERC for the CAM and CPM Ejector Theories

Thermodynamic model of the EERC is established only considering the efficiencies of the motive nozzle, suction nozzle, and diffuser in addition to the compressor as the first step. The main objective is to investigate the low-GWP refrigerants in the EERC taking both of the ejector mixing theories into account. Performance improvement is analyzed under both the optimum suction nozzle pressure drop and a specific pressure drop approaches for each mixing assumption. Optimum suction nozzle pressure drop assumption yields evaluations at the design conditions; whereas the constant value pressure drop approach results in the analyses out of the design (off-design) conditions. The discrepancy of the performance improvement ratios obtained according to both pressure drop assumptions is expressed using the pressure drop profiles within the same operation ranges. The geometrical parameter, area ratio ($\phi$) is analyzed under both of the mixing assumptions. The variation of the area ratios is explained interpreting the density ratio and velocity ratio of the secondary flow to the primary flow at the mixing section inlet. Lastly, the effect of the efficiency definitions for each ejector section (component) on the overall performance improvement is studied to determine the most important parameter based on the optimum operation conditions. The most essential outcomes presented with reference to Atmaca et al. (2019a), Atmaca, Erek, & Ekren (2018a), and Atmaca, Erek, & Ekren (2017a) are given in this section.

#### *4.1.1 Modelling Assumptions*

Some of the crucial assumptions with reference to Kornhauser (1990) and Li & Groll (2005) are as follows;

- In CPM ejector, the pressure stays the same throughout the mixing process. Under both of the mixing assumptions, the refrigerants have the same pressure at the inlet of the mixing section and this pressure is lower than the evaporator pressure.
- The pressure of the refrigerants at the inlet of the mixing section is assumed under two different approaches as the optimum pressure and as the saturation pressure corresponding to 5 K below the evaporator temperature (Lawrence, 2012) since it cannot be calculated directly with the inputs including no geometrical parameters. It is regarded that the nozzles have kind of geometries that the assumed pressure drops occur at the exits as a result of the expansion processes.
- Irreversibilities in the ejector sections and the compressor are taken into account with the definition of the constant efficiency values. Effect of the geometrical parameters for the ejector sections are taken into account with those section efficiency terms under the 0D thermodynamic modeling approach.

- Properties and velocities are constant throughout the cross-sections except for the ejector mixing section inlet.
- Pressure drop occurring in the pipeline, evaporator, and the condenser is negligible.
- All heat transfers from or to the surroundings are ignored except for the evaporator and condenser.
- Homogeneous equilibrium flow model approach stating both mechanical and thermodynamic equilibrium at all points is used.
- The primary and secondary fluid flows are in the compressed liquid and the superheated vapor states at the outlet of the condenser and the evaporator, respectively.
- Separator is 100% efficient.
- Velocity of all fluids at the inlet and outlet of the ejector is negligible.
- The process is isenthalpic throughout the expansion valves in the VCRC and the EERC.

### *4.1.2 Governing Equations of EERC*

The outputs to be calculated iteratively from the thermodynamic model of the EERC are the pressure and the quality of the two-phase flow at the diffuser exit. Iterations stop when the quality of the refrigerant flow at the diffuser outlet satisfy the entrainment ratio of the ejector which is the ratio of the secondary fluid mass flow rate to the primary fluid mass flow rate as given in Equation 2.1. The other important performance parameter, which is the pressure lift ratio, is given in Equation 2.2.

The suction chamber pressure is defined according to Lawrence (2012) as formulated below when the optimum values are not used. Determining pressure drops with respect to operation conditions and the types of the refrigerants is a reasonable assumption since flow structure and mixing characteristics of the ejectors not only varies according to geometrical parameters, but the refrigerants and the operation conditions as well.

$$P_s = P_{sat}(T_e - 5K) \tag{4.1}$$

Equations of CPM and CAM ejectors are summarized with reference to Kornhauser (1990) and Li & Groll (2005), respectively. The expansion process throughout the motive nozzle is explained by the following equations. Motive and suction nozzle efficiencies are expressed by Equation 2.3 and Equation 2.4. Actual enthalpy, velocity, and the occupied area of the primary flow at the motive nozzle outlet section per unit total mass flow of the ejector are as follows;

$$h_{m,out} = (1-\eta_m)h_{m,in} + \eta_m h(s_{m,in}, P_s) \tag{4.2}$$

$$u_{m,out} = \sqrt{2(h_{m,in} - h_{m,out})} \tag{4.3}$$

$$a_{m,out} = \left(\frac{1}{w+1}\right)\left(\frac{1}{u_{m,out}\,\rho(P_s, h_{m,out})}\right) \tag{4.4}$$

The same equation set is given for the suction nozzle as

$$h_{s,out} = (1-\eta_s)h_{s,in} + \eta_s h(s_{s,in}, P_s) \tag{4.5}$$

$$u_{s,out} = \sqrt{2(h_{s,in} - h_{s,out})} \tag{4.6}$$

$$a_{s,out} = \left(\frac{w}{w+1}\right)\left(\frac{1}{u_{s,out}\,\rho(P_s, h_{s,out})}\right) \tag{4.7}$$

Equations of the mixing section based on the CPM approach considering the same pressure at the inlet and outlet are expressed as

$$u_{mix,out} = \left(\frac{w}{w+1}\right)u_{s,out} + \left(\frac{1}{w+1}\right)u_{m,out} \tag{4.8}$$

$$h_{mix,out} = \left(\frac{w}{w+1}\right)h_{s,in} + \left(\frac{1}{w+1}\right)h_{m,in} - \frac{u_{mix,out}^2}{2} \tag{4.9}$$

$P_{mix,out}$ and $P_s$ are the same for the CPM assumption; whereas mixing section outlet pressure is different than the suction pressure for CAM approach and requires another iterative calculation procedure based on the application of the conservation of mass, momentum, and energy on the control volume comprised of the constant area mixing section.

$$P_s(a_{m,out}+a_{s,out})+\left(\frac{w}{w+1}\right)u_{s,out}+\left(\frac{1}{w+1}\right)u_{m,out}= \\ P_{mix,out}(a_{m,out}+a_{s,out})+u_{mix,out} \tag{4.10}$$

$$h_{mix,out}=\left(\frac{w}{w+1}\right)h_{s,in}+\left(\frac{1}{w+1}\right)h_{m,in}-\frac{u^2_{mix,out}}{2} \tag{4.11}$$

$$\rho(P_{mix,out},h_{mix,out})(a_{m,out}+a_{s,out})u_{mix,out}=1 \tag{4.12}$$

Diffuser equations to recover the rest of the kinetic energy for more pressure rise are as given below. Diffuser efficiency is given previously by Equation 2.5.

$$s_{mix,out}=s(h_{mix,out},P_{mix,out}) \tag{4.13}$$

$$h_{d,out}=h_{mix,out}+\frac{u^2_{mix,out}}{2} \tag{4.14}$$

$$h_{d,out,isen}=h_{mix,out}+\eta_d\,\frac{u^2_{mix,out}}{2} \tag{4.15}$$

The pressure and the quality at the diffuser outlet are the target outputs.

$$P_{d,out}=P(s_{mix,out},h_{d,out,isen}) \tag{4.16}$$

$$r_{d,out}=r(P_{d,out},h_{d,out}) \tag{4.17}$$

The entrainment ratio of the refrigerant for 100% efficient liquid-vapor separator could also be expressed as a function of the quality as

$$w = \frac{1}{r_{d,out}} - 1 \tag{4.18}$$

After ejector, a liquid-vapor separator is used to send the vapor portion of the two-phase mixture to the compressor and the liquid portion to the evaporator. The refrigerants at the liquid and vapor ports of the separator are in saturated states and the enthalpies are formulated as follows;

$$h_{sep,l,out(rslp)} = h(P_{d,out}, r_{sep,l,out(rslp)} = 0) \tag{4.19}$$

$$h_{sep,v,out(rsvp)} = h(P_{d,out}, r_{sep,v,out(rsvp)} = 1) \tag{4.20}$$

The rest of the cycle components are modelled in the same way that VCRC equations are established taking the primary and secondary fluid flow rates into account as well. The ratio of the performance coefficient of the EERC to the VCRC is defined as the performance improvement ratio (coefficient), *R* and formulated below.

$$R = \frac{COP_{EERC}}{COP_{VCRC}} \tag{4.21}$$

Volumetric cooling capacity (*VCC*) improvement of both cycles is compared considering the $VCC_{VCRC}$ and $VCC_{EERC}$ defined based on the specific suction volume of the compressor as follows;

$$VCC_{VCRC} = (h_{e,out} - h_{e,in})\rho(P_{comp,in}, h_{comp,in}) \tag{4.22}$$

$$VCC_{EERC} = w(h_{s,in} - h_{sep,l,out})\rho(P_{d,out}, r_{sep,v,out} = 1) \tag{4.23}$$

The area ratio which is the ratio of the cross-sectional area occupied by the total flow in the suction nozzle to the cross-sectional area of the primary flow at the motive nozzle outlet is expressed as

$$\phi = \frac{a_{m,out} + a_{s,out}}{a_{m,out}} \tag{4.24}$$

Elbel & Hrnjak (2008b) defined the ejector efficiency as the ratio of the expansion work rate recovery to the maximum potential expansion work rate recovery. Efficiency definition of Elbel & Hrnjak (2008b) is used to display the variation of the overall ejector efficiency with respect to the assumed pressure of the refrigerants in the suction nozzle.

$$\eta_{ej} = w \frac{h(P_{d,out}, s_{s,in}) - h_{s,in}}{h_{m,in} - h(P_{d,out}, s_{m,in})} \tag{4.25}$$

### *4.1.3 Solution Algorithm of the Thermodynamic Modelling Equations*

Theoretical EERC models are constructed in MATLAB® and thermodynamic states of the refrigerants were obtained using REFPROP version 9.1 (Lemmon et al., 2013). 0D thermodynamic models are established by applying the conservation equations of mass, momentum, and energy to the inlet and outlet of each ejector section (motive nozzle, suction nozzle, mixing section, and diffuser) and the refrigeration system components. A constant efficiency value is assigned to each ejector section and the compressor to solve the relevant governing equation.

The solution algorithm is summarized in Figure 4.1. Suction nozzle pressure drop could be defined as a specific value or the iteratively calculated optimum value. The entrainment ratio as well is determined iteratively and iterations would end when the assumed and calculated entrainment ratios are close enough to each other within an acceptable error band. If the suction nozzle pressure is defined directly with respect to the assumption of Lawrence (2012), the second iterative process in order to optimize suction nozzle pressure drop in Figure 4.1 would be unnecessary. However, the resultant outcomes ($P_s$, $\phi$, $P_{d,out}$, $w$, and $R$) under this approach are not the optimum values.

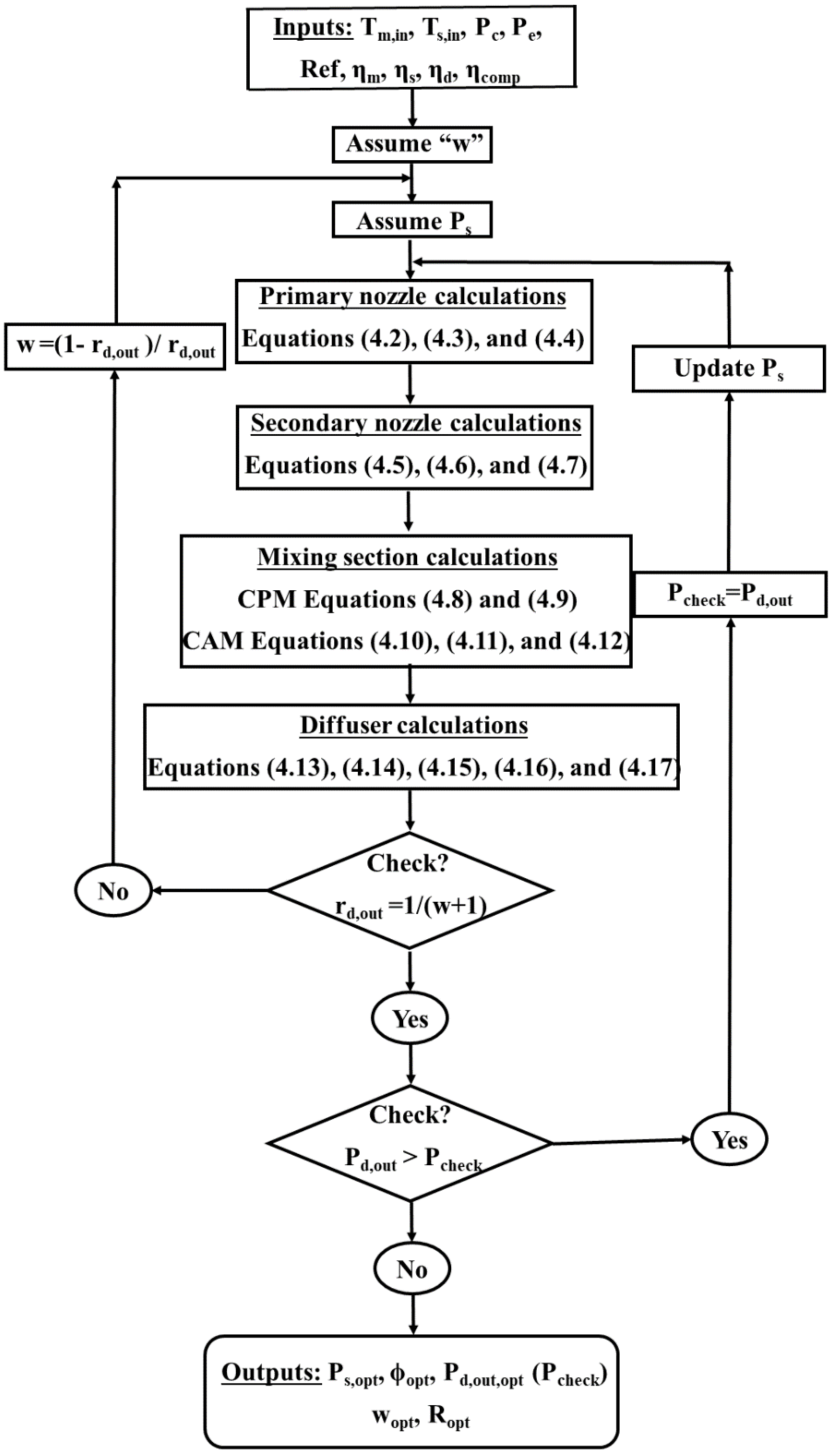


Figure 4.1 Solution algorithm of the EERC

To present a more generalized solution algorithm, the flowchart in Figure 4.1 is given to define the optimum values based on the optimum suction nozzle pressure drop. $P_{check}$ is introduced to control the increase or decrease in the diffuser outlet pressure which attains its maximum at the optimum operation conditions. At the first iteration, $P_{check}$ could be the evaporator pressure since diffuser outlet pressure would certainly be higher than the pressure of the secondary fluid for an ejector operating properly. For the rest of the iterations after the first step, $P_{check}$ gets the value of the diffuser outlet pressure calculated in the previous step. Whenever a higher diffuser outlet pressure is calculated, $P_s$ is updated in order to obtain the optimum operation conditions. After obtaining the maximum, when it is seen that the diffuser outlet pressure starts decreasing, the value of the diffuser outlet pressure at the previous step which is $P_{check}$ is defined as the maximum and the corresponding condition at which the maximum value is obtained is the optimum suction nozzle pressure. Optimum values of the area ratio, entrainment ratio, performance improvement ratio as well are calculated using the same optimum pressure drop. $P_{check}$ is expected to be higher than the evaporator pressure after the first iteration and lower than the condenser temperature, but closer to the evaporator pressure.

When CAM approach is used, one more iterative procedure is necessary to estimate the mixing section outlet pressure. Figure 4.1 simply describes the general calculation procedure; hence the iterative procedure of the mixing section under the CAM assumption is not displayed in it.

#### *4.1.4 Experimental Validation of the Thermodynamic Models*

Mathematical models are validated in this section through medium of the global parameters, i.e., entrainment ratio and diffuser outlet pressure. The thermodynamic model is validated firstly with the experimental data provided by Ersoy & Sag (2014) as given in Table 4.1 for a subcritical EERC utilizing R134a. The CAM assumption is chosen for the model validation of the EERC since the ejector of the reference study (Ersoy & Sag, 2014) is manufactured according to CAM theory. The numerical results are presented for two cases in terms of the arbitrary efficiency values of the motive nozzle, suction nozzle, and the diffuser. The efficiency cases for numerical results 1 and 2 in Table 4.2 are used with reference to previous thermodynamic modelling studies (Ersoy & Bilir, 2010; Lawrence, 2012; and Li & Groll, 2005). The last arbitrary point is the pressure of the refrigerants in the suction nozzle for the thermodynamic models and it is defined according to saturation pressure corresponding to 5 K below of the evaporator inlet temperature which is 8.67 ˚C for the first validation case.

Table 4.1 Experimental data (Ersoy & Sag, 2014) for the validation of the calculated results by means of the thermodynamic models

| Parameters | Values |
|---|---|
| Primary nozzle inlet temperature (˚C) | 52.62 |
| Primary nozzle inlet pressure (kPa) | 1483.94 |
| Secondary nozzle inlet temperature (˚C) | 20.88 |
| Secondary nozzle inlet pressure (kPa) | 392.11 |
| Diffuser outlet pressure (kPa) | 421.34 |
| Compressor mass flow rate (kg/s) | 0.0341 |
| Evaporator mass flow rate (kg/s) | 0.0217 |

Table 4.2 Percentage error for the entrainment ratio and the diffuser outlet pressure under two different cases of the section efficiencies with respect to experimental data (Ersoy & Sag, 2014)

| **Validation Parameters** | **Experimental Data** | **Numerical-1 ($\eta_m$= $\eta_s$=0.9 &$\eta_d$=0.8)** | **Error 1 (%)** | **Numerical-2 ($\eta_m$= $\eta_s$=0.8 &$\eta_d$=0.75)** | **Error 2 (%)** |
|---|---|---|---|---|---|
| w | 0.6364 | 0.6617 | **4.0** | 0.6511 | **2.3** |
| $P_{d,out}$ (kPa) | 421.34 | 460.18 | **9.2** | 439.02 | **4.2** |

The whole model equations are established based on the same manner by means of the conservation of mass, momentum, and energy for both CAM and CPM ejectors. Hence verification of CAM model assures that CPM model could also be used in the thermodynamic models. Study of Liu, Groll et al. (2012) is secondly utilized to obtain the experimental operation conditions of the transcritical EERC using $CO_2$ as the working fluid. Validated test run is displayed in Table 4.3.

Comparisons between the experimental data and thermodynamic results are given in Table 4.4. Liu, Groll et al. (2012) provide with the experimental component efficiencies as well except for the diffuser. CPM ejector theory is used this time in the second validation case. Two options are analyzed for the diffuser efficiency as *0.80* and *0.75* with reference to Li & Groll (2005) and Lawrence (2012), respectively as given in Table 4.4. Suction nozzle pressure drop is defined in the same way of the first validation case. In this validation case, evaporator temperature is estimated according to saturation temperature of the suction nozzle inlet pressure since it is not given directly.

Table 4.3 Experimental data (Liu, Groll et al., 2012) in order to validate the thermodynamic model of the transcritical EERC

| Parameters | Values |
|---|---|
| Motive nozzle inlet pressure (MPa) | 12.855 |
| Motive nozzle inlet temperature (˚C) | 50.88 |
| Suction nozzle inlet pressure (MPa) | 3.748 |
| Suction nozzle inlet temperature (˚C) | 21.63 |
| Motive nozzle mass flow rate (kg/s) | 0.18 |
| Suction nozzle mass flow rate (kg/s) | 0.07 |
| Entrainment ratio (-) | 0.3889 |
| Diffuser outlet pressure (MPa) | 4.499 |
| Motive nozzle efficiency (-) | 0.986 |
| Suction nozzle efficiency (-) | 0.972 |
| Mixing section efficiency (-) | 0.882 |

Table 4.4 Display of the percentage error between the numerical calculations and the experimental data (Liu, Groll et al., 2012) under two different diffuser efficiency assumptions

| Validation Parameters | Experimental Data | Numerical-1 ($\eta_d$=0.8) | Error 1 (%) | Numerical-2 ($\eta_d$=0.75) | Error 2 (%) |
|---|---|---|---|---|---|
| w | 0.3889 | 0.3922 | **0.8** | 0.3932 | **1.1** |
| $P_{d,out}$ (kPa) | 4499 | 4999 | **11.1** | 4864 | **8.1** |

Under these conditions, the maximum percentage error is around 10% and the agreement is satisfactory for both of the validation cases. All these experiments were conducted using highly accurate components. For example, the accuracy of the pressure transmitter was ±0.25% of the exact scale and the accuracy of the flow meters was ±1.6% of the exact scale in the experimental set-up of Ersoy & Sag (2014).

### *4.1.5 Results of the Thermodynamic Analyses*

Performance comparison of the refrigerants in the EERC under two different ejector mixing and suction nozzle pressure drop assumptions are discussed in this section. The operating conditions for the performance analyses of the EERC are given in Table 4.5. The refrigerants having the highest exergy destruction percentages in the expansion valve, namely R1234yf, R290, R1234ze(E), R134a, and R600a, are investigated in the EERC at various operation conditions as in Figure 4.2 (a) and (b) under both CPM and CAM assumptions.

Table 4.5 Operating conditions for the EERC performance analyses for a typical air-conditioning application

| **Parameters** | **Values** |
|---|---|
| Evaporator temperature ($T_e$) | 5 ˚C |
| Evaporator outlet superheat temperature difference ($\Delta T_{sh}$) | 5 K |
| Condenser Temperature ($T_c$) | 40 ˚C |
| Condenser outlet subcooling temperature difference ($\Delta T_{sc}$) | 3 K |
| Compressor efficiency ($\eta_{comp}$) | 0.75 |
| Primary nozzle efficiency ($\eta_m$) | 0.9 |
| Suction nozzle efficiency ($\eta_s$) | 0.9 |
| Diffusor efficiency ($\eta_d$) | 0.8 |

In Figure 4.2, both of the mixing assumptions are evaluated considering the same suction nozzle pressure assuming to be the saturation pressure corresponding to 5 K below the evaporation temperature. It is seen that at some operation ranges CAM is superior; whereas after that range CPM yields higher performance improvement ratio. The reason for the dependency of the superior mixing assumption upon the operation conditions is about the closeness of the assumed suction pressure to the optimum value.

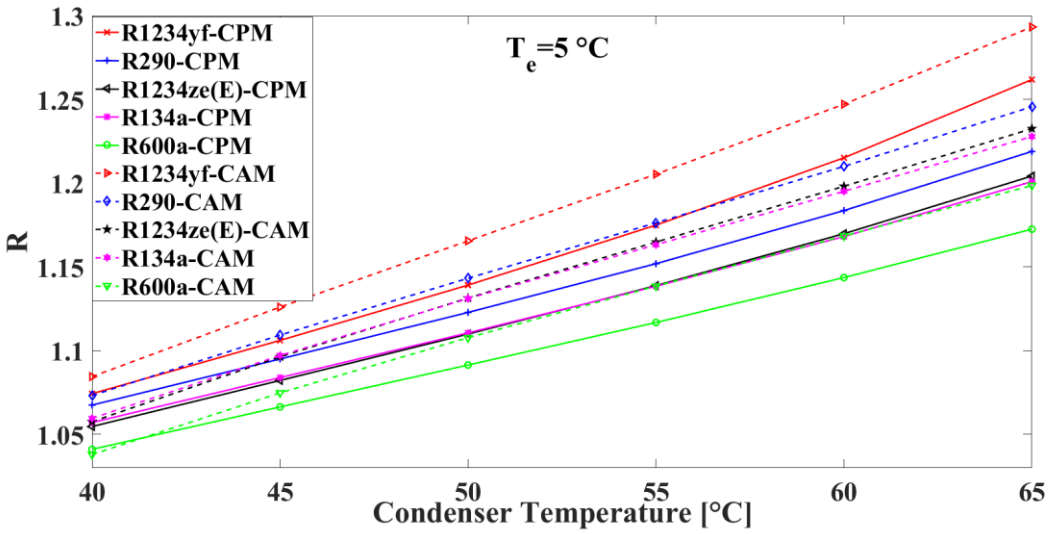


(a)

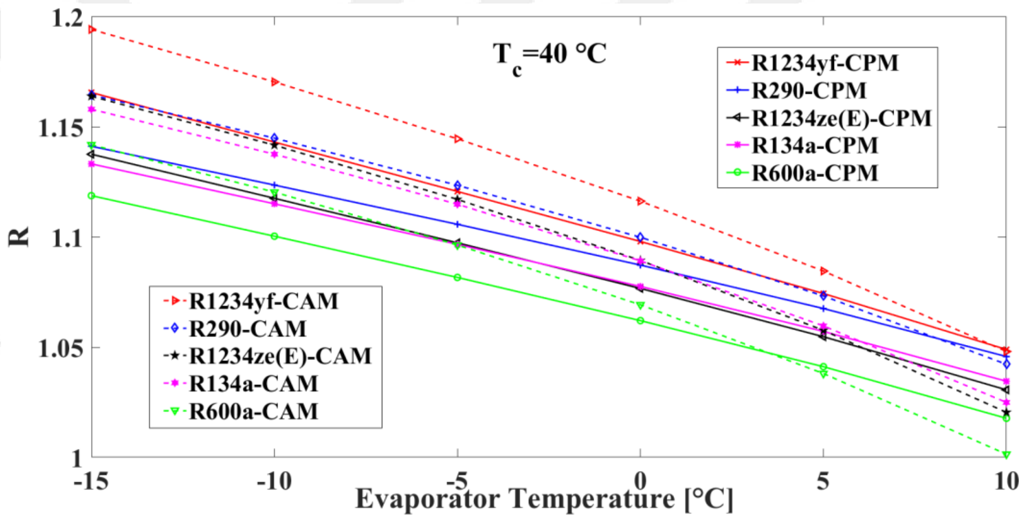


(b)

Figure 4.2 Comparison of the improvement potential of the refrigerants in the EERC for various (a) condenser and (b) evaporator temperatures

Under the suction nozzle pressure drop assumption of Lawrence (2012), the superiority of the CAM and CPM approaches depend on the operation conditions and surely the refrigerants. Discrepancy between the effects of the optimum and specific suction chamber pressure assumptions on the overall performance is analyzed within the same operation ranges in Figure 4.3 (a) and (b) for R1234yf under both mixing assumptions.

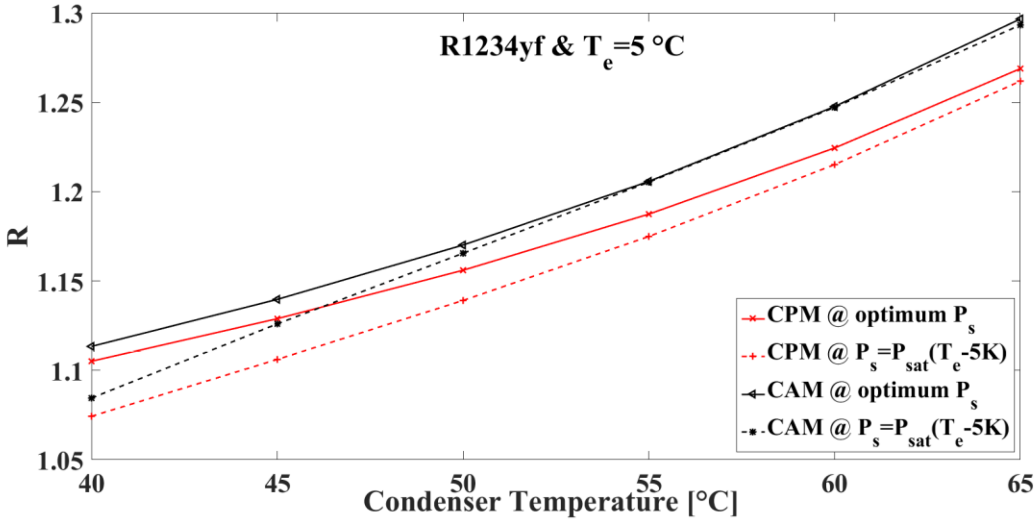


(a)

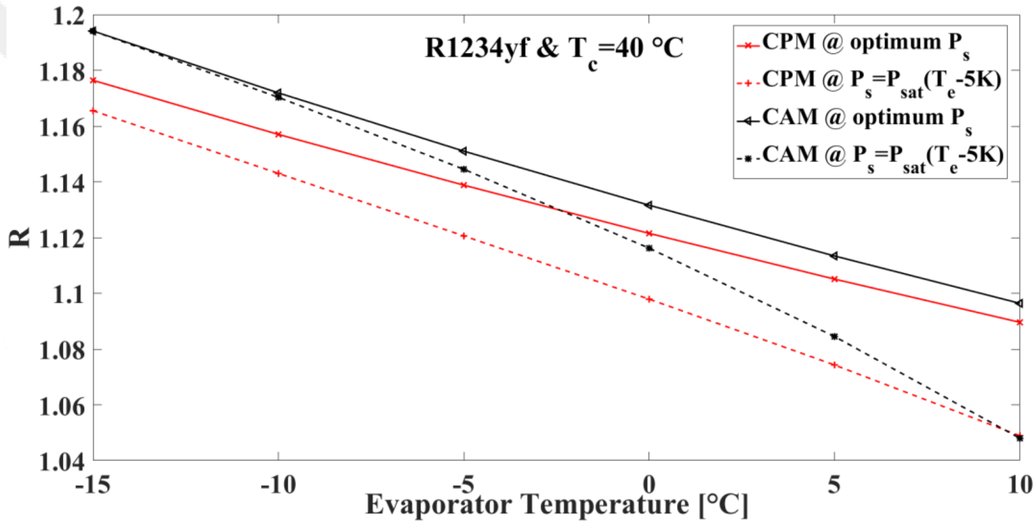


(b)

Figure 4.3 Comparison of the performance improvement ratios for two different suction chamber pressure assumptions under CAM and CPM approaches at various (a) condenser and (b) evaporator temperatures for R1234yf

When the pressure drop increases between the evaporator and the suction nozzle, the velocity of the secondary flow starts increasing as well. Increase of the pressure drop in the suction nozzle yields the increase in the velocity of the refrigerant fluid flows. Primary and secondary fluids having higher velocities result in higher velocity of the total flow and thus better pressure recovery potential. However, the increased amount of the pressure drop in the suction nozzle adversely affects the pressure recovery potential of the ejector since part of the potential used to compensate for the pressure drop that the refrigerant experiences in the suction nozzle increases. Therefore, there is an optimum operation point for the refrigerant fluid flows having higher velocities in terms of the pressure drop in the suction nozzle yielding the best performance improvement. In this study, performance improvement is presented under both of the pressure drop assumptions and the agreement between them is focused with respect to each mixing assumption.

At higher condenser temperatures and lower evaporator temperatures, it is seen that *R* values calculated according to the suction chamber pressure assumption corresponding to saturation pressure at 5 K below the evaporator temperature best match with the R values defined with reference to the optimum suction pressure approach. Under CAM assumption, the agreement of both pressure drop definitions are better when compared to CPM approach in all investigated ranges.

Effect of the suction nozzle pressure drop assumption on the overall ejector efficiency is displayed in Figure 4.4 for R1234yf and R1234ze(E) under both of the mixing assumptions. Efficiency definition of Elbel & Hrnjak (2008b) is used in the analysis. The assumed pressure in the suction nozzle is displayed parametrically with respect to designation of the saturation pressures corresponding to specific temperatures below the evaporator temperature of each refrigerant other than the actual values.

Suction nozzle pressure drops are compared in Figure 4.5 (a) and (b) to obtain the relationship between the pressure drop approaches and the operation conditions for R1234yf. Optimum pressure drop of CAM approach converges and diverges to the specifically defined pressure drop profile with reference to Lawrence (2012) as seen in Figure 4.5 (a); hence there is a wide range that CAM approach offers similar results at higher condenser temperatures. Optimum pressure drops nearly stay the same under CPM assumption at various evaporator temperatures; whereas, it reacts more to the changes under the CAM assumption as shown in Figure 4.5 (b).

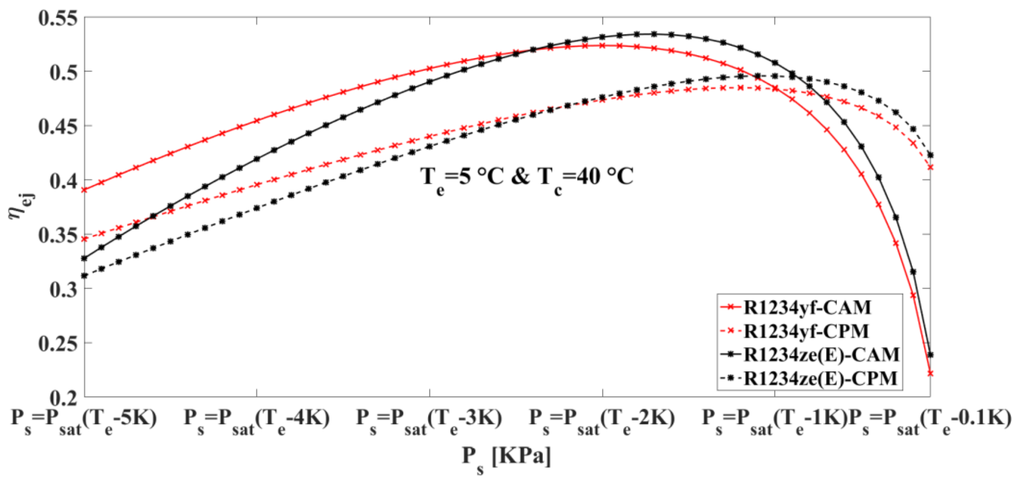


Figure 4.4 Variation of the overall ejector efficiency with respect to suction nozzle pressure assumption for R1234yf and R1234ze(E)

The assumption of Lawrence (2012) is better to be used at lower evaporator and higher condenser temperatures in order to produce performance improvement values similar to the obtained results at the optimum suction nozzle pressure. In other words, at lower evaporator and higher condenser temperatures, an ejector could operate at off-design conditions yielding similar performance improvement values to the design conditions.

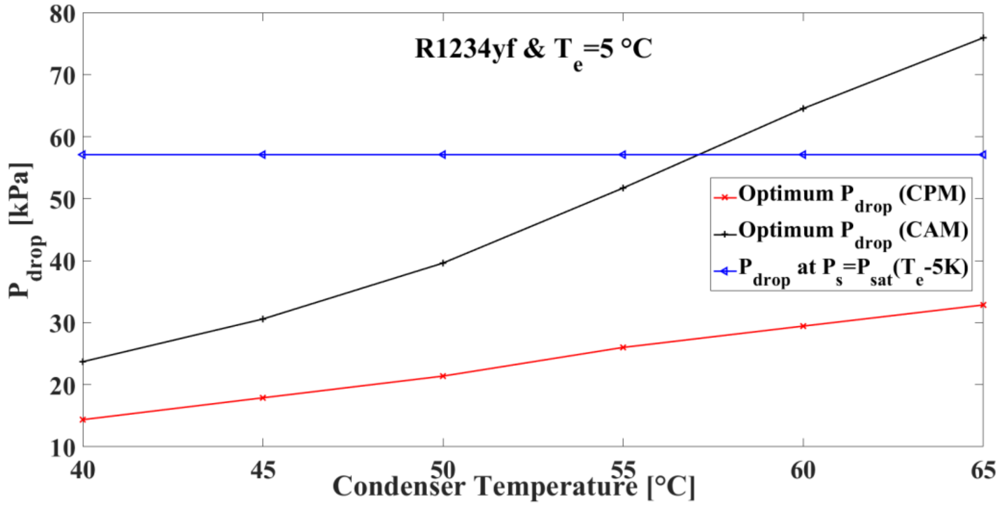


**(a)**

Figure 4.5 Variation of the pressure drops with respect to optimum and specific suction chamber pressure assumptions according to (a) condenser and (b) evaporator temperatures for R1234yf

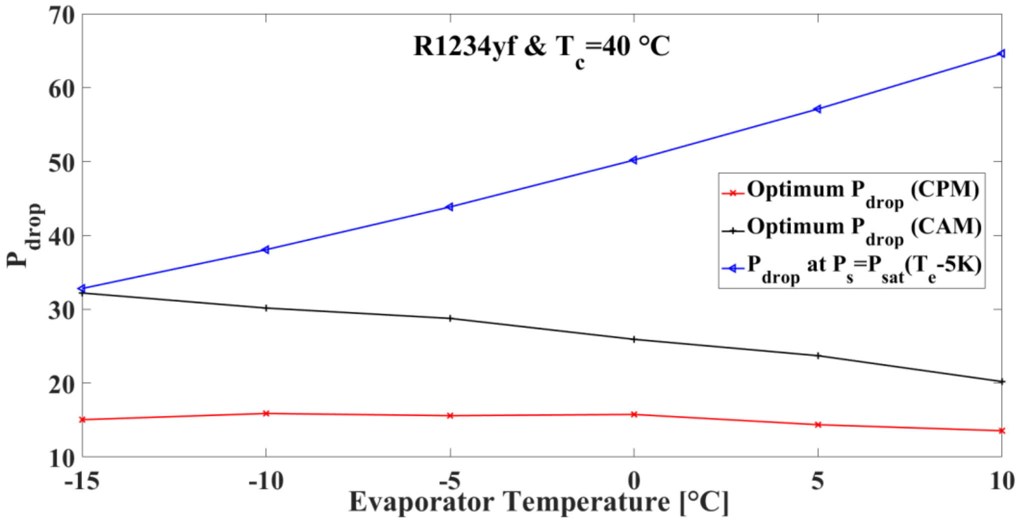


**(b)**

Figure 4.5 continues

In Figure 4.3, the performance improvement ratios with respect to the both mixing assumptions in all ranges are so close to each other under the optimum suction chamber pressure drop approach. For all investigated operation conditions, maximum difference between the optimum performance improvement percentages with respect to CAM and CPM assumptions is 2.78% for R1234yf. The difference between the assumptions is that in CPM, the refrigerant mixture leaves the mixing section at higher velocities when compared to CAM. Therefore, the kinetic energy recovered in the diffuser is higher in CPM approach and the difference is nearly compensated by the pressure increase gained throughout the mixing according to CAM assumption. Such being the case, both of the assumptions could be used to obtain the typical performance improvement ratios since they are just modeling assumptions. With respect to these findings, Table 4.6 summarizes the improvement aspects of the ejectors by means of the thermodynamic modelling.

Dependence of the optimum area ratio on various operation conditions for both R1234yf and R1234ze(E) is shown in Figure 4.6 under both of the mixing assumptions. Optimum entrainment ratio calculated with respect to two different mixing assumptions is very close to each other for a refrigerant. Meanwhile, it is observed that the velocity ratio of the secondary fluid flow to the primary fluid flow just before mixing is yielding higher values according to CAM assumption than the CPM approach for the refrigerant at issue within all investigated ranges.

Table 4.6 Comparison of the optimum COP and VCC improvement percentages and pressure lift values of an ejector with respect to mixing assumptions for a typical air-conditioning application

| Refrigerants | $COP_{imp}$ (%) | | $VCC_{imp}$ (%) | | $P_{lr}$ | |
|---|---|---|---|---|---|---|
| | CAM | CPM | CAM | CPM | CAM | CPM |
| **R1234yf** | 11.3 | 10.5 | 10.2 | 9.5 | 1.10 | 1.09 |
| **R290** | 10.5 | 9.8 | 8.7 | 8.1 | 1.08 | 1.08 |
| **R1234ze(E)** | 9.5 | 8.8 | 9.3 | 8.6 | 1.09 | 1.09 |
| **R134a** | 9.6 | 9.0 | 9.3 | 8.7 | 1.09 | 1.08 |
| **R600a** | 8.2 | 7.6 | 7.7 | 7.2 | 1.08 | 1.07 |

Density ratio of the secondary fluid to the primary fluid increases as reaction to the increased condenser temperature. The rate of change of density ratio according to condenser temperature is higher than the rate of change of velocity ratio and hence in accordance with both of the mixing assumptions, area ratio decreases accompanied by the increase in the condenser temperature as shown in Figure 4.6 (a).

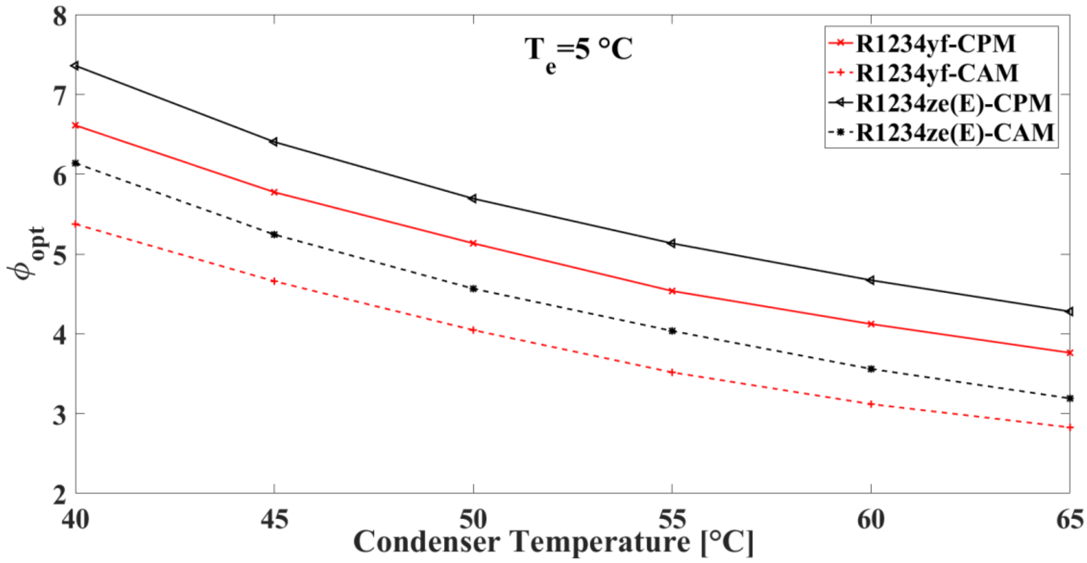


**(a)**

Figure 4.6 Dependency of the optimum area ratios with respect to (a) condenser and (b) evaporator temperatures for R1234yf and R1234ze(E)

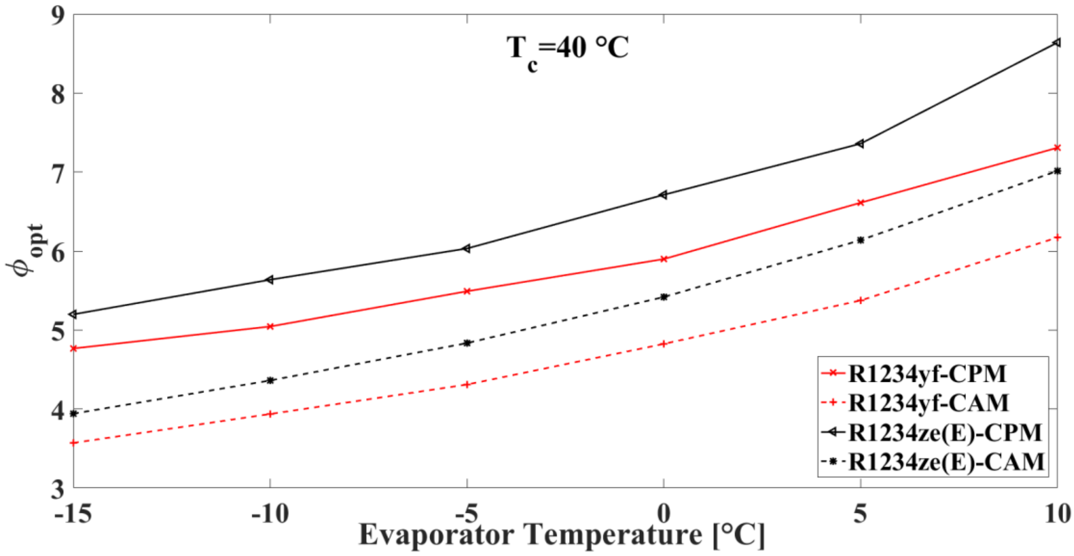


**(b)**

Figure 4.6 continues

Considering the effect of the higher values of the velocity ratio calculated according to CAM assumption at each investigated operation condition, the area ratio yields smaller values when compared to CPM approach for R1234yf. Density ratio of the secondary fluid to the primary fluid as well decreases according to the increased evaporator temperature as shown in Figure 4.6 (b) and density ratio profiles typically have similar tendency to decrease according to each operation condition under both of the mixing assumptions. Similar to previous increased condenser temperature case, rate of change is calculated higher in the density ratio variations compared to velocity ratio variations. Therefore, the total effect under both of the mixing assumptions is the increase of the area ratios when the evaporator temperature is increased. However, CPM assumption yields higher area ratios owing the lower velocity ratio values calculated under CPM approach at each operation condition for both of the refrigerants.

Up to this point, the efficiency of the mixing section is assumed to be unity and all analyses are conducted from this point of view. In this section, the effect of all section efficiencies, namely primary nozzle, suction nozzle, mixing section, and diffuser are discussed for R1234yf under the optimum pressure drop and CPM assumptions as shown in Figure 4.7 (a). The mixing section efficiency is defined as (Eames, Aphornratana, & Haider, 1995);

$$\eta_{mix} = \frac{u_{mix,out}}{\left(\frac{1}{1+w}\right)u_{m,out} + \left(\frac{w}{w+1}\right)u_{s,out}} \tag{4.26}$$

Atmaca, Erek, Ekren (2017b) compared all ejector section (component) efficiencies similar to Li et al. (2014), but they defined the mixing section efficiency according to Eames et al. (1995) and considered superheated and subcooled refrigerants at the outlet of the evaporator and condenser, respectively. They defined the suction nozzle pressure drop according to the saturation pressure corresponding to the temperature 5 K below the evaporator temperature. Moreover, the following comparison of the ejector sections is made through the optimum performance improvement with reference to Atmaca et al. (2019a).

Investigated range for all sections varies between *0.75-0.95* corresponding to the limits of worst and best cases, respectively. It is seen from Figure 4.7 (a) that the most important section is the mixing section and it is followed by the diffuser. When a section efficiency changes, not only performance, but also the optimum area ratio and the entrainment ratio are affected as seen from Figure 4.7 (b).

As a result of the performance analyses of a group of environmentally friendly refrigerants, R1234yf displays the lowest performance and second-law efficiency accompanied by the highest percentage expansion losses in the VCRC. Due to the highest percentage expansion losses resulting in the best performance improvement potential in the EERC, R1234yf is used in the elaborate investigations of the cycle at issue. For some of the declarations R1234ze(E) as well is used because of the same reason.

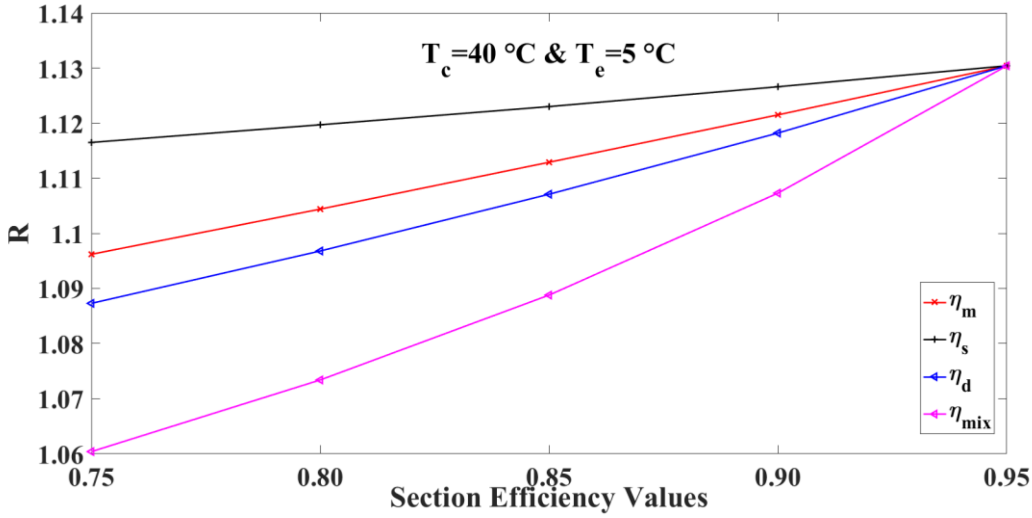


(a)

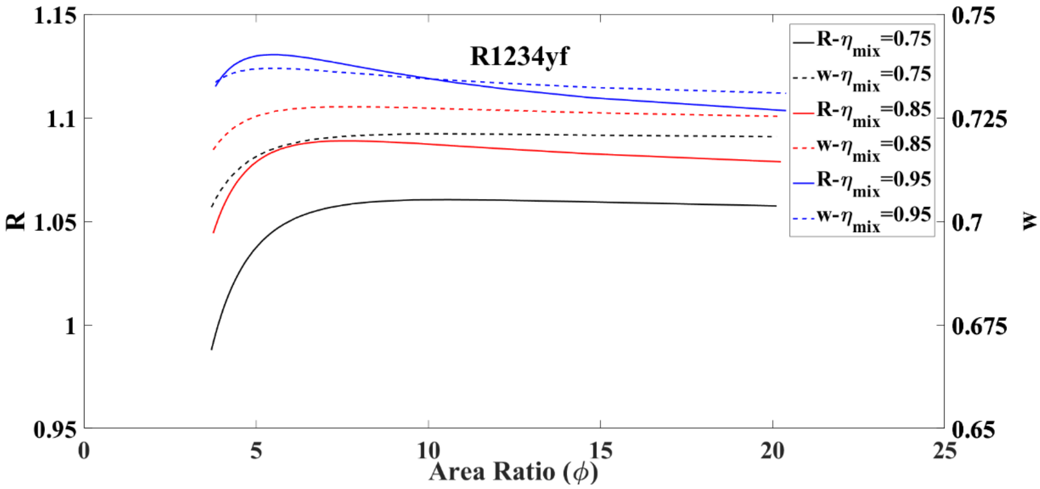


(b)

Figure 4.7 (a) The effects of the ejector section efficiencies on the overall performance improvement ratio and (b) the influence of the mixing section efficiency on the performance improvement ratio and the entrainment ratio based on the area ratio for R1234yf

Performance improvement ratio of R1234yf in the EERC is investigated under both CAM and CPM ejector theories with respect to optimum and specific suction nozzle pressure drop assumptions. The summary of the mixing assumption comparisons based on the suction chamber pressure and the investigations concerning the effects of the ejector section efficiencies on the overall performance is as given below;

- At higher condenser temperatures and lower evaporator temperatures, both of the suction chamber pressure drop approaches provide with similar performance improvement ratios under each mixing assumption although CAM assumption yields better agreement between these two pressure drop assumptions corresponding to the design and off-design conditons when compared with CPM approach within the same ranges. It is directly because of the optimum pressure drop profile of CPM ejector which is farther from the specific pressure drop curve when compared to CAM approach under the same operation conditions.
- Another point is that the optimum pressure profile for both of the mixing theories varies more with respect to condenser temperature rather than the evaporator temperature.
- When optimum performance values under both of the mixing assumptions are compared, CAM assumption offers slightly higher performance results for the EERC configuration.
- In addition to these aspects, optimum area ratio of the refrigerants decreases when the condenser temperature increases and the evaporator temperature decreases for both of the mixing assumptions. The area ratio of CAM ejector is calculated less as compared with the CPM ejector due to the fact that velocity ratio of the secondary fluid to the primary fluid is higher for CAM approach at each investigated point. The variation of the density ratio of the refrigerants determines the tendency of the area ratio change.
- Mixing section is found to be the most important and the suction nozzle is the least effective one in terms of their influence on the overall perfromance improvement. Mixing section efficiency is to be added to the thermodynamic models for more realistic performance predictions.

## 4.2 Comprehensive Investigations on the Velocity and Density Ratios of the Secondary and Primary Fluid Flows

Variations of the velocity and density ratios of the primary and secondary fluid flows according to the operating conditions are explained in the previous section with reference to the analyses made on R1234yf. Hence, the variations of the area ratio could be displayed more clearly. Actually, it is a typical behavior. In other words, the variation tendency of the density and velocity ratios stay the same for all refrigerants although the physical magnitudes of these values differ numerically from refrigerant to refrigerant. In this section, R600a and R290 among the natural refrigerants having relatively high expansion losses are investigated through medium of performance improvement in the EERC with reference to optimum operating conditions. The first target is focusing on another refrigerant group, i.e., natural refrigerants, having expansion work recovery potential through medium of the ejector technology to display the critical performance metrics. The second target is to declare graphically the variations of the density and velocity ratios which are verbally expressed in the previous section based on the area ratio and mixing assumptions for R1234yf and R1234ze(E). Some part of the results obtained by Atmaca, Erek, & Ekren (2018c) is presented in this section.

0D thermodynamic models are established in Matlab® considering only inlet and outlet of the ejector sections and refrigeration cycle components. Conservation equations of mass, momentum, and energy are applied to each control volume to derive the equations. The thermodynamic properties of the refrigerants at each state is calculated with the help of REFPROP version 9.1 (Lemmon et al., 2013). Refrigerant properties are declared in Table 3.3. Operating conditions are the same conditions for a typical air-conditioning application.

### *4.2.1 Results of the Thermodynamic Analyses*

For the refrigerants under issue the maximum expansion loss is over 35% for R290; whereas it is around 30% for R600a at the highest condenser temperature as it is obvious from Figure 3.5. Figure 4.8 displays the differences between the optimum performance improvement ratio and optimum entrainmet ratio for both of the refrigerants. As seen from Figure 4.8 (a), R290 has more performance improvement potential and operates with lower entrainment ratios over the investigated condenser temperature range when compared to R600a. The same comments could be made for R290 and R600a considering the investigated evaporation temperature range as given in Figure 4.8 (b). Entrainmet ratio of a refrigerant is very close to each other for both of the mixing assumptions at the optimum operation conditions. Moreover, the performance improvement ratios are very close to each other although CAM assumption yielded higher values for both of the refrigerants. However, both of the models could be used in any comparative investigations.

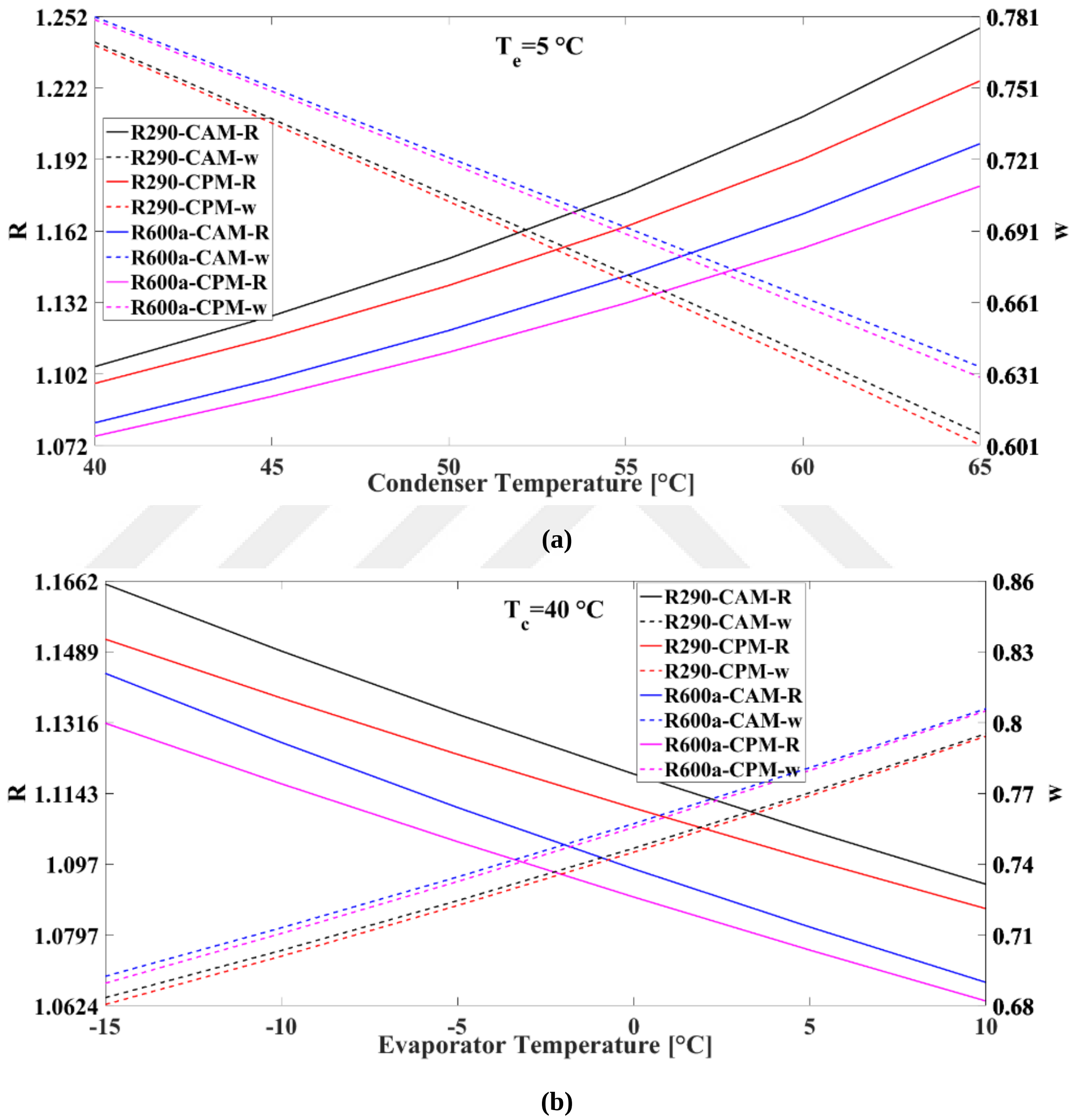


Figure 4.8 Variations of the optimum performance improvement ratio and the optimum entrainment ratio according to (a) condenser and (b) evaporator temperatures

Figure 4.9 shows the comparison of the optimum area ratio of the refrigerants according to both of the mixing assumptions at various condenser and evaporator temperatures. The area ratio is calculated higher for R600a in comparison with R290. As also seen from Figure 4.9 (a) and (b), smaller area ratio is calculated for the CAM approach when compared to CPM assumption. Similar conclusions are derived in the previous section and explained in detail for R1234yf and R1234ze(E). The current analyses are as well aiming to explain the differences of the area ratios according to the mixing theories visualizing the velocity and the density ratios of the secondary fluid flow to the primary fluid flow in the suction chamber.

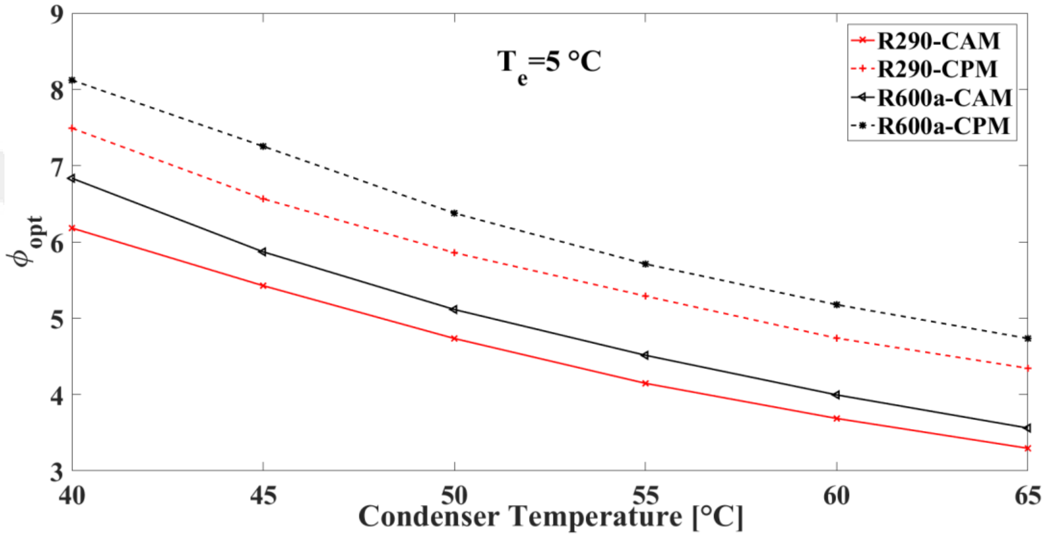


(a)

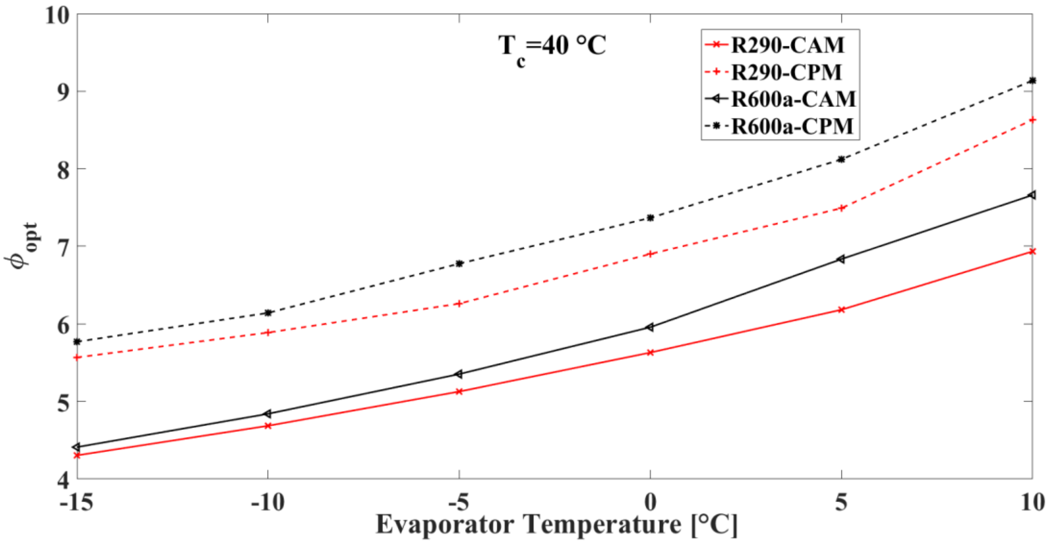


(b)

Figure 4.9 Dependency of the optimum area ratio with respect to (a) the condenser and (b) the evaporator temperatures

In order to explain the differences between the mixing assumptions and the variations of the optimum area ratio in accordance with the operation conditions, pressure drop in the suction chamber and velocity and density ratios of the refrigerants are investigated as shown in Figure 4.10 and Figure 4.11, respectively. As seen from Figure 4.10 (a) and (b), optimum pressure drop varies more for R290.

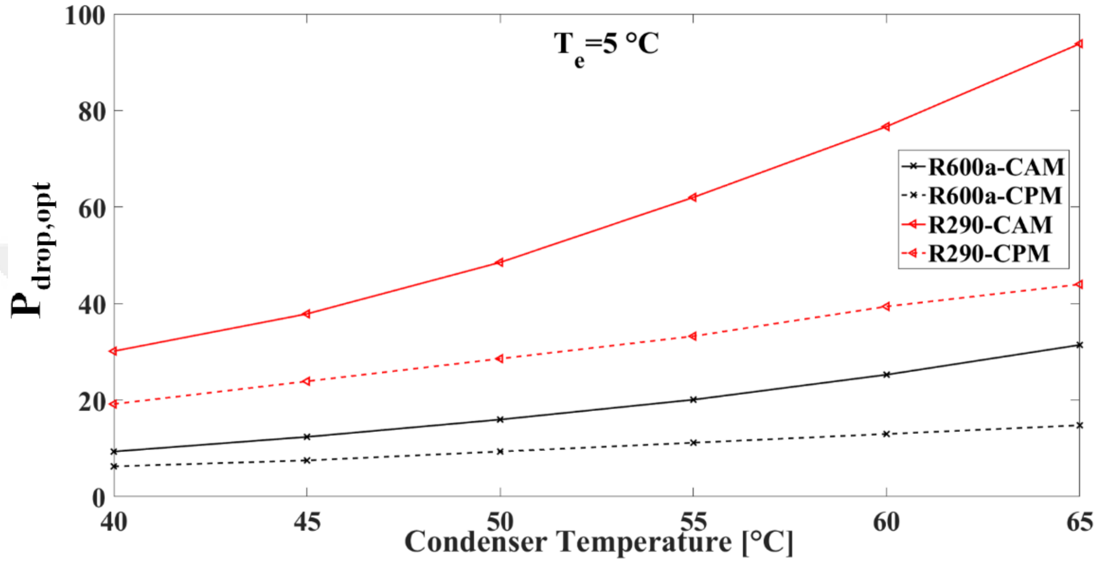


(a)

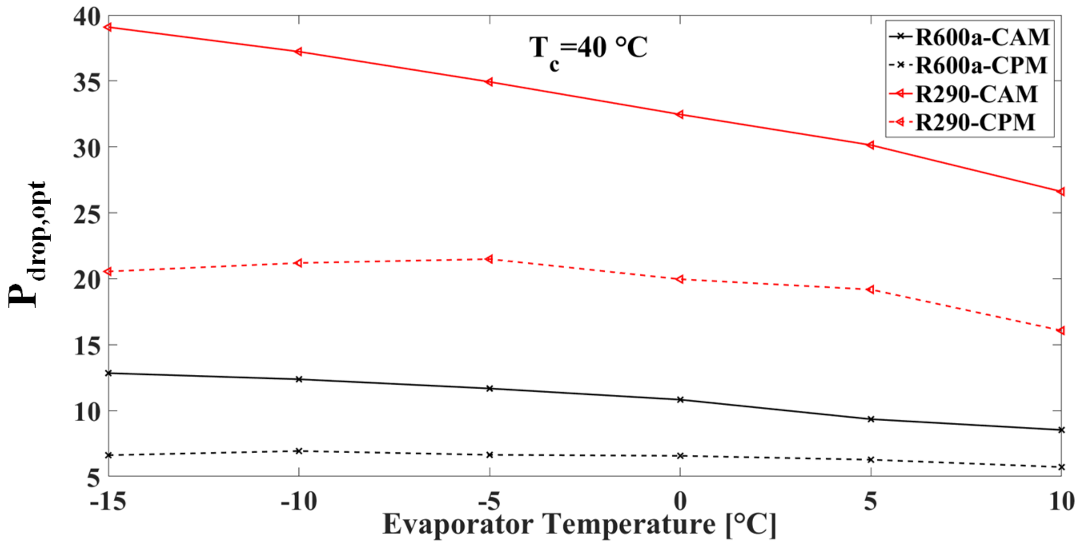


(b)

Figure 4.10 Optimum pressure drops for R600a and R290 at various (a) condenser and (b) evaporator temperatures

The optimum pressure drop profile varies less under CPM assumption for both of the refrigerants when compared to CAM approach. As seen from Figure 4.8 and Figure 4.10, when condenser temperature is increased, the optimum pressure drop in the suction chamber increases resulting the increase in the quality of the refrigerants at the diffuser outlet. Hence the entrainment ratio decreases. On the other hand, when the evaporator temperature is increased, the optimum pressure drop decreases. Therefore, the entrainment ratio increases.

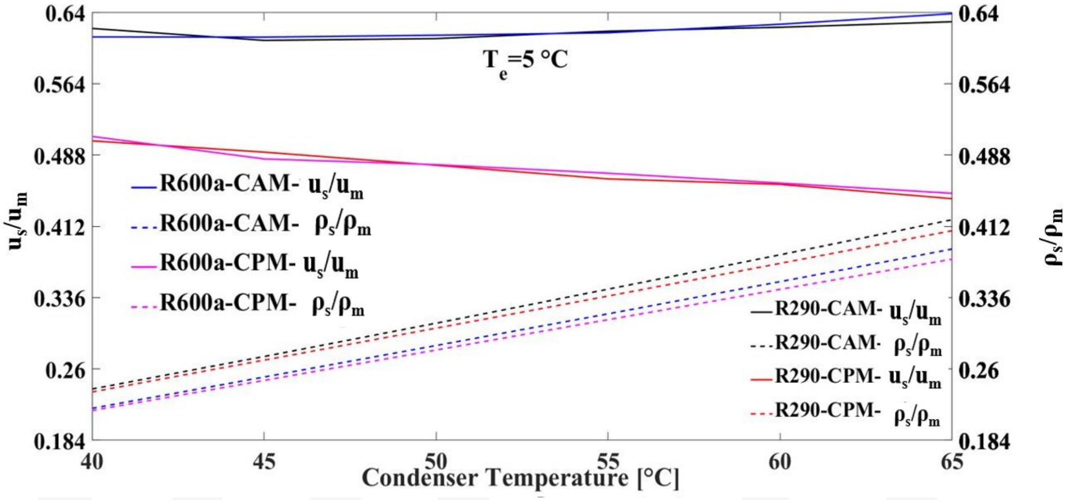


**(a)**

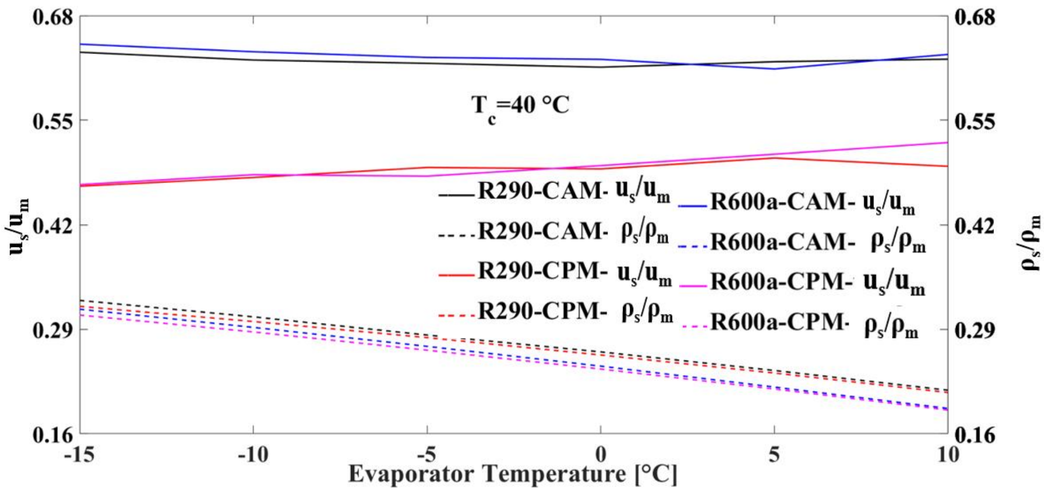


**(b)**

Figure 4.11 Variations of the velocity ratio and density ratio for R600a and R290 according to (a) the condenser and (b) the evaporator temperatures at the optimum operation conditions

The velocity and density ratio is plotted for the same evaporator and condenser temperatures to understand the change in the area ratio better as given in Figure 4.11. As seen from Figure 4.11 (a) and (b), density ratio changes more when compared to velocity ratio and it is the factor determining the tendency of the area ratio variations. The velocity ratio is calculated higher under the CAM assumption at each operation condition. That's why, the area ratio is calculated less under CAM approach in comparison to CPM assumption.

All in all, optimum values of the pressure drop in the suction nozzle, area ratio, entrainment ratio, performance improvement ratio are presented using R600a and R290 for the case of 100% efficient ejector mixing chamber and liquid-vapor separator. The differences between the optimum area ratios are clarified focusing on the density ratio and velocity ratio of the secondary and primary fluid streams in the suction nozzle.

In conclusion, the velocity ratio at the optimum conditions is calculated higher for the CAM approach rather than CPM assumption. That's why, the area ratio is calculated less under CAM ejector theory for each operation condition. Moreover, the density ratio changes more when compared to velocity ratio with respect to the variations of the operation conditions. Hence it is the determining factor on the variation of the area ratio.

### 4.3 Analyses of the Transcritical EERC

The investigations of the EERC only focus on the subcritical cycles so far and the next issue is the performance analyses of the transcritical EERC. When compared to the subcritical cycle, the COP improvement provided by the ejector in the transcritical $CO_2$ cycle is more significant (Sarkar, 2012). Because of the emphasis on the performance improvement of the transcritical EERC with the high pressure refrigerants, the performance analyses are made for a couple of high-pressure refrigerants. Among the candidate working fluids, R744 (carbon dioxide or $CO_2$), R170 (ethane), and R41 (fluoromethane) are selected to be investigated parametrically in this section. Performance comparison is made for these three working fluids individually in both transcritical (supercritical) refrigeration cycle and modification of this cycle with ejector expansion.

The energy and exergy analyses of the transcritical refrigeration cycle are established firstly in order to evaluate the performance and the calculate the percentage exergy destruction occurring in the expansion valve. As the first step, the effects of the gas cooler outlet temperature, evaporator temperature, and evaporator outlet superheat temperature difference on the overall performance and percentage expansion losses are investigated within a specific gas cooler pressure range. Evaporator outlet superheat temperature difference is found to be the least effective parameter on the performance; hence the transcritical ejector expansion refrigeration cycle is analyzed considering only evaporator temperature and gas cooler outlet temperature based on the same gas cooler pressure ranges as for the second objective.

Modelling equations of the ejector and liquid-vapor separator are established in this section according to previously defined assumptions. Inputs of the model are gas cooler pressure, gas cooler outlet temperature, evaporator temperature, and evaporator outlet superheat temperature difference, and the efficiency values of the ejector sections. One of the assumptions is concerned with the pressure of the refrigerants at the inlet of the mixing section, also known as the suction chamber pressure. The governing equations for the CPM ejector are established with reference to Kornhauser (1990) who first constructed the model.

As a result of the preliminary thermodynamic analyses on the EERC, the mixing section efficiency of the ejector is added to the modelling equations of transcritical EERC according to Eames et al. (1995). Moreover, the compressor efficiency as well is added to the model with the correlation of Brunin, Feidt, & Hivet (1997). Hence the effect of a correlation use for the compressor efficiency on the overall performance improvement is presented based on the analyses of the transcritical EERC. The thermodynamic properties of the refrigerants at each state are calculated with the help of REFPROP version 9.1 (Lemmon et al., 2013). The principal outcomes of Atmaca, Erek, Ekren, & Çoban (2018) based on the preliminary research of Atmaca, Erek, Çoban, & Ekren (2018) are presented in this section.

### 4.3.1 Refrigerant Properties

The thermodynamic properties, safety classes, and environmental characteristics of R744, R170, R41, and some of the other natural refrigerants are given in Table 4.7.

Table 4.7 Properties of the R744, R170, R41, and some of the natural refrigerants (a: Lemmon et al., 2013; b: The Linde Group (n.d.); c: Cox, Mazur, & Colbourne, 2008)

| **Refrigerants** | **R744** | **R170** | **R41** | **R717** | **R290** | **R600a** | **R1270** |
|---|---|---|---|---|---|---|---|
| **Chemical name**[a] | Carbon dioxide | Ethane | Fluoromethane | Ammonia | Propane | Isobutane | Propylene |
| **Chemical formula**[a] | $CO_2$ | $CH_3CH_3$ | $CH_3F$ | $NH_3$ | $CH_3CH_2CH_3$ | $CH(CH_3)_3$ | $CH_2$=CH-$CH_3$ |
| **Molar mass (kg/kmol)**[a] | 44.01 | 30.069 | 34.033 | 17.03 | 44.096 | 58.122 | 42.08 |
| **NBP (°C)**[a] | -78.46 | -88.58 | -78.31 | -33.33 | -42.11 | -11.75 | -47.62 |
| **Critical temperature (°C)**[a] | 31.98 | 32.17 | 44.13 | 132.25 | 96.74 | 134.66 | 91.06 |
| **Critical pressure (MPa)**[a] | 7.3773 | 4.8722 | 5.897 | 11.333 | 4.2512 | 3.629 | 4.555 |
| **ASHRAE safety group** | A1[b] | A3[b] | A2[c] | B2L[b] | A3[b] | A3[b] | A3[b] |
| **ODP** | 0[b] | 0[b] | 0[c] | 0[b] | 0[b] | 0[b] | 0[b] |
| **GWP** | 1[b] | 6[b] | 97[c] | 0[b] | 3[b] | 3[b] | 2[b] |

### 4.3.2 Cycle Definitions

Most of the refrigeration systems are designed to be able to reject heat to the atmosphere at the temperatures above 25 ºC. Therefore, R744, R170, and R41 having low critical temperatures are investigated in the transcritical (supercritical) refrigeration cycle in which the heat rejection process occurs above the critical temperature and the pressure as shown in Figure 4.12 (a). The second cycle shown in Figure 4.12 (b) is the modification of the base cycle with ejector expansion.

As it is seen from the *P-h* diagrams, heat rejection processes occur above the critical temperature and pressure of the $CO_2$. The notations used in the *P-h* diagrams in Figure 4.13 are consistent with that of the schematic views given in Figure 4.12.

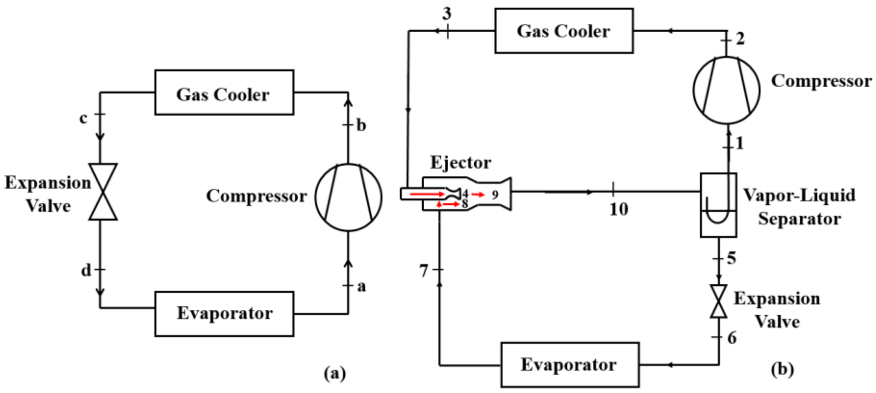


Figure 4.12 Schematic views of (a) the transcritical refrigeration cycle and (b) the transcritical EERC

CPM assumption stating that the pressure stays the same throughout mixing process (Kornhauser, 1990) is used in order to model the ejector mixing section. It is seen from Figure 4.13 (b) that the pressure does not change throughout mixing process represented from number 4 (the state of the primary fluid) and number 8 (the state of the secondary fluid) to the number 9 (the state of the total fluid flow).

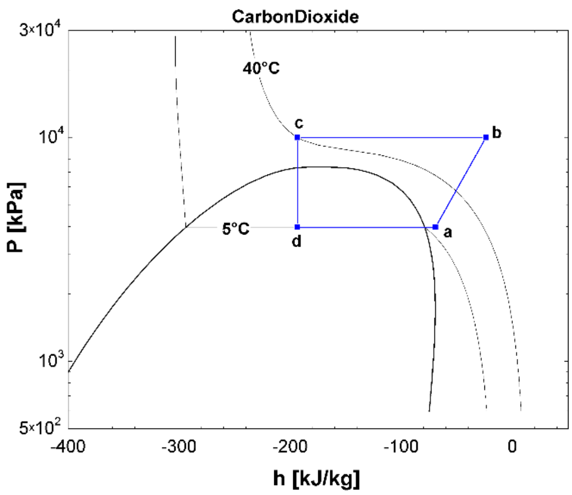


**(a)**

Figure 4.13 *P-h* diagrams of (a) the transcritical refrigeration cycle and (b) the EERC including CPM ejector for $CO_2$ (Klein, 2017)

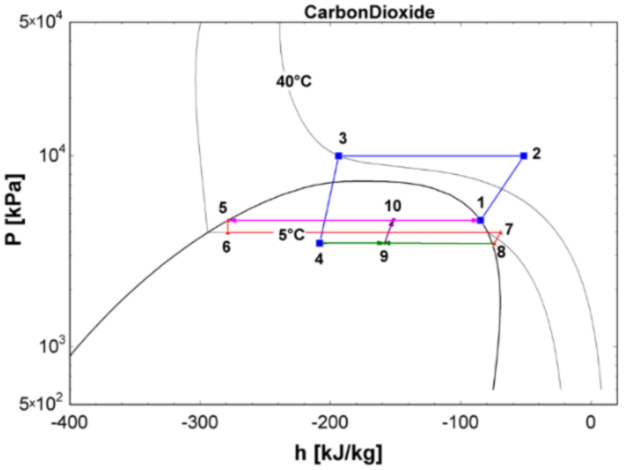


**(b)**

Figure 4.13 continues

### *4.3.3 Results of the Transcritical VCRC and EERC*

Results are divided into two sections. First group is focusing on the parametric comparison of the refrigerants in the transcritical VCRC; whereas the second group is giving the comparisons of the modified cycle with the ejector expansion. Operation conditions are defined for a typical air-conditioning application and given in Table 4.8.

Table 4.8 Parametric operation ranges of the refrigerants according to their critical temperatures and pressures for a typical air-conditioning application

| **Parameters** | **Values** | | |
|---|---|---|---|
| | **R744** | **R170** | **R41** |
| Gas cooler pressure ($P_{gc}$) | 8.5-10 MPa | 5.5-12 MPa | 6-12 MPa |
| Gas cooler outlet temperature ($T_{gc,o}$) | 40 ˚C | 40 ˚C | 46 ˚C |
| Evaporator temperature ($T_e$) | 5 ˚C | 5 ˚C | 5 ˚C |
| Evaporator outlet superheat temperature difference ($\Delta T_{sh}$) | 5 ˚C | 5 ˚C | 5 ˚C |
| Primary nozzle efficiency ($\eta_m$) | 0.9 | 0.9 | 0.9 |
| Suction nozzle efficiency ($\eta_s$) | 0.9 | 0.9 | 0.9 |
| Mixing section efficiency ($\eta_{mix}$) | 0.9 | 0.9 | 0.9 |
| Diffusor efficiency ($\eta_d$) | 0.8 | 0.8 | 0.8 |

The gas cooler outlet temperature is varied between 40-46 ºC for R744 and R170 and the range is defined between 46-49 ºC for R41. Since the critical temperature for R41 is around 44.1 ºC, it is necessary to select a higher temperature in order to be assured of staying in the transcritical refrigeration cycle region. That's why, the operation conditions are given in Table 4.8 for each refrigerant individually. For the rest of the parametric analyses, 40 ºC for R744 and R170 and 46 ºC for R41 are used as the reasonable gas cooler outlet temperatures for staying within the transcritical cycle region and calculating COP values making sense.

All parameters are investigated with reference to gas cooler pressure since its value yielding the highest performance is dependent not only on the refrigerant, but also the operation conditions. Each solid line in the rest of the following figures represents one configuration of the investigated parameter, i.e., variations in the gas cooler outlet temperature, evaporator temperature, evaporator outlet superheat temperature difference, based on the gas cooler pressure and the same color dashed line belongs to the counterpart of the same aspect. Figure 4.14 shows the effects of the gas cooler outlet temperature based on the gas cooler pressure.

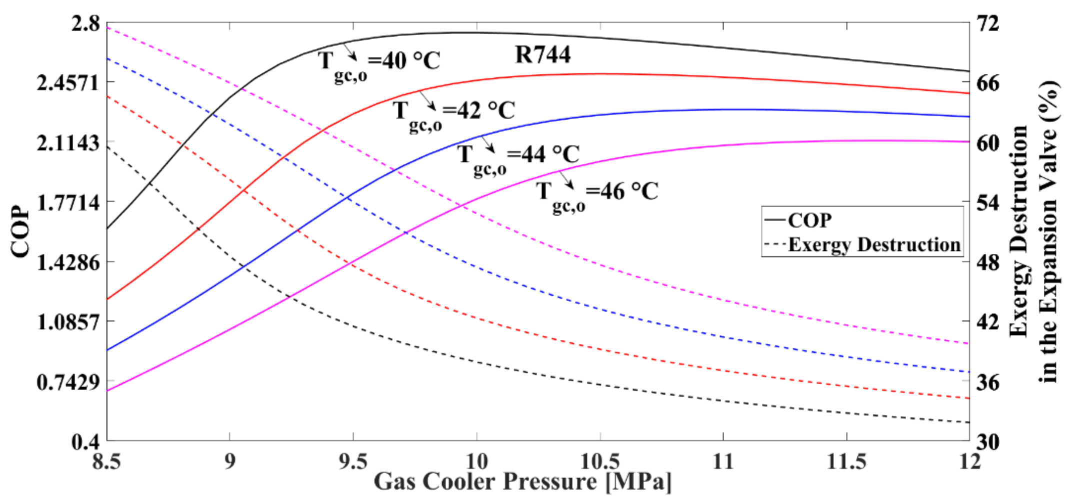


(a)

Figure 4.14 Effects of the gas cooler outlet temperature according to the gas cooler pressure on the performance and percentage expansion losses for (a) R744, (b) R170, and (c) R41

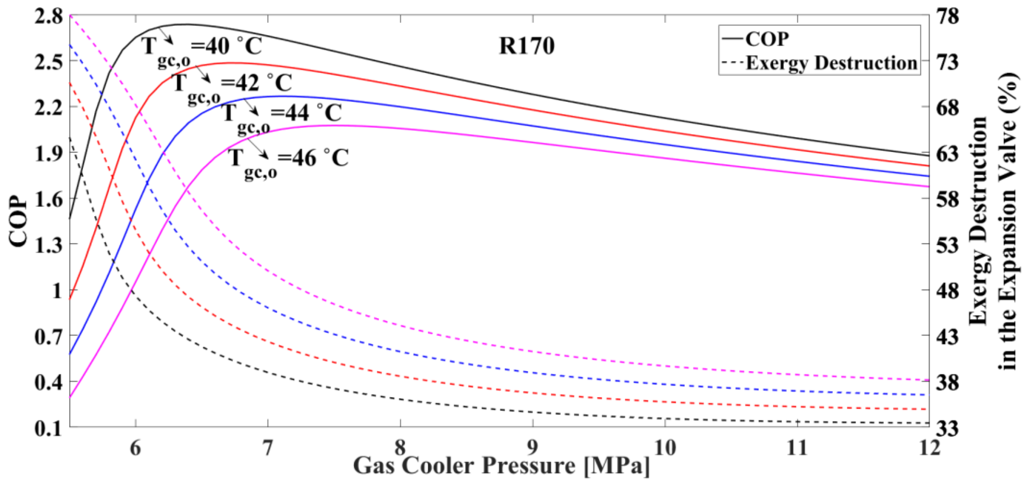


(b)

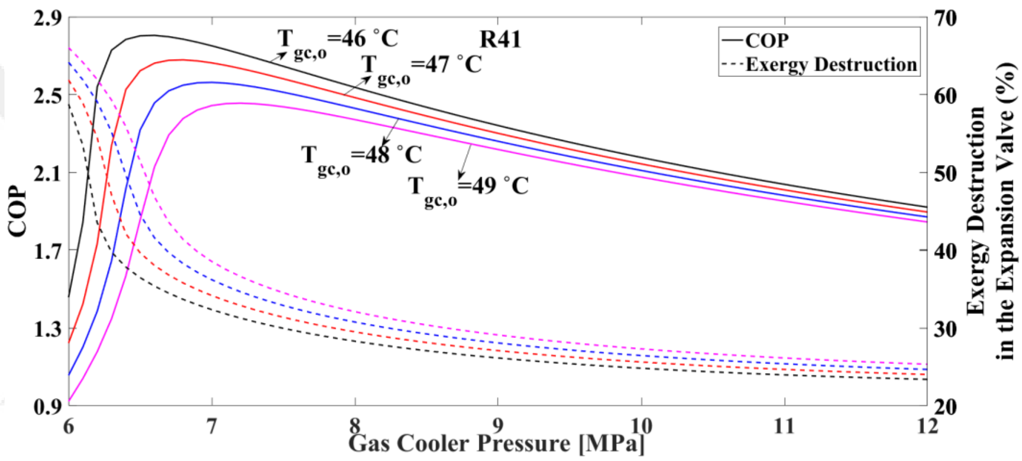


(c)

Figure 4.14 continues

Maximum performance curve is obtained at gas cooler outlet temperature of 40 ºC for R744 and R170 as shown in Figure 4.14 (a) and (b); whereas it is at 46 ºC for R41 as given in Figure 4.14 (c). Generally speaking, when gas cooler outlet temperature increases the performance of the refrigerants decrease and the percentage exergy destruction in the expansion valve increases.

As shown in Figure 4.14, the highest gas cooler pressure range at the refrigerants' best performance belongs to R744. When gas cooler outlet temperature increases, the gas cooler pressure yielding the highest performance increases as well for each refrigerant. Variation of change in the performance profile around this pressure point is more steep for R41 and R170 when compared to R744 with reference to investigated gas cooler outlet temperatures. Another interpretation from Figure 4.14 is that the performance variation around the gas cooler pressure yielding the highest performance becomes more gradual for all refrigerants as the gas cooler outlet temperature increases. Furthermore, the value of the gas cooler pressure resulting in the highest performance varies more as reaction to the changes in the gas cooler outlet temperature for R744 than R170 and R41.

The expansion losses decrease dramatically around the gas cooler pressure of the highest performance and start stabilizing after this pressure point is achieved. In other words, rate of change of expansion losses have a different tendency before and after the operation pressure yielding the maximum performance for a specific gas cooler outlet temperature. When the gas cooler outlet temperature increases, the percentage exergy destruction in the expansion valve as well increases. The gas cooler outlet temperature affects the expansion losses mostly for R744 and R170 rather than R41. Within the investigated ranges of gas cooler pressure and outlet temperature, R744 and R170 experience very high expansion losses around 30-40%; whereas it stabilizes around 23-25% for R41. Although the improvement potentials of these three refrigerants are different in the EERC due to the variations of the percentage expansion losses based on the investigated operation ranges, they are all promising candidates to be investigated in the transcritical cycle with the ejector expansion.

Figure 4.15 presents the general overview related to these three refrigerants for the investigated operation points at which they display their highest performance. Operation pressure of R41 and R170 resulting in the highest performance are very close to each other at the gas cooler outlet temperatures yielding their own maximum performance. Moreover, within the investigated operation conditions, maximum performance is calculated for R41.

The effect of the evaporator temperature on the cycle performance and percentage expansion losses are displayed in Figure 4.16 (a), (b), and (c) for R744, R170, and R41, respectively based on the gas cooler pressure as in the same way of gas cooler outlet temperature investigations. Standard comments regarding the general trends of the percentage exergy destruction in the expansion valve and the cycle COP could be interpreted from these plots.

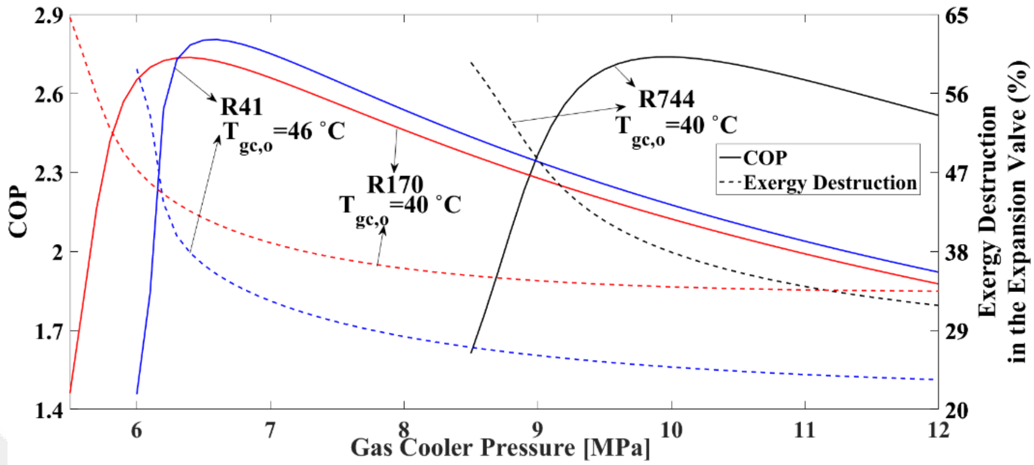


Figure 4.15 Comparisons of the COP, percentage expansion losses, and gas cooler pressure of the highest performance point for R744, R170, and R41 with respect to different gas cooler outlet temperatures at which they perform their highest performance

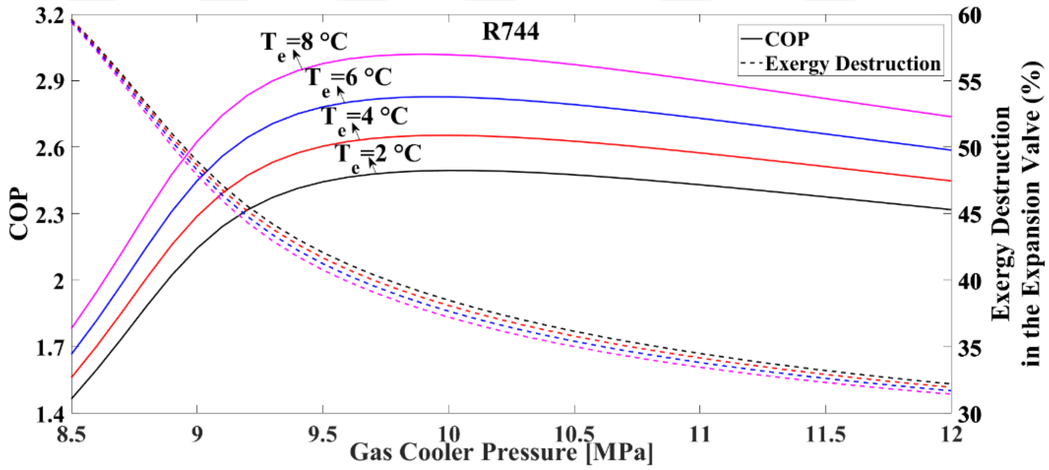


(a)

Figure 4.16 Effects of the evaporator temperature on the performance and percentage expansion losses for (a) R744, (b) R170, and (c) R41 with respect to the gas cooler pressure

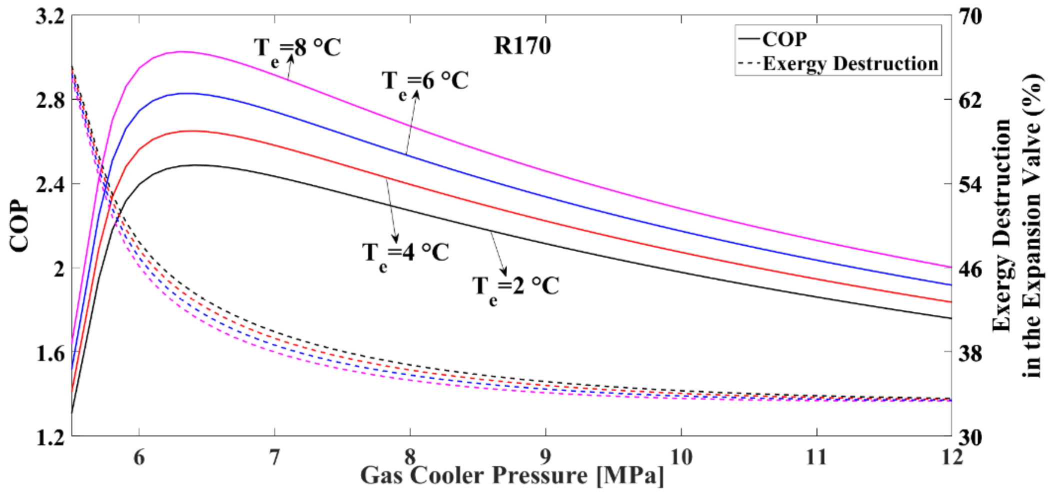


(b)

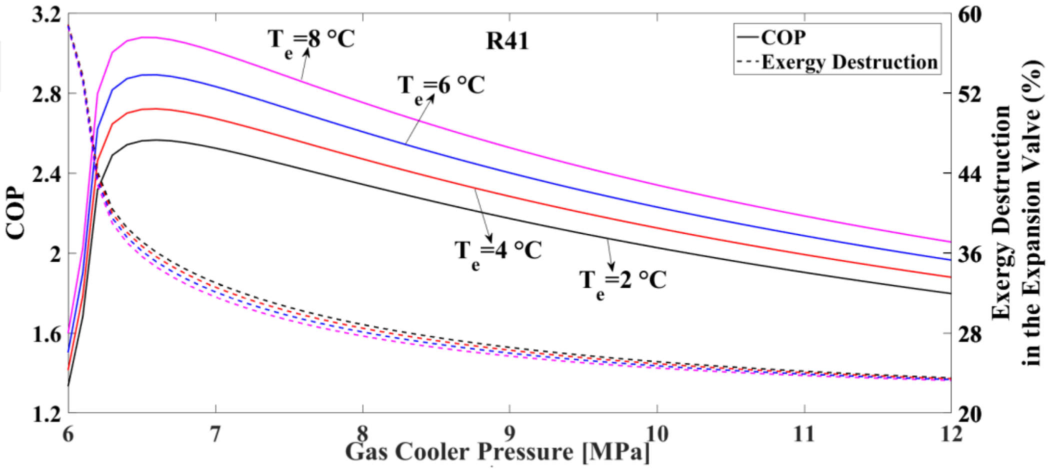


(c)

Figure 4.16 continues

Gas cooler pressure yielding the highest performance with respect to the evaporation temperature nearly stays the same for each refrigerant in contrast to the variations observed in the gas cooler outlet temperature analyses. When evaporator temperature increases, the refrigerants display better performance while they experience less expansion losses as shown in Figure 4.16.

The percentage exergy destruction of each refrigerant in the expansion valve is calculated very similar to each other and stabilized around a constant value for the investigated evaporation temperatures. The stabilized percentages could be expressed roughly as 32%, 33%, and 23% for R744, R170, and R41, respectively. Hence, it is obvious that R744 and R170 has the highest improvement potentials in the transcritical EERC. The effect of the last operational parameter, evaporator outlet superheat temperature difference, is shown in Figure 4.17 (a), (b), and (c) for R744, R170, and R41, respectively. When evaporator outlet superheat temperature difference increases, the performance increases and the percentage exergy destruction in the expansion valve decreases. When compared to R744 and R170, R41 is the least sensitive refrigerant to the changes in this parameter and has less expansion losses.

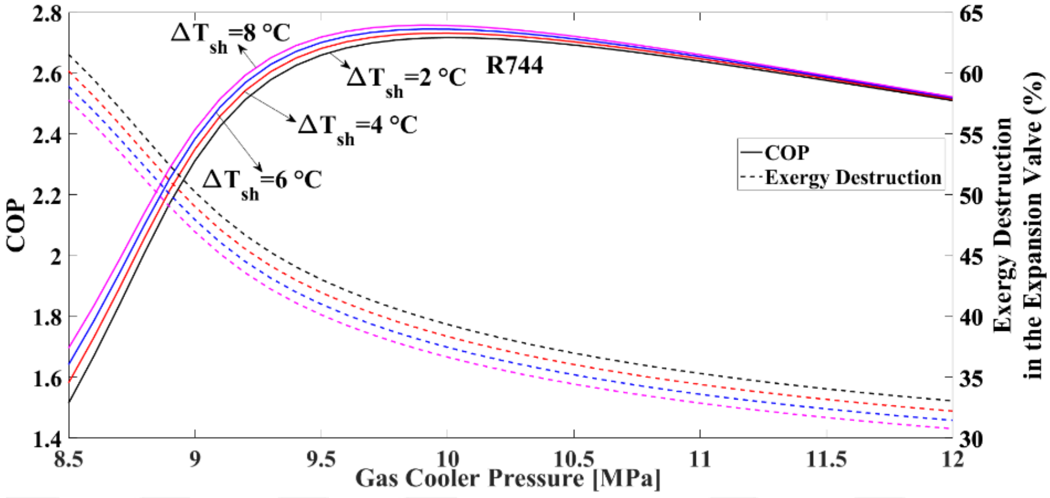


**(a)**

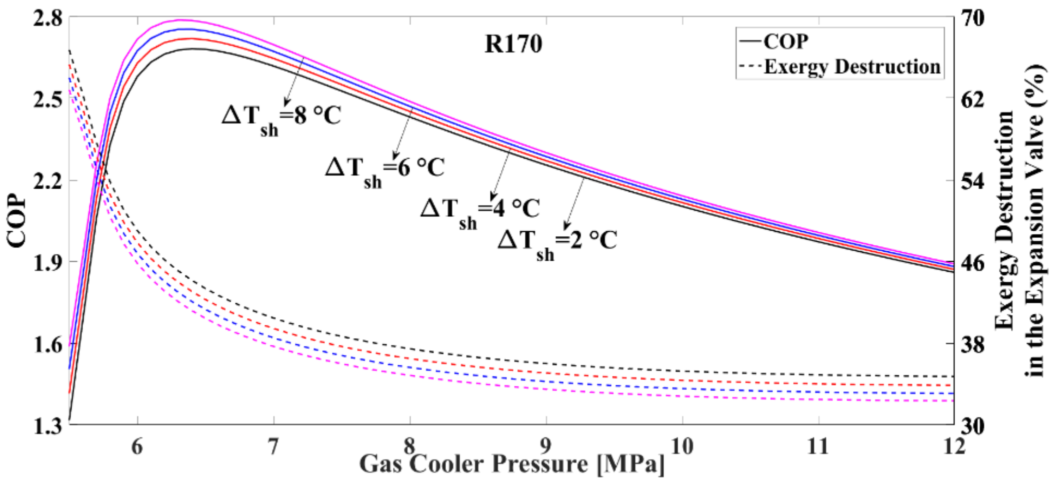


**(b)**

Figure 4.17 Effects of the evaporator outlet superheat temperature difference on the performance and percentage expansion losses based on the gas cooler pressure for (a) R744, (b) R170, and (c) R41

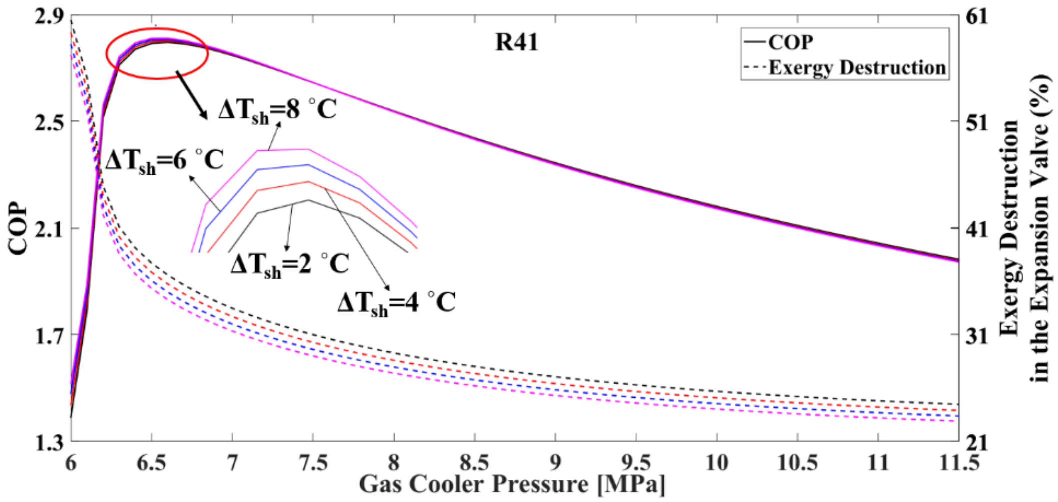


**(c)**

Figure 4.17 continues

As shown in Figure 4.16 and Figure 4.17, the least effective parameter is the evaporator outlet superheat temperature difference in terms of the performance; whereas it is the evaporator temperature for the percentage expansion losses. All in all, the most important parameters are the gas cooler pressure and outlet temperature on the performance variations and expansion losses. In terms of the expansion losses, the most effective parameters are the gas cooler outlet temperature and the evaporator outlet superheat temperature with reference to analyses based on the gas cooler pressure. However, the similar amounts of the expansion losses are calculated according to evaporator temperature and evaporator outlet superheat temperature difference for each refrigerant.

Rest of the analyses concerned with the performance improvement potentials in the transcritical EERC are conducted according to the most important critical parameters of the performance based on the gas cooler pressure as in the same way of the previous analyses. As stated before, mixing section efficiency is added to the model for more realistic performance improvement estimations. Optimum performance improvement ratio and entrainment ratio is calculated iteratively based on the optimum suction chamber pressure ($P_s$) yielding the maximum performance.

Figure 4.18 displays the performance improvement potential of the refrigerants in the transcritical EERC when gas cooler outlet temperature is changed based on the gas cooler pressure. Higher gas cooler outlet temperatures result in higher performance improvement ratios due to the higher expansion losses at those ranges for all refrigerants. After the gas cooler pressure yielding the maximum performance improvement ratio is achieved for each gas cooler outlet temperature, a slight decrease is observed in the optimum performance improvement ratio for R744 and R170.

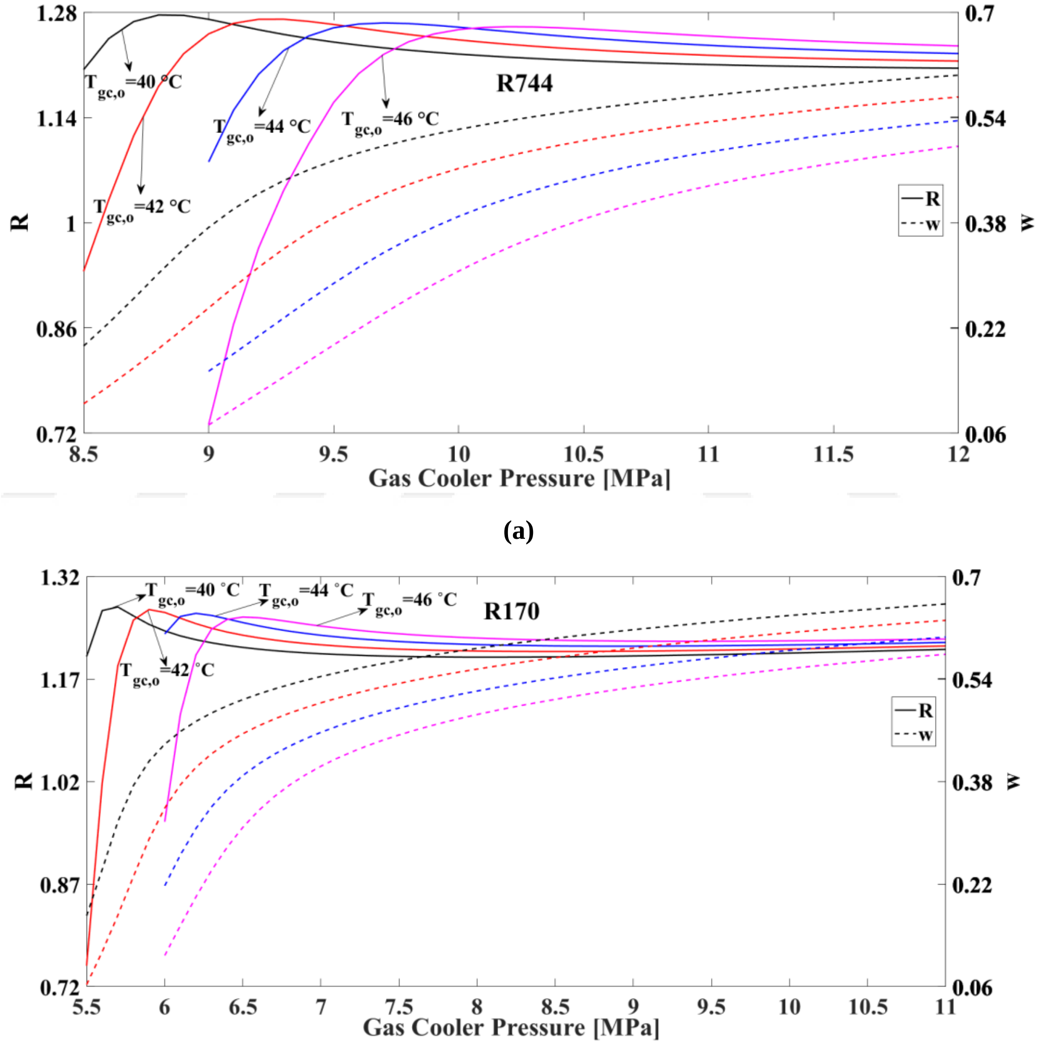


(a)



(b)

Figure 4.18 Effects of the gas cooler outlet temperature based on the gas cooler pressure on the optimum performance improvement ratio and entrainment ratio for (a) R744, (b) R170, and (c) R41

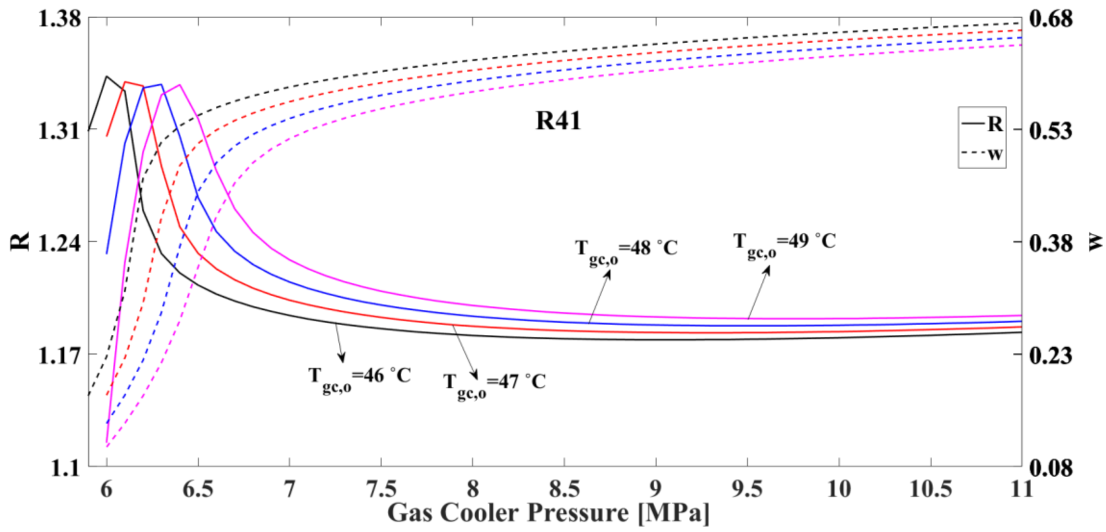


**(c)**

Figure 4.18 continues

On the other hand, the decrease is more dramatic for R41 after the gas cooler pressure of the maximum performance point. The performance improvement ratio is stabilized more or less around a specific interval which are 20%-24%, 21%-23%, and 18%-19% for R744, R170, and R41, respectively for a wide range of the gas cooler pressures. R170 and R744 display better performance improvement potential in the transcritical EERC within the stabilized region of the performance improvement ratio.

Moreover, when the gas cooler outlet temperature increases, the entrainment ratio decreases for each refrigerant within the same investigated gas cooler pressure range. Trend of the entrainment ratio for each gas cooler outlet temperature curve displays an increasing profile with respect to gas cooler pressure increments. R744 and R170 exhibit more gradual increase in the entrainment ratio in contrast to the dramatic increase of the entrainment ratio calculated for R41 around their own gas cooler pressures resulting in the highest performance improvement ratio.

Figure 4.19 shows the effects of the evaporator temperature on the optimum performance improvement ratio and the entrainment ratio in the transcritical EERC utilizing R744, R170, and R41. Performance improvement ratio increases as the evaporator temperature is decreased. However, entrainment ratio decreases as a result of the decrease in the evaporator temperature for a specific gas cooler pressure range. For each evaporator temperature analysis, the entrainment ratio increases as reaction to increases in the gas cooler pressures. After the operation pressure of the highest performance point for each evaporator temperature configuration, there is a decrease in the performance improvement ratios of all refrigerants. The gas cooler pressures yielding the best performance improvement ratios according to variations in the evaporator temperatures nearly stay the same for each refrigerant.

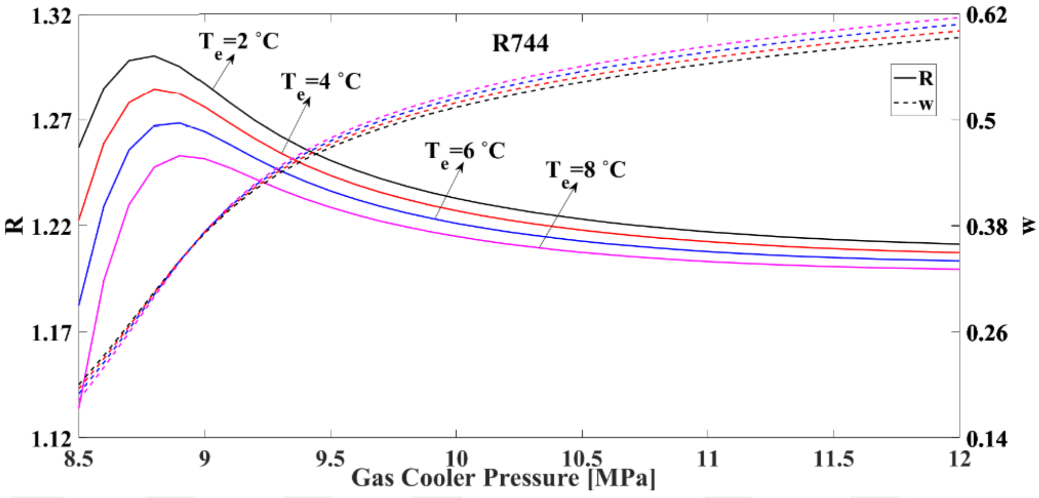


(a)

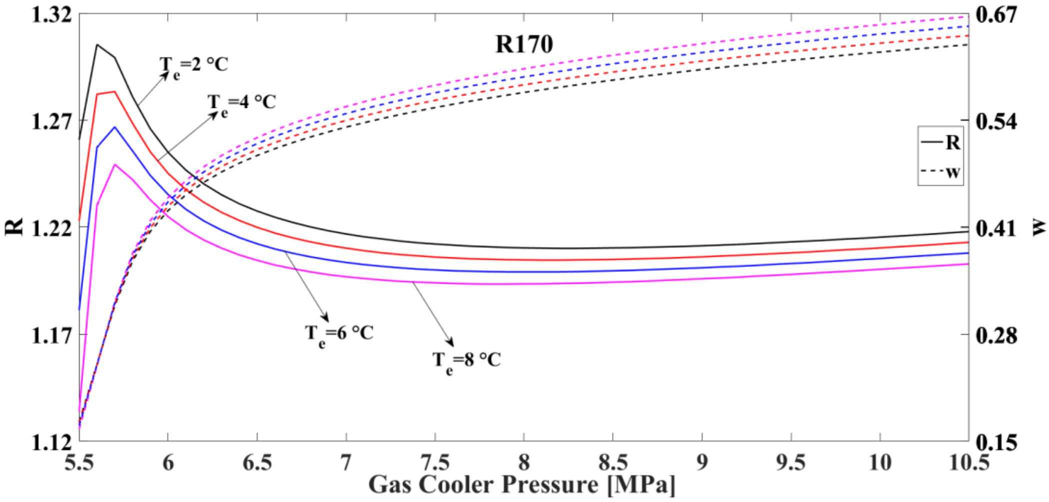


(b)

Figure 4.19 Effects of the evaporator temperature based on the gas cooler pressure on the optimum performance improvement ratio and entrainment ratio for (a) R744, (b) R170, and (c) R41

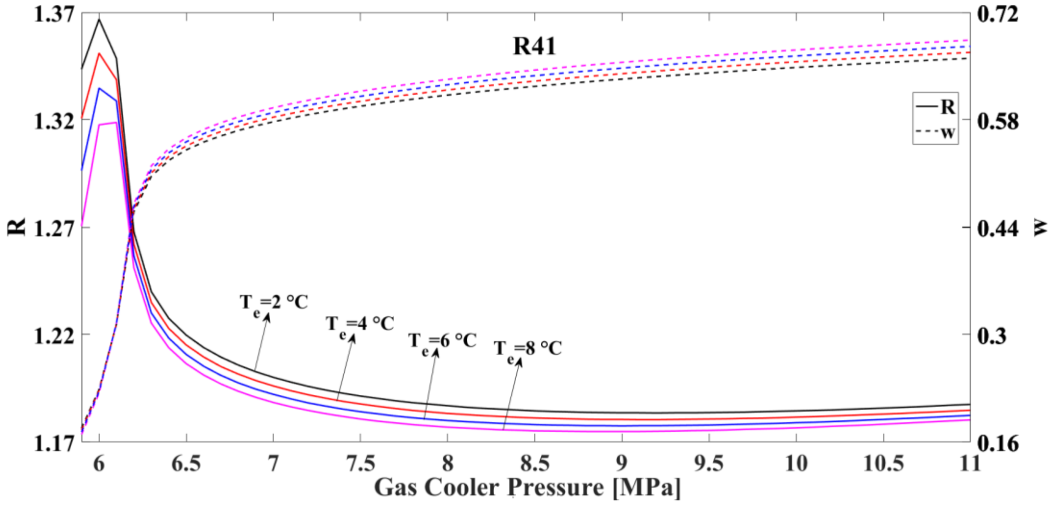


**(c)**

Figure 4.19 continues

The rate of decrease in the performance improvement ratio profile for each evaporator temperature is more sudden in comparison with the corresponding profile of the gas cooler outlet temperatures after the best performance pressure point is achieved at the analyzed conditions. Among these three refrigerants, R41 performs the most sudden decrease in the performance improvement ratio and the most dramatic increase in the entrainment ratio after the gas cooler pressure of the maximum performance improvement ratio for each evaporator temperature. The performance improvement potential stabilizes around 22-20% for R744 and R170; whereas it is about 18% for R41 at various evaporator temperature configurations.

As it is seen from Figure 4.18 and Figure 4.19, there is a region that the entrainment ratio is very low around the operation pressure of the highest performance improvement ratio for each refrigerant and the transcritical EERC is not applicable actually within that range. These kinds of performance lines for various operation conditions and refrigerants could be beneficial to display the actual operation ranges of the refrigerants in the EERC.

To sum up, the objectives of this section are divided into two branches, i.e., comparing the environmentally-friendly refrigerants having low critical temperatures, namely R744, R170, and R41, parametrically in the transcritical refrigeration cycle and calculating the improvement potential of these high-pressure refrigerants in the modified cycle with ejector expansion. Firstly, the effects of the gas cooler outlet temperature, evaporator temperature, evaporator outlet superheat temperature difference on the performance and percentage expansion losses with respect to the specific gas cooler pressure ranges are investigated for these three refrigerants in the transcritical refrigeration cycle.

Gas cooler pressure yielding the highest performance is dependent sensitively on the gas cooler outlet temperature rather than the evaporator and evaporator outlet superheat temperature difference in the transcritical cycle. The most effective parameters are gas cooler outlet temperature and the evaporator temperature in terms of the performance; whereas the gas cooler outlet temperature and evaporator outlet superheat temperature difference according to the percentage exergy destruction in the expansion valve as a result of the analyses based on a specific gas cooler pressure range for each refrigerant. When all these refrigerants are compared according to their performance values at the gas cooler outlet temperatures yielding their own highest COP, it is seen that the best performance is calculated for R41 at a low gas cooler pressure.

The rest of the analyses relative to EERC configuration is conducted with reference to two critical parameters which are effective mostly on the performance. The performance improvement potential of the refrigerants is different from each other and depends on the operation conditions. To sum up, thermodynamic analyses show that the improvement potential in the EERC is higher for R744 and R170 than R41 with respect to the investigated parameters.

### *4.3.4 Effect of the Compressor Isentropic Efficiency*

In most of the thermodynamic models regarding the ejector expansion refrigeration cycles, compressor isentropic efficiency is added to the model as a constant value. It is reasonable to assume the compressor isentropic efficiency as *0.75* for the investigated refrigerants and the operation condition ranges according to Li & Groll (2005), Lawrence (2012), Bilir & Ersoy (2009). However, in some of the modelling approaches, the compressor isentropic efficiency is calculated using a correlation (Li et al., 2014; Nehdi et al., 2007; and Wang et al., 2016) according to Brunin et al. (1997) as follows;

$$\eta_{comp} = 0.874 - 0.0135\tau \tag{4.27}$$

τ in the isentropic efficiency formula is the pressure ratio and presents the ratio of the high pressure to the low pressure. Low pressure is the inlet pressure of the compressor and high pressure is the outlet pressure of it. For a subcritical or transcritical refrigeration cycle, high pressure corresponds to the condensation pressure or gas cooler pressure and low pressure is the evaporation pressure. With this kind of isentropic efficiency relation, both operation conditions and the type of the refrigerant could be taken into account. Hence it is a kind of modelling assumption regarding the compressor isentropic efficiency.

In ejector expansion refrigeration cycle, since the pressure of the refrigerant flowing through the compressor increases due to the ejector, the isentropic efficiency of the compressor as well increases. Therefore, in addition to the increase in the volumetric cooling capacity and decrease in the compressor work, increase in the compressor efficiency contributes to the performance improvement. If a constant efficiency value for the compressor is introduced to the model, the percentage increase in the compressor efficiency owing to addition of the ejector into the cycle cannot be calculated or observed. Taking the variable compressor efficiency approach into account in the thermodynamic models is beneficial for obtaining the percentage increase based on the operation conditions and the refrigerant selection.

In the two-phase ejector models, one of the most important assumptions is the pressure drop in the suction chamber and according to each operation condition, there is an optimum pressure drop selection yielding the maximum performance for the refrigerant under discussion. Therefore, defining the optimum pressure drop in the suction chamber results in an optimum (highest) pressure of the refrigerant at the outlet of the ejector diffuser. When a variable compressor efficiency is introduced into the model, the improvement in the compressor isentropic efficiency also could be calculated since the diffuser outlet pressure is the compressor inlet pressure for the cycle evaluations.

In this section, firstly, the effect of the variable and constant compressor efficiency is discussed based on the refrigerants R744 (carbon dioxide) and R170 (ethane). The effect of variable or constant compressor efficiency assumption is tested on the transcritical refrigeration cycle for various gas cooler pressures as shown in Figure 4.20. As seen from Figure 4.20, there is a big difference between the COP values calculated according to the variable and the constant compressor efficiencies. The difference is averagely 13% for R744 and 12% for R170. The result says that variable compressor efficiency assumption calculates higher results nearly more than 10% for the investigated refrigerants. It is because of the highly calculated compressor isentropic efficiency with the correlation of Brunin et al. (1997).

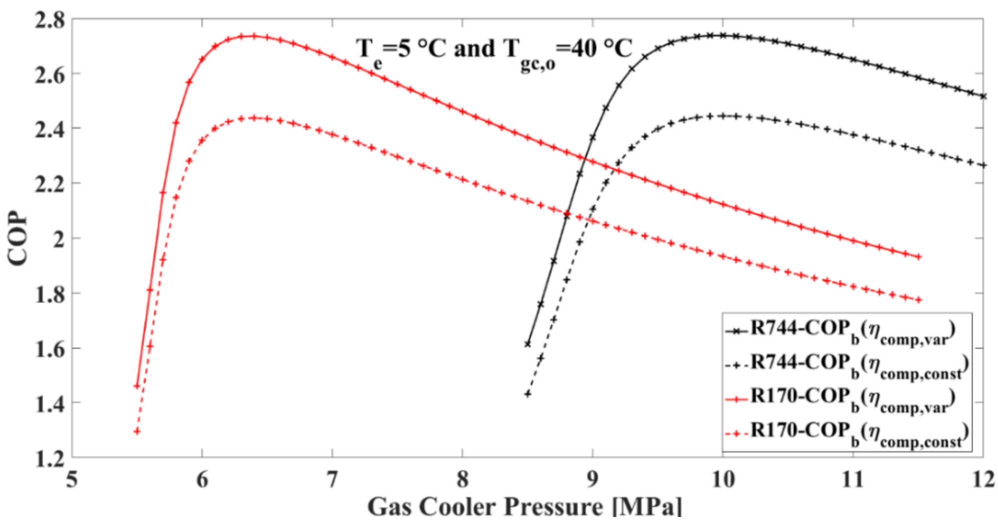


Figure 4.20 COP of the transcritical refrigeration cycle for R170 and R744 according to various gas cooler pressures under constant and variable compressor isentropic efficiency assumptions ($T_e$=5 ºC, $T_{gc,o}$=40 ºC, and $\Delta T_{sh}$=5 ºC)

Figure 4.21 and Figure 4.22 include both COP and the performance improvement ratio (R) for R744 and R170, respectively. For the performance and performance improvement ratio comparisons, the optimum operation conditions based on the optimum suction nozzle pressure drop assumption are used.

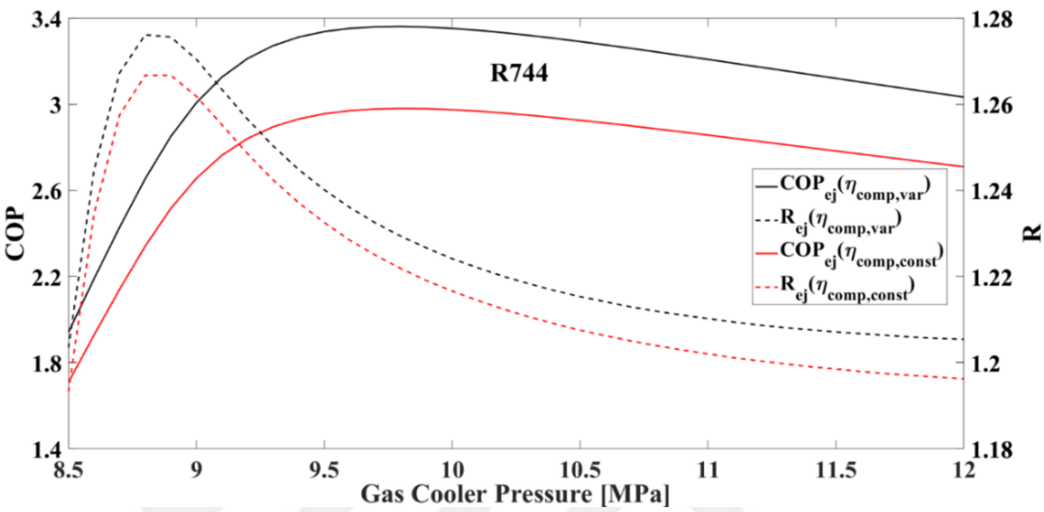


Figure 4.21 COP and R values of the transcritical ejector expansion refrigeration cycle for R744 under the variable and the constant compressor efficiency assumptions according to the gas cooler pressure ($T_e$=5 ºC, $T_{gc,o}$=40 ºC, and $\Delta T_{sh}$=5 ºC)

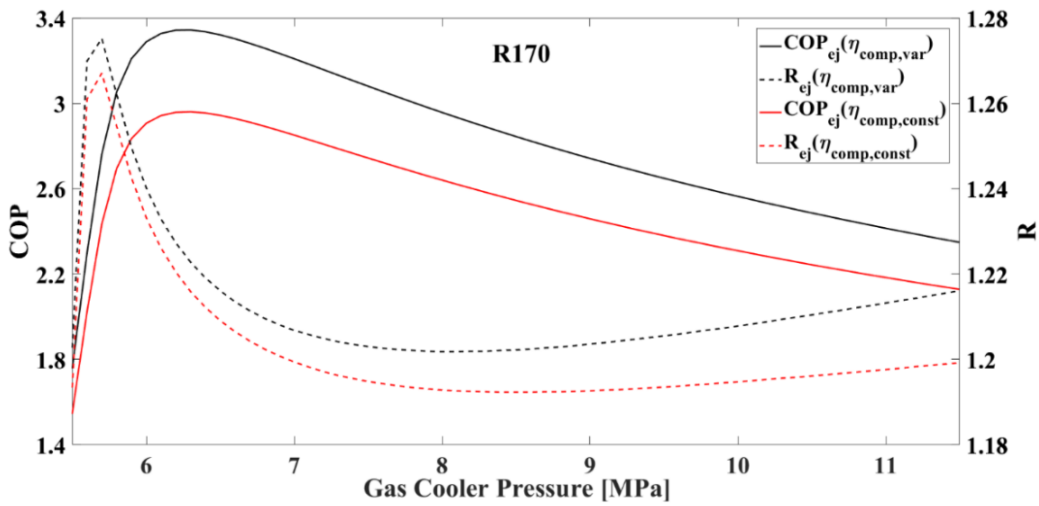


Figure 4.22 COP and R values of the transcritical ejector expansion refrigeration cycle for R170 under the variable and the constant compressor efficiency assumptions according to the gas cooler pressure ($T_e$=5 ºC, $T_{gc,o}$=40 ºC, and $\Delta T_{sh}$=5 ºC)

With reference to Atmaca et al. (2019a), comparing any parameter based on the optimum conditions is a better approach since it yields the maximum performance for any operation conditions and refrigerants. For both of the refrigerants, low pressure term of the isentropic efficiency correlation corresponds to the diffuser outlet pressure when ejector expansion cycle is analyzed. Therefore, results are obtained according to the optimum pressure drop and the optimum (highest) diffuser outlet pressure thereby yielding the maximum compressor efficiency. In other words, results are presented under the highest achievable compressor isentropic efficiency values corresponding to the optimum operation conditions in the ejector expansion refrigeration cycle.

When COP values obtained from the ejector expansion refrigeration cycles are compared, it is seen that nearly 13% higher results for R744 are calculated under the variable compressor isentropic efficiency assumption since the isentropic efficiency is higher than the assumed arbitrary constant value (*0.75*); whereas it is about 12% for R170 because of the same reason. The percentage difference between the performance improvement coefficients (R) are 0.7% and 0.9% for R744 and R170, respectively calculated according to variable compressor efficiency and constant compressor efficiency.

It may be considered that the higher COP in the ejector expansion refrigeration cycle is arisen from the improvement in the compressor efficiency due to the pressure increase of the refrigerant at the compressor inlet. Under variable compressor efficiency approach, the percentage increase of the compressor isentropic efficiency due to the ejector in the cycle is presented in Figure 4.23 according to various operation conditions for R170 and R744. Such kind of percentage efficiency increase for the compressor cannot be calculated under the constant efficiency assumption.

As it is seen from Figure 4.23, percentage compressor efficiency improvement decreases while getting closer to the optimum gas cooler pressure. Then, it goes on increasing after this optimum value. However, the increase is around 1% and will not yield a very high difference in the individual COP values. It surely could be concluded that the effect of the improved compressor efficiency is negligible on the COP value calculated higher according to variable compressor efficiency assumption when compared to constant compressor efficiency approach. It is directly because of the higher compressor efficiency value calculated with the efficiency relation. It is seen from Figure 4.24 that at each operation condition it is higher than the constant value *0.75* for both R170 and R744.

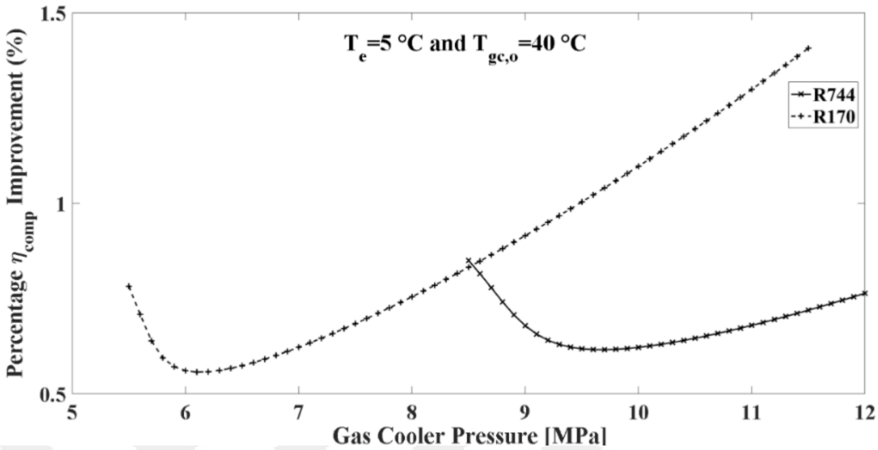


Figure 4.23 Percentage increase in the compressor isentropic efficiency for R744 and R170 according to various gas cooler pressures under variable compressor efficiency approach ($T_e$=5 ºC, $T_{gc,o}$=40 ºC, and $\Delta T_{sh}$=5 ºC)

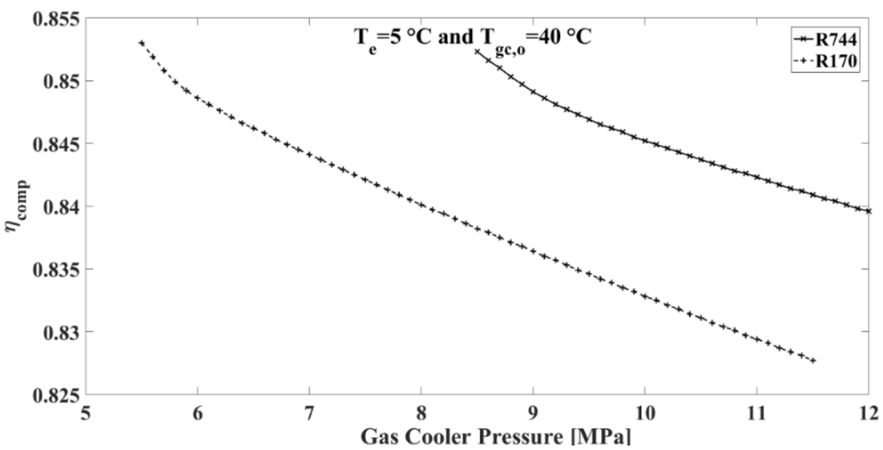


Figure 4.24 Variations of the compressor isentropic efficiency calculated in the EERC according to gas cooler pressure for R170 and R744 ($T_e$=5 ºC, $T_{gc,o}$=40 ºC, and $\Delta T_{sh}$=5 ºC)

The difference between *R* values is negligible with reference to constant and variable compressor efficiency approaches. Because the effect of the efficiency values on the performance of both basic cycle and the ejector expansion refrigeration cycle cancels out each other. For general representations of performance improvement through the ejector expansion refrigeration cycle, performance improvement ratio (R) is better to be used rather than the individual COP values since any model assumption could change the overall cycle COP substantially. Therefore, when more general representations are preferred such as the case of R, it does not matter which compressor efficiency assumption is preferred since the results are nearly the same.

Figure 4.24 shows that the optimum compressor efficiency decreases continuously. However, the rate of change of decrease (slope of the lines) varies around the optimum gas cooler pressures for both of the refrigerants. Although they decrease with reference to the gas cooler pressure, they show a percentage improvement for each operation condition. As seen from Figure 4.23, percentage improvement decreases to some extent around the optimum gas cooler pressure, but starts increasing after a peak at the bottom.

## 4.4 Thermodynamic Model of the EERC Including the Efficiency of All Ejector Components and Liquid-Vapor Separator under CPM Assumption

In this section, EERC with reference to constant pressure mixing theory is investigated to display the effects of the liquid-vapor separator efficiency on the performance, entrainment ratio, and area ratio at various operation conditions. R1234yf and R1234ze(E) having low global warming potential values are used in the analyses. When compared to all previously summarized literature studies, a thermodynamic model including the efficiency of all ejector components, namely motive nozzle, suction nozzle, mixing section, and diffuser, and liquid-vapor separator is established in this section. Therefore, the first objective of this section is comparing the effects of the typical mixing section and the liquid-vapor separator efficiency values in addition the other component efficiencies thereby calculating more realistic performance improvement ratios at various operating conditions. The second objective of this study is the comparison of the optimum performance improvement ratio, entrainment ratio, and area ratio according to vapor and liquid separation efficiencies for a typical air-conditioning application.

Modelling equations of the EERC are presented considering the efficiencies of the all ejector components and liquid-vapor separator. With this established model, the effects of the vapor and liquid separation efficiencies are investigated elaborately with respect to the optimum values of the performance improvement ratio, entrainment ratio, and area ratio when compared with the limited literature findings. To compare the influence of the mixing section and separator efficiency based on the operation conditions, three efficiency case combinations are proposed. The first case considers only the efficiency of the motive nozzle, suction nozzle, and the diffuser and assumes that the ejector mixing section and the liquid-vapor separator have efficiency equal to unity. The second case take the efficiency of the mixing section into consideration as well. Then, the third case evaluates the efficiency of the separator in addition to all ejector components. The comparison between the assumed ejector component efficiencies and the separator efficiency is of valuable contribution to the literature in terms of displaying their effects on the optimum performance improvement ratio, entrainment ratio, and the area ratio.

Equations of the mathematical model are established with reference to CPM assumption of Kornhauser (1990) with the efficiency of all ejector components and liquid-vapor separator. Thermodynamic properties of the working fluids are calculated via REFPROP version 9.1 program (Lemmon et al., 2013). Equations are established for all ejector components and for each component of the EERC. The modelling assumptions are typically the same as the previously stated ones. CPM ejector assumption is selected to investigate the effects of the separator and ejector mixing section efficiencies since this mixing theory is easier to be modified when compared to CAM ejector theory. CAM ejector solution algorithm includes one more iteration to calculate the outlet pressure of the CAM section and requires an additional area increment parameter for the mixing section in order to compensate for the effect of the mixing section efficiency term and to satisfy the mass conservation. This aspect would be clarified in Chapter Seven. The models are validated previously as well. The essential outcomes of Atmaca, Erek, & Ekren (2020a) are presented in this section.

### 4.4.1 Liquid-vapor Separator Efficiency

In this section, the separator has the liquid and vapor separation efficiencies at the liquid and vapor ports as opposed to most of the thermodynamic models in the literature. If perfect separation occurs in the separator as shown in Figure 4.25 (a), primary fluid mass flow rate is equal to the available vapor refrigerant flow in the two-phase fluid entering the separator per second. Similarly, the secondary fluid mass flow rate is the same as the liquid refrigerant flow in the two-phase fluid flowing into the separator per second. Moreover, the following equation is valid whenever the perfect separation condition is satisfied.

$$r_{d,out} = \frac{1}{1+w} \tag{4.28}$$

Vapor separation efficiency is defined as the ratio of the mass flow rate of the vapor leaving the separator (at the separator vapor port) to the vapor portion of the total mass flow rate entering the separator (Lawrence, 2012; Lawrence & Elbel, 2012). Also, the liquid separation efficiency is expressed as the ratio of the mass flow rate of the liquid leaving the separator (at the separator liquid port) to the liquid portion of the total mass flow rate entering the separator (Lawrence, 2012; Lawrence &Elbel, 2012).

$$\eta_{vap} = \frac{\dot{m}_{vsvp}}{\dot{m}_{v}} \tag{4.29}$$

$$\eta_{liq} = \frac{\dot{m}_{lslp}}{\dot{m}_{l}} \tag{4.30}$$

$\dot{m}_l$ and $\dot{m}_v$ are the available mass of the liquid and vapor refrigerants, respectively, entering the separator per second and expressed as

$$\dot{m}_l = \dot{m}_t (1 - r_{d,out}) \tag{4.31}$$

$$\dot{m}_v = \dot{m}_t \, r_{d,out} \tag{4.32}$$

However, if the separator has inefficiency at the vapor ($\eta_{vap}$) and liquid ($\eta_{liq}$) ports as shown in Figure 4.25 (b), primary fluid is comprised of basically vapor refrigerant and a small amount of liquid refrigerant; whereas the secondary flow is composed of the liquid refrigerant in main and a minute quantity of vapor refrigerant. Therefore, instead of the saturated liquid and vapor at the liquid and vapor ports of the separator, respectively as given in Figure 4.25 (a), the primary and secondary fluid flows have both qualities with respect to the separation efficiencies as shown in Figure 4.25 (b) and the relationship between the quality of the refrigerant at the diffuser outlet and the entrainment ratio for an imperfect separator is given below

$$w = \frac{(1 - r_{d,out})\eta_{liq} + r_{d,out}(1 - \eta_{vap})}{r_{d,out}\eta_{vap} + (1 - r_{d,out})(1 - \eta_{liq})} \tag{4.33}$$

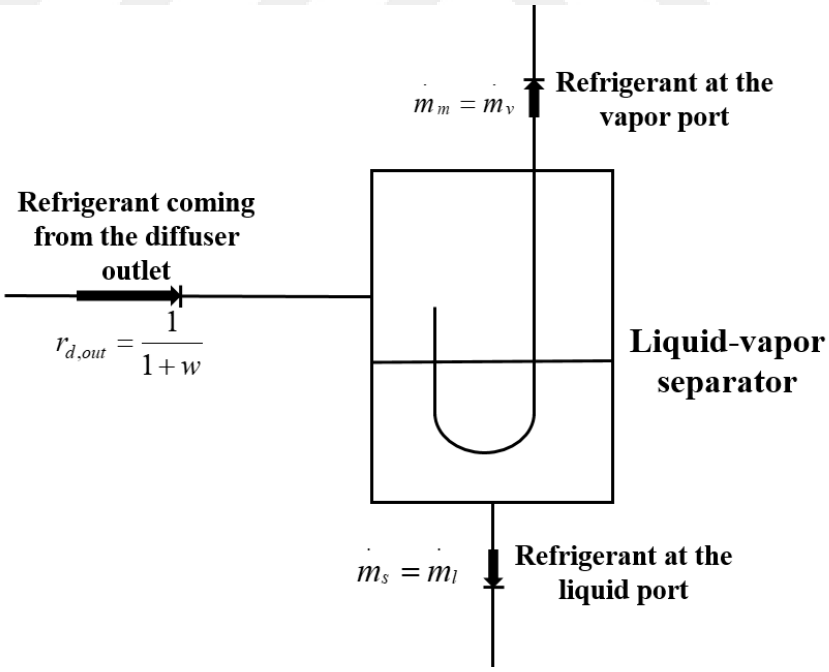


**(a)**

Figure 4.25 Comparison of the primary and secondary fluid flows for the liquid-vapor separator (a) having perfect separation and (b) having liquid and vapor separation efficiencies of $\eta_{liq}$ and $\eta_{vap}$, respectively

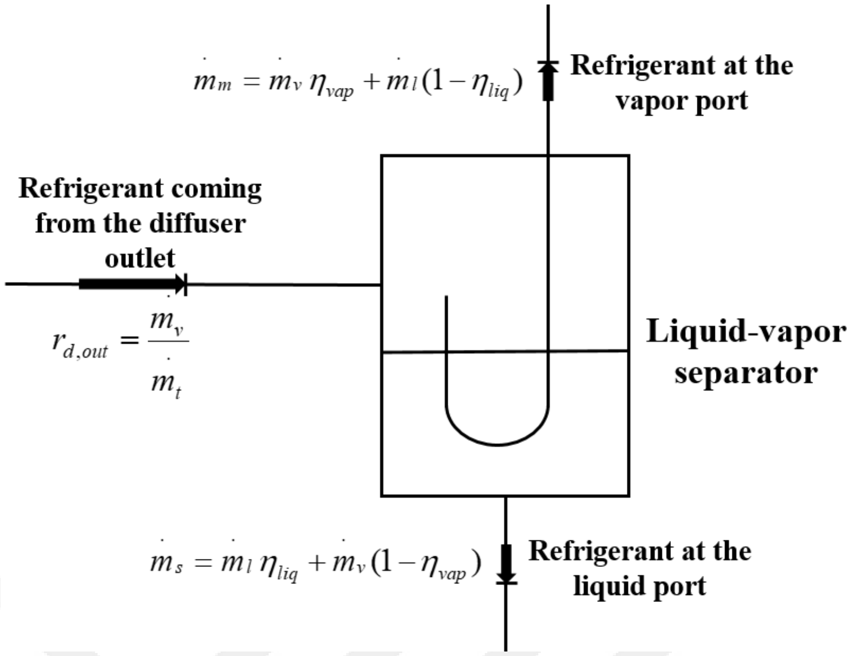


**(b)**

Figure 4.25 continues

### *4.4.2 Thermodynamic Modelling Equations of the EERC Including the Efficiencies of the All Ejector Components and Liquid-Vapor Separator*

Equations of the mathematical model are established with reference to CPM assumption of Kornhauser (1990) with the efficiency of all ejector components and liquid-vapor separator. Actual enthalpy and velocity of the primary fluid are calculated as given in Equation 4.2 and Equation 4.3. The occupied area of the primary flow per unit total mass flow of the ejector at the motive nozzle outlet section as a result of the expansion process through the nozzle is as given;

$$a_{m,out} = \left(\frac{r_{d,out}\eta_{vap} + (1-r_{d,out})(1-\eta_{liq})}{u_{m,out}\rho(P_s, h_{m,out})}\right) \tag{4.34}$$

Actual enthalpy and velocity of the secondary fluid are calculated as given in Equation 4.5 and Equation 4.6. The occupied area of the secondary flow per unit total mass flow of the ejector at the suction nozzle outlet section as a result of the expansion process through the nozzle is expressed as;

$$a_{s,out} = \frac{(1-r_{d,out})\eta_{liq} + r_{d,out}(1-\eta_{vap})}{u_{s,out}\rho(P_s, h_{s,out})} \tag{4.35}$$

The pressure at the end of the mixing process stays the same with reference to CPM ejector theory, hence $P_{mix,out}$ and $P_s$ are equal to each other.

$$\begin{aligned} u_{mix,out} = \eta_{mix} u_{m,out}(r_{d,out}\eta_{vap} + (1-r_{d,out})(1-\eta_{liq})) + \\ \eta_{mix} u_{s,out}((1-r_{d,out})\eta_{liq} + r_{d,out}(1-\eta_{vap})) \end{aligned} \tag{4.36}$$

$$\begin{aligned} h_{mix,out} = h_{m,in}(r_{d,out}\eta_{vap} + (1-r_{d,out})(1-\eta_{liq})) + \\ h_{s,in}((1-r_{d,out})\eta_{liq} + r_{d,out}(1-\eta_{vap})) - 0.5u_{mix,out}^2 \end{aligned} \tag{4.37}$$

Rest of the thermodynamic modelling equations are the same as given by Equations 4.13, 4.14, 4.15, 4.16, and 4.17. The quality values of the refrigerants at the vapor and liquid ports of the separator as a result of the imperfect separation are formulated as;

$$r_{rsvp} = \frac{\eta_{vap} r_{d,out}}{\eta_{vap} r_{d,out} + (1-r_{d,out})(1-\eta_{liq})} \tag{4.38}$$

$$r_{rslp} = \frac{(1-\eta_{vap}) r_{d,out}}{(1-\eta_{vap}) r_{d,out} + (1-r_{d,out})\eta_{liq}} \tag{4.39}$$

The enthalpy of the refrigerants at the vapor and liquid ports of the separator are as follows;

$$h_{rsvp} = h(P_{d,out}, r_{rsvp}) \tag{4.40}$$

$$h_{rslp} = h(P_{d,out}, r_{rslp}) \tag{4.41}$$

The rest of the cycle components are modelled in the same way that VCRC equations are established and COP of the EERC is given as

$$COP_{EERC} = \left( \frac{(1-r_{d,out})\eta_{liq} + r_{d,out}(1-\eta_{vap})}{r_{d,out}\eta_{vap} + (1-r_{d,out})(1-\eta_{liq})} \right) \left( \frac{h_{e,out} - h_{e,in}}{h_{comp,out} - h_{comp,in}} \right) \tag{4.42}$$

### *4.4.3 Solution Algorithm*

Solution procedure is summarized in Figure 4.26. Efficiency of the motive nozzle, suction nozzle, mixing section, diffuser, compressor, and liquid-vapor separator are given as the inputs in addition to the temperature and pressure of the primary and secondary fluids. Quality of the refrigerant at the diffuser outlet is assumed for the first iteration to initiate the calculations and solved iteratively. If the assumed quality at the beginning and calculated quality at the end of the diffuser equations are close enough to each other within a determined error band (Ɛ), iteration steps stop and the exact quality and entrainment ratio is defined. All results are presented according to the optimum suction chamber pressure which is also the mixing pressure for the CPM ejector. Therefore, another iterative procedure is required to define the optimum suction chamber pressure, $P_s$.

$P_{check}$ is introduced at this step to control the increase or decrease in the diffuser outlet pressure which attains its maximum at the optimum operation conditions. At the first iteration, $P_{check}$ could be defined as the evaporator pressure since for an ejector operating properly, diffuser outlet pressure would certainly be higher than the pressure of the secondary fluid. For the rest of the iterations after the first step, $P_{check}$ gets the value of the diffuser outlet pressure calculated in the previous step. Whenever a higher diffuser outlet pressure is calculated, $P_s$ is updated in order to obtain the optimum operation conditions with respect to the pressure drop in the suction nozzle. After obtaining the maximum, when it is seen that the diffuser outlet pressure starts decreasing at the current iteration, the value of the diffuser outlet pressure at the previous step which is $P_{check}$ is defined as the maximum and the corresponding suction nozzle pressure drop at which the maximum value is obtained is stated as the optimum operation condition. Optimum values of the area ratio, entrainment ratio, performance improvement ratio as well are calculated according to this optimum pressure drop.

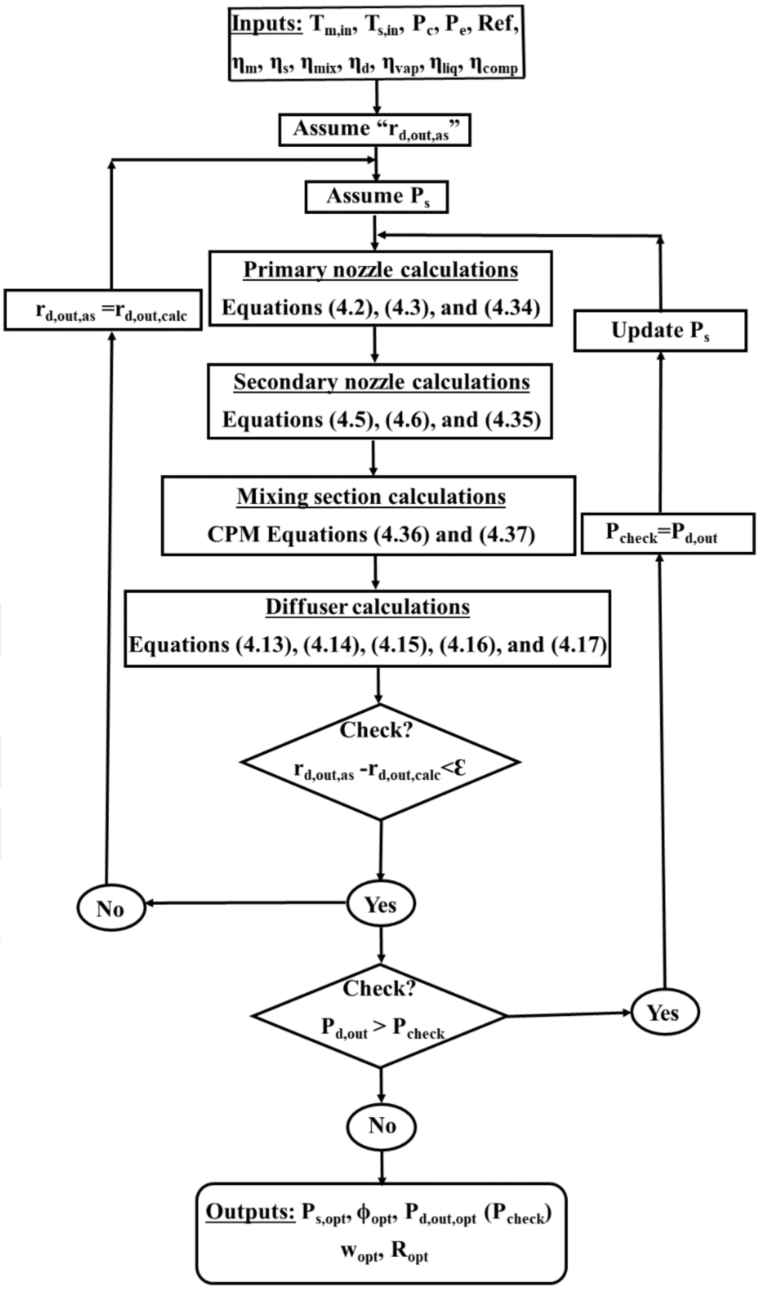


Figure 4.26 Flowchart of the calculation procedure for the EERC including the efficiency of the liquid-vapor separator and all ejector components

### *4.4.4 Results of the Thermodynamic Analyses for the EERC with the Efficiency of the Liquid-Vapor Separator and All Ejector Components*

There are two important result groups of this investigation. As for the first target, various efficiency cases of ejector components and separator are analyzed according to the operation conditions considering the optimum performance improvement ratio, entrainment ratio, and the area ratio. Secondly, the effects of the vapor and liquid separation efficiencies are analyzed for the same parameters. The operation conditions for a typical air-conditioning application are given in Table 4.9 (Lawrence, 2012). Figure 4.27 compares the optimum performance improvement ratios of R1234yf and R1234ze(E) at various operation conditions considering three types of efficiency cases for the liquid-vapor separator and the ejector components.

Table 4.9 Operation conditions for the EERC with the efficiency of the liquid-vapor separator and all ejector components

| **Parameters** | **Values** |
|---|---|
| Evaporator temperature ($T_e$) | 5 ˚C (Lawrence, 2012) |
| Evaporator outlet superheat temperature difference ($\Delta T_{sh}$) | 5 K (Lawrence, 2012) |
| Condenser Temperature ($T_c$) | 40 ˚C (Lawrence, 2012) |
| Condenser outlet subcooling temperature difference ($\Delta T_{sc}$) | 3 K (Lawrence, 2012) |
| Compressor efficiency ($\eta_{comp}$) | 0.75 (Bilir & Ersoy, 2009; Lawrence, 2012; Li & Groll, 2005) |
| Primary nozzle efficiency ($\eta_m$) | 0.9 (Bilir & Ersoy, 2009; Li & Groll, 2005) |
| Suction nozzle efficiency ($\eta_s$) | 0.9 (Bilir & Ersoy, 2009; Li & Groll, 2005) |
| Mixing section efficiency ($\eta_{mix}$) | 0.90 (Liu, Groll et al., 2012) |
| Vapor separation efficiency ($\eta_{vap}$) | 0.95 (Elbel et al., 2012; Lawrence, 2012) |
| Liquid separation efficiency ($\eta_{liq}$) | 0.90 (Elbel et al., 2012; Lawrence, 2012;) |
| Diffusor efficiency ($\eta_d$) | 0.8 (Bilir & Ersoy, 2009; Li & Groll, 2005;) |

The solid lines in Figure 4.27, 4.28, and 4.29 represent the curves of R1234yf; whereas the same color dashed lines are the counterpart curves of the same efficiency cases for R1234ze(E). The first case takes only the efficiency of the motive nozzle, suction nozzle, and the diffuser of the ejector into the account. In other words, it considers that the mixing section and the liquid-vapor separator are 100% efficient.

The second case adds the efficiency of the mixing section to the thermodynamic model and shows how the performance improvement ratios deviate from the first case when the mixing section efficiency is introduced to the model. Lastly, the third case evaluates the effects of the liquid-vapor separator in addition to all ejector component efficiencies on the overall cycle performance in order to calculate more realistic results.

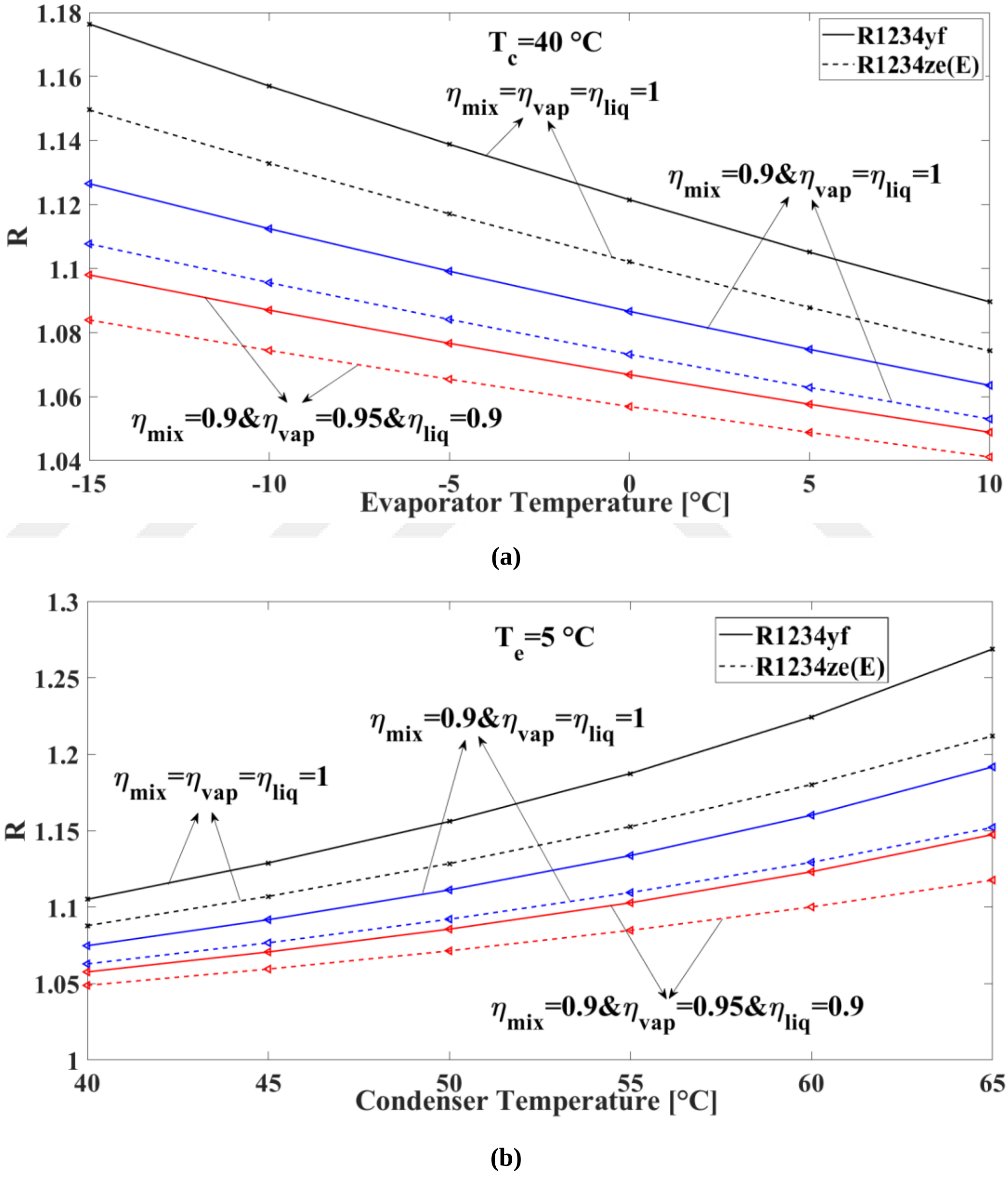


Figure 4.27 Dependency of the optimum performance improvement ratio on the (a) evaporation and (b) condensation temperatures with respect to various efficiency combinations of the ejector components and liquid-vapor separator for R1234yf and R1234ze(E)

At each operation points, R1234yf performs better than R1234ze(E) as seen from Figure 4.27. The first case considering the efficiency of the separator and mixing section as unity yields the highest performance improvement ratios at each operation condition as expected. It is important to display the effects of the other two factors from the viewpoint of the overall performance improvement. At higher condenser temperatures, percentage performance decrease is higher when the mixing section and the separator efficiency is introduced into the model in comparison with the lower evaporator temperatures.

For R1234yf, the percentage performance improvement decrease is around 8% while moving from the first case to the second one and about 5% while passing from the second case to the third case at the highest condensation temperature at issue. However, deviation is approximately 5% and 3% between the first and second cases and the second and third cases, respectively for the same refrigerant at the lowest evaporation temperature. Moreover, the percentage performance reduction between these three cases with respect to the evaporation and condensation temperatures are lower for R1234ze(E) in comparison with R1234yf.

R1234yf reacts more to the changes in the component efficiencies in terms of the EERC performance improvement potentials because of the higher expansion losses experienced during the throttling process of the VCRC. For example, percentage performance improvements are compared benefiting from the numerical values above at the highest condensation and the lowest evaporation temperatures since the ejector is used more effectively at these operation ranges due to the largest expansion losses.

R1234ze(E) has higher entrainment ratios than R1234yf at the optimum suction chamber pressure drop for each efficiency combination of the ejector components and the separator as seen from Figure 4.28. At higher condensation temperatures and lower evaporator temperatures second and third cases of efficiency combinations yield closer entrainment ratios. However, at higher evaporator and lower condenser temperatures, the first and second combinations result in closer entrainment ratios. Liquid-vapor separator affects more the performance of the ejector through medium of the entrained flows especially at higher evaporator and lower condenser temperatures. The third case including all ejector sections and liquid-vapor separator inefficiencies yields the lowest entrainment ratio for both of the refrigerants at each operation point.

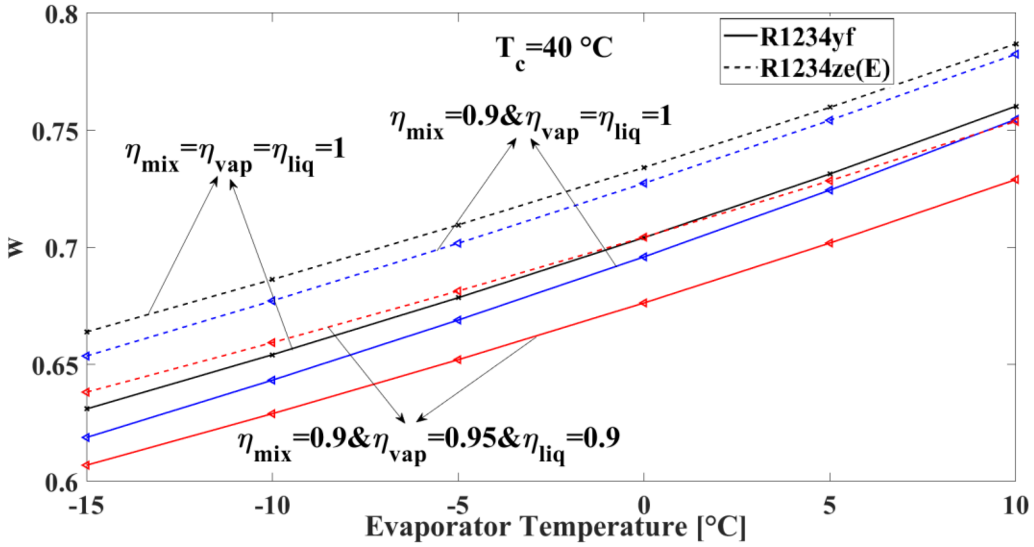


(a)

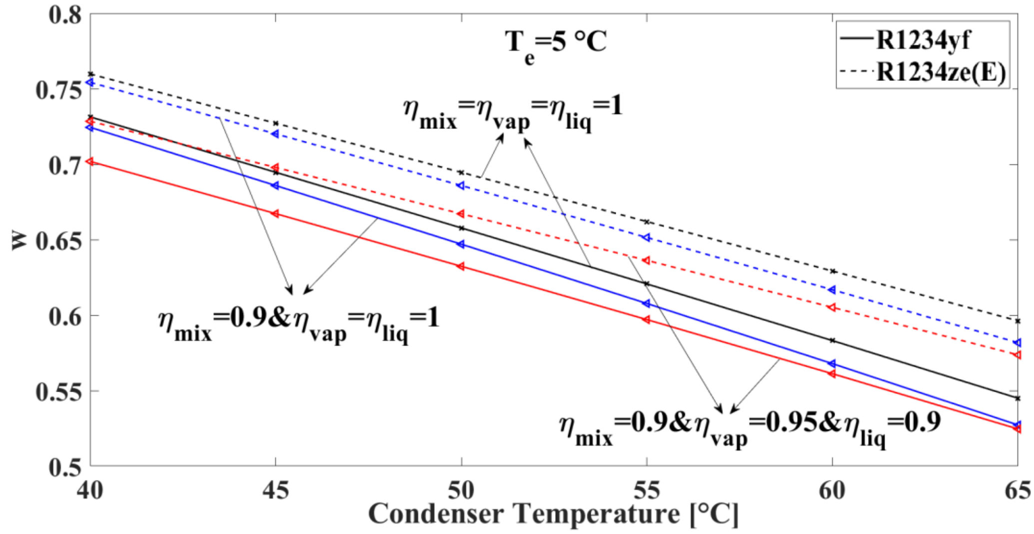


(b)

Figure 4.28 Effect of the liquid-vapor separator and ejector component efficiencies on the optimum entrainment ratio according to various (a) evaporation and (b) condensation temperatures for R1234yf and R1234ze(E)

That's why, the diffuser outlet pressures are calculated slightly higher under the efficiency combination of the third case when compared the second case which only considers the efficiency of all ejector components. Figure 4.29 displays the variations of the area ratio which is the ratio of the total cross-sectional area occupied by the total flow at the exit of the primary and suction nozzles to the area occupied by only primary fluid flow with respect to operation conditions under the same efficiency combinations.

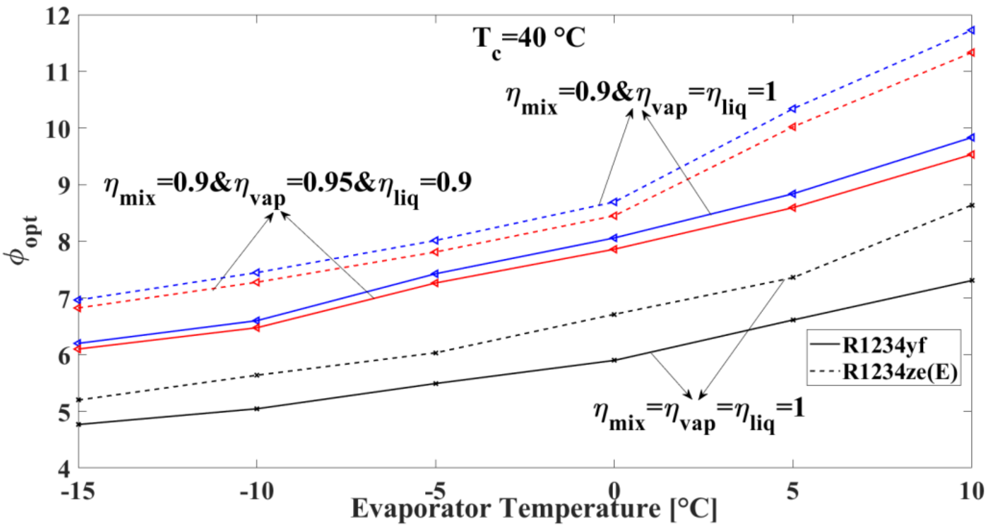


(a)

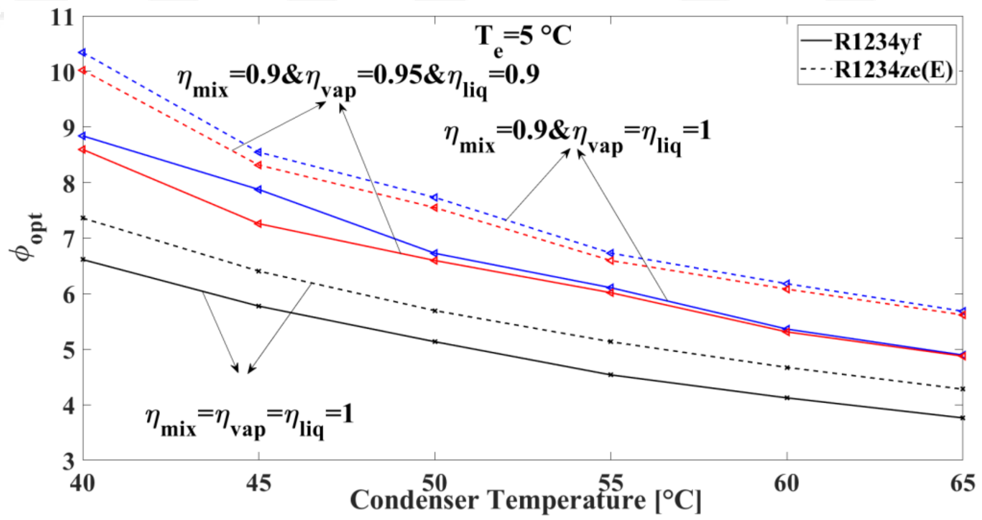


(b)

Figure 4.29 Variations of the optimum area ratio with respect to (a) evaporation and (b) condensation temperatures based on the three efficiency cases of the ejector components and the liquid-vapor separator for R1234yf and R1234ze(E)

Area ratios are defined at the optimum suction chamber pressure drop for each case. When evaporator temperature is increased the entrainment ratio increases as seen from Figure 4.28 (a), but density ratio of the secondary flow to the primary flow decreases. Rate of change of density ratio is higher than the velocity change rate; hence area ratio increases to compensate for the decrease in the density ratio as seen from Figure 4.29 (a). When the condenser temperature is increased, entrainment ratio decreases and density ratio having higher rate change when compared to the velocity ratio increases thereby causing the decrease in the area ratio as shown in Figure 4.29 (b). As for the comparison between the effects of the mixing section and the separator efficiency, the mixing section efficiency has more influence on the variation of the area ratio rather than the separator as seen from the slight decrease when the efficiency of the separator is added to the model including all ejector component efficiencies with respect to the operating conditions of the investigated cases.

Figure 4.30 presents the effects of the vapor and liquid separation efficiencies separately on the optimum performance improvement ratio, entrainment ratio, and area ratio for a typical air-conditioning application with respect to optimum suction chamber pressure drop. Solid lines in Figure 4.30 display the cases at which liquid separation efficiency is equal to unity and the vapor separation efficiency is varied; whereas the dashed lines shows the reverse order. Figure 4.30 (a) shows that both the vapor and liquid separation efficiencies have the same effects on the overall performance improvement after an efficiency value around 85% is achieved at the investigated conditions. Before this point, liquid separation efficiency has more influence on the performance.

When the vapor separation efficiency increases, entrainment ratio decreases since the mass going through the separator vapor port outlet increases as seen from Figure 4.30 (b). However, entrainment ratio increases when the liquid separation efficiency is improved since the mass flow rate going through the liquid port increases. The required occupied area increases for the motive flow as seen also from the decrease in the entrainment ratio. Hence, area ratio decreases when vapor separation efficiency increases as shown in Figure 4.30 (c). In the opposite case, the occupied area by the motive flow decreases as a result of the liquid separation efficiency improvement, hence the optimum area ratio increases for both of the refrigerants. The mixing section and separator efficiency certainly is better to be implemented in the thermodynamic models for more realistic results. However, in most of the models, perfect separation and mixing is assumed.

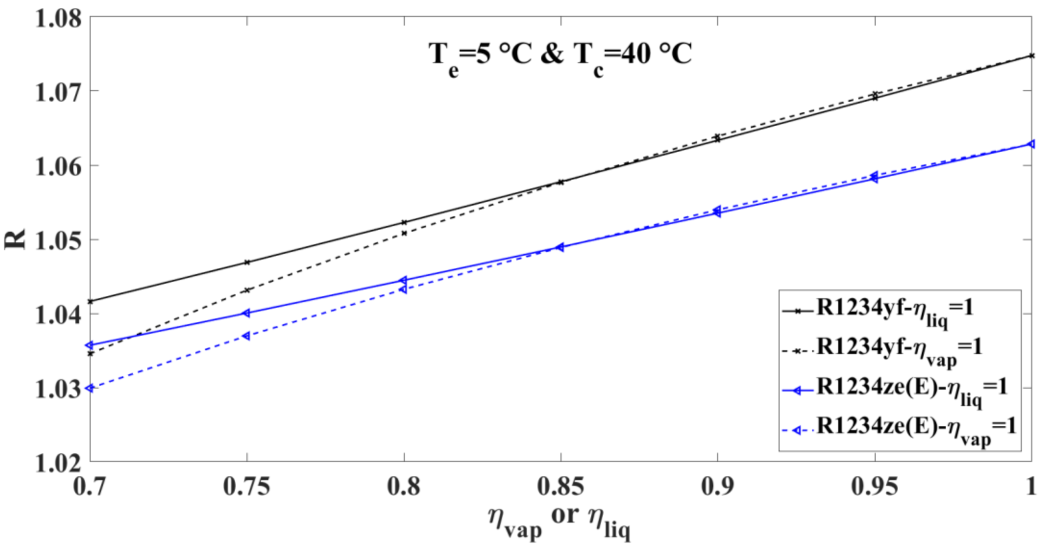


(a)

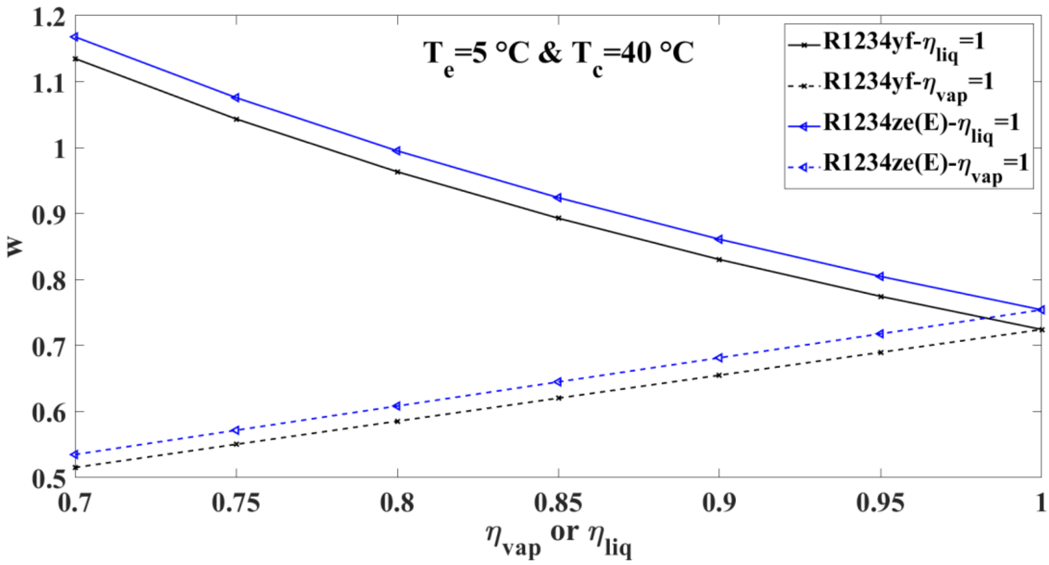


(b)

Figure 4.30 Effects of the vapor and liquid separation efficiencies on (a) the optimum performance improvement ratio, (b) the optimum entrainment ratio, and (c) the optimum area ratio for R1234yf and R1234ze(E)

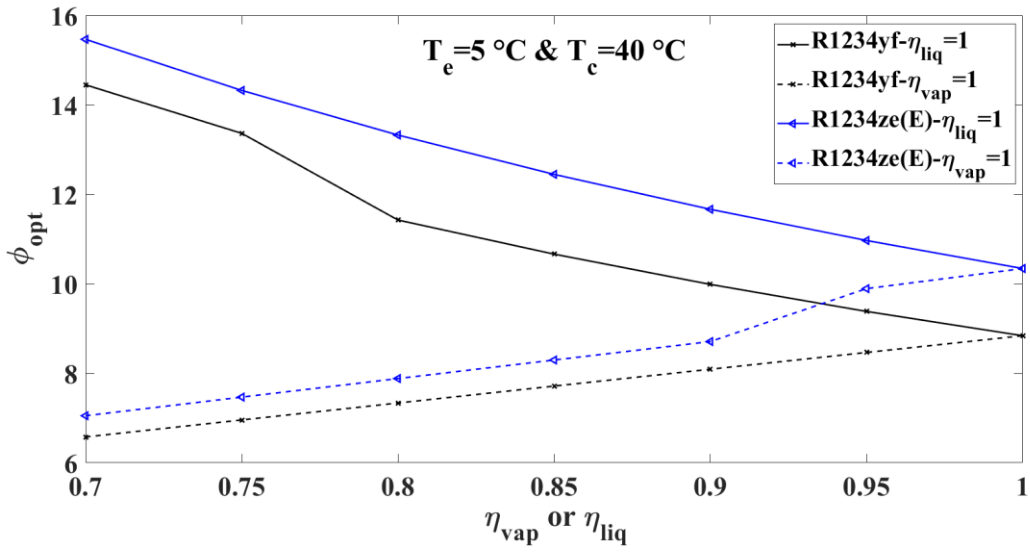


**(c)**

Figure 4.30 continues

Effects of the separation efficiency on the optimum area ratio display the fact that although it is an external component, separator is to be taken into account for the sensitive design of the ejector. Optimum design with respect to the operation conditions is of vital importance especially to the low-pressure refrigerants such as R134a and R1234yf.

Results of the current section concerned with the vapor and liquid separation efficiencies differ from the available data in the literature since optimum suction pressure approach yielding the maximum performance is used within the content of this section. Furthermore, the effects of the vapor and liquid separation efficiencies are compared not only in terms of the performance improvement ratio, but also entrainment ratio and area ratio. A brief summary of the concluding remarks are as follows;

• The performance improvement potential may be calculated as low as 8% at the highest investigated condenser temperature for R1234yf when the mixing section efficiency is introduced to the base thermodynamic model considering only the efficiency of the motive nozzle, suction nozzle, and diffuser. Moreover, when the separator efficiency is considered in addition to the efficiency of all ejector components, the difference could be as much as 12% when compared to the same base case for the same refrigerant.

• R1234yf has higher performance improvement potential than R1234ze(E) within the investigated ranges; whereas the entrainment ratio is calculated higher for R1234ze(E).

• When compared to R1234yf, R1234ze(E) experiences less percentage performance improvement decrease within each interval when the mixing section and separator efficiency is introduced to the model considering only ejector component efficiencies of motive nozzle, suction nozzle, and the diffuser.

• Liquid-vapor separator efficiency affects the entrainment ratio more at higher evaporator and lower condenser temperatures for both of the refrigerants within the investigated operational ranges.

• Mixing section efficiency is more effective than the separator efficiency on the area ratio at the given operation conditions for both of the refrigerants.

• Liquid separation efficiency influences more the optimum performance improvement ratio in comparison with the vapor separation efficiency until the efficiency point of 0.85 is achieved within the investigated conditions. After this point, both efficiencies have the same effect on the optimum performance improvement ratio.

All in all, since the thermodynamic models are simple and easily provide with the quick results about the performance evaluations, they are favorably preferred in the cyclic device analyses. However, they present limited results since they only consider the inlet and outlet of the ejector or cycle components. The efficiencies of all ejector components and the separator are to be implemented into the thermodynamic models in order to present more sensitive analyses. However, computation fluid dynamic analyses are required in order to obtain more comprehensive results and elaborate flow structures for a specific refrigerant at the investigated operation conditions.

### 4.5 Typical Behavior of the CAM and CPM Ejectors

The main outputs from the study of Atmaca et al. (2017a) is presented in this section. When the effect of the mixing chamber inlet pressure on the performance is analyzed, it is seen that there is an optimum suction nozzle pressure for both of the theories. This pressure does not change throughout the mixing process only for constant pressure mixing ejector, whereas it increases to some extent for the constant area mixing ejector as previously discussed in detail. If they are compared according to common points defined with reference to evaporation temperature, for example based on suction pressure values determined with respect to saturation pressure of each refrigerant corresponding to various temperatures lower than the evaporator temperature, each theory displays a similar behavior for the refrigerants at issue as shown in Figure 4.31.

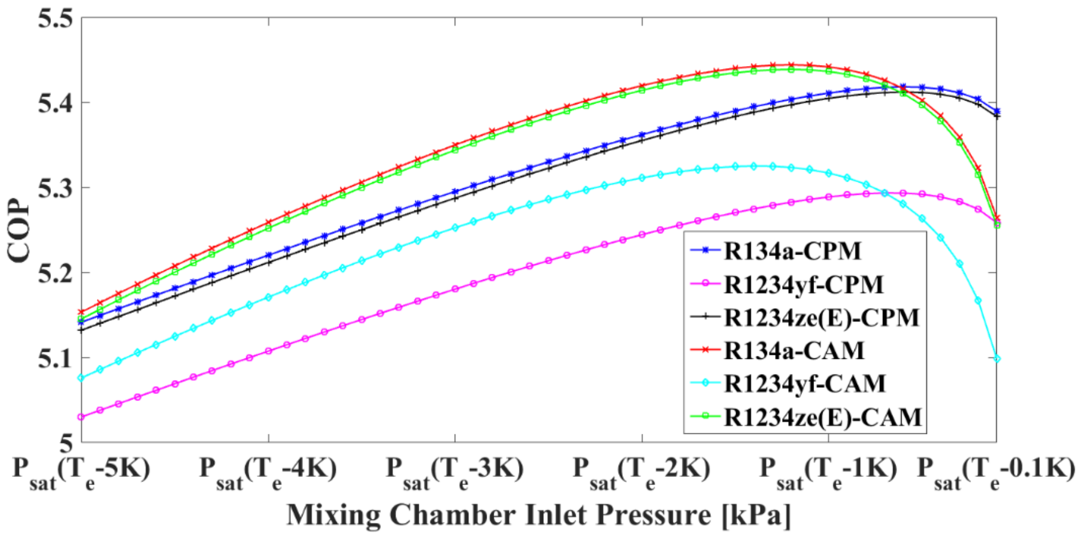


Figure 4.31 Evaluation of the performance of the cycles according to the probable pressure variations of the refrigerants at the mixing chamber inlet based on the parametric declaration

However, when the actual data is displayed as shown in Figure 4.32, each refrigerant has different operation ranges although they display typical performance curves under the same mixing theories. Performance of the refrigerants of R134a and R1234ze(E) are very close to each other under each mixing theory. It could be seen directly when comparison is especially made according to the corresponding saturation pressures of temperature values lower than the evaporator temperature though R134a and R1234yf have closer operation pressure range in terms of the actual data. Constant pressure mixing ejector theory is harder to be achieved since its optimum pressure for maximum performance is much closer to the evaporation pressure when compared to the constant area mixing theory.

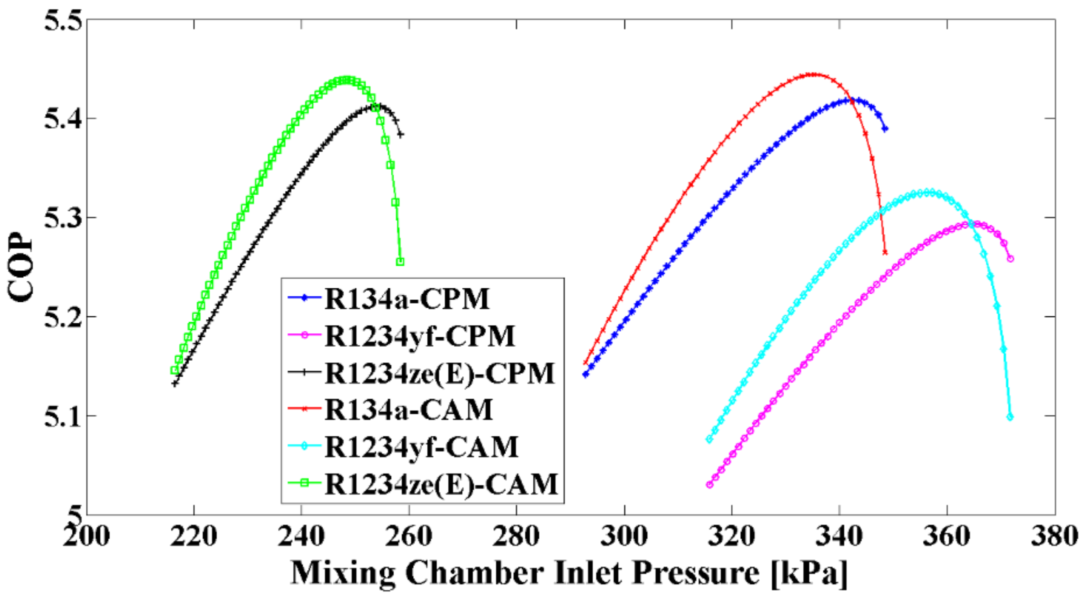


Figure 4.32 Evaluation of the performance of the cycles according to the probable pressure variations of the refrigerants at the mixing chamber inlet based on the actual operation ranges

To sum up, each theory displays similar performance profile as the general view for all refrigerants when the pressure before mixing section (in the suction nozzle) is defined in accordance with the evaporator temperature parametrically. In other words, there is a typical performance curve specific to mixing theory which is independent of the refrigerants. However, the actual operational ranges of the refrigerants are different from each other.

## 4.6 Thermodynamic Assessment of the EERC under Reversible Ejector Assumption

Reversible ejector assumption is used for the highest theoretical performance limit; whereas the efficiencies of the liquid-vapor separator and all ejector components are added to the model to calculate more realistic performance improvement potentials. The difference between the percentage performance improvement of the reversible ejector cycle and the realistic ejector cycle including the separator and ejector components efficiencies is as high as 35% at the highest investigated condenser temperature for R1234yf with reference to thermodynamic analyses made in this section.

Since analyzing the EERC under reversible ejector assumption is an important aspect to display the highest theoretical performance improvement limit that could be achieved by the cycle, the objective of this section is comparing the realistic performance improvement ratio (taking all ejector component efficiencies and liquid-vapor separator efficiency into account) with the maximum performance improvement ratio (under reversible ejector assumption) at various operation conditions. Some part of the conclusions obtained by Atmaca et al. (2020a) is presented in this section.

### *4.6.1 Reversible Ejector*

There are various reversible ejector approaches in the literature. Chunnanond & Aphornratana (2004) previously defined the reversible ejector concept schematically in order to eliminate the losses caused by the shock waves and mixing process. As it is seen from Figure 4.33, the performance improvement potential is higher due to the net work provided by the isentropic turbine-compressor assembly under the reversible ejector assumption.

Atmaca, Erek, & Ekren (2018b) analyzed the performance of R1234yf, R290, R1234ze(E), R134a, and R600a in the EERC according to reversible ejector definition of Chunnanond & Aphornratana (2004) and made comparison between the performance improvement of the reversible ejector cycle and the corresponding EERC taking all ejector component efficiencies into consideration. Since analyzing the EERC under reversible ejector assumption is an important aspect to display the highest theoretical performance improvement limit that could be achieved by the cycle, Atmaca et al. (2020a) compared the realistic performance improvement ratio (taking all ejector component efficiencies and liquid-vapor separator efficiency into account) with the maximum performance improvement ratio (under reversible ejector assumption) at various operation conditions.

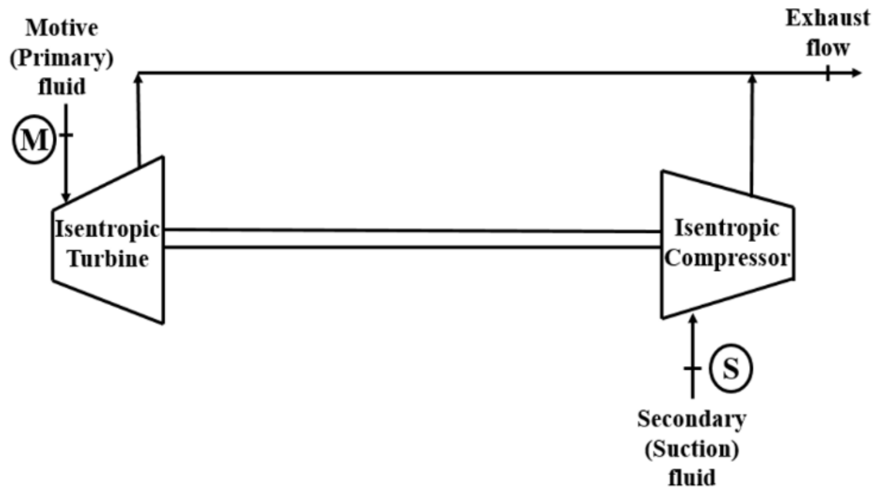


Figure 4.33 Schematic view of the reversible ejector as an isentropic turbine-compressor assembly (Chunnanond & Aphornratana, 2004)

The implementation scenario of the concept in Figure 4.33 for the EERC requires a discharge pressure definition based on the various operation conditions. This pressure is defined according to the optimum diffuser outlet pressure of the ejector considering all component efficiencies. However, this optimum diffuser outlet pressure taking all component efficiencies into account is slightly different than the optimum diffuser outlet pressure considering the separator efficiency as well in addition to all ejector component efficiencies at the investigated conditions. Since the reversible ejector definition is constructed based on the expansion and compression processes of the ejector solely, it is more reasonable to calculate the optimum diffuser outlet pressure considering only ejector component efficiencies. Hence, the separator is assumed to have perfect separation for all reversible ejector calculations since a kind of maximum limit is aimed to be achieved under the reversible ejector assumption.

Moreover, a comparative base is created in order to evaluate the performance improvement ratio of the EERC under reversible ejector assumption and the EERC including the efficiency of all ejector components and the separator. The latter is for simulating the actual operation of the EERC in order to yield more realistic performance improvement ratios. The entrainment ratio in the reversible case is calculated higher than the actual case. The work produced and consumed by the isentropic turbine-compressor assembly, COP, and the entrainment ratio of the EERC under reversible ejector approach is described as follows;

$$\dot{W}_{isen,turb} = \dot{m}_{m,rev}(h_{m,in} - h(P_{d,out(opt)}, s_{m,in})) \tag{4.43}$$

$$\dot{W}_{isen,comp} = \dot{m}_{s,rev}(h(P_{d,out(opt)}, s_{s,in}) - h_{s,in}) \tag{4.44}$$

$$COP_{EERC,rev} = \frac{\dot{m}_{s,rev}(h_{e,out} - h_{e,in})_{rev}}{\dot{W}_{comp} + \dot{W}_{isen,comp} - \dot{W}_{isen,turb}} \tag{4.45}$$

$$w_{rev} = \frac{\dot{m}_{s,rev}}{\dot{m}_{m,rev}} \tag{4.46}$$

#### *4.6.2 Results of the Thermodynamic Analyses under Reversible Ejector Assumption*

The entrainment ratio under the reversible ejector assumption as well is calculated iteratively according to previously defined optimum diffuser outlet pressures at various evaporation and condensation temperatures. As discussed previously, literature studies show that ejector has very high exergy destructions within the ejector components and it is possible to decrease the irreversibilities using a better ejector design thereby improving the overall cycle performance. Hence, ignoring these losses, it is possible to propose a maximum thermodynamic limit that an EERC could achieve.

The equations of the reversible ejector for the isentropic turbine-compressor assembly eliminating all mixing and shock wave losses are given previously. Therefore, total cycle performance is evaluated with respect to this reversible ejector assumption as well. Estimating the overall cycle performance under reversible ejector assumption is beneficial to obtain the highest theoretical performance limit rather than the practical implementation of the isentropic turbine-compressor assembly into the cycle instead of the ejector. The optimum diffuser outlet pressures for the discharge pressure of the isentropic turbine-compressor assembly are given in Table 4.10 and Table 4.11 at various evaporation and condensation temperatures, respectively.

Table 4.10 Optimum diffuser outlet pressures for various evaporator temperatures

| **Refrigerants** | **Diffuser outlet pressure (kPa) $T_e$ (ºC ) ($T_c$=40 ºC)** | | | | | |
|---|---|---|---|---|---|---|
| | -15 | -10 | -5 | 0 | 5 | 10 |
| **R1234yf** | 217.7074 | 254.8733 | 297.1280 | 345.0215 | 399.1550 | 460.1920 |
| **R1234ze(E )** | 141.0995 | 168.1095 | 199.2600 | 235.0446 | 276.0118 | 322.7556 |

Table 4.11 Optimum diffuser outlet pressures for various condenser temperatures

| **Refrigerants** | **Diffuser outlet pressure (kPa) $T_c$ (ºC ) ($T_e$=5 ºC)** | | | | | |
|---|---|---|---|---|---|---|
| | 40 | 45 | 50 | 55 | 60 | 65 |
| **R1234yf** | 399.1550 | 407.9314 | 418.3302 | 430.5431 | 444.8680 | 461.6879 |
| **R1234ze(E )** | 276.0118 | 281.5915 | 288.1388 | 295.7487 | 304.5608 | 314.7252 |

Figure 4.34 compares the performance improvement ratio of the EERC under the reversible ejector assumption and the realistic EERC including the efficiency of the all ejector components and liquid-vapor separator. In the actual case, efficiency of all components are defined properly in the thermodynamic model. The efficiency of the mixing section is ignored in most of the studies in the literature; whereas it is defined as 0.90 in these comparisons. Moreover, the efficiency of the liquid-vapor separator as well is added to the model as given in Table 4.9 to obtain more realistic performance improvement values at the investigated operation conditions. Vapor and liquid separation efficiencies are defined as 0.95 and 0.90, respectively.

The realistic performance improvement ratio is determined based on the optimum suction nozzle pressure with respect to the described conditions. The difference between the highest improvement potential and the performance improvement under the realistic operation conditions are higher for R1234yf in comparison with R1234ze(E). The difference is as much as 20% and 35% at the lowest evaporator and highest condenser temperatures, respectively for R1234yf.

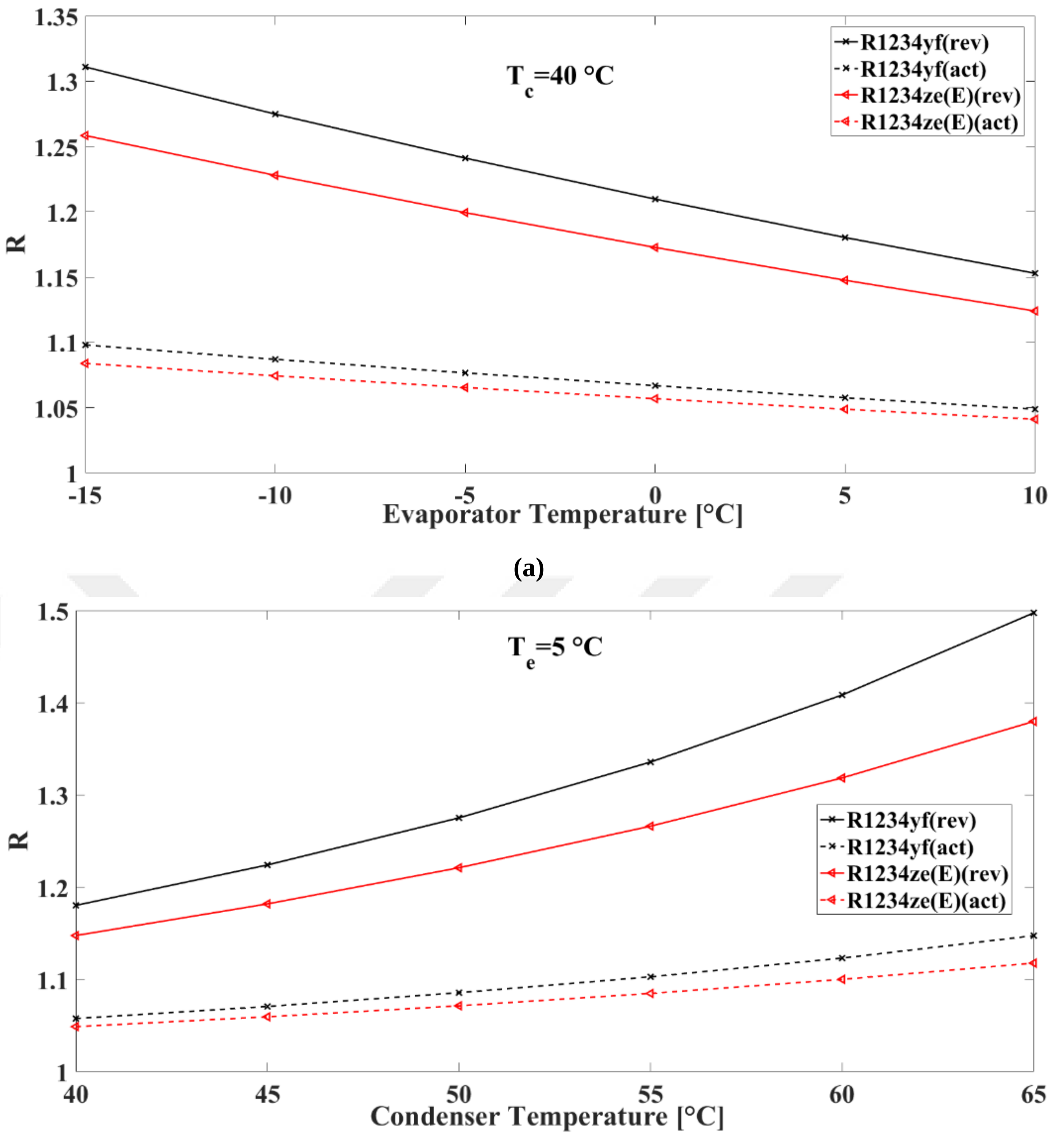


(b)

Figure 4.34 Comparison between the performance improvement ratios of the EERC modelled under the reversible ejector assumption and EERC including efficiency values of all ejector components and the liquid-vapor separator according to various (a) evaporator and (b) condenser temperatures

To sum up, maximum differences between the percentage performance improvements of the realistic (actual) and reversible cases are around 35% and 25% for R1234yf and R1234ze(E), respectively at the highest investigated condenser temperature. Amount of irreversibilities caused by the ejector highlights the improvement potential of this component in the EERC. Hence the highest performance limit achieved by the EERC could be calculated under the reversible ejector assumption. Although there are conceptual definitions or analyses based on reversible process assumption for the ejector as a component solely, investigations commenting on the overall EERC performance with respect to this assumption is not available in the literature.

The outcomes of this section is of primary value since the maximum performance improvement potential that could be achieved by an EERC under reversible ejector assumption is compared with the realistic performance improvement potential of the EERC considering the efficiency of all ejector components and the liquid-vapor separator. Thus, improvement potential within the ejector is highlighted by means of the displayed maximum performance difference.

## 4.7 Effect of the Ejector Component and Liquid-Vapor Separator Efficiency according to Operating Conditions

The importance of the ejector component efficiencies in the subcritical EERC was discussed in the previous sections of this chapter. Atmaca et al. (2017b) and Atmaca et al. (2019a) investigated the superiority of the ejector component efficiencies at a specified operating condition for design and off-design conditions. The importance order of the ejector component efficiencies is the same for both of the design conditions. The mixing section efficiency is found to be the most important component. The second one is the diffuser. Moreover, the effect of the motive nozzle and the mixing section efficiencies on the overall performance improvement are similar to each other. The least important one is the suction nozzle.

In this section, the effect of the ejector component efficiencies is discussed for the transcritical $CO_2$ EERC concept in terms of the performance improvement ratio and entrainment ratio. The analyses are the rest of the previous investigations conducted by Atmaca, Erek, Ekren et al. (2018). The main issue in this section is the effect of the ejector component efficiencies for the transcritical EERC at two different operating conditions. Hence the importance order of the ejector component efficiencies in the transcritical EERC is discussed based on the operating conditions. Optimum suction nozzle pressure drop assumption is used. However, the lower limit of this assumption is defined according to the saturation pressure corresponding to temperature 5 K below the evaporator temperature according to Lawrence (2012) since the velocity of the secondary fluid nearly catches the velocity of the motive flow for the pressure ranges lower than the declared limit. For an ejector operating properly, the secondary fluid is expected to be accelerated by the primary fluid. Similar to previously presented performance curves of Atmaca, Erek, Ekren et al. (2018), the analyses of this section is displayed with respect to a wide gas cooler pressure range.

The second important aim of this section is investigating the effects of the liquid-vapor separator efficiency with reference to various operating conditions. The second subtitle of this section is directly related to influence of the liquid-vapor separator on the performance improvement ratio at various operating conditions for R134a, R1234yf, and R1234ze(E). The second section is the rest of the previous investigations presented by Atmaca et al. (2020a). To sum up, the importance of the ejector component efficiencies at two different operating conditions is studied for the transcritical $CO_2$ EERC and the effects of the liquid-vapor separator is discussed for R1234yf, R1234ze(E), and R134a. In other words, the main objective is comparing the effects of the ejector design aspects and operating conditions. To accomplish these objectives, various modelling scenarios are proposed.

### *4.7.1 Analyses on the Transcritical $CO_2$ EERC for the Ejector Component Efficiencies at Two Different Gas Cooler Outlet Temperatures*

The operating conditions for the component efficiency analyses of the transcritical EERC are presented in Table 4.12. The isentropic efficiency of the compressor is calculated with reference to Brunin et al. (1997) similar to analyses of Atmaca, Erek, Ekren et al. (2018). Two gas-cooler outlet temperatures are selected according to investigation range of the previously mentioned study of Atmaca, Erek, Ekren et al. (2018). The principal outcomes of Atmaca, Erek, Ekren, & Çoban (2019) are presented within the content of this section. The efficiency of the investigated component is varied between the declared range (0.7-0.95) in Table 4.12 and the others are attained to the assumed highest efficiency value of 0.95.

Table 4.12 Operating conditions for the component efficiency investigations

| **Operating Parameters** | **Values** |
|---|---|
| Evaporator temperature ($T_e$) | 5 ˚C |
| Evaporator outlet superheat temperature difference ($\Delta T_{sh}$) | 5 K |
| Gas cooler outlet temperature ($T_{gc,out}$) | 40 ˚C and 46 ˚C |
| Primary nozzle efficiency ($\eta_m$) | 0.7-0.95 |
| Suction nozzle efficiency ($\eta_s$) | 0.7-0.95 |
| Mixing section efficiency ($\eta_{mix}$) | 0.7-0.95 |
| Diffusor efficiency ($\eta_d$) | 0.7-0.95 |

Figure 4.35 shows the effects of the motive nozzle efficiency on the performance improvement ratio and entrainment ratio for two different gas cooler outlet temperatures. The entrainment ratio curve is typically the same for all motive nozzle efficiency values for each gas cooler outlet temperature. The highest performance is obtained for the highest motive nozzle efficiency as expected for each gas cooler outlet temperature. Performance improvement curves show a maximum point, but this point is not applicable since the entrainment ratio is very low at that point. It could be thought that the entrained flow per unit primary mass flow is very low; hence ejector operates around that point yielding higher entrainment ratios.

Motive nozzle efficiency does not have any effects on the gas cooler pressure yielding the maximum performance improvement. However, this pressure is higher for the gas cooler outlet temperature of 46 ºC than that of 40 ºC. The gas cooler pressure for the maximum performance improvement is dependent upon the operating conditions, i.e., gas cooler outlet temperature. This point does not provide beneficial results since the entrainment ratio is very low at that point. Moreover, since the expansion losses are very high at those locations, the highest performance improvement ratio is expected to be observed. The performance improvement percentage as well is higher for 46 ºC gas cooler outlet temperature as a result of the same reason.

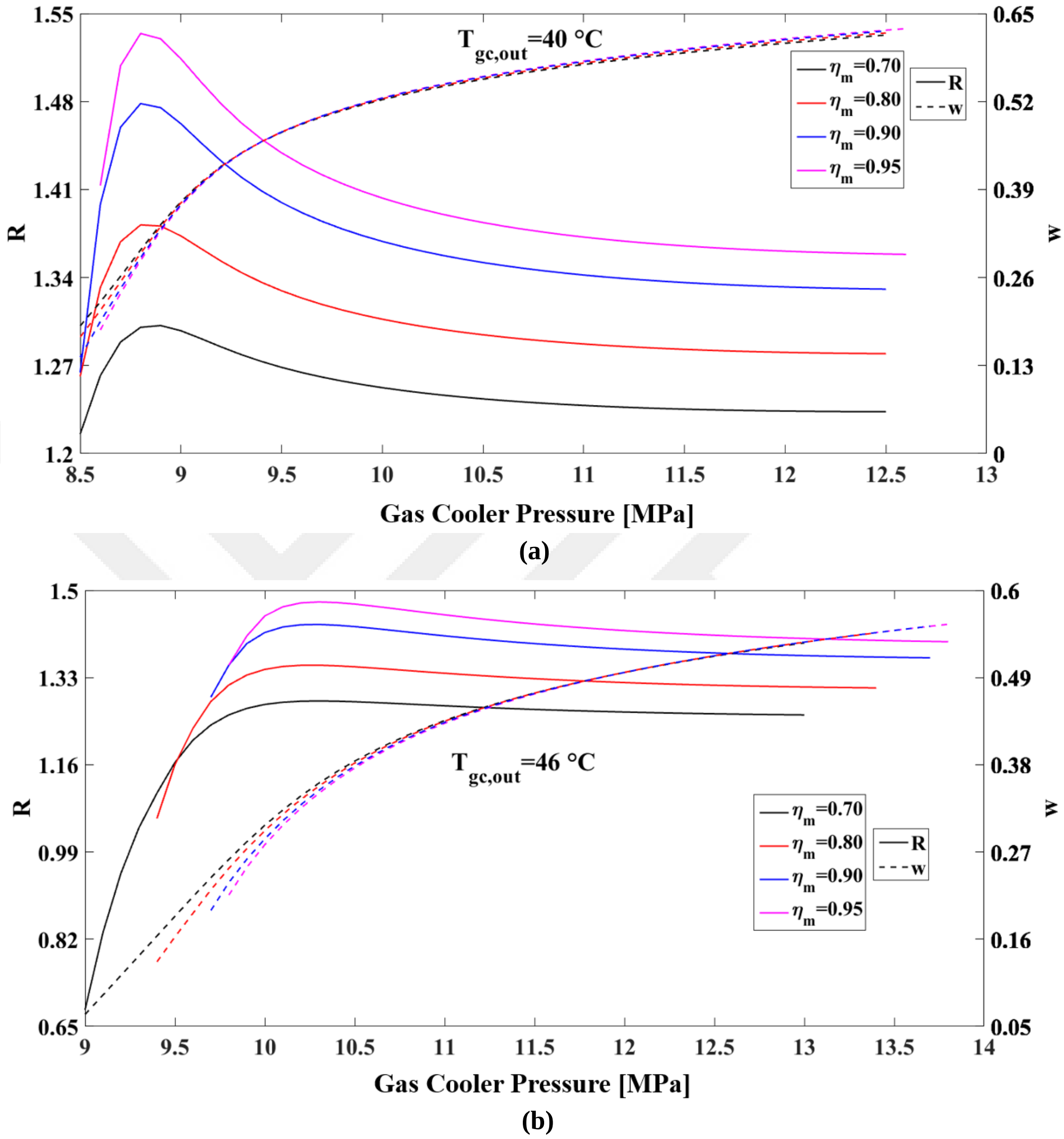


Figure 4.35 Effect of the motive nozzle efficiency on the performance improvement ratio and entrainment ratio for the gas cooler outlet temperatures of (a) 40 ºC and (b) 46 ºC

The variations in the performance improvement ratio around this maximum performance point is higher for 40 ºC than 46 ºC. In other words, the performance improvement curves changes more for 40 ºC around the gas cooler pressure yielding the maximum performance. When the motive nozzle efficiency increases, the percentage increase in the performance improvement increases while passing from 40 ºC to 46 ºC. Figure 4.36 displays the effects of the suction nozzle efficiency for the same gas cooler outlet temperatures. Similar observations are made for the Figure 4.36 (a) and (b).

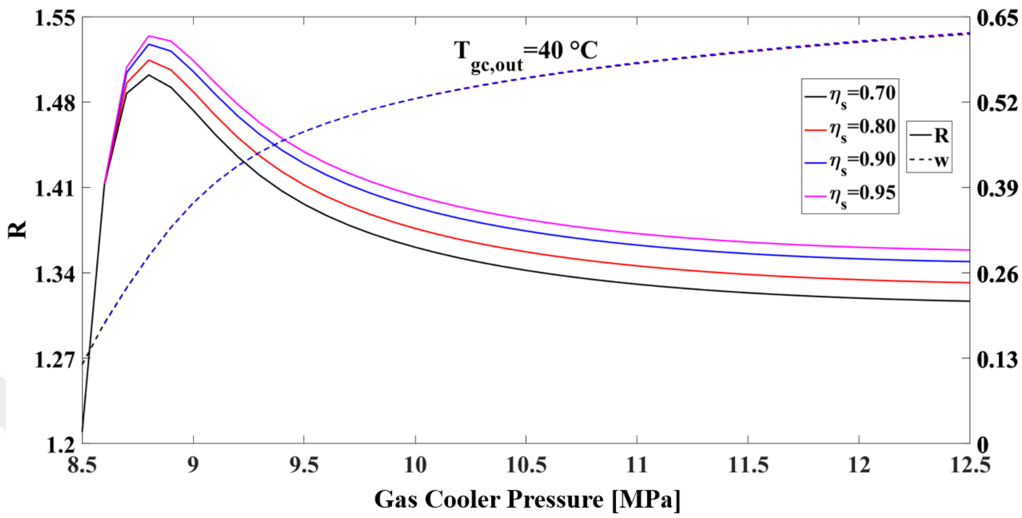


(a)

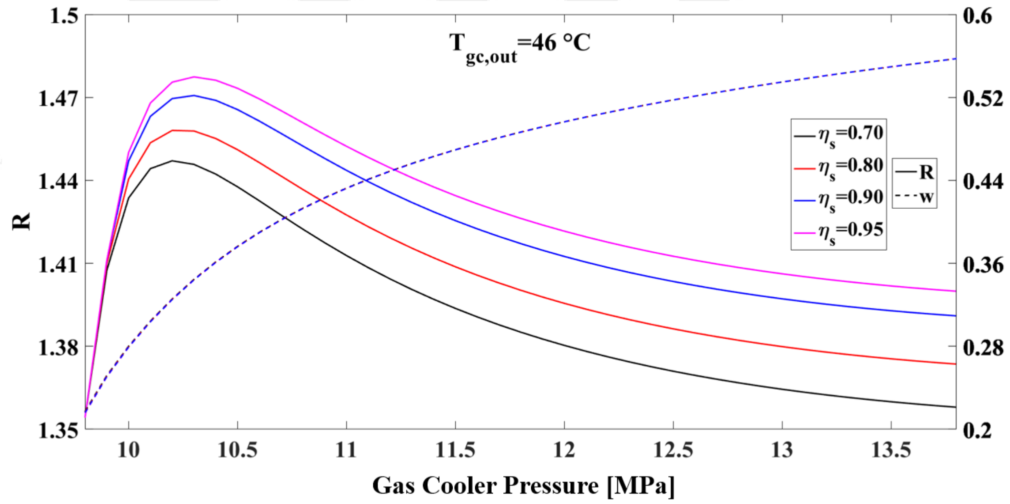


(b)

Figure 4.36 Effect of the suction nozzle efficiency on the performance improvement ratio and entrainment ratio for the gas cooler outlet temperatures of (a) 40 ºC and (b) 46 ºC

The variations in the performance improvement curve around the pressure point yielding the maximum performance are much more for 40 ºC gas cooler outlet temperature. The rate of change in the performance curve around the gas cooler pressure point of the maximum performance improvement decreases when the suction nozzle efficiency increases. The opposite reaction is observed in the same rate of change when motive nozzle efficiency is increased.

When the effects of motive and suction nozzles are compared, the variations of the performance improvement profiles around the pressure point resulting in the maximum performance change more with respect to the suction nozzle efficiency. Figure 4.37 declares the effects of the mixing section efficiency on the performance improvement ratio and entrainment ratio for the same gas cooler outlet temperatures. Similar to performance of motive nozzle efficiency, the variations around the pressure point resulting in the maximum performance point increases when the mixing section efficiency increases. The effect of the diffuser efficiency is shown in Figure 4.38 for the same gas cooler outlet temperatures. Similar performance curves are presented with reference to diffuser efficiency as well.

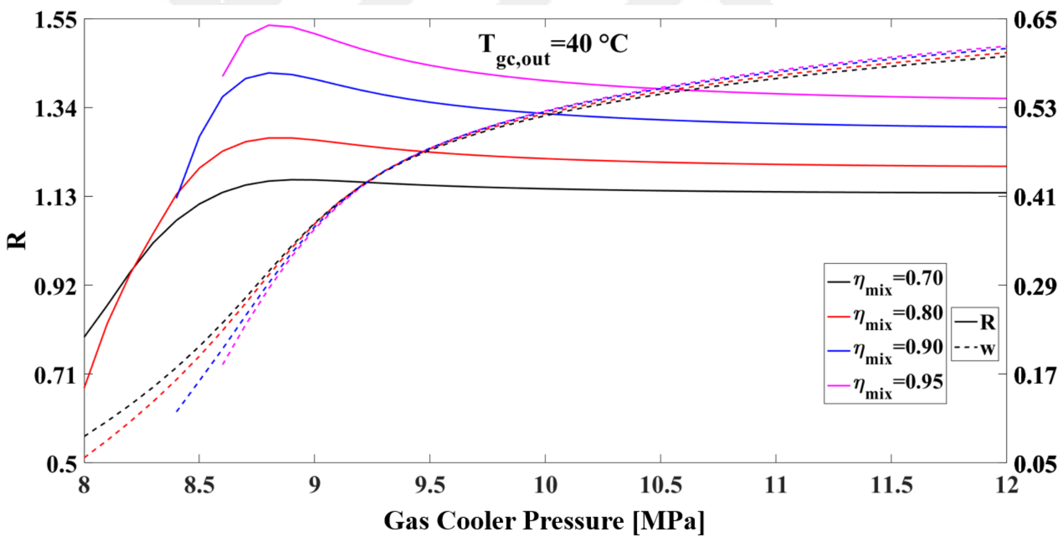

(a)

Figure 4.37 Effect of the mixing section efficiency on the performance improvement ratio and entrainment ratio for the gas cooler outlet temperatures of (a) 40 ºC and (b) 46 ºC

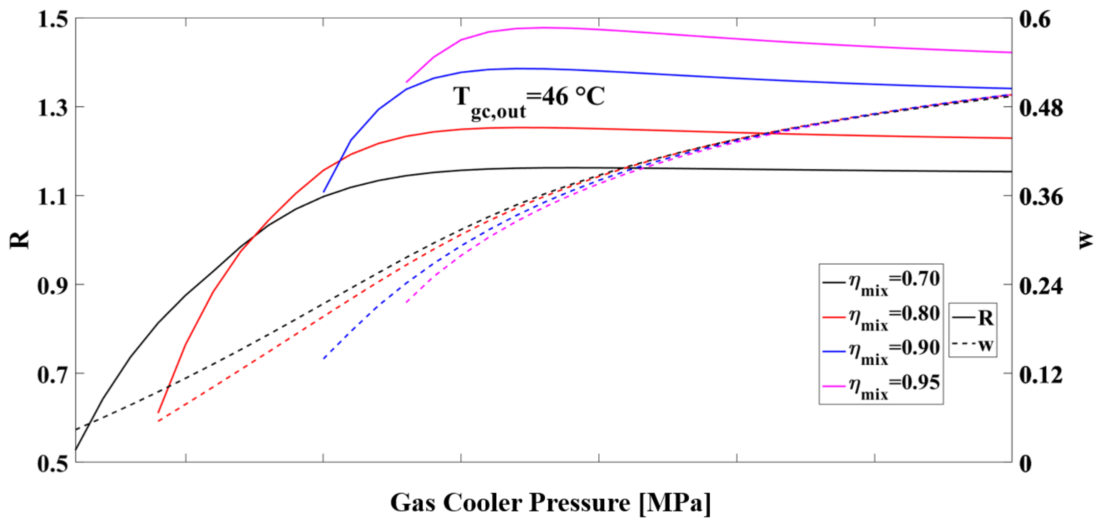


**(b)**

Figure 4.37 continues

The common point obtained for all section efficiencies is that the pressure point yielding the maximum performance is not dependent on the section efficiencies. It just depends on the region experiencing high expansion losses, hence the operating conditions. However, since the entrainment ratio is very low at that point, this point is not meaningful. Moreover, these kinds of performance curves are necessary to display the effective operational regions of the transcritical EERC.

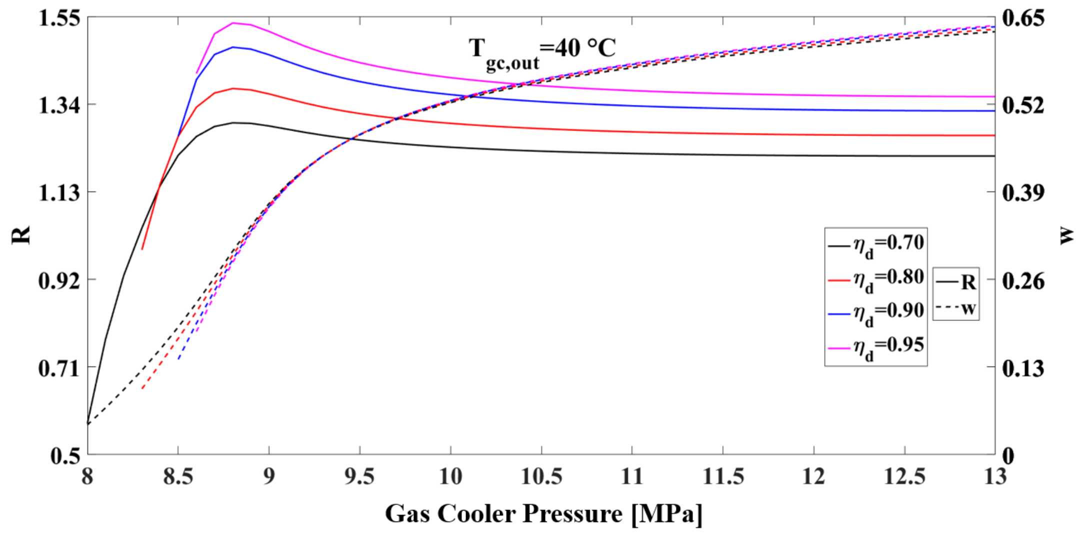


**(a)**

Figure 4.38 Effect of the diffuser efficiency on the performance improvement ratio and entrainment ratio for the gas cooler outlet temperatures of (a) 40 °C and (b) 46 °C

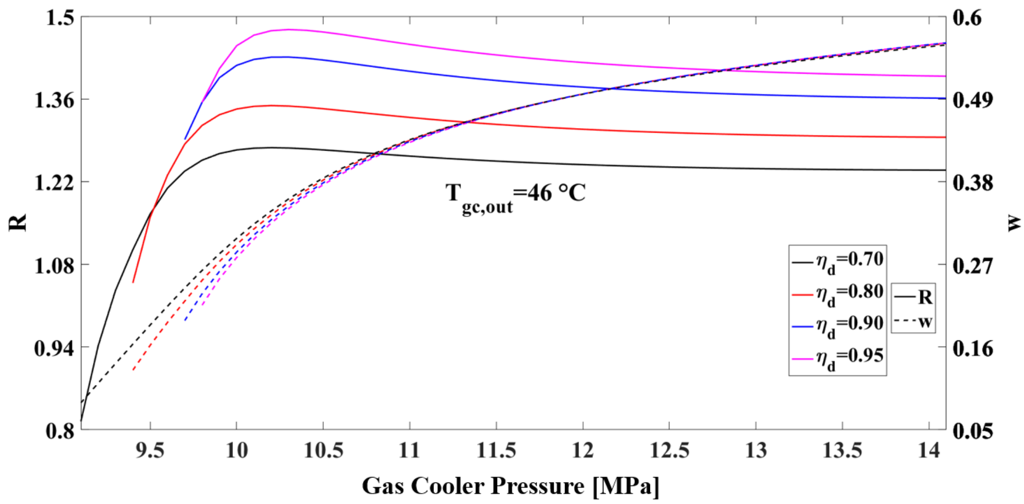


(b)

Figure 4.38 continues

It is seen that performance improvement lines at the optimum suction nozzle pressure drops have different profiles with reference to ejector component efficiencies. In Figure 4.39, the effect of all ejector components are compared. The efficiency value of 0.8 is chosen for each component. When the value of a component efficiency is set at 0.8, the others are selected as 0.95 for the investigated case under question. Hence performance improvement ratio and entrainment ratio is presented in this order for two gas cooler outlet temperatures.

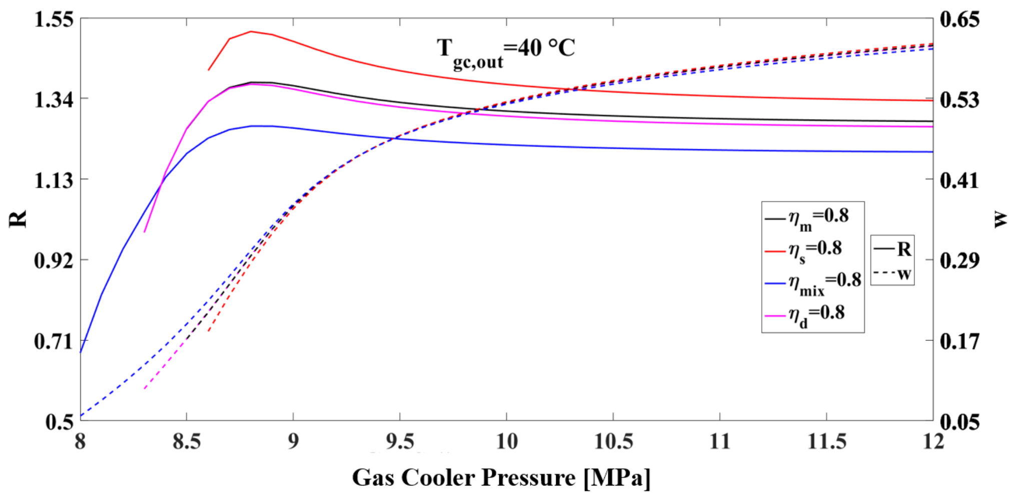


(a)

Figure 4.39 Comparison of all ejector component efficiencies in terms of the performance improvement ratio and entrainment ratio for the gas cooler outlet temperatures of (a) 40 ºC and (b) 46 ºC

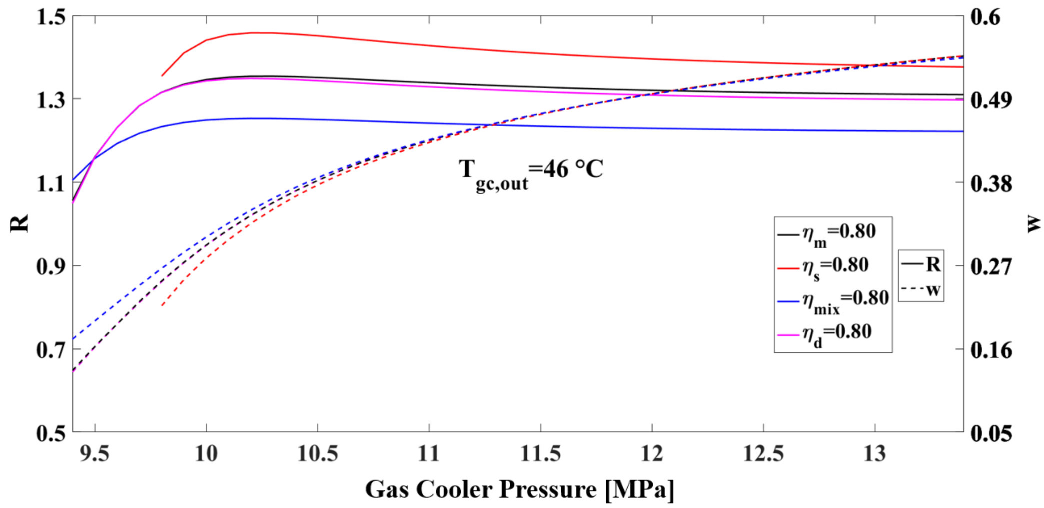


**(b)**

Figure 4.39 continues

Therefore, the most important component efficiency could be defined for the transcritical EERC. The importance order of the component efficiencies is the same as the outcomes of Atmaca et al. (2019a) focusing on the subcritical EERC. The most effective parameter on the performance is the mixing section for the transcritical EERC. Diffuser and the motive nozzle have similar effects on the performance. On the other hand, the diffuser has the second rank for the performance. Compatible with the primary outcomes of Atmaca et al. (2019a), the suction nozzle efficiency is the least effective parameter.

Figure 4.40 compares a moderate efficiency value for all component efficiencies at two different gas cooler outlet temperatures. For this comparison, the efficiency value of 0.8 is selected for each component efficiency. The rest is set at 0.95 under that investigation. Figure 4.40 (a) evaluates the effects of the motive nozzle efficiency of 0.8 at two gas cooler outlet temperatures on the performance improvement ratio and entrainment ratio. Figure 4.40 (b), (c), and (d) is presented in the same way for suction nozzle, mixing section, and diffuser, respectively.

For each component efficiency, the maximum performance improvement is observed at 40 ºC gas cooler outlet temperature. However, these maximum points are not useful since the entrainment ratio is very low at those regions as stated previously.

When the points having higher entrainment ratios are investigated, it is seen that the higher performance improvement ratio is attained at 46 ºC gas cooler outlet temperature. It is reasonable since the expansion losses are higher at 46 ºC gas cooler outlet temperature when compared to 40 ºC gas cooler outlet temperature. Hence, performance improvement ratio is expected to be higher at 46 ºC. The entrainment ratio is higher for 40 ºC for all component efficiencies.

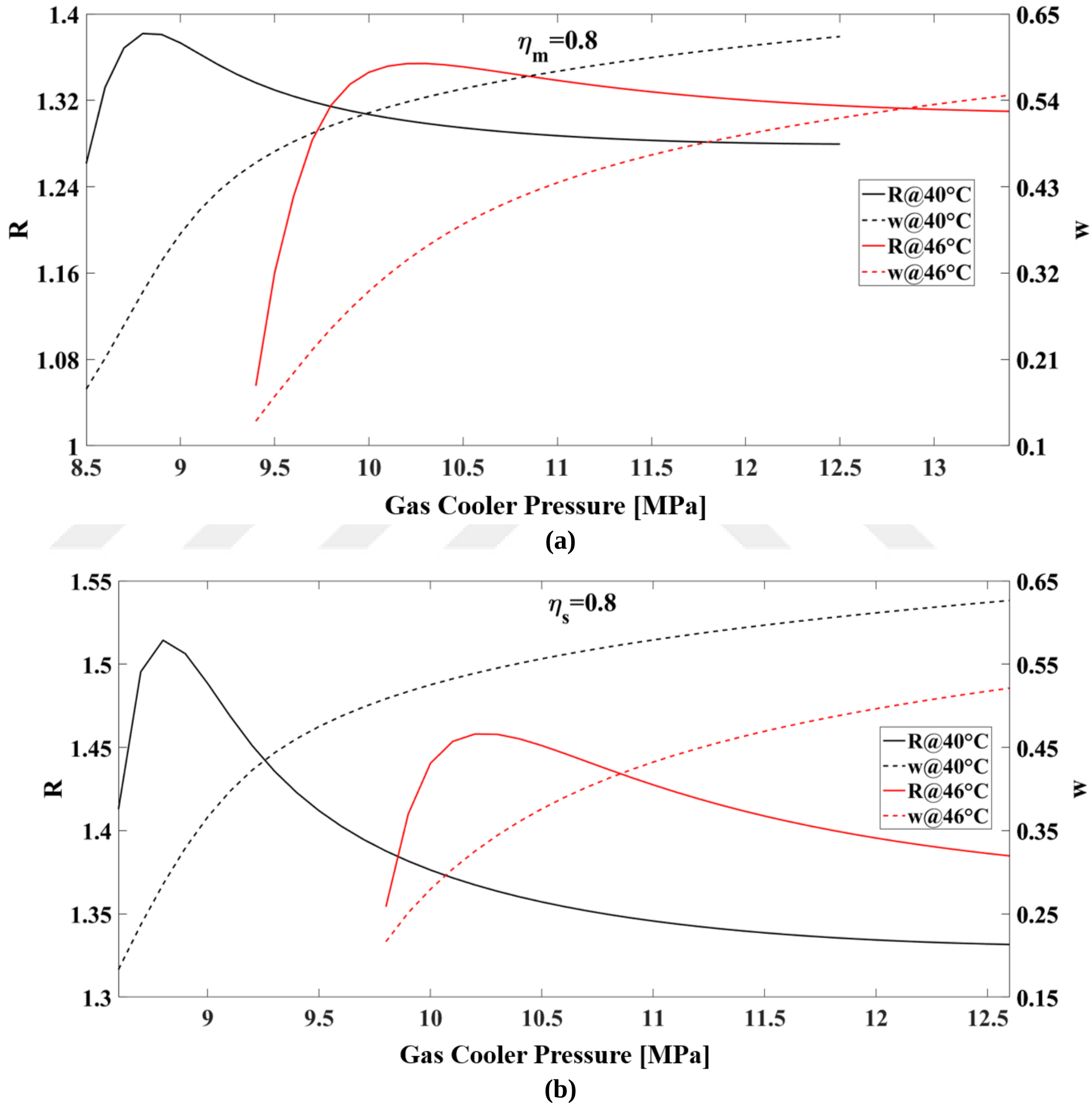


Figure 4.40 Comparing the effect of the gas cooler outlet temperature on the performance improvement ratio and entrainment ratio for (a) motive nozzle, (b) suction nozzle, (c) mixing section, and (d) diffuser efficiencies

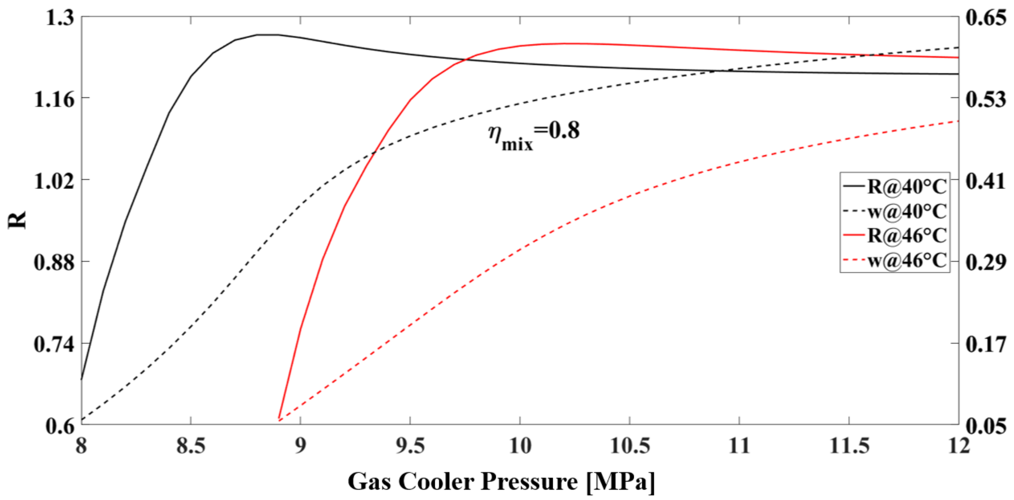


(c)

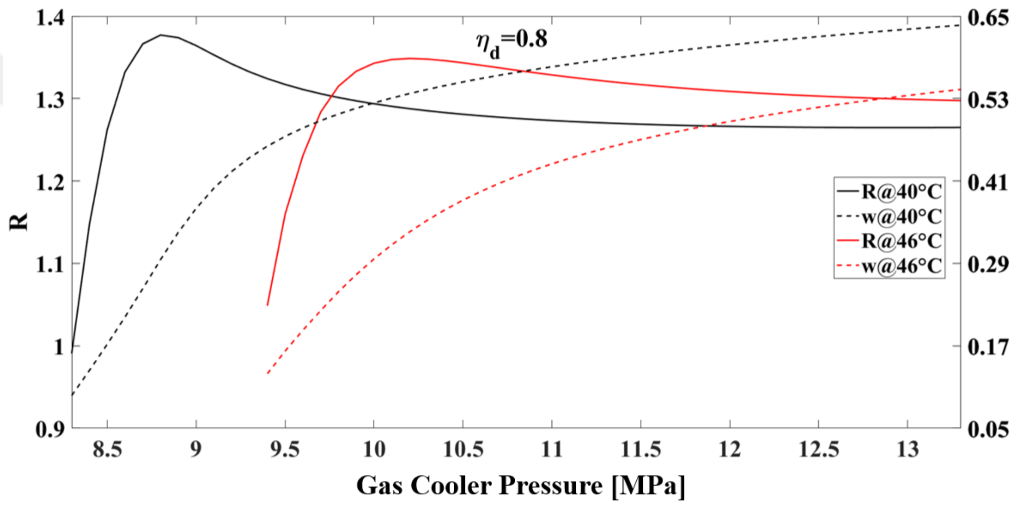


(d)

Figure 4.40 continues

The maximum performance values for both of the gas cooler outlet temperatures are very close to each other for the mixing section efficiency. However, the same difference between the maximum performance points of two different temperatures has the highest value for the suction nozzle efficiency. The same comment could be made at the regions where the performance improvement ratios are stabilized. Since the entrainment ratio increases at those regions, the performance improvement ratios corresponding to those regions are useful to be declared. As a result, for the regions where the performance improvement ratio is stabilized, the difference between the performance improvement ratios according to gas cooler outlet temperatures is highest for the suction nozzle efficiency and lowest for the mixing section efficiency. Motive nozzle and the diffuser displayed similar performance improvements while passing from 40 ºC gas cooler outlet temperature to 46 ºC. Since the mixing section efficiency is the most important parameter, it affects the performance improvement more than the operating conditions.

It is well known that the ejector operates better at higher gas cooler outlet temperatures due to the higher expansion losses. Hence, it is an advantage to use the ejector at higher gas cooler outlet temperatures. However, this advantage become invisible if the ejector is not designed properly. In other words, suction nozzle efficiency is the least effective parameter, therefore the effect of the operating conditions could be observed apparently. For the efficiency value of 0.8, the motive nozzle and diffuser experiences 3% performance improvement passing from gas cooler outlet temperature of 40 ºC to 46 ºC. For the same efficiency value and gas cooler outlet temperatures, the difference is approximately 4% and 2% for the suction nozzle and the mixing section, respectively. The most important conclusion to be derived is the importance of the ejector designs. If the ejector is not designed appropriately, the ejector would not operate efficiently even in the most appropriate operating conditions. This conclusion highlights the importance of a well-designed ejector to achieve performance improvement over the base cycle. The low pressure refrigerants are more sensitive to the ejector design when compared to the high-pressure working fluids. As a result, the importance of the ejector design is highlighted twice when the low pressure refrigerants are the issue.

The effects of the operating conditions on the ejector component efficiencies are discussed in detail making use of the thermodynamic modelling approach. The results are clarified the achievable performance improvement limits according to both ejector component efficiencies and operating conditions. However, the entrainment ratio stays nearly the same although the component efficiencies are varied. Actually, it is known that the entrained flow as well is dependent upon the ejector component designs, in other words, ejector component efficiencies. It is the deficiency in the thermodynamic modelling approach. Despite of the fact that they provide with typical performance curves, the results are limited. Comprehensive CFD analyses are required to evaluate the ejector performance elaborately.

### *4.7.2 Analyses of the Liquid-Vapor Separator Efficiency for R134a, R1234yf, and R1234ze(E) according to Operating Conditions*

To finalize this chapter, lastly the effect of the liquid-vapor separator efficiency according to operating conditions would be discussed. In the previous section, the importance of the ejector design has been displayed with reference to the performance analyses of the transcritical $CO_2$ EERC at two different gas cooler outlet temperatures. In this section, the effect of an external component efficiency, i.e. liquid-vapor separator is discussed according to operating conditions.

Performance improvement ratio is presented based on the optimum suction nozzle pressure drop. The analyses presented in this section are evaluated as the ongoing part of the previous research of Atmaca et al. (2020a). The striking results of Atmaca, Erek, & Ekren (2019b) are presented in this section. Atmaca et al. (2020a) analyzed the effects of the liquid and vapor separation efficiencies on the overall performance improvement for 5 ºC evaporation temperature and 40 ºC condensation temperature for R1234yf and R1234ze(E) as one of their outcomes.

All investigations of this section are presented for R134a, R1234yf, and R1234ze(E). Hence, the following figure, Figure 4.41, is partially from Atmaca et al. (2020a), but the performance curves of R134a is added with respect to research target of this section. These kinds of typical curves are presented with respect to the parametric operating conditions in Table 4.13. The main objective is investigating the influence of the vapor and liquid separation efficiencies with reference to various evaporation and condensation temperatures. Moreover, when both of the separation efficiencies are selected moderately low and high, i.e., 0.8 and 0.9, the variations of the performance improvement ratios are displayed.

Table 4.13 Operating conditions for the parametric analyses

| Parameters | Values |
|---|---|
| Evaporation temperature range ($T_e$) | -10-10 ˚C |
| Evaporator outlet superheat temperature difference ($\Delta T_{sh}$) | 5 K |
| Condensation temperature range ($T_c$) | 35-65 ˚C |
| Condenser outlet subcooling temperature difference ($\Delta T_{sc}$) | 3 K |
| Compressor efficiency ($\eta_{comp}$) | 0.75 |
| Motive nozzle efficiency ($\eta_m$) | 0.9 |
| Suction nozzle efficiency ($\eta_s$) | 0.9 |
| Mixing section efficiency ($\eta_{mix}$) | 0.90 |
| Diffuser efficiency ($\eta_d$) | 0.8 |
| Vapor separation efficiency range ($\eta_{vap}$) | 0.70-1.0 |
| Liquid separation efficiency range ($\eta_{liq}$) | 0.70-1.0 |

Solid lines in Figure 4.41 declares the cases at which liquid separation efficiency is equal to unity and the vapor separation efficiency is varied; whereas the dashed lines show that vapor separation efficiency is 100% and liquid separation efficiency is varied. The same designation is applied to Figure 4.42 and Figure 4.43 presenting the effects of the evaporation and condensation temperatures, respectively.

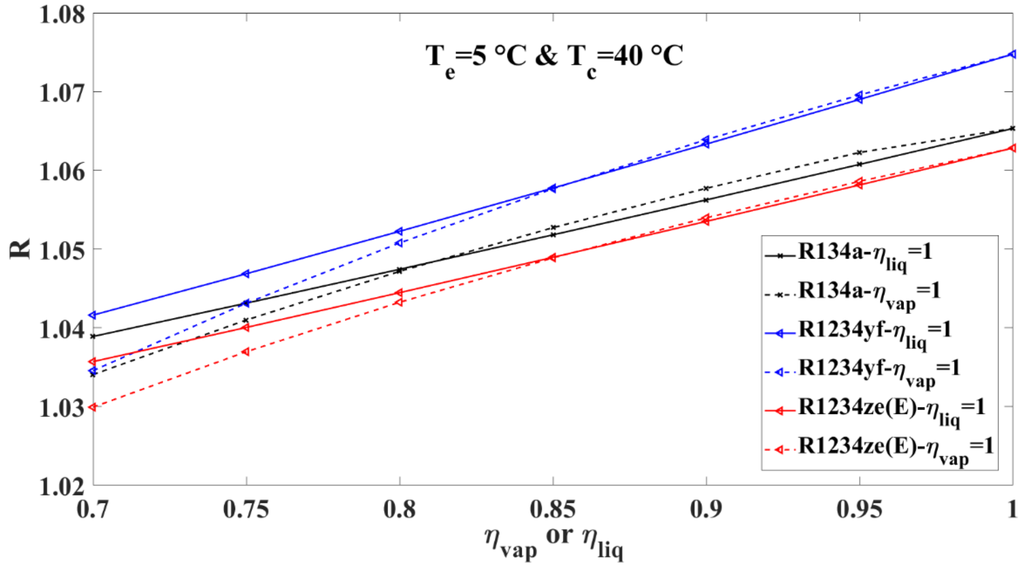


Figure 4.41 The effects of the vapor and liquid separation efficiency for R134a, R1234yf, and R1234ze(E) on the overall performance improvement at evaporation temperature of 5 ºC and condensation temperature of 40 ºC

It is seen that after the efficiency point of 0.85, the changes in the vapor and liquid separation efficiencies affect the performance improvement ratio similarly for R1234yf and R1234ze(E). The same point at which the effects of the vapor and liquid separation efficiencies become equal is after the efficiency value of 0.80 for R134a. Therefore, it is concluded that the vapor and liquid separation efficiency affects each refrigerant in a different way. Before this critical point, liquid separation efficiency affects more to the overall performance improvement. Figure 4.42 displays the effects of the liquid and vapor separation efficiencies at three different evaporator temperature for R134a, R1234yf, and R1234ze(E). It is seen that when evaporation temperature decreases, the efficiency point where the vapor and liquid separation efficiencies affects the performance similarly decreases.

The efficiency point after which the separation efficiencies affect the performance in the same way corresponds a lower value for R134a for all investigated evaporation temperatures when compared to other two refrigerants. The point under discussion are very close to each other for R1234yf and R1234ze(E).

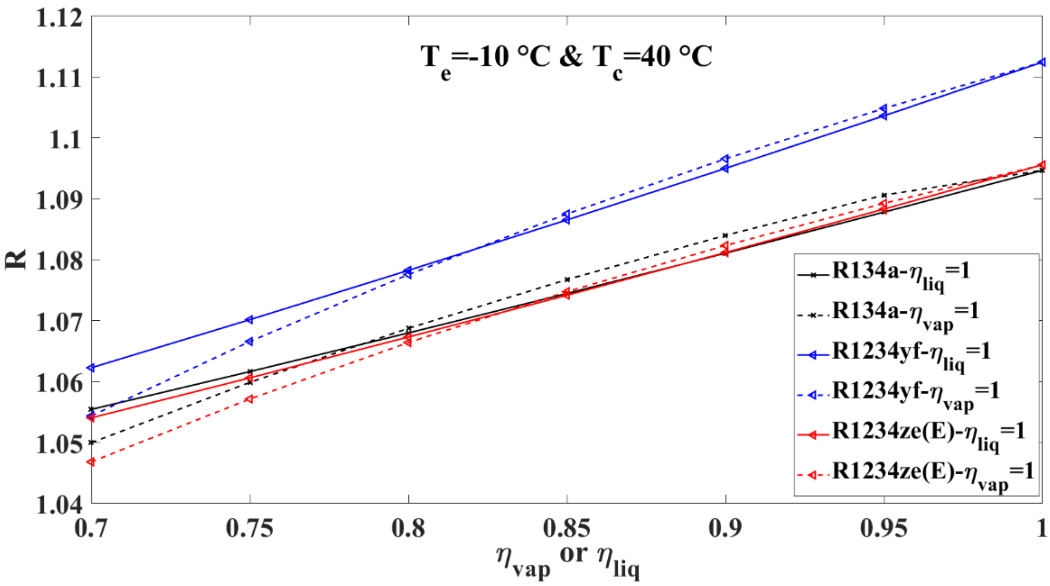

(a)

Figure 4.42 The effects of the vapor and liquid separation efficiencies on the performance improvement ratio for operating conditions of (a) $T_e$=-10 °C and $T_c$= 40 °C, (b) $T_e$=0 °C and $T_c$= 40 °C, and (c) $T_e$=10 °C and $T_c$= 40 °C for R134a, R1234yf, R1234ze(E)

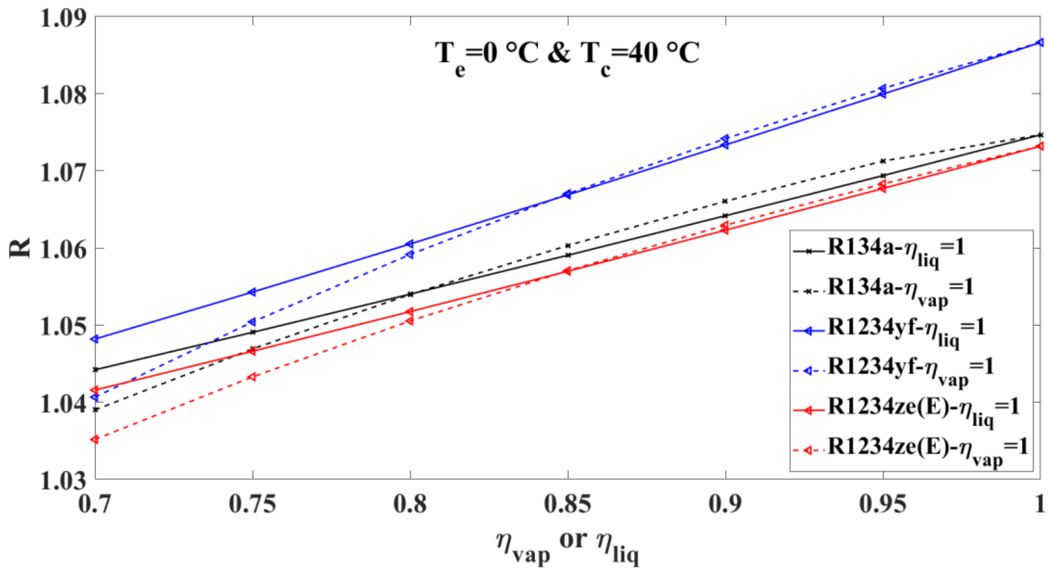


(b)

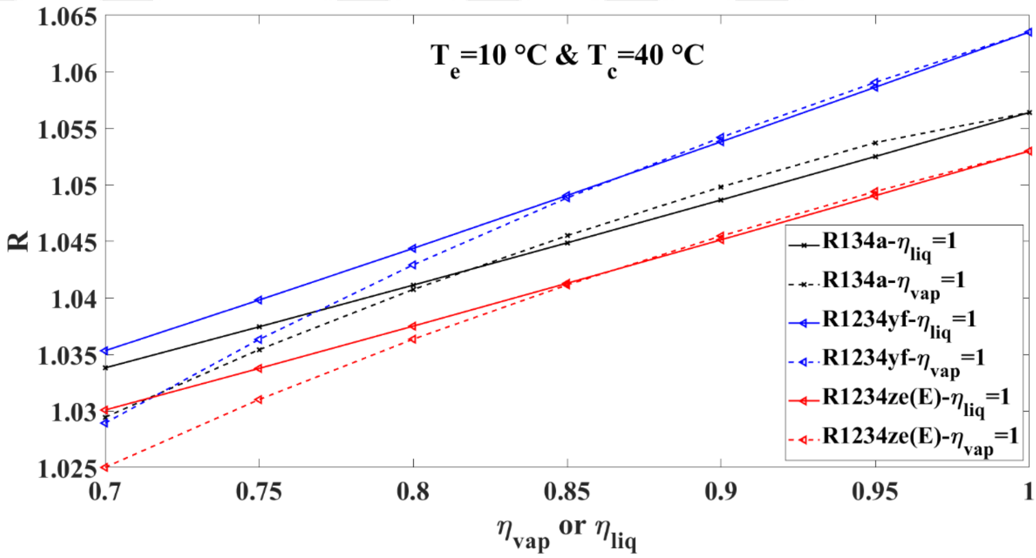


(c)

Figure 4.42 continues

When the effects of the separation efficiencies are declared at the optimum suction nozzle pressure, it is seen that the performance improvement coefficient stays over unity for the investigated ranges. In other words, ejector functions appropriately providing performance improvement over the base cycle under the optimum operating conditions. For example, Lawrence (2012) evaluated the performance improvement for the suction nozzle pressure corresponding to saturation pressure of the temperature 5K below the evaporation temperature. According to results of Lawrence (2012), the performance improvement ratio resulted in values lower than unity for some of the analyses. It means that the ejector could not be operated properly. The main conclusion to be derived from this finding is that if the operating conditions are different from the optimum conditions, the ejector may fail to perform over the conventional cycle.

The primary findings of Lawrence (2012) as well are beneficial since the investigations on the performance improvement of the ejector at the conditions different than the optimum conditions are necessary. Only one optimum design could be proposed based on one operating condition. Therefore, it is not possible to change the design with reference to all operating conditions. As a result, the performance improvement analyses according to conditions different than the optimum ones lead more comprehensive performance evaluations. Totally, it could be stated that not only ejector design but the system components as well is needed to be selected appropriately for better performance improvements.

R1234yf reacts more to the changes in the separation efficiencies for the investigated operation ranges when compared to other two refrigerants. Moreover, when the evaporation temperature decreases, the reactions to the separation efficiencies increases for all of the refrigerants. For example, the percentage performance improvement increases approximately 5% at the evaporation temperature of -10 ºC as shown in Figure 4.42 (a) while it increases around 2.8% at the evaporation temperature of 10 ºC as given in Figure 4.42 (c) with reference to variations in vapor separation efficiency. This is because of the higher expansion losses at the lower evaporator temperatures. Since ejector is used at those operation ranges more effectively, the separation efficiencies have more influences at those operation ranges.

Figure 4.43 investigates the effects of the vapor and liquid separation efficiencies at three different condensation temperatures. The influence of the vapor and liquid separation efficiencies increases when the condensation temperature increases due to the higher expansion losses in those regions. Similar to previous investigations with reference to evaporation temperature, R1234yf is affected mostly within the investigated ranges when compared to R134a and R1234ze(E). The point at which the liquid and vapor separation efficiencies affect the overall performance improvement in the same way decreases when condensation temperature is increased.

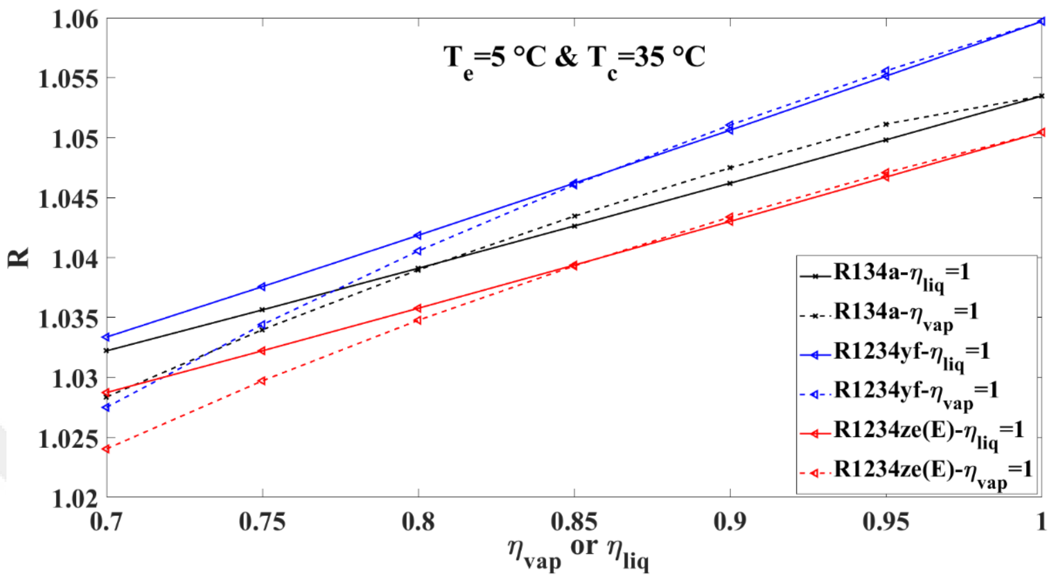


(a)

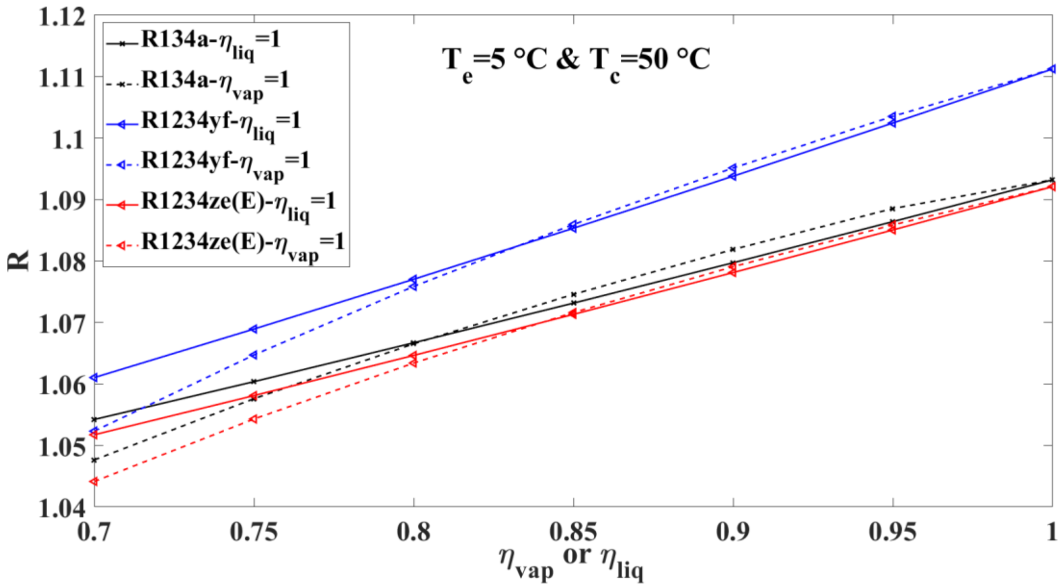


(b)

Figure 4.43 The effects of the vapor and liquid separation efficiencies on the performance improvement ratio for operating conditions of (a) $T_e$=5 °C and $T_c$= 35 °C, (b) $T_e$=5 °C and $T_c$= 50 °C, and (c) $T_e$=5 °C and $T_c$= 60 °C for R134a, R1234yf, R1234ze(E)

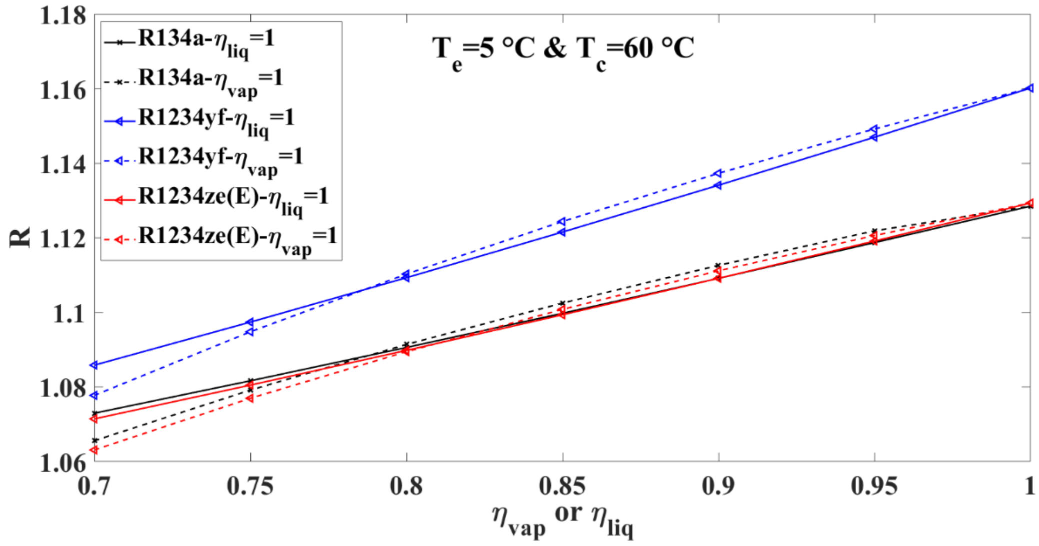


**(c)**

Figure 4.43 continues

Figure 4.44 displays the performance improvement curves with respect to the various evaporation and condensation temperatures when both of the vapor and liquid separation efficiencies are applied at the same time. The vapor and liquid separation efficiencies are set at 0.8 and 0.9. The efficiency of 0.9 results in higher performance improvement as expected. However, the focusing point is that the performance improvement changes more with respect to the variations of the operating temperatures. The performance improvement increases when condensation temperature is increased and evaporator temperature is decreased. However, this increment with reference to variations in the operating temperatures is less when an inappropriate separator is implemented into the system. In other words, if the vapor and liquid separation efficiencies are low, even in the operating regions where ejector use provides more performance improvement, ejector may fail or very low performance improvement may be obtained.

For both of the efficiency cases, R1234yf reacts more to the changes in the operating conditions. Moreover, reactions to the investigated condensation temperatures are higher for all of the refrigerants. Percentage performance improvement difference is nearly 4% for R1234yf according to variations in the condensation temperature for the efficiency case of 0.8; whereas it is approximately

8% for the same refrigerant and same condensation temperature range for the efficiency case of 0.9.

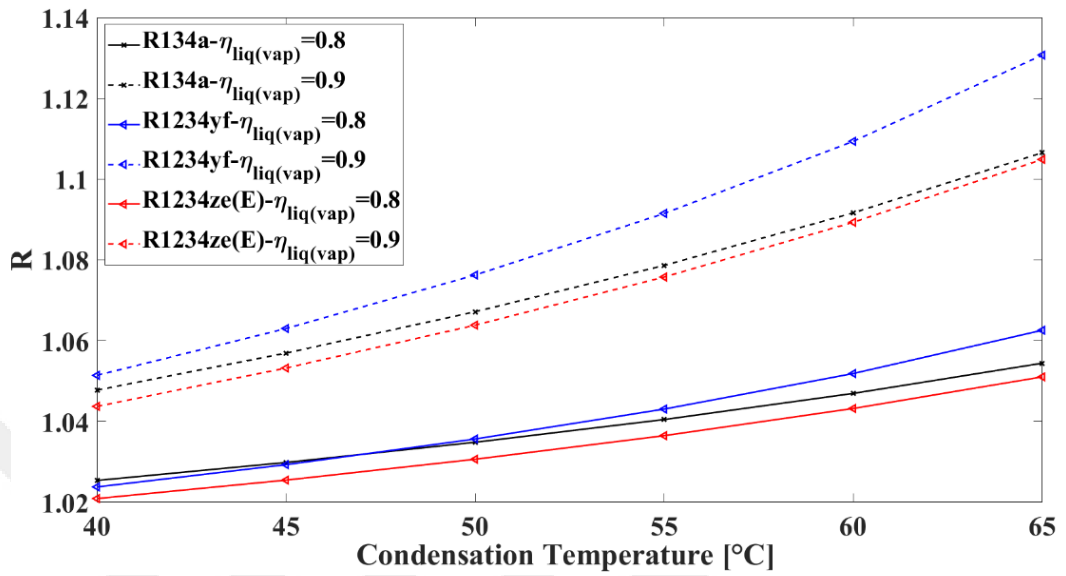


(a)

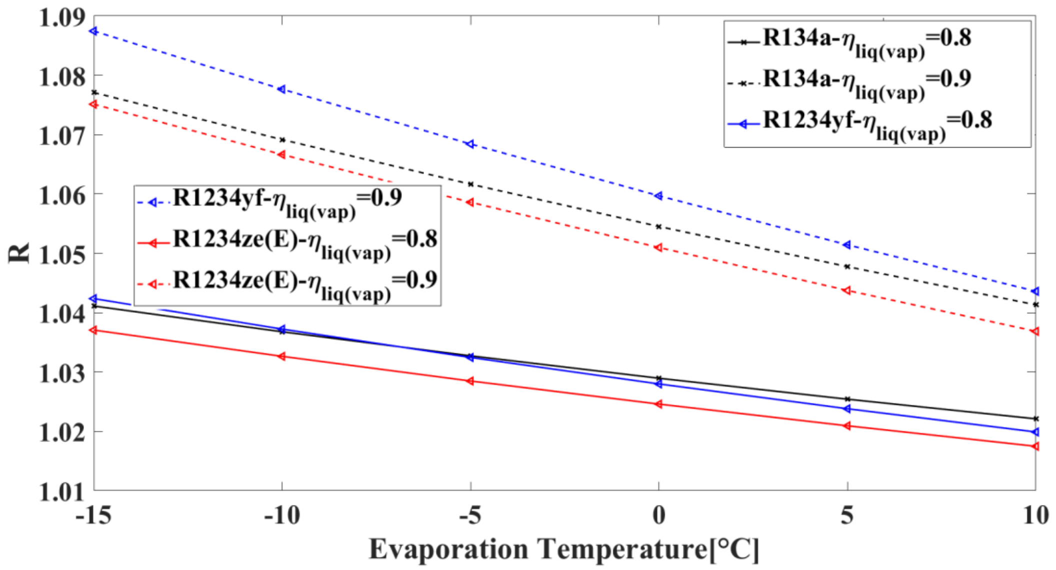


(b)

Figure 4.44 Comparison of the performance improvement when liquid and vapor separation efficiencies, i.e. 0.8 and 0.9, are simultaneously applied at various (a) condensation and (b) evaporation temperatures

To sum up, in the previous section, the importance of the high-efficiency ejector design is emphasized with the help of the thermodynamic analyses of the transcritical $CO_2$ EERC. Although it is an auxiliary component of the EERC, the separator efficiency is a critical aspect with reference to overall performance improvement of the cycle. If the separation efficiencies are low in the cycle, the performance improvement of the cycle could not be improved even in the operating conditions where ejector performs efficiently. Hence, the last conclusion from the thermodynamic modelling approach is the importance of the both ejector and separator designs for higher performance improvement over the base cycle.

# CHAPTER FIVE
# DESIGN OF THE TWO-PHASE EJECTORS BASED ON THE THERMODYNAMIC MODELLING APPROACH

In this section, main geometrical parameters of an ejector, i.e. diameters of the motive nozzle throat, motive nozzle outlet, suction nozzle outlet, and constant area mixing section are calculated at various operation conditions for the preliminary design. The thermodynamic model for the preliminary design of the ejector is established with reference to constant area mixing assumption. R1234yf, R1234ze(E), and R134a are used in the analyses. When compared to the previous literature findings, the outcomes of this section aim to compare the dimensions of a two-phase ejector to be used in an experimental system having a specified cooling capacity for these three refrigerants. Therefore, this section aims to estimate the critical design parameters of the ejector for further experimental studies aiming to achieve 5 kW cooling capacity. The primary results of Atmaca, Erek, & Ekren (2019c) is presented in this section.

Thermodynamic analyses are previously made on the EERC for environmentally-friendly refrigerant alternatives at various operating conditions in the previous chapter. Benefiting from the outcomes of the thermodynamic analyses, optimum values of the entrainment ratio, suction nozzle pressure, and enthalpy difference through the evaporator at various operating conditions under constant area mixing assumption are used to calculate the specified diameters of the two-phase ejector for a 5 kW experimental system. Modelling equations for the critical geometrical parameters of the two-phase ejector are solved in MATLAB®. Thermodynamic properties of the refrigerants are calculated by REFPROP version 9.1 (Lemmon et al., 2013).

## 5.1 Ejector Models Based on the Mixing Assumptions

In this section, schematics are provided considering the differences of the mixing assumptions in terms of geometrical aspects to be calculated. For constant area mixing, the geometry provided by Banasiak & Hafner (2011) is used as the template. With respect to thermodynamic modelling approach, the motive nozzle outlet is directly located at the inlet of the constant area mixing section under CAM ejector theory. However, in the reference template, there is a premixing chamber where the motive nozzle is located inside.

It is claimed in the literature that the mixing process and the momentum transfer between the primary and secondary fluids does not take place directly when they meet (Sherif et al., 2000). There is a core region for the motive flow while it is expanding. The geometry of this pre-mixing section is actually a part of the mixing section and means a lot to the ejector performance. In other words, geometrical aspects concerned with this section is to be investigated with the help of the CFD analyses (Metin et al., 2019; Palacz et al., 2017). However, according to the geometrical template of this section, the conceptual definition of Sumeru et al. (2012) as shown in Figure 5.1 (a) and the proposed template of Banasiak & Hafner (2011) as given in Figure 5.1 (b) are the same. Actually, there is a tapered inlet at the inlet of the mixing section in the inherent definition of the ejector (Elbel & Hrnjak, 2008a). The main outputs of this section are given for both of the configurations as given in Figure 5.1 and they are calculated in the same way under the modelling assumptions of this section.

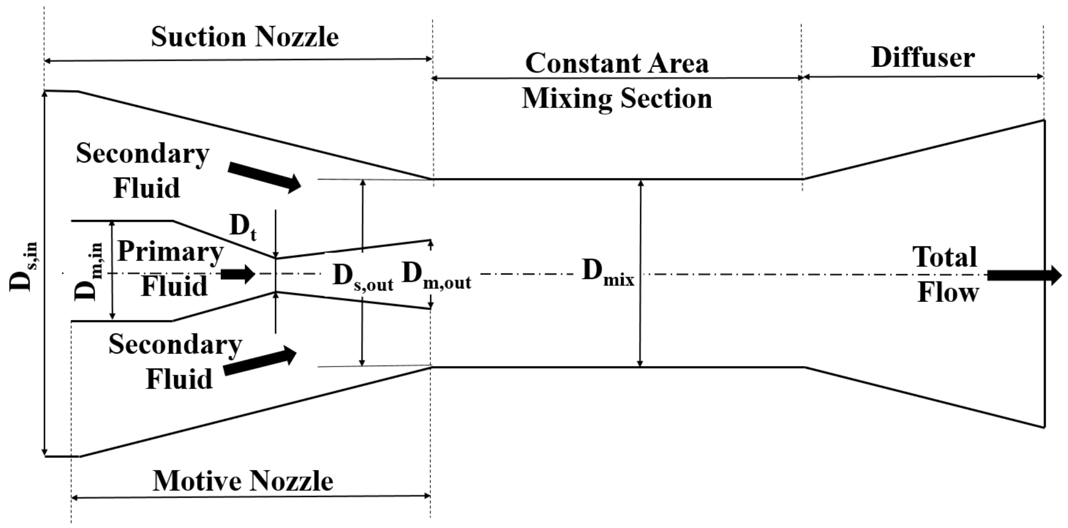


**(a)**

Figure 5.1 Design parameters of a CAM ejector with (a) motive nozzle outlet coinciding with the constant area section inlet and (b) motive nozzle outlet located within the suction nozzle creating a pre-mixing chamber

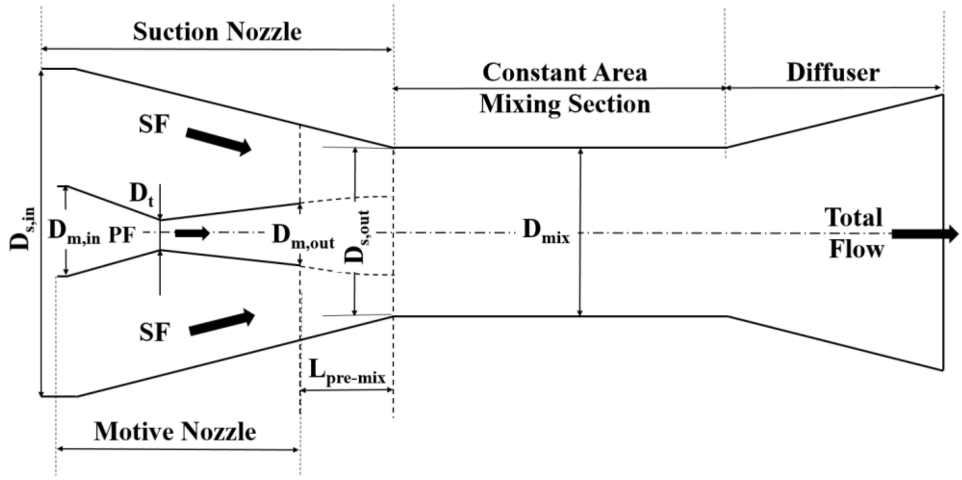


**(b)**

Figure 5.1 continues

Since this section focuses on the CAM ejector only, there is no need to define CPM geometry template. On the other hand, it is given in order to express the future research targets better. Comparative design proposals are made in terms of the mixing assumptions in the future studies. Hence constant pressure mixing ejector template is defined with reference to Sherif et al. (2000) as given in Figure 5.2. Meanwhile, the reason for the constant area mixing selection is not the superior performance improvement of this approach to the constant pressure mixing assumption.

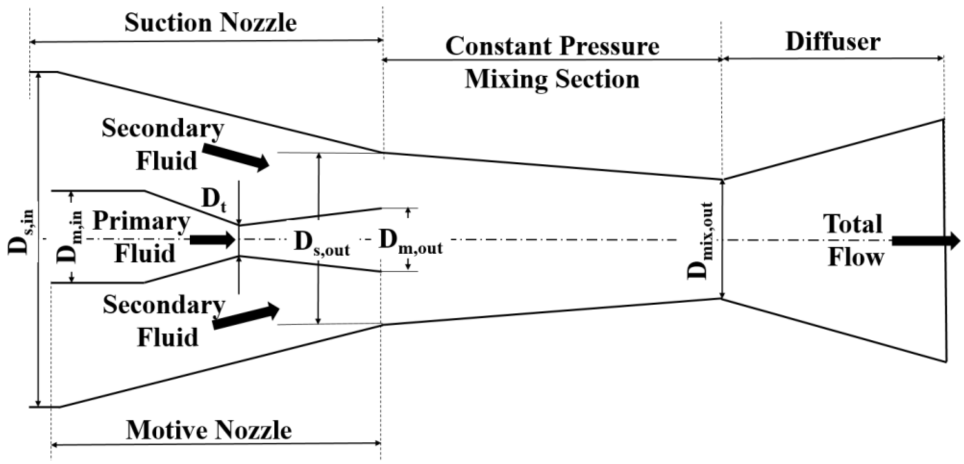


Figure 5.2 Design parameters of a CPM ejector with mixing section of variable cross-sectional area enabling constant pressure mixing

According to the results of the thermodynamic analyses, CAM theory yields just a slight increase in the optimum performance when compared to CPM assumption and the main conclusion is that they are just modelling assumptions. Hence, both of them could be used in the thermodynamic models. The motivating issue to select the CAM approach in this study is that it is commonly encountered in the EERC applications. As stated by Elbel & Hrnjak (2008a) as well, the two-phase ejectors having a constant cross-sectional mixing chamber with a tapered inlet constituting a pre-mixing chamber are used commonly in the experimental works and CFD analyses (Metin et al., 2019; Palacz et al., 2017; Disawas & Wongwises, 2004; Chaiwongsa & Wongwises, 2008).

## 5.2 Thermodynamic Modelling

The model to be presented in this section is established with reference to Hassanain et al. (2015) for a refrigeration system having 5 kW cooling capacity. However, the model presented in this section does not include the total mass flow rate among the inputs when compared to the study of Hassanain et al. (2015). Hence, the modelling approaches presented in this section and Hassanain et al. (2015) slightly differ from each other.

Hassanain et al. (2015) calculated the mass flux at the motive nozzle throat using Henry and Fauske model (Henry & Fauske, 1971) since it considered the metastable effects in the motive nozzle caused by the delayed flashing of the primary fluid flow. One of their conclusions was that the motive nozzle throat diameter was constant when section efficiencies were varied. However, at least the throat diameter should react to the changes in the motive nozzle efficiency. Hence, especially for further research proposed to be accomplished after this investigation, all cross-sectional areas are calculated according to the homogeneous equilibrium model (Sherif et al., 2000) to analyze the effect of all section efficiencies on the design comprehensively.

The primary and secondary fluid flows have the same pressures which is called the suction nozzle pressure at the inlet of the mixing section. Irreversibilities of the ejector sections and the compressor are implemented into the thermodynamic model through medium of constant efficiency values. Ejector mixing section and the liquid-vapor separator is assumed to have efficiency equal to unity. All equations are obtained based on the HEM for the two-phase flow. Velocity of the refrigerants are nearly zero at the inlet and outlets of the ejector. The previously stated assumptions in the previous thermodynamic models are used for this design model as well.

The calculation steps or modelling equations are divided into two branches. The first group equations are for analyzing the refrigerants at various operation conditions and obtaining global performance outputs. Inputs of such a thermodynamic model includes the inlet temperature and pressures of the primary and secondary fluid flows (evaporator temperature, condenser temperature, evaporator outlet superheat temperature difference, and condenser outlet subcooling temperature difference), ejector section efficiencies, and compressor efficiency. The outputs necessary to obtain from this thermodynamic model to carry on with the design calculations which is the second design step of the overall model are the entrainment ratio, suction nozzle pressure, and enthalpy difference between the evaporator inlet and outlet at the optimum conditions yielding the highest performance.

Therefore, the second design step uses the above-mentioned three calculated parameters in addition to proposed refrigeration or cooling capacity which is defined as 5 kW in this study. Furthermore, the inlet diameters of the motive and suction nozzles ($D_{m,in}$ and $D_{s,in}$) are necessary. They are chosen in a way that the selected values satisfy the nearly zero entrance velocity condition of the ejector according to the investigated operating conditions. The outputs of the second step are mass flow rates of the primary and secondary fluid flows, the throat and exit diameters of the motive nozzle, suction nozzle outlet diameter which is equal to the constant area mixing section diameter according to the presented geometrical ejector templates in Figure 5.1 (a) and (b). Thermodynamic modelling equations are the same as the given equations in the previous chapter. Only design equations are described accordingly.

### *5.2.1 Equations for the Ejector Design*

Primary dimension calculation equations are established in main with reference to Hassanain et al. (2015). There are some differences between the equations presented in this section and the modelling equations presented in that paper (Hassanain et al., 2015). These kinds of differences contribute to the future research targets as well. First of all, mass flow rate of the secondary flow is determined in accordance with the defined cooling capacity and the enthalpy difference of the evaporator for the optimum suction nozzle pressure at the investigated operation temperature. Subsequently, the primary fluid mass flow rate is calculated from the optimum entrainment ratio for that operation condition and the previously obtained secondary fluid mass flow rate from the cooling capacity. Mass flow rates of the primary and secondary fluids are as follows;

$$\dot{m}_s = \frac{\dot{Q}_e}{\Delta h_{e,opt}} \tag{5.1}$$

$$\dot{m}_m = \frac{\dot{m}_s}{w_{opt}} \tag{5.2}$$

After defining mass flow rates of the primary and secondary fluids, throat pressure, $P_t$ is calculated iteratively. An initial value is assumed for the throat pressure and the throat velocity is calculated for the converging part of the motive nozzle with respect to the assumed motive nozzle efficiency. Since Mach number at the throat must be equal to unity, the difference between the sound velocity according to the assumed throat pressure and the calculated velocity from the energy equation is checked. If the difference is higher than the accepted error value, iteration steps are repeated with new throat pressure trials. Sound velocity (Minnaert, 1933; Kong & Qi, 2018) and void fraction for homogeneous flow ($u_g/u_l$=1) (Smith, 1969) are given as

$$c = \left[ \rho_m \left( \frac{\alpha}{\rho_g c_g^2} + \frac{1-\alpha}{\rho_l c_l^2} \right) \right]^{-1/2} \tag{5.3}$$

$$\rho_m = \alpha\rho_g + (1-\alpha)\rho_l \tag{5.4}$$

$$\alpha = \frac{X_m}{X_m + (1 - X_m)\dfrac{\rho_g}{\rho_l}} \tag{5.5}$$

Density of the two-phase flow calculated by Equation 5.4 is the same as the value obtained from REFPROP program (Lemmon et al., 2013). By the way, the motive nozzle efficiency is assumed to be the same for each section of the nozzle. Throat velocity as well is calculated from the energy equation applied to the converging part of the motive nozzle as

$$h_t = (1-\eta_m)h_{m,in} + \eta_m h(s_{m,in}, P_t) \tag{5.6}$$

$$u_t = \sqrt{2(h_{m,in} - h_t) + u_{m,in}^2} \tag{5.7}$$

When the exact throat pressure is estimated iteratively, the throat diameter is calculated as follows;

$$D_t = \sqrt{\frac{4\dot{m}_m}{\pi\rho_t u_t}} \tag{5.8}$$

Motive nozzle outlet and suction nozzle outlet diameters are calculated according to the optimum expansion pressure at the outlets, $P_{s,opt}$. Constant area mixing section diameter is the same as the suction nozzle outlet diameter. The formulation is given separately for this section, but it is already known from the assumptions and templates of Figure 5.2 that they are equal. The expressions for these three diameters for a constant area mixing ejector are given as

$$D_{m,out} = \sqrt{\frac{4\dot{m}_m}{\pi\rho_{m,out}u_{m,out}}} \tag{5.9}$$

$$D_{s,out} = \sqrt{\frac{4\dot{m}_s}{\pi\rho_{s,out}u_{s,out}} + D_{m,out}^2} \tag{5.10}$$

$$D_{mix} = \sqrt{\frac{4(\dot{m}_m + \dot{m}_s)}{\pi\rho_{mix,out}u_{mix,out}}} \tag{5.11}$$

### *5.2.2 Solution Algorithm*

The solution procedure in order to obtain the optimum entrainment ratio and suction nozzle pressure is explained in detail in the previous chapter. However, the iterative procedure for ejector performance calculations is clearly defined in most of the studies from the literature (Kornhauser, 1990; Li & Groll, 2005). For the design calculations at various operation conditions, enthalpy difference of the evaporator as well are obtained from the same model to calculate the mass flow rates of the refrigerants. The solution procedure for the second part of the ejector design considerations is summarized in Figure 5.3.

Only inputs of the second part for the design calculations are given in the flowchart. Density and velocity terms in the equations are defined in the same way of the previous performance analyses for motive nozzle outlet, suction nozzle outlet, and mixing section outlet. For the expansion processes through the nozzles, optimum outlet pressure of $P_{s,opt}$ is considered.

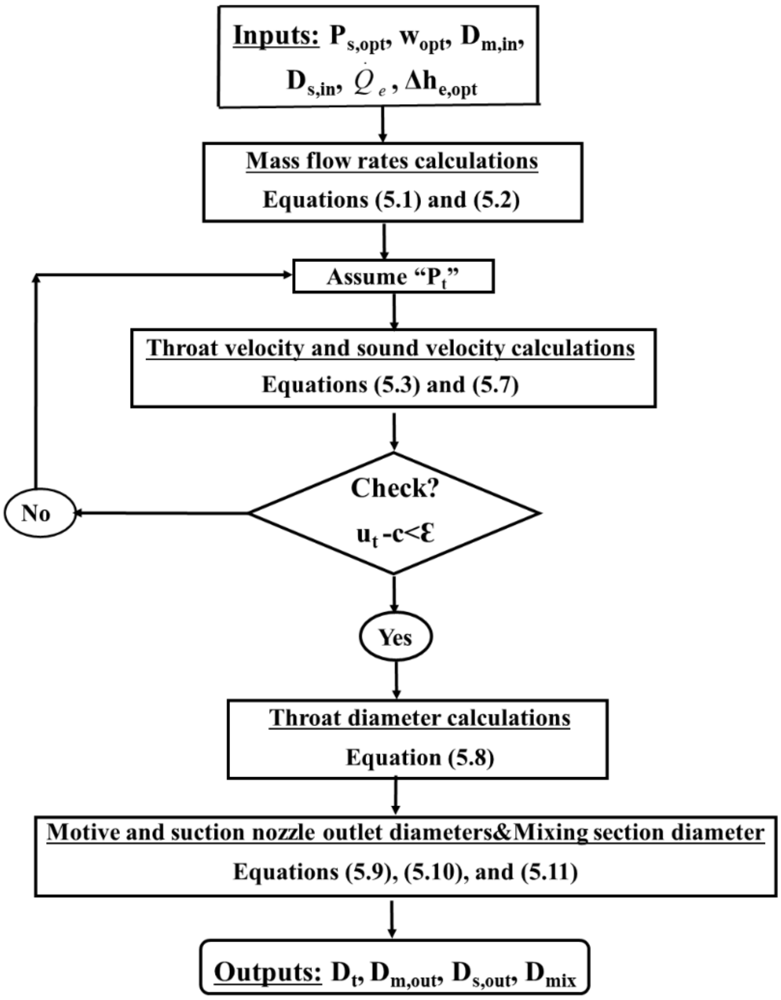


Figure 5.3 Flowchart for the second part of the model to calculate the geometrical parameters

### 5.3 Results and Discussion

Inputs of the whole model are presented in Table 5.1. They are typically for an air-conditioning application. The ranges for the evaporator and condenser temperatures are -15 °C-5 °C and 40 °C-65 °C, respectively. First of all, the variation of $w_{opt}$ and $P_{s,opt}$ are displayed with respect to various evaporator and condenser temperatures as shown in Figure 5.4. In Figure 5.5, enthalpy difference of the evaporator at the optimum suction nozzle pressure is presented for the same operating points.

In Figure 5.6, mass flow rates of the primary and secondary fluid flows are shown. Lowest mass flows are observed for R134a at each operation point since highest enthalpy difference through the evaporator is calculated for it. However, the highest mass flows are calculated for R1234yf due to the lowest enthalpy difference values at the investigated operating points. R1234ze(E) and R134a yielded closer mass flow rates of the primary and secondary fluids.

Table 5.1 Operating conditions for the thermodynamic model of the design calculations

| Parameters | Values |
|---|---|
| Evaporator temperature ($T_e$) | 5 ˚C |
| Evaporator outlet superheat temperature difference ($\Delta T_{sh}$) | 5 K |
| Condenser Temperature ($T_c$) | 40 ˚C |
| Condenser outlet subcooling temperature difference ($\Delta T_{sc}$) | 3 K |
| Compressor efficiency ($\eta_{comp}$) | 0.75 |
| Primary nozzle efficiency ($\eta_m$) | 0.9 |
| Suction nozzle efficiency ($\eta_s$) | 0.9 |
| Diffusor efficiency ($\eta_d$) | 0.8 |
| Cooling (Refrigeration) capacity (kW) | 5 |
| $D_{s,in}$ (mm) | 60 |
| $D_{m,in}$ (mm) | 15 |

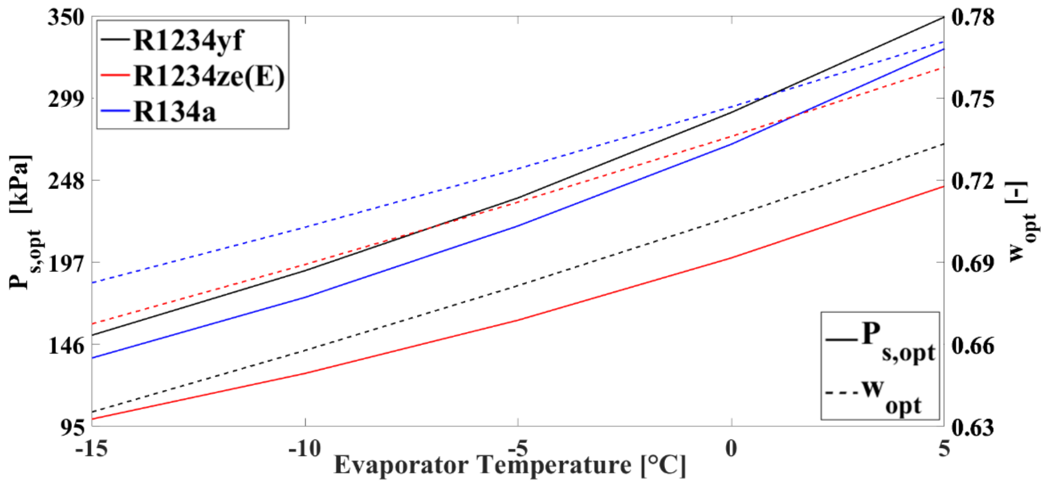


(a)

Figure 5.4 Variation of the optimum suction pressure and entrainment ratio as the inputs of the second step ejector design model according to the (a) evaporator and (b) condenser temperatures

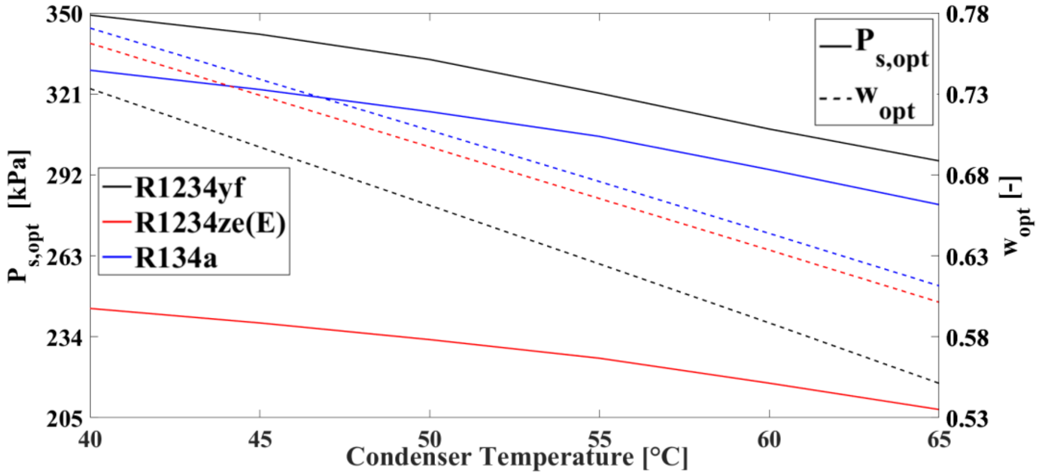


**(b)**

Figure 5.4 continues

Secondary fluid mass flows have lower rate of change (around 4-5%) for three of the refrigerants according to evaporation temperature as obvious from Figure 5.6 (a). On the other hand, rate of change varies more (6-9%) for the primary fluid mass flow rate at the same evaporation temperature range.

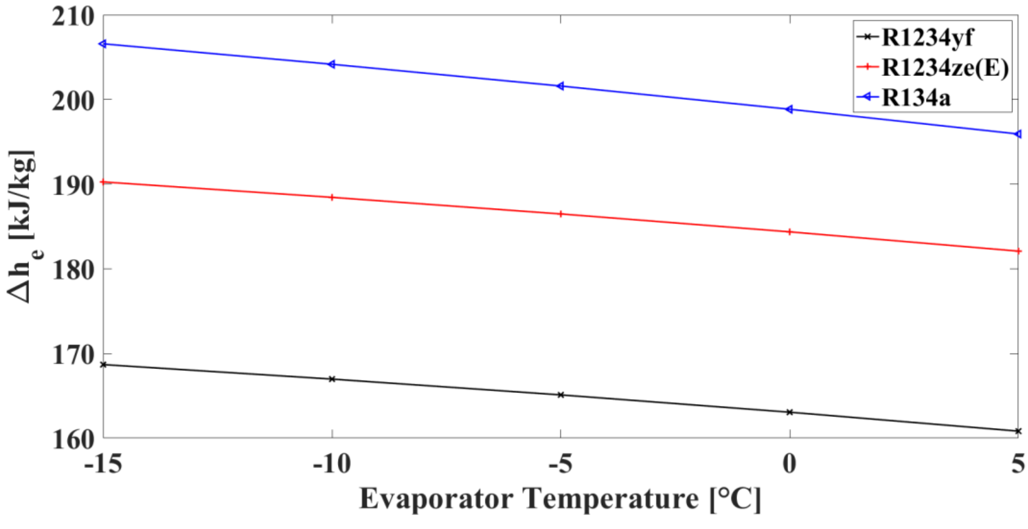


**(a)**

Figure 5.5 Variation of the evaporator enthalpy difference at the optimum suction nozzle pressure as the inputs of the second step ejector design model with respect to the (a) evaporator and (b) condenser temperatures

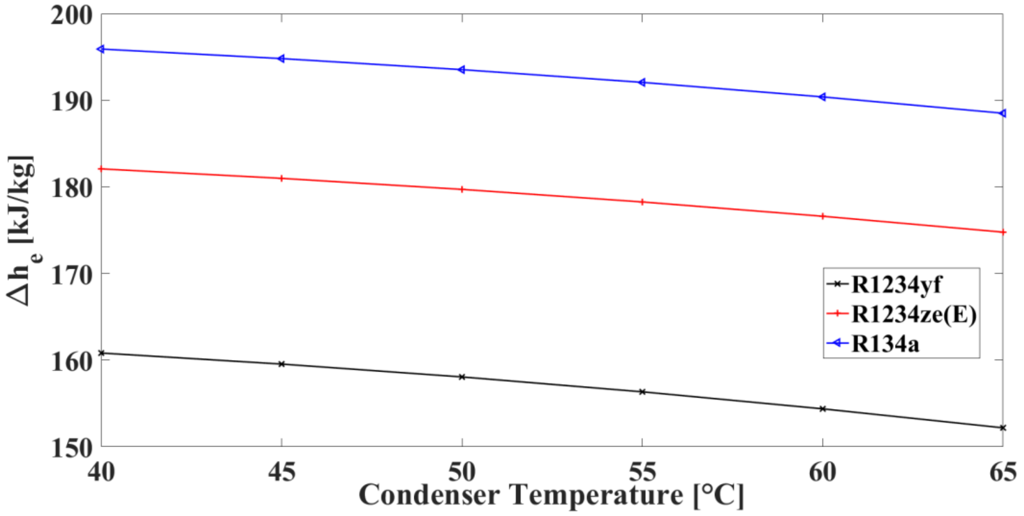


**(b)**

Figure 5.5 continues

Primary fluid mass flow rate decreases according to evaporator temperature; whereas secondary fluid mass flow rate increases. When condenser temperature is increased, mass flow rates of the primary and secondary fluid increase as shown in Figure 5.6 (b). Rate of change for the primary fluid mass flow rate is higher than the change rate of the secondary fluid mass flow rate according to the condenser temperature.

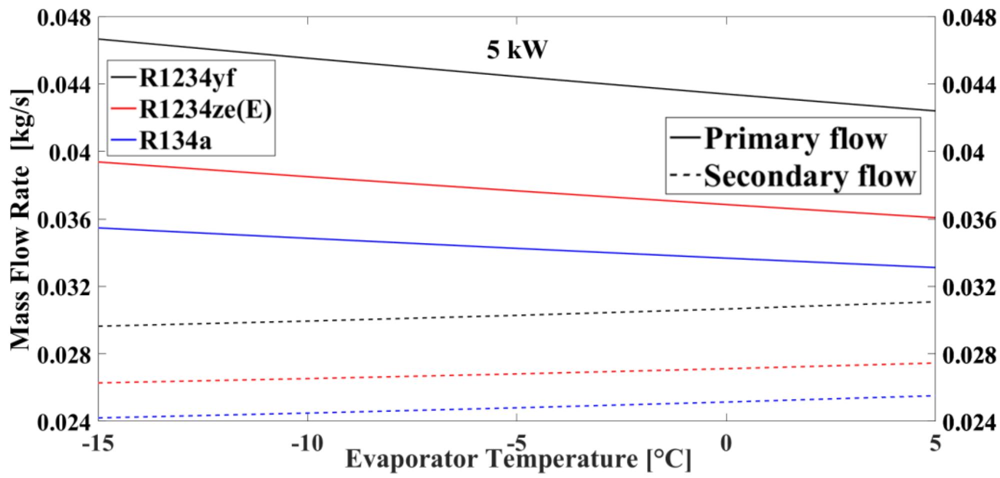


**(a)**

Figure 5.6 Mass flow rates of the primary and secondary fluid flows for 5 kW cooling capacity at the optimum suction nozzle pressure with respect to the (a) evaporator and (b) condenser temperatures

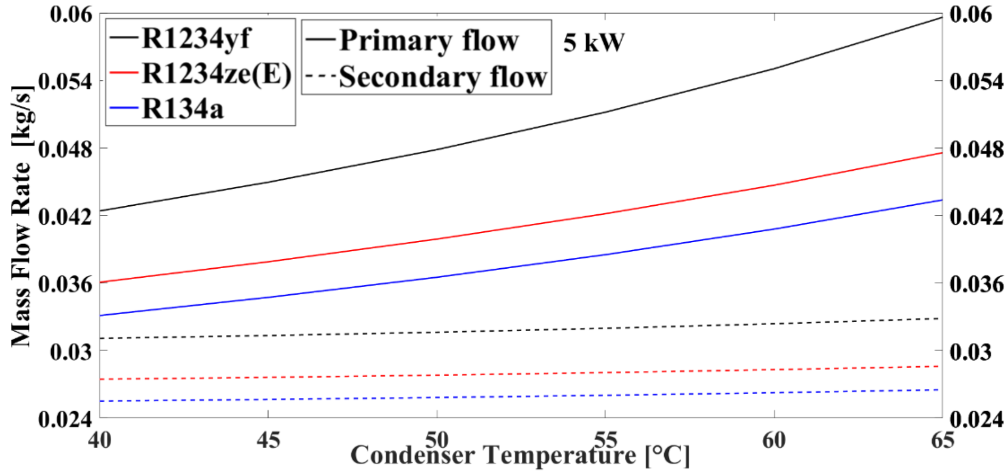


**(b)**

Figure 5.6 continues

Figure 5.7 shows the variation of the motive nozzle throat and outlet diameters according to the evaporator and condenser temperatures. Motive nozzle throat diameters decrease when condenser and evaporator temperatures increase. Throat diameter changes more when condenser temperature is increased in comparison with the evaporator temperature variations for all three refrigerants.

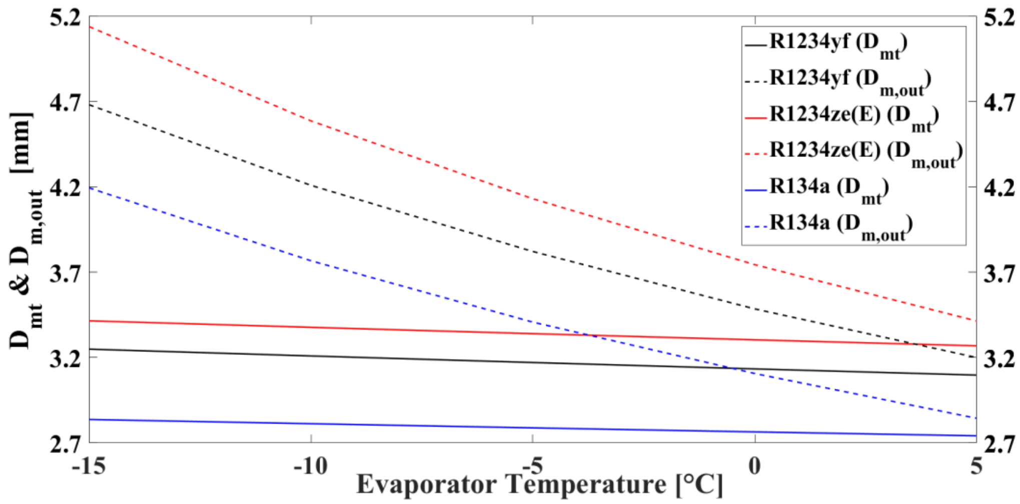


**(a)**

Figure 5.7 Variation of the motive nozzle throat and exit diameters according to the (a) evaporator and (b) condenser temperatures

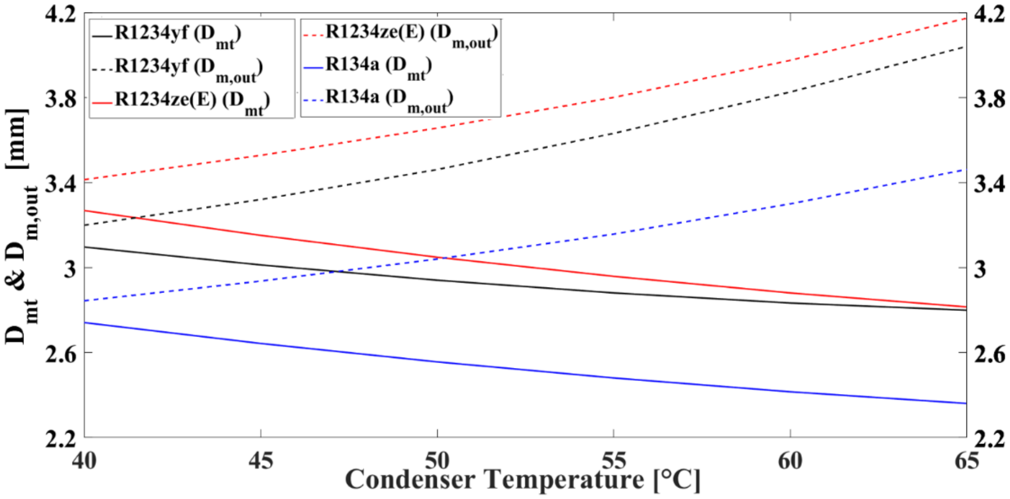


**(b)**

Figure 5.7 continues

As shown from Figure 5.7 (a) and (b), motive nozzle outlet diameter is affected mostly by the changes in the evaporator temperature since the optimum suction nozzle pressure reacts more to the changes in the evaporator temperature. Thermodynamic analyses declare in the previous chapter that the pressure drop at the optimum conditions is influenced mostly by the condenser temperature. However, it is the pressure drop defined with reference to evaporator temperature. In this section, optimum suction nozzle pressures as shown in Figure 5.4 is directly used as the inputs of the geometrical parameter calculations.

In Figure 5.8, the suction nozzle outlet diameter or the constant area mixing section diameter is presented for the same operating conditions. Hassanain et al. (2015) established a model having one more input than the inputs of this investigation. Hence, they could define both of the geometrical parameters separately. Mixing section diameter is affected mostly by the evaporator temperature. Although R1234yf and R1234ze(E) yield closer values for the motive nozzle throat and outlet diameters, R134a and R1234yf resulted in closer diameters in terms of mixing section diameter as given in Figure 5.8 (a) and (b).

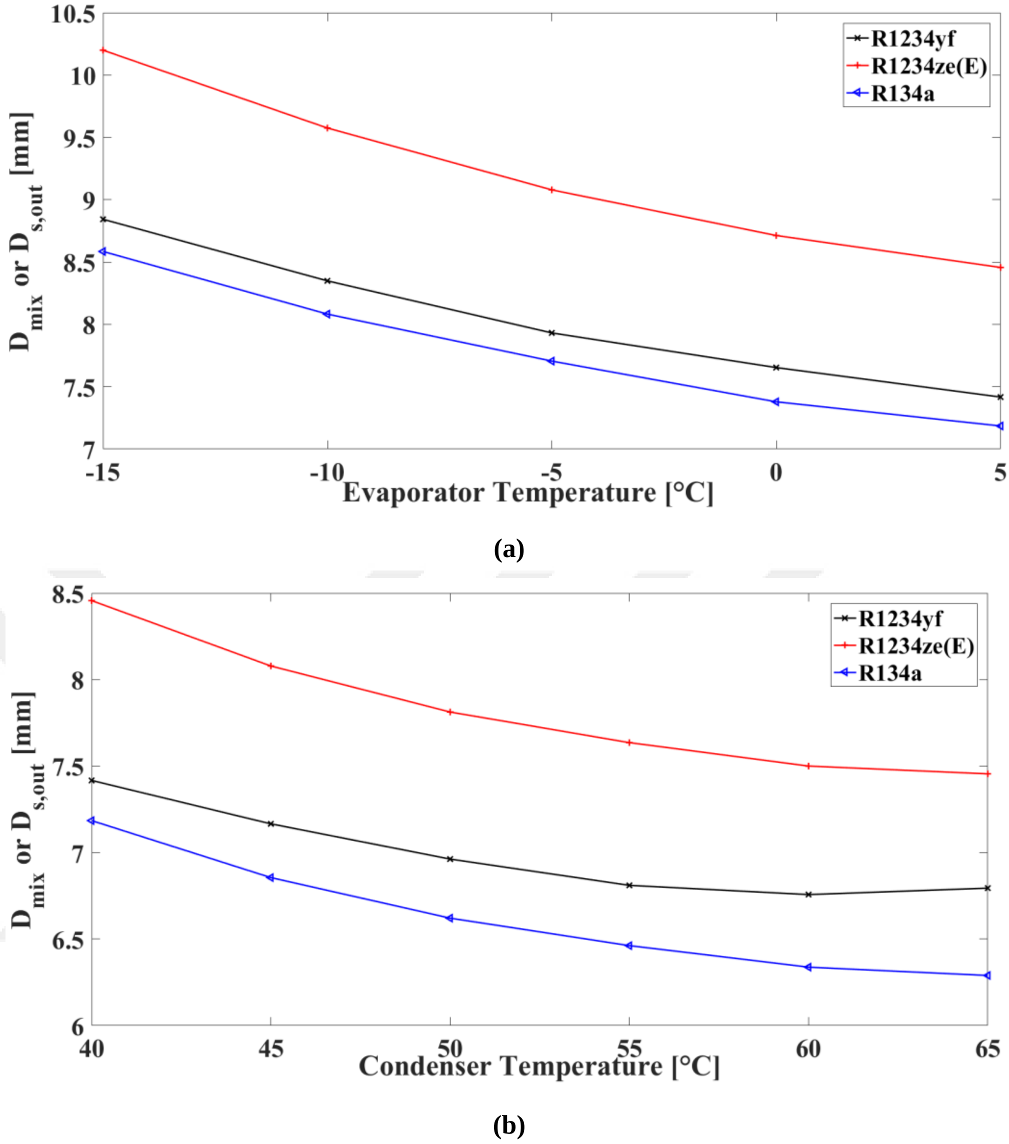


Figure 5.8 Dependency of the constant area mixing section (suction nozzle outlet diameter) on various (a) evaporator and (b) condenser temperatures

The mostly affected parameter by the operating conditions is the motive nozzle outlet diameter. The percentage decrease with respect to the evaporator temperature is around 31-33%; whereas the percentage increase in accordance with the condenser temperature is between 16-20% for these three investigated refrigerants.

To sum up, the mixing process of the ejector is modelled according to CAM assumption. First of all, mass flow rates of the primary and secondary fluid mass flow rates are obtained to calculate the design parameters. Effects of the evaporator and condenser temperatures on the secondary fluid mass flow rate are low and close to each other for the three refrigerants. Mass flow rates of R1234yf is more dependent to the changes in the operating temperatures when compared to the other investigated refrigerants.

Motive nozzle throat diameter changes more when condensation temperature is increased. However, motive and suction nozzle outlet diameters are more dependent on the evaporator temperature. Motive nozzle outlet diameter is the mostly affected geometrical parameter by the operating conditions. All geometrical calculations are given with reference to optimum suction nozzle pressure assumption figuring out the ideal operation of the ejector. When Ma numbers at the outlet of the motive nozzle is investigated for some operating ranges, it is seen that the optimum suction nozzle pressure is nearly obtained directly after the converging section. Hence, for higher evaporator temperatures, converging nozzles could be used with reference to the investigated conditions since the optimum motive nozzle outlet pressure is nearly the same as the throat pressure.

Lastly, this modelling approach presented in this section specifies the design in terms of the critical diameters. Benefiting from the previously published papers in the literature, some more details could be calculated such as the relations between the length and diameter of a section. However, this section only focuses on the design aspects covering the optimum operating conditions. The modelling approach presented in this section is required to be improved since design calculations based on the actual operating conditions are necessarily demanded. The actual pressure at the motive nozzle outlet according to the geometry and operating conditions of the nozzle is to be calculated in the thermodynamic models. Hence, 1D model of the motive nozzle is to be established and implemented into the thermodynamic models. As a result, the design of the ejector could be evaluated more accurately and the performance of the EERC could be estimated in a more realistic way.

# CHAPTER SIX

# ONE-DIMENSIONAL MODEL OF THE MOTIVE NOZZLE

The motive nozzle which is of generally converging-diverging form is the critical section of the ejector since it creates the necessary pressure drop for the secondary fluid to be sucked into the ejector. Therefore, calculating the pressure distribution throughout the motive nozzle is important to the overall performance evaluation of the ejector expansion refrigeration cycle for a typical operating condition and nozzle geometry. In this section, the flow analyses are made for a converging-diverging nozzle to be used as the motive nozzle of an ejector. The motive flow is expected to be in compressed liquid or saturated liquid state at the nozzle inlet with reference to the state of the motive fluid of the two-phase ejector utilized in the EERC.

One-dimensional model of the nozzle is established based on the conservation equations of mass, momentum, and energy and equation of state. Pressure, temperature, and Mach number distributions are validated experimentally and numerically with the help of the previous studies from the literature and the maximum difference between the literature data and the calculated results for the pressure drop throughout the nozzle is around 6%. R134a, R1234yf, and R1234ze(E) are selected as the working fluids. Subcooling temperature difference, mass flow rate, motive nozzle outlet diameter, and motive nozzle inlet pressure are investigated parametrically. In summary, this section touches mainly on the 1D modelling of the motive nozzle of a two-phase ejector in order to analyze flow characteristics, i.e., distributions of the pressure, temperature, velocity, and Mach number.

In comparison with the previously summarized literature, the main objective of this section is calculating the motive nozzle outlet pressure and motive nozzle efficiency exactly for the thermodynamic analyses. Effect of the subcooling temperature difference with respect to the saturation temperature at the inlet pressure as the motive nozzle operating conditions is investigated for R1234yf, R1234ze(E), and R134a. The pressure, temperature, and velocity distributions throughout the nozzle are compared for these three refrigerants. Moreover, pressure distribution, throat diameter, nozzle efficiency, and Mach number at the motive nozzle outlet are compared according to mass flow rate for the refrigerants at issue. Motive nozzle outlet pressure, Mach number at the motive nozzle outlet, and motive nozzle efficiency are analyzed with reference to motive nozzle outlet diameter. Lastly, the influence of the motive nozzle inlet pressure (condenser pressure) on the pressure distribution throughout the motive nozzle, outlet velocity, and Mach number at the nozzle outlet is investigated.

The biggest motivation of this investigation is calculating the motive nozzle outlet pressure exactly according to the design and operating conditions of the motive nozzle. Hence, the EERC performance is evaluated in a more realistic way under thermodynamic modelling approach. Effects of the operating parameters, namely subcooling temperature difference, mass flow rate, and inlet pressure and the design parameter, i.e., the motive nozzle outlet diameter are tested numerically. When compared to previously published studies and their outcomes, the comparative results of the current section are beneficial for the subsequent experimental and numerical studies regarding the EERC concept including the newly used HFOs such as R1234yf and R1234ze(E). This section aims to enlighten the design and performance aspects of the convergent-divergent motive nozzles to be used the two-phase ejectors.

1D model of the motive nozzle is established under steady flow, equilibrium, and adiabatic nozzle assumptions. Conservation equations of mass, momentum, and energy with the equation of state are applied to the discretized grids (cells) of the computational zones including the converging and diverging sections of the motive nozzle. Therefore, a set of the ordinary differential equations are presented for each cell with reference to Banasiak & Hafner (2011). The total derivative of the pressure, velocity, specific enthalpy, and density are the system unknowns and they are solved implicitly. The model at issue is verified experimentally using the pressure and temperature distributions provided by Tsuru et al. (2014). What’s more, the numerical validations of the model are presented according to the pressure and temperature distributions of Tsuru et al. (2014) and pressure and Mach number distributions of Banasiak & Hafner (2011).

Principal results published by Atmaca, Erek, & Ekren (2020b) are presented in this section. Atmaca et al. (2020b) constructed 1D model of the motive nozzle, validated the model, and made parametric analyses of the motive nozzle according to subcooling temperature difference, motive nozzle inlet pressure (condenser pressure of the EERC) mass flow rate, and motive nozzle outlet diameter.

## 6.1 Mathematical Modelling

1D model of the motive nozzle is established applying the governing equations of mass, momentum, and energy with the equations of the state to each computational grid of the overall calculation domain for the convergent and divergent sections as shown in Figure 6.1 (a). The expanded view of the first computational grid including the inlet and outlet properties of the refrigerant is shown as the example representation in Figure 6.2 (b). Most of the modelling assumptions and all equations are presented with reference to Banasiak & Hafner (2011).

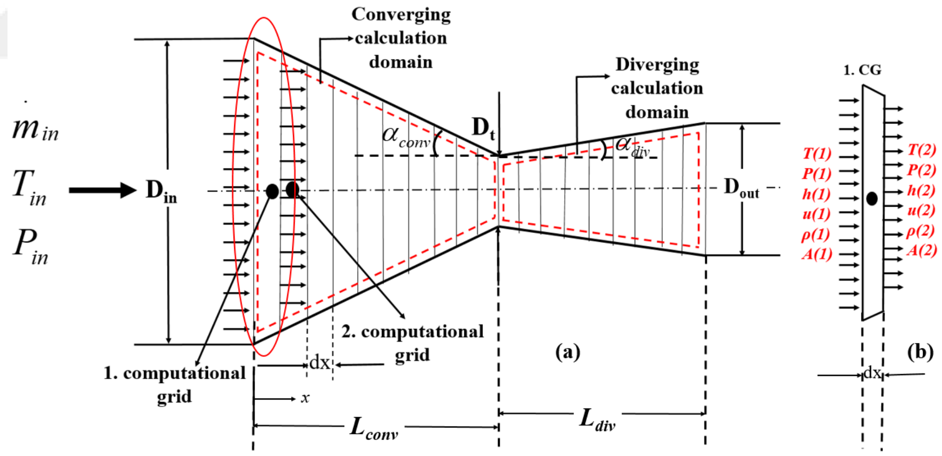


Figure 6.1 (a) Calculation domains and computational grids displaying the dimensions of the motive nozzle with boundary conditions of the flow and (b) refrigerant flow at the inlet and outlet of the first computational grid (CG)

The total derivatives of the pressure, specific enthalpy, velocity, and density are presented in the ordinary differential equation system as the modelling equations. Differential equation system is solved implicitly to define the variation of these quantities, i.e., velocity, density, pressure, and specific enthalpy, for each computational grid. The equation set for each computational set is solved in MATLAB®. Thermodynamic properties of the refrigerants are obtained from REFPROP version 10.0 (Lemmon et al., 2018).

### *6.1.1 Basic Assumptions and Boundary Conditions*

There are typical assumptions required to be presented as follows;

- The homogeneous equilibrium model for two-phase flow is considered. In other words, mechanical and thermal equilibrium is stated to be established between the phases (Atmaca et al., 2019a).
- Equal local (average) flow velocities, temperatures, and pressures are considered for both of the liquid and gas phases and given in a respective order as follows (Staedtke, 2006);

$$u_g = u_l = u \tag{6.1}$$

$$T_g = T_l = T \tag{6.2}$$

$$P_g = P_l = P \tag{6.3}$$

- The flow is steady, adiabatic, viscous, and chemically uniform.
- Properties and velocities are constant throughout the variable cross-sections of the converging-diverging nozzles for each computational zone created under 1D modelling approach (Atmaca et al., 2019).
- The effects of the surface tension and thermal diffusion is neglected (Banasiak & Hafner, 2011).
- The turbulence effects are considered with the implementation of the friction factor into the conservation of momentum equation (Banasiak & Hafner, 2011).

- The inlet velocity of the refrigerant is comparatively small when compared to the outlet velocity, hence the definition of the motive nozzle efficiency is declared ignoring the inlet velocity.

Boundary conditions are the inlet temperature, pressure, and mass flow rate. Banasiak & Hafner (2011) added the vaporization index as well to the boundary conditions since they defined the thermodynamic state of the two-phase fluid according to DEM approach for the motive nozzle. However, since the metastable effects are ignored under the equilibrium assumption of the current investigation, there is no need to define an additional boundary condition.

### *6.1.2 Equations of the Mathematical Model*

With reference to previously defined assumptions, the conservation equations of mass, momentum, and energy are given as

$$\frac{1}{u}\frac{du}{dx} + \frac{1}{A_{cs}}\frac{dA_{cs}}{dx} + \frac{1}{\rho}\frac{d\rho}{dx} = 0 \tag{6.4}$$

$$A_{cs}\frac{dP}{dx} + \rho u A_{cs}\frac{du}{dx} + f\rho\frac{u^2}{2}\frac{dA_{lt}}{dx} = 0 \tag{6.5}$$

$$\frac{dh}{dx} + u\frac{du}{dx} = 0 \tag{6.6}$$

Equation of state as well is required to complete the system of ordinary differential equations for the total derivatives of the pressure, velocity, enthalpy, and density.

$$\rho = \rho(P, s) \tag{6.7}$$

$$\frac{d\rho}{dx} = \left(\frac{\partial\rho}{\partial P}\right)_s \frac{dP}{dx} + \left(\frac{\partial\rho}{\partial s}\right)_P \frac{ds}{dx} \tag{6.8}$$

The total derivative of the entropy is rewritten using the thermodynamic relations as follows;

$$s = s(h, P) \tag{6.9}$$

$$\frac{ds}{dx} = \left(\frac{\partial s}{\partial h}\right)_P \frac{dh}{dx} + \left(\frac{\partial s}{\partial P}\right)_h \frac{dP}{dx} \tag{6.10}$$

$$dh = Tds + vdP \tag{6.11}$$

From Equation 6.11 partial derivatives could be read

$$\left(\frac{\partial s}{\partial h}\right)_P = \frac{1}{T} \tag{6.12a}$$

$$\left(\frac{\partial s}{\partial P}\right)_h = -\frac{1}{\rho T} \tag{6.12b}$$

$$\frac{ds}{dx} = \left(\frac{1}{T}\right)\frac{dh}{dx} - \left(\frac{1}{\rho T}\right)\frac{dP}{dx} \tag{6.13}$$

Therefore, the final expression combining Equation 6.8 and Equation 6.13 for the total derivative of the density is given as

$$\left[\left(\frac{\partial \rho}{\partial P}\right)_s - \left(\frac{\partial \rho}{\partial s}\right)_P \left(\frac{1}{\rho T}\right)\right]\frac{dP}{dx} + \left[\left(\frac{\partial \rho}{\partial s}\right)_P \left(\frac{1}{T}\right)\right]\frac{dh}{dx} - \frac{d\rho}{dx} = 0 \tag{6.14}$$

Furthermore, the speed of sound is defined accordingly.

$$c = \sqrt{\left(\frac{\partial P}{\partial \rho}\right)_s} \tag{6.15}$$

Lastly, presenting the efficiency of the motive nozzle according to the design and operating parameters are among the objectives of this study. Hence, the efficiency of the motive nozzle is formulated according to Dixon (1998). The derivatives $(\partial\rho/\partial P)_s$ and $(\partial\rho/\partial s)_P$ are evaluated numerically for the density changes corresponding to the infinitesimally small pressure changes at constant specific entropy and the density changes resulting in the infinitesimally small specific entropy changes at the constant pressure, respectively. Thermal properties are determined via REFPROP version 10.0 (Lemmon et al., 2018). Hence, the viscosity for the single-phase flow is obtained using the same program. However, the viscosity of the homogeneous two-phase fluid is defined using the Effective Medium Theory according to Awad & Muzychka (2008) as in the same way of Banasiak & Hafner (2011).

$$\mu_{tp,mix} = \frac{1}{4}((3r_{tp,mix} - 1)\mu_g + \left[3(1 - r_{tp,mix}) - 1\right]\mu_l + \sqrt{\left[(3r_{tp,mix} - 1)\mu_g + (3(1 - r_{tp,mix}) - 1)\mu_l\right]^2 + 8\mu_l\mu_g}\,) \tag{6.16}$$

Similarly, friction factor, $f$ is estimated based on the model presented by Churchill (1977) according to Banasiak & Hafner (2011) as well. Equation of Churchill (1977) is valid for all $Re$ and $\varepsilon/D$.

$$f = \left[\left(\frac{8}{\mathrm{Re}}\right)^{12} + \frac{1}{(A+B)^{3/2}}\right]^{1/12} \tag{6.17}$$

$$A = \left[2.457\ln\frac{1}{\left(\frac{7}{\mathrm{Re}}\right)^{0.9} + \frac{0.27\varepsilon}{D}}\right]^{16} \tag{6.18}$$

$$B = \left[\frac{37530}{\mathrm{Re}}\right]^{16} \tag{6.19}$$

Heretofore, the differential equation set is presented for the derivatives of density, velocity, enthalpy, and pressure. Next, the implicit solution algorithm is described step by step to calculate the variations of the aforecited parameters throughout the computational domains.

### *6.1.3 Solution Algorithm*

The solution algorithm is shown schematically in Figure 6.2. Inlet temperature, pressure, and mass flow rate are the boundary conditions for a compressed liquid. Specific enthalpy and density is determined based on the specified inlet temperature and pressure. The geometrical parameters are as well among the inputs. Hence, the inlet velocity could be calculated from the mass flow rate. Diverging and converging angles of the motive nozzle in addition to inlet diameter are constant for all of the analyses. Motive nozzle outlet diameter is the design parameter to be investigated. Throat diameter is an output determined with respect to the operating conditions and other design parameters of the nozzle. Length of the converging and diverging ducts of the motive nozzle would be changed under the constant angle design constraint for these sections.

The differential equation set is established and solved for each computational grid implicitly. Therefore, the coefficient matrix (CM), right-hand side vector (RHSV), and the solution vector (SV) are presented for each grid. The SV includes the total derivatives of the density, velocity, enthalpy, and pressure. After obtaining the variations for these parameters through each computational grid, the outlet values of these parameters are calculated numerically for the reference grid. Therefore, calculated outlet values of these parameters for the previous grids would be the inlet values of these parameters for the subsequent cell. The distribution of these parameters are calculated throughout the nozzle as displayed by the solution algorithm in Figure 6.2. The required parameters for the RHSV and CM such as velocity, density, pressure, enthalpy, are used according to the outlet conditions of the previous cell. At the same time, it is the inlet conditions of the current grid through which the variations of the density, velocity, pressure, and enthalpy are calculated.

Lastly, although roughly estimated at the beginning of the analyses, exact position of the throat and the value of the throat diameter are to be defined according to the Mach number variations. The exact point where Mach number attains unity is defined as the position of the throat and the diameter of the nozzle at that point is the critical diameter.

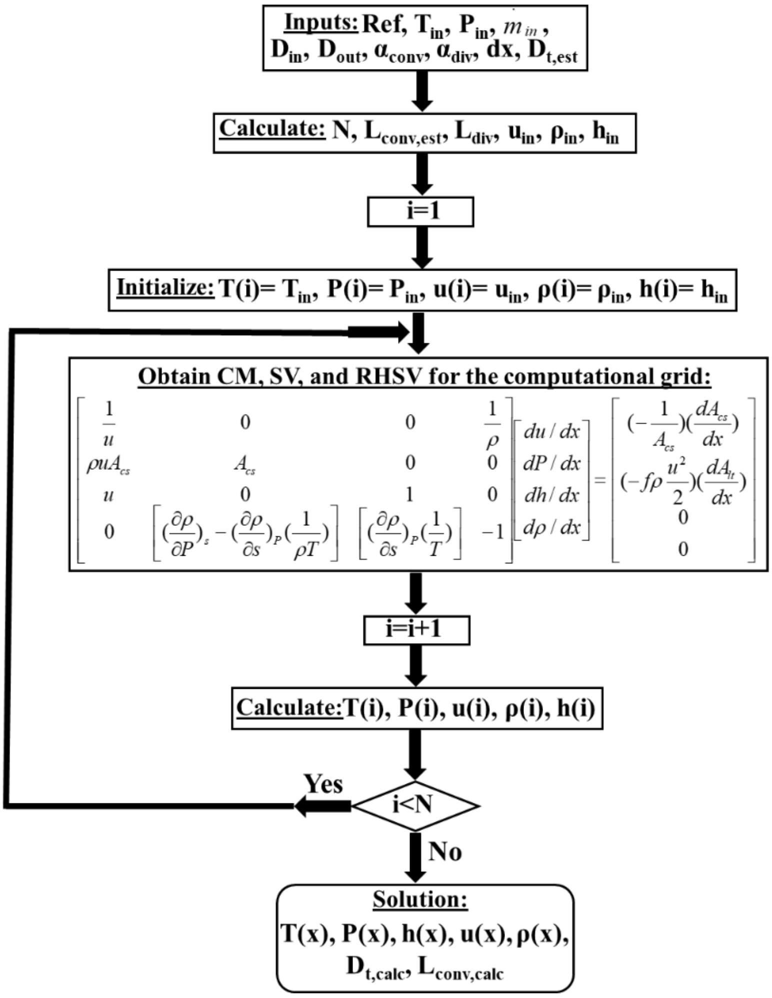


Figure 6.2 Flowchart of the solution algorithm

### *6.1.4 Grid Independence Analyses*

Grid independence analyses are displayed for frictional and frictionless flows as given in Table 6.1 and Table 6.2, respectively. Various lengths for the computational grids are compared, i.e., 0.01 mm, 0.001 mm, 0.0005 mm, 0.0002 mm, and 0.0001 mm. The geometry of the nozzle to be simulated is taken from the study of Tsuru et al. (2014). Hence $CO_2$ is used as the refrigerant in the grid independence analyses. Their reference nozzle includes rectangular cross-section. The calculated height of the motive nozzle is different than the declared height in the study of Tsuru et al. (2014).

Table 6.1 Results of the grid independence analyses for the frictional flow

| Length of the CGs | $\eta_m$ [-] | $P_{out}$ [kPa] | $T_{out}$ [K] | $u_{out}$ (m/s) | $h_{out}$ (J/g) | $\rho_{out}$ (kg/m$^3$) | Number of the nodes |
|---|---|---|---|---|---|---|---|
| **dx=0.01 mm** | 0.9443 | 1106.721 | 235.815 | 223.594 | 257.916 | 60.786 | 8399 |
| **dx=0.001 mm** | 0.9346 | 1095.630 | 235.535 | 222.855 | 258.008 | 62.126 | 83962 |
| **dx=0.0005 mm** | 0.9336 | 1094.336 | 235.502 | 222.777 | 258.017 | 62.276 | 167920 |
| **dx=0.0002 mm** | 0.9334 | 1094.172 | 235.498 | 222.762 | 258.019 | 62.299 | 419795 |
| **dx=0.0001 mm** | 0.9334 | 1094.156 | 235.498 | 222.759 | 258.020 | 62.303 | 839586 |

As seen from Table 6.1, the safe length for the computational grid could be defined as 0.0005 mm. It is better to give length of each computational cell instead of the total grid number since the length of the nozzle would be changed. The total length of the nozzle for the grid independence analyses is around 84 mm. Table 6.2 presents the grid independence analyses for the frictionless nozzle. Frictionless flow is simpler form of this nozzle model. Hence, computational grid length of 0.001 mm even results in better accuracy when compared to the frictional flow. In the second case of the grid independence analyses, friction which is the only irreversibility source is removed from the model. Thus, the nozzle efficiency is around unity.

Table 6.2 Results of the grid independence analyses for the frictionless nozzle

| Length of the CGs | $\eta_m$ [-] | $P_{out}$ (kPa) | $T_{out}$ (K) | $u_{out}$ (m/s) | $h_{out}$ (J/g) | $\rho_{out}$ (kg/m$^3$) | Number of the nodes |
|---|---|---|---|---|---|---|---|
| **dx=0.01 mm** | 1.0116 | 1038.883 | 234.068 | 236.080 | 255.031 | 57.781 | 8399 |
| **dx=0.001 mm** | 1.0017 | 1028.991 | 233.806 | 235.384 | 255.135 | 58.847 | 83963 |
| **dx=0.0005 mm** | 1.0006 | 1027.851 | 233.776 | 235.310 | 255.146 | 58.965 | 167922 |
| **dx=0.0002 mm** | 1.0003 | 1027.504 | 233.767 | 235.285 | 255.150 | 59.003 | 419800 |

Table 6.1 and Table 6.2 are presented for the same nozzle and operating conditions provided by Tsuru et al. (2014). Velocity is calculated higher in the frictionless flow calculations since some part of the kinetic energy is not converted into frictional heat.

As a result, nozzle operates more effectively and the outlet pressure is calculated lower in the frictionless flow analyses when compared to the frictional flow analyses. In the frictional flow case, some part of heat is dissipated as seen from the increase in the outlet enthalpy. Totally, in the frictional flow, the refrigerant leaves the nozzle with a higher pressure.

### *6.1.5 Experimental and Numerical Validation*

Two numerical and one experimental validations are presented in this section to display that this model could be used in the parametric analyses. First of all, experimental temperature and pressure distributions of Tsuru et al. (2014) is used to validate the numerical results obtained under frictional flow assumption as presented in Figure 6.3 (a) and (b). The difference between the numerical and experimental data is approximately 6% for the pressure drop and around 11 K for the temperature drop.

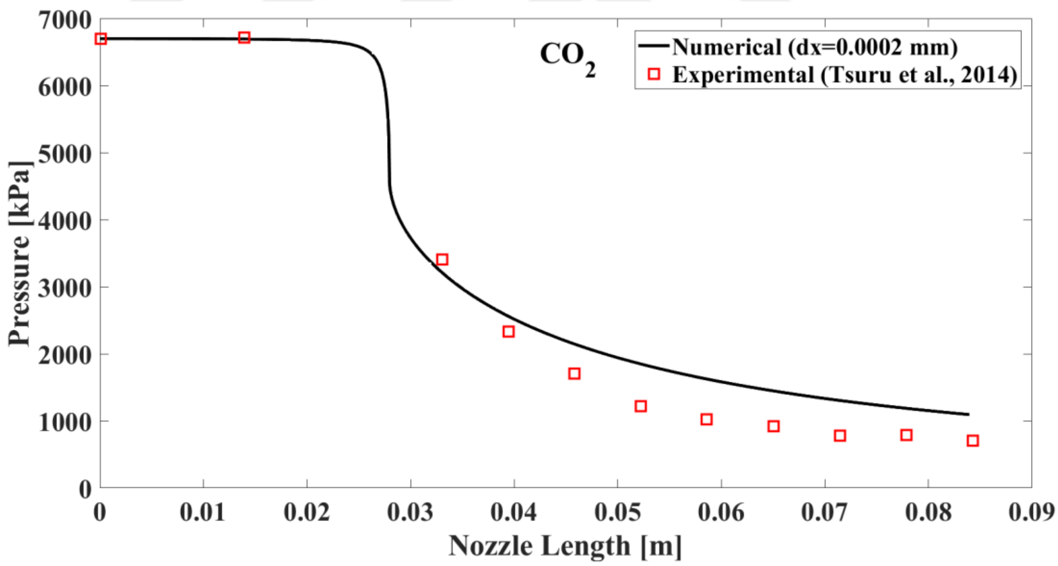


**(a)**

Figure 6.3 Comparison of the experimental data from the literature (Tsuru et al., 2014) and the numerical results of the present model in terms of the (a) pressure and (b) temperature distributions for $CO_2$

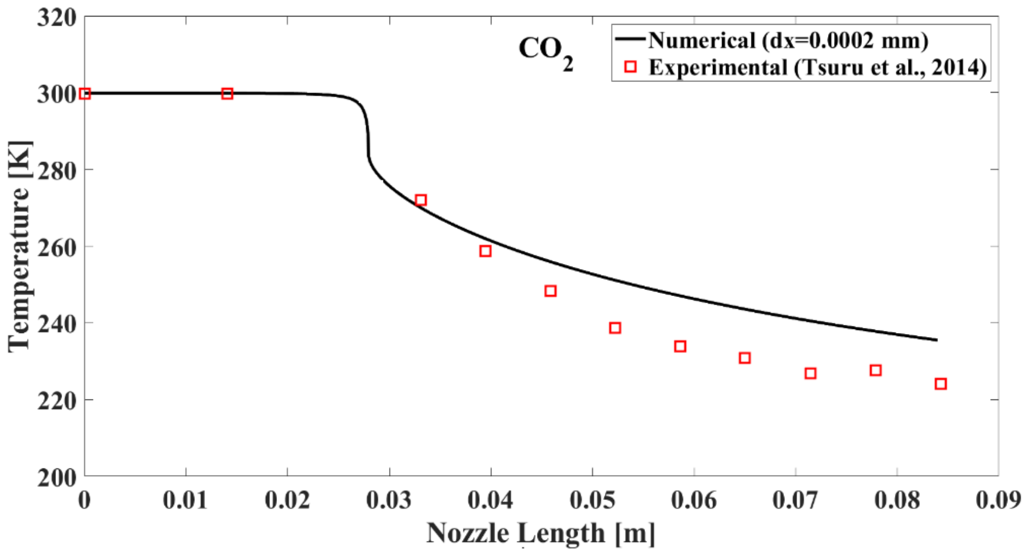


**(b)**

Figure 6.3 continues

Tsuru et al. (2014) conducted their model under frictionless flow assumption. Hence, one more comparison is made according to the numerical data of Tsuru et al. (2014). This time, the numerical results of the model presented in this section are calculated under the same assumption and shown in Figure 6.4 (a) and (b).

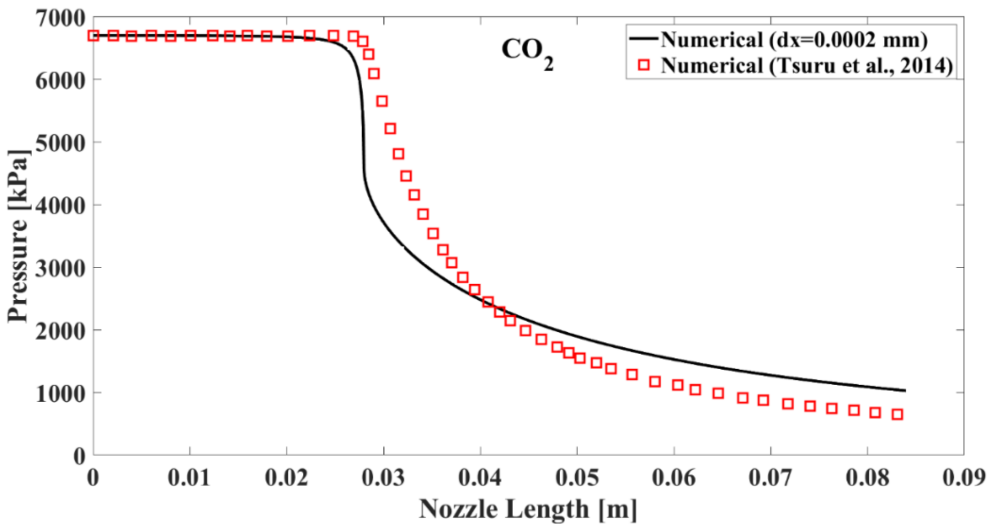


**(a)**

Figure 6.4 Comparison of numerical results from the literature (Tsuru et al., 2014) and numerical results of the model presented in this section under frictionless flow assumption according to (a) pressure and (b) temperature distributions

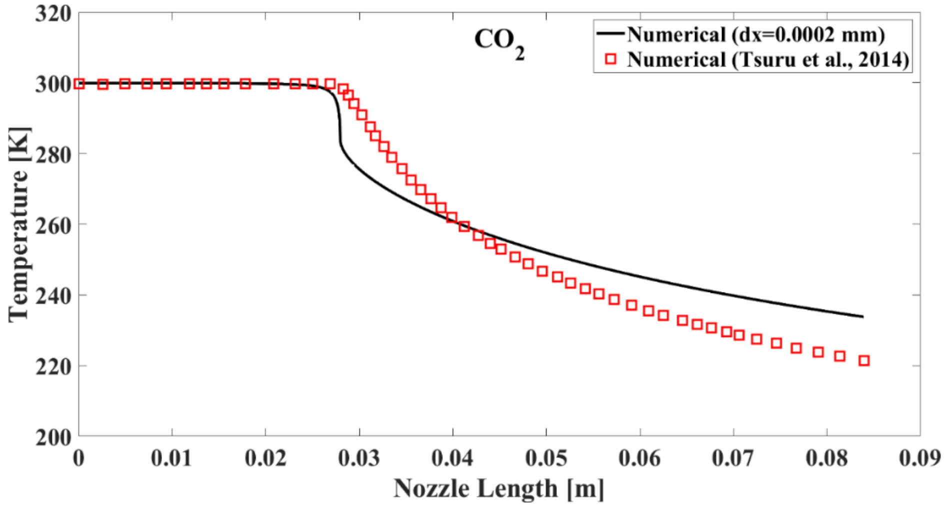


**(b)**

Figure 6.4 continues

When the numerical results are compared, the percentage and absolute differences between the numerical results are around 6.2% and 12 K for the pressure drop and temperature drop, respectively. Furthermore, as seen from the pressure and temperature distributions, the location of the critical diameter and its value slightly different from each other. The reason for this difference is directly related to constructing assumptions of the mathematical models. Tsuru et al. (2014) described two equation sets for the single-phase and two-phase flows and assumed that the single-phase flow turned into two-phase directly after the throat. However, the model presented in this section proposes only one equation set and the quality is checked at each computational grid. The location of the point where the flow turns into two-phase is defined according to the state of the refrigerant.

Next comparison is made between the numerical results of Banasiak & Hafner (2011) and the results of the current model with respect to the pressure and Mach number distributions as seen in Figure 6.5 (a) and (b). This comparison shows good agreements between the models for both Mach number and pressure distributions. Only Mach numbers slightly differ from each other at the outlet of the nozzle. The position of the throat is nearly the same for both of the models. The basic difference between the models is the approaches to define the thermodynamic states. Banasiak &

Hafner (2011) used DEM approach; whereas HEM approach is used in the model presented in this study. To sum up, the established mathematical model under the specified assumptions could be used to investigate flow throughout the nozzle according to design and operating parameters.

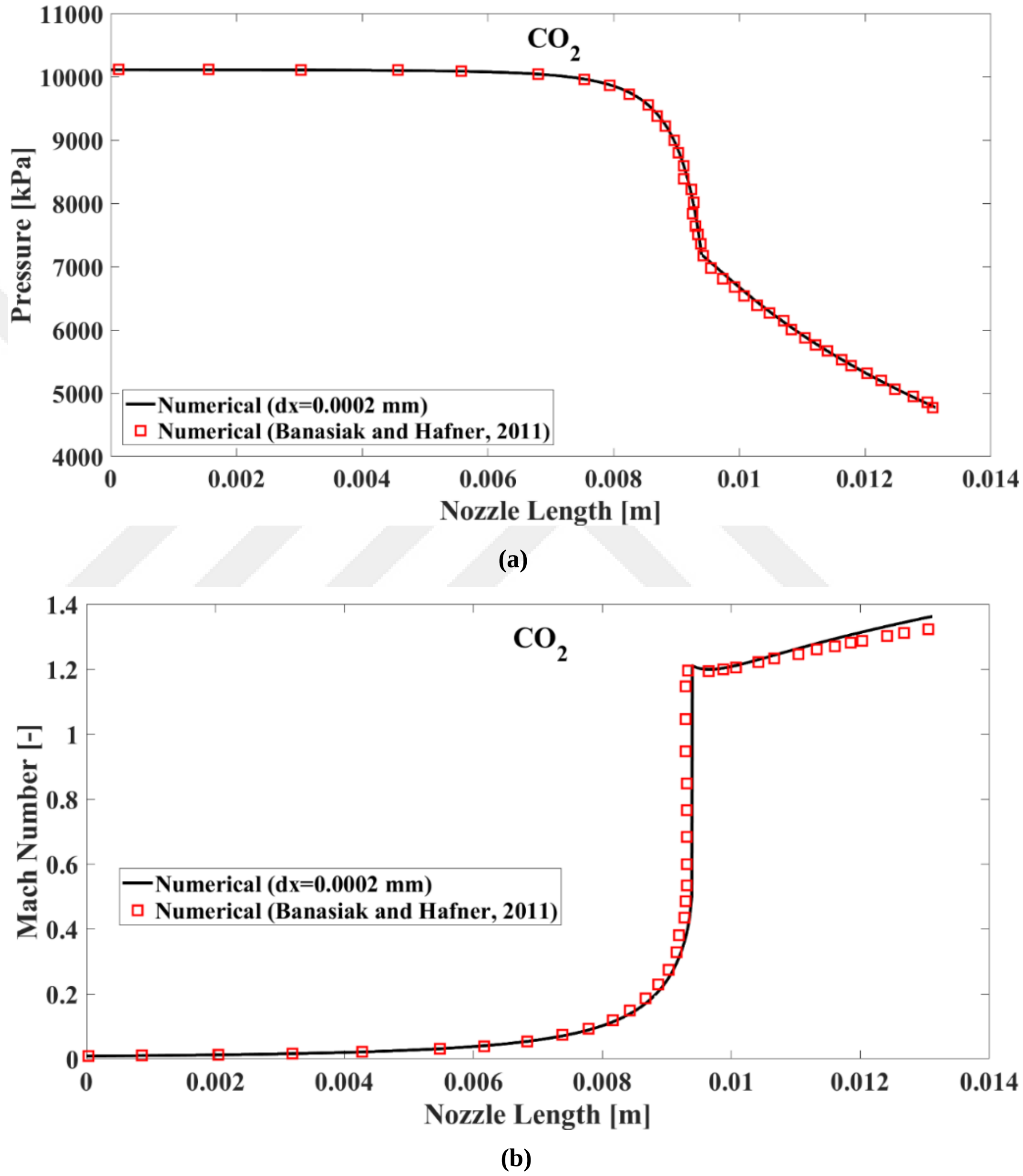


Figure 6.5 Comparison of numerical results from the literature (Banasiak & Hafner, 2011) and numerical results of the present model according to (a) pressure and (b) Mach number distributions

## 6.2 Results of the Motive Nozzle Investigations

After validating the model both experimentally and numerically, parametric analyses with reference to subcooling temperature difference, inlet pressure (condenser pressure of the EERC), mass flow rate, and motive nozzle outlet diameter are conducted for R134a, R1234yf, and R1234ze(E). Total errors for conservation of mass and momentum are kept in the order of $10^{-6}$ and $10^{-4}$, respectively when the grid size is chosen as 0.00004 mm for all of the analyses. The grid size is lower than the safe grid size, hence the variations in the critical flow parameters are investigated sensitively. Additionally, the total error for the energy conservation is calculated around 2-5 W as well according to the same grid size. This total error is approximately 0.06% of the total energy of the fluid passing thorough the nozzle per second. As a result, the total errors for the conservation equations are accepted low enough to calculate the flow characteristics sensitively. Reference operating conditions and design parameters are given in Table 6.3.

Table 6.3 Base operating conditions and design parameters

| Base Operating Conditions & Design Parameters | Values |
|---|---|
| Condenser temperature ($T_c$) | 40 °C |
| Subcooling temperature difference ($\Delta T_{sc}$) | 2 K |
| Motive nozzle mass flow rate ( $\dot{m}_{in}$ ) | 0.03 kg/s |
| Motive nozzle inlet diameter ($D_{in}$) | 12 mm |
| Motive nozzle converging half angle ($\alpha_{conv}$) | 12° |
| Motive nozzle diverging half angle ($\alpha_{div}$) | 1.15° |
| Motive nozzle outlet diameter ($D_{out}$) | 3 mm |

Boundary conditions for this problem are motive nozzle inlet pressure, temperature, and mass flow rate. Since this problem is arisen from the requirements of the deep investigations concerned with the EERC concept, one of the operating conditions is the condenser temperature. Motive nozzle inlet pressure is the saturation pressure corresponding to the condensation temperature. Inlet temperature of the refrigerant which is in compressed liquid state at the motive nozzle inlet is defined with respect to condensation temperature and subcooling temperature difference. Motive nozzle mass flow rate and subcooling temperature difference is roughly determined with reference to the experimental study of Ersoy & Sag (2014). Motive nozzle inlet diameter and motive nozzle converging half angle are specified with respect to Ersoy & Sag (2014) and Rusly, Aye, Charters, & Ooi (2005), respectively. Diverging half angle as well is given according to Lawrence (2012). Outlet diameter of the motive nozzle is slightly larger than the nozzle samples of Lawrence (2012).

Mass flow rate, subcooling temperature difference, inlet pressure (condensation temperature/pressure of the EERC), and motive nozzle outlet diameter are investigated parametrically within the scope of this section. The parametric range for the mass flow rate is 0.01-0.035 kg/s. The effect of the subcooling temperature difference is declared for 2 K, 1 K, and 0.1 K. 0.1 K is intentionally chosen to represent the boundary condition of nearly saturated liquid. The range for the motive nozzle outlet diameter is between 2.8-4.8 mm. Condensation temperature is varied between 40 °C-65 °C. Figure 6.6 (a), (b), and (c) shows the effects of the subcooling temperature difference variations on the pressure, temperature, and velocity distributions. Inlet pressure is lower for R1234ze(E) when compared to R134a and R1234yf according to the saturation pressure corresponding to motive nozzle inlet temperature of 40 °C.

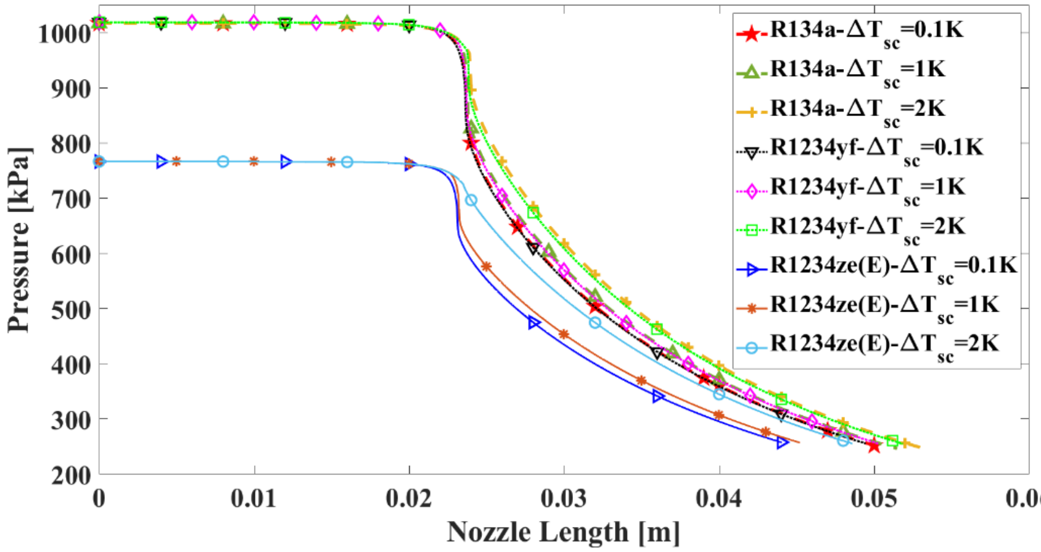


**(a)**

Figure 6.6 Effects of the subcooling temperature difference on (a) the pressure, (b) the temperature, and (c) the velocity distributions

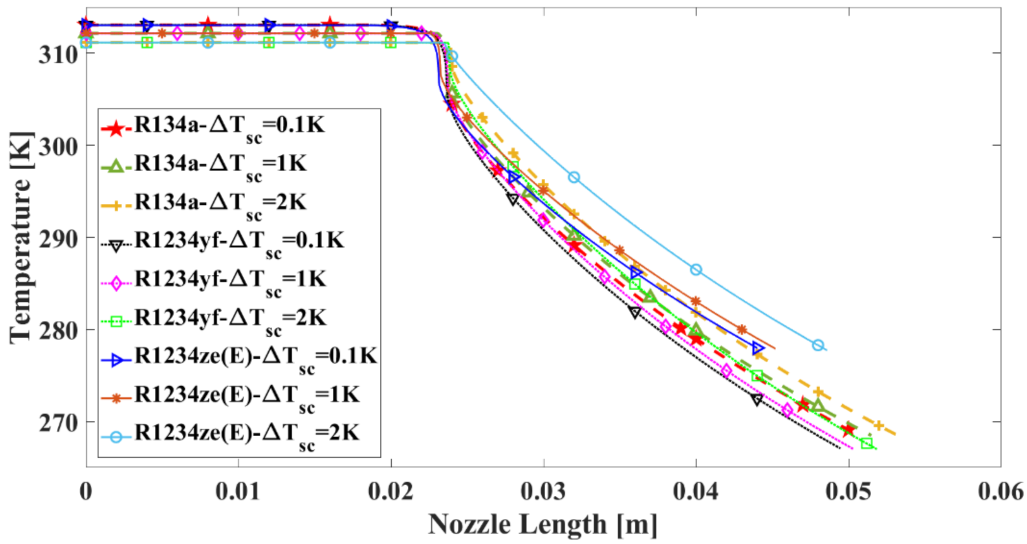


**(b)**

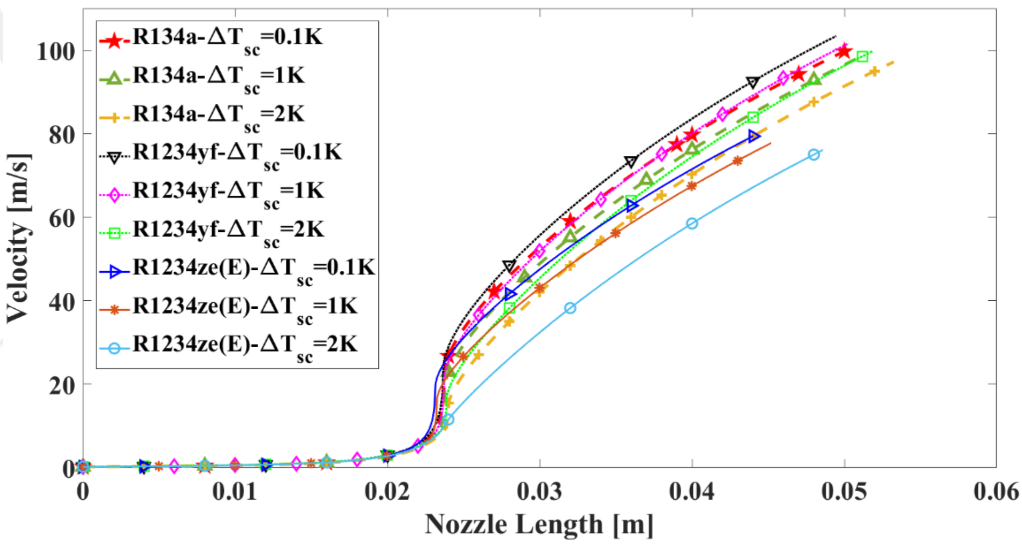


**(c)**

Figure 6.6 continues

As seen from Figure 6.6 (a), the outlet pressure nearly stays the same for each refrigerant at the investigated subcooling temperature difference values. Moreover, the outlet pressures of these three refrigerants are very close to each other. However, R134a has the lowest outlet pressure. When subcooling temperature difference increases, throat diameter decreases. For example, while increasing the subcooling temperature difference from 0.1 K to 2 K for R134a, the throat diameter decreases approximately 5%.

The distance between the throat and the point at which phase change occurs decreases when subcooling temperature difference increases. For the analyses of R134a in the described nozzle geometry, the refrigerant starts having phase change 5 mm earlier behind the throat at 0.1 K subcooling temperature difference. Furthermore, the position of the throat slightly moves backward due to the increase in the throat diameter when the subcooling temperature difference is decreased since the converging angle is kept constant under the design constraint of this study. When subcooling temperature is increased to 2 K, formation of the two-phase flow starts nearly at the throat. As seen from Figure 6.6 (b), the outlet temperature of R1234ze(E) is approximately 10 K higher than R1234yf and R134a for all of the subcooling temperature differences.

The outlet velocity of R1234ze(E) is lower when compared to R1234yf and R134a as shown in Figure 6.6 (c). R1234yf has slightly higher velocity than R134a. Although subcooling temperature difference has a little effect on the outlet velocity for a refrigerant, velocity profile is affected by this parameter. While the subcooling temperature difference is increased, outlet velocity of the refrigerant decreases. Hence Mach number at the outlet decreases. The reason for the velocity decrease at higher subcooling differences is the lower quality of the refrigerant at the nozzle outlet. When the vapor content of the flow increases, the velocity of the refrigerant increases as well. That’s way, the velocity increment profile of a refrigerant from inlet to the throat is completely different from the profile from the throat the outlet.

The change in the motive nozzle efficiency as well is negligible with respect to subcooling temperature differences for a specific mass flow rate. Figure 6.7 (a), (b), and (c) display the pressure distributions throughout the motive nozzle at various mass flow rates for R134a, R1234yf, and R1234ze(E), respectively. Similar to subcooling temperature difference, the outlet pressure is very close to each other for R1234yf and R1234ze(E) at the investigated mass flow rates. R134a as well typically displays similar outlet pressures at the investigated cases, but they are lower than the others. Moreover, for lower mass flow rates, the outlet pressures are nearly identical for these three refrigerants as displayed better in Figure 6.8 (a).

There is a typical pressure profile displayed by the refrigerants with respect to the increased mass flow rate as seen from Figure 6.7. Outlet pressure increases when the mass flow rate is increased for these refrigerants. For all analyzed mass flow rates, R1234yf has the highest outlet velocity because of the highest quality at each mass flow rate when compared to the others; whereas R1234ze(E) displayed the lowest outlet velocity. However, when the mass flow rate is increased, the outlet velocity of R134a and R1234yf approaches to each other.

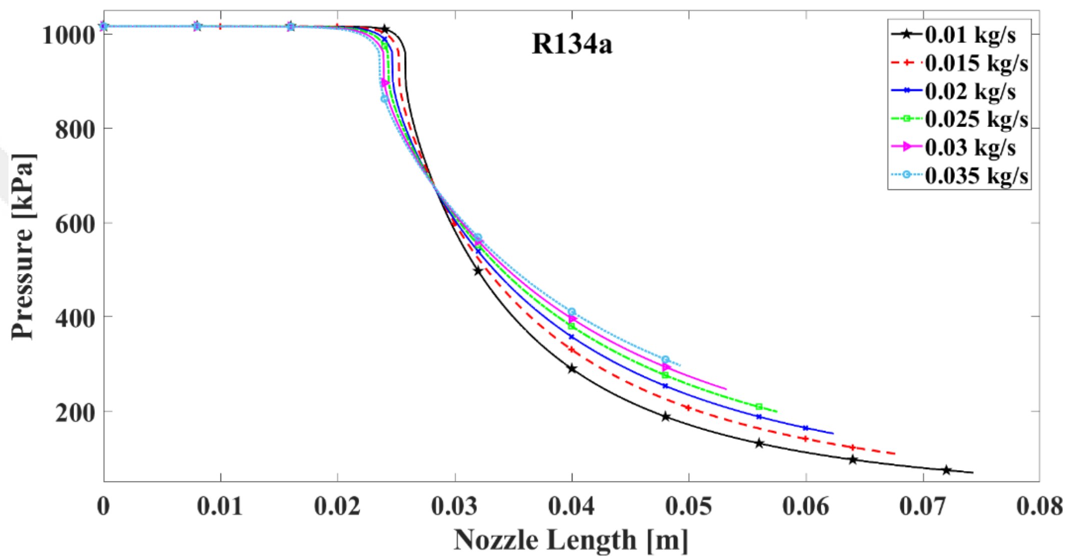


**(a)**

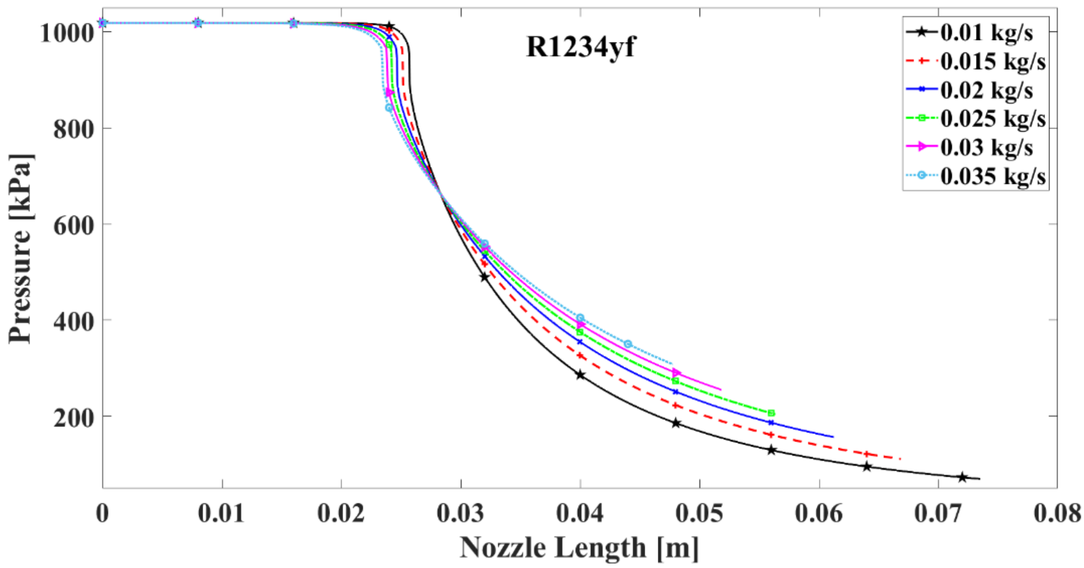


**(b)**

Figure 6.7 Effects of the mass flow rate on the pressure distributions throughout the motive nozzle for (a) R134a, (b) R1234yf, and (c) R1234ze(E)

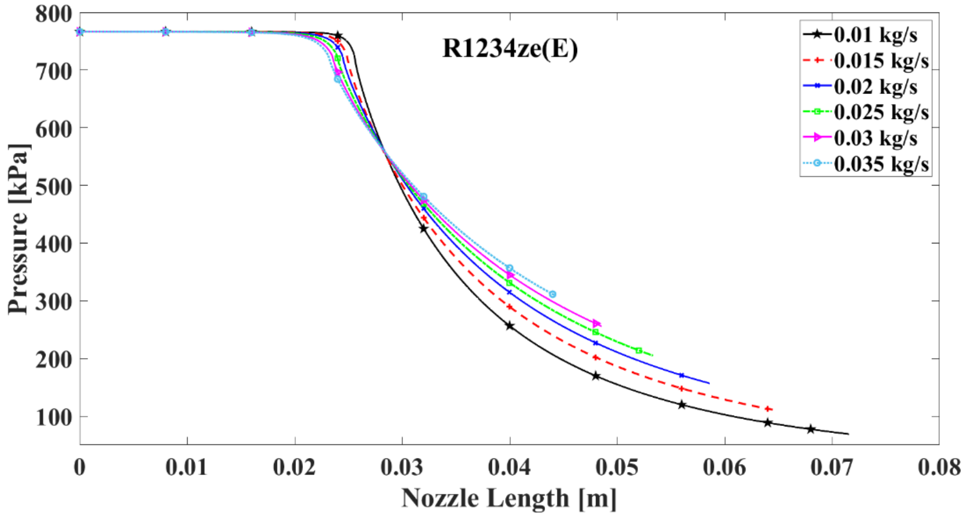


(c)

Figure 6.7 continues

Mach numbers at the outlet of the nozzle are very close to each other for R134a and R1234yf; whereas it is lower for R1234ze(E) as seen from Figure 6.8 (b). Furthermore, the outlet velocity decreases thereby decreasing the Mach number when the mass flow rate is increased for all of the refrigerants. The decrease in the outlet velocity corresponding to the increased mass flow rates is consistent with the decrease in quality of the two-phase fluid at the outlet.

The nozzle efficiency increases with the increased mass flow rates for all of the refrigerants as seen from Figure 6.8 (c). Lowest nozzle efficiency is calculated for R134a. The throat diameter as well is affected by the mass flow rate variations as seen from Figure 6.8 (d). Critical throat diameter is larger for R1234ze(E) than R1234yf and R134a while the throat diameter is calculated closer to each other for R1234yf and R134a. Figure 6.9 shows the influence of the motive nozzle outlet diameter on the outlet pressure, the Mach number at the motive nozzle outlet, and the motive nozzle efficiency. First of all, motive nozzle throat diameter stays the same with respect to the variations in the outlet diameter. The outlet pressure is nearly identical for R1234yf and R1234ze(E) as seen from Figure 6.9 (a). R134a as well displays a similar pressure distribution to the other two refrigerants although the outlet pressure of R134a is slightly lower. For higher outlet diameters, the outlet pressure is the same for these three refrigerants.

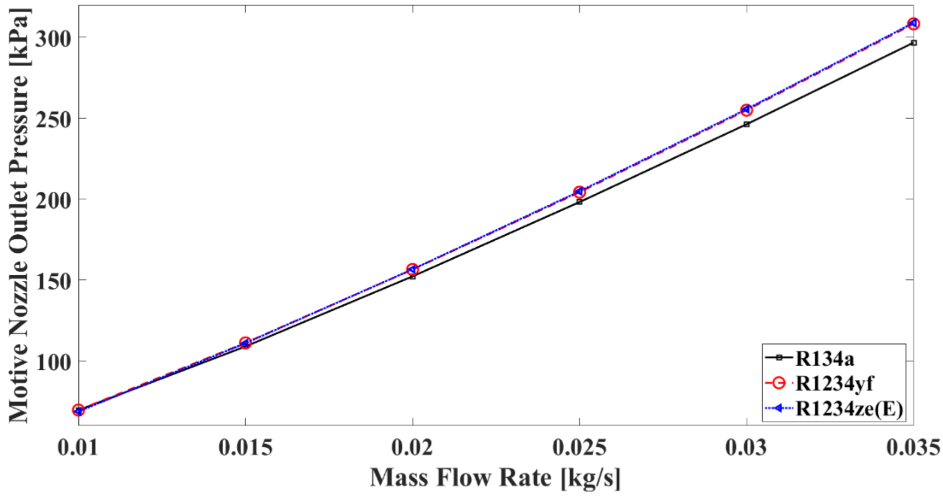


(a)

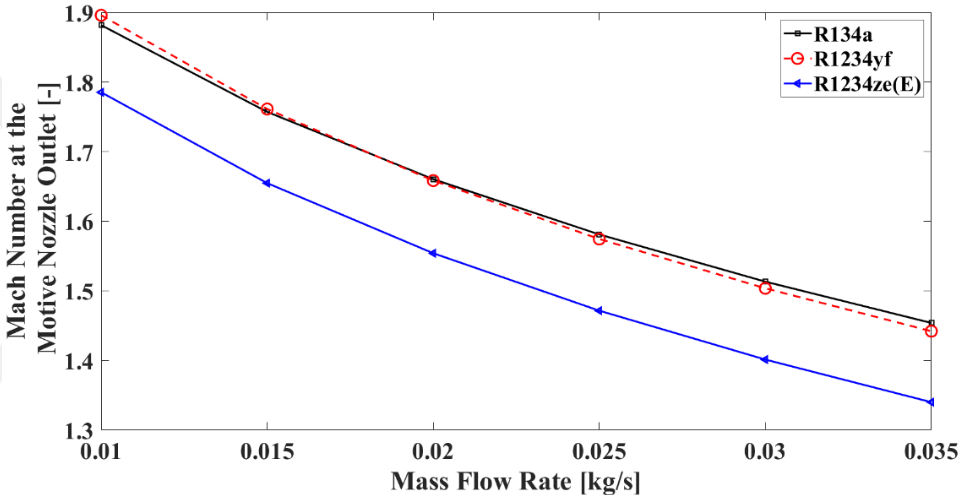


(b)

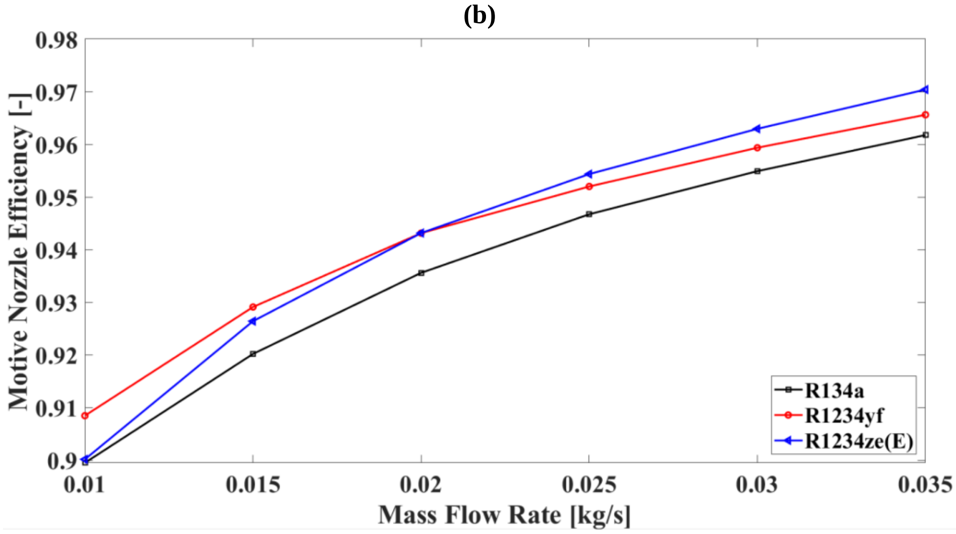


(c)

Figure 6.8 Effects of the mass flow rate variations on (a) the outlet pressure, (b) the Mach number at the motive nozzle outlet, (c) the motive nozzle efficiency, and (d) the throat diameter

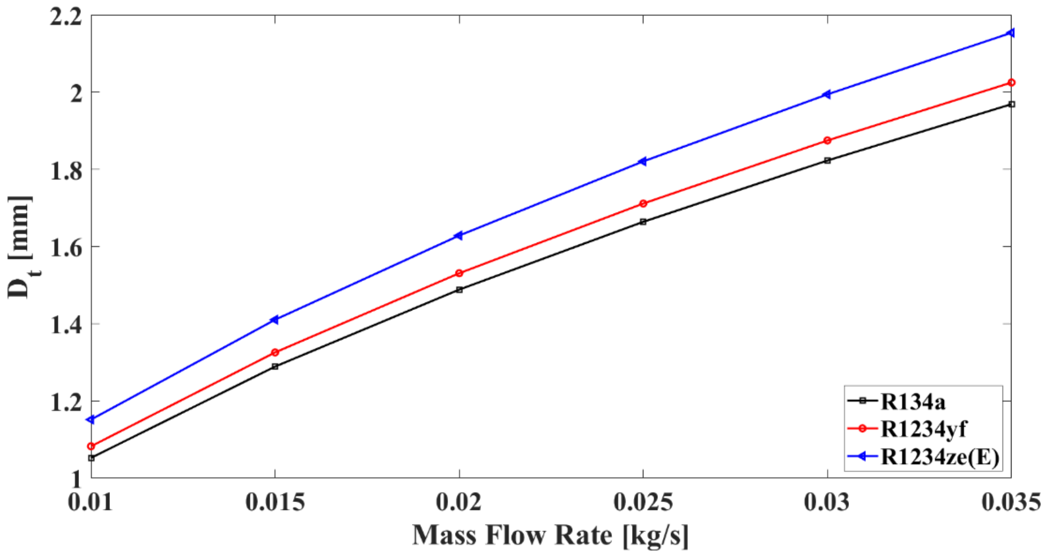


**(d)**

Figure 6.8 continues

As for the typical behavior of the nozzle, the outlet pressure decreases while the outlet diameter is increased. When the outlet diameter is increased for any refrigerant, the motive nozzle efficiency decreases as shown in Figure 6.9 (b) as opposed to efficiency variations with reference to increased mass flow rate. Similar to parametric mass flow rate investigations, R134a yields the lower nozzle efficiency with respect to the variations of the motive nozzle outlet diameter.

The outlet velocity increases when the outlet diameter is increased. The reason for the increase in the outlet velocity according to variations of the outlet diameters is the increase in the quality of the two-phase flow at the outlet. R1234yf has the highest velocity since the quality of the two-phase R1234yf is the highest for each investigated outlet diameter when compared to R1234ze(E) and R134a. Similarly, R1234ze(E) displays the lowest velocity at each outlet diameter because of the same reason concerned with the quality. As seen from Figure 6.9 (c), the Mach numbers at the outlet of the nozzle are practically the same for R134a and R1234yf, but R1234ze(E) has lower Mach numbers at the outlet according to various nozzle outlet diameters.

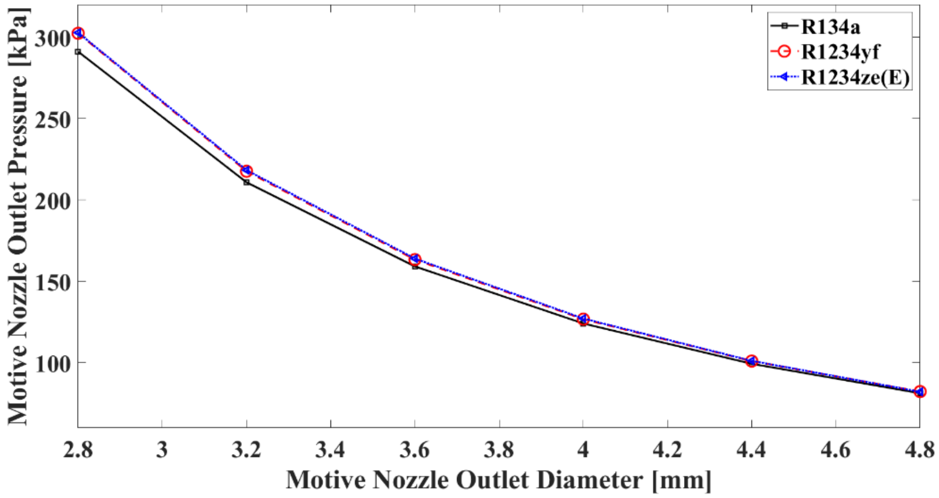


**(a)**

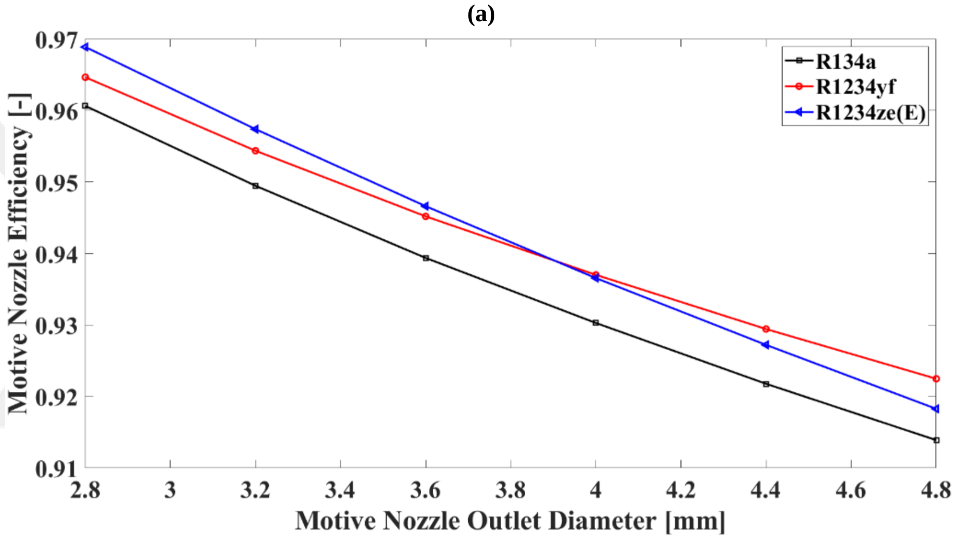


**(b)**

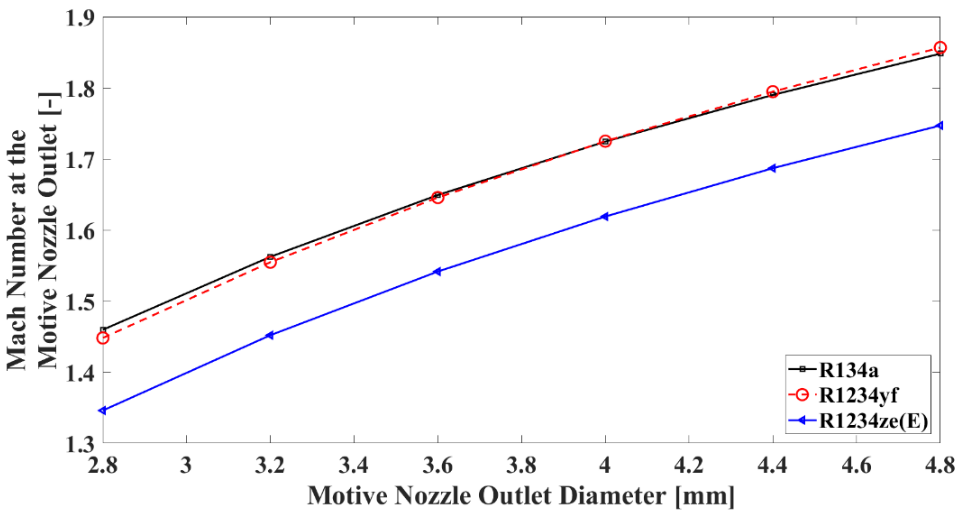


**(c)**

Figure 6.9 Influence of the motive nozzle outlet diameter on (a) the outlet pressure, (b) the Mach number at the motive nozzle outlet, and (c) the motive nozzle efficiency

There are three more results to be presented concerned with the effect of the inlet pressure or condensation temperature. First of all, pressure distributions are presented for R134a, R1234yf, and R1234ze(E) at various condensation temperatures in Figure 6.10 (a), (b), and (c). The operating parameter of condensation temperature is chosen intentionally to establish the link between the analyses of the motive nozzle and the EERC. Hence, the inlet temperature of the motive nozzle is determined with respect to the difference between the condenser temperature and subcooling temperature difference. As seen from Figure 6.10 (a) and (b), inlet pressures determined as the saturation pressures corresponding to condenser temperatures are very close to each other for R134a and R1234yf. The corresponding saturation pressure is lower for R1234ze(E) as shown in Figure 6.10 (c).

The outlet pressure nearly stays the same for each refrigerant when the inlet pressure is changed. Outlet pressure is very close to each other for R1234yf and R1234ze(E). On the other hand, R134a has the lowest outlet pressures among these three. In other words, although the inlet pressure is increased with respect to the increased condensation temperatures, outlet pressure is not affected. Actually, there is a very slight increase in the outlet pressure with respect to the increased inlet pressure, but it is regarded as negligible.

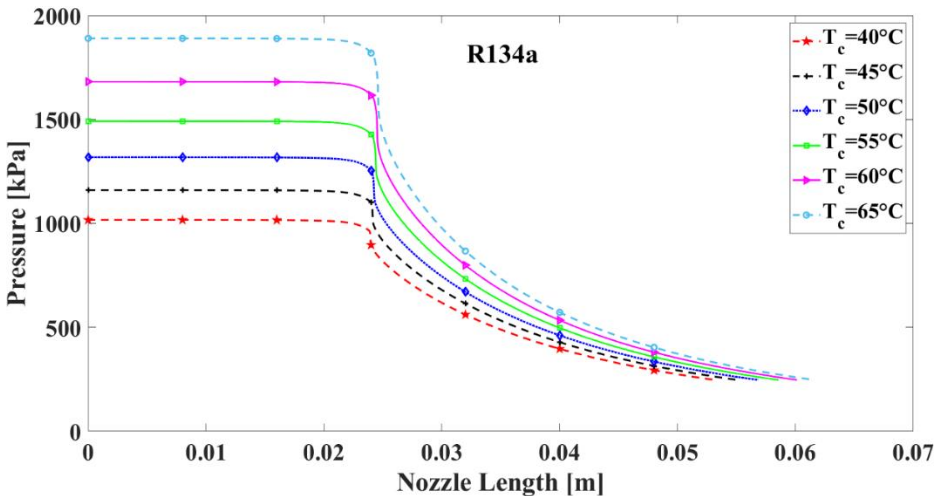


**(a)**

Figure 6.10 Pressure distributions throughout the motive nozzle at various condensation temperatures for (a) R134a, (b) R1234yf, and (c) R1234ze(E)

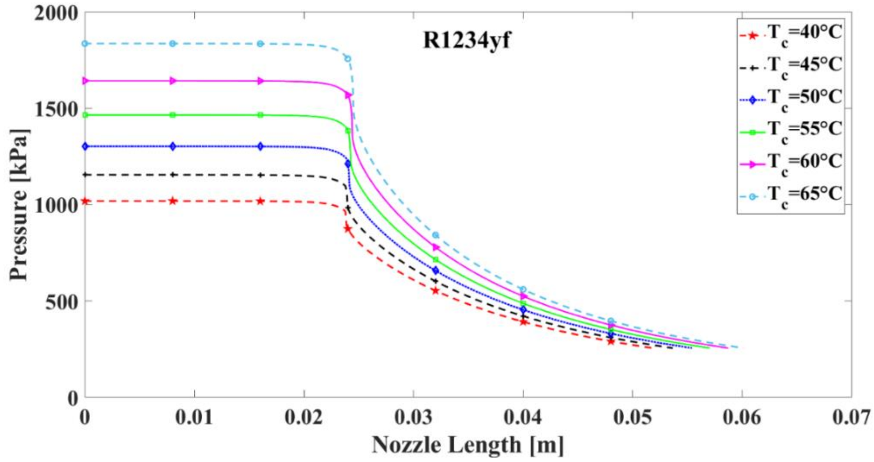


**(b)**

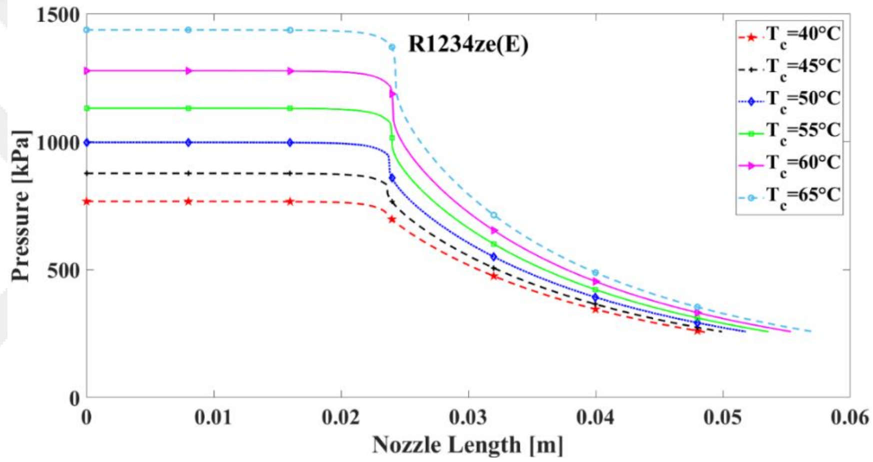


**(c)**

Figure 6.10 continues

The same trend is observed as well in the study of Tsuru et al. (2014). Tsuru et al. (2014) compared numerical temperature and pressure distributions based on the same nozzle with the experimental data obtained for the tank pressure of 7.2, 8.0, 9.2, and 10.3 MPa in some part of their study. When the inlet pressure was increased in their study, the outlet pressure slightly and negligibly increased with respect to the numerical results. By the way, experimental inlet conditions could not be adjusted for 8.0, 9.2, and 10.3 MPa. For all of these three experiments, experimental inlet pressure was approximately 7 MPa. The reason for this discrepancy was explained in the original manuscript as setting the tank pressure to the supercritical pressures (since the critical pressure of $CO_2$ is 7.38 MPa) and the condition of the experiment which was not saturated. As a result, only the case of 7.2 MPa tank pressure corresponding to 6.7 MPa motive nozzle inlet pressure is used even in the experimental validation presented in this section.

As seen from Figure 6.11 (a), (b), and (c), the pressure distribution throughout the nozzle has a similar profile for all of the refrigerants. Phase change nearly starts at the throat for all of the investigated inlet pressure cases. When the inlet pressure or condensation temperature is increased, the pressure decreases more from the inlet to the throat.

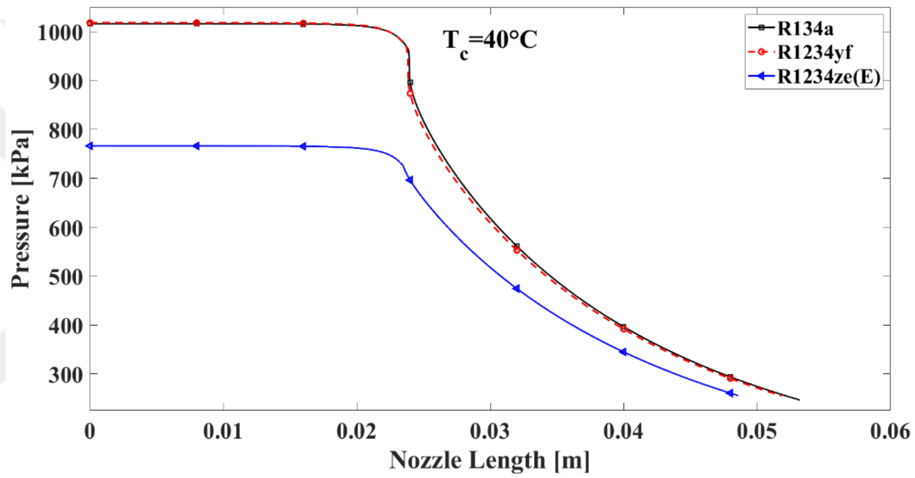


(a)

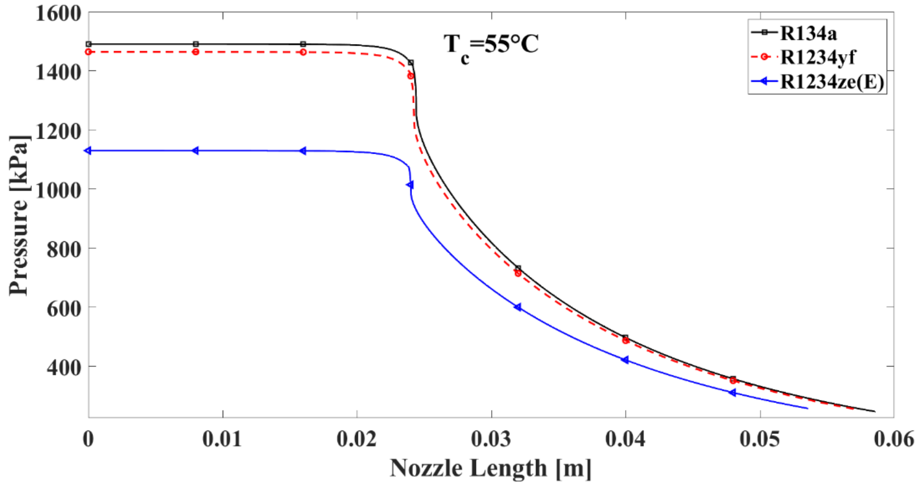


(b)

Figure 6.11 Comparison of the pressure distributions for R134a, R1234yf, and R1234ze(E) at the condensation temperatures of (a) 40 °C, (b) 55 °C, and (c) 65 °C

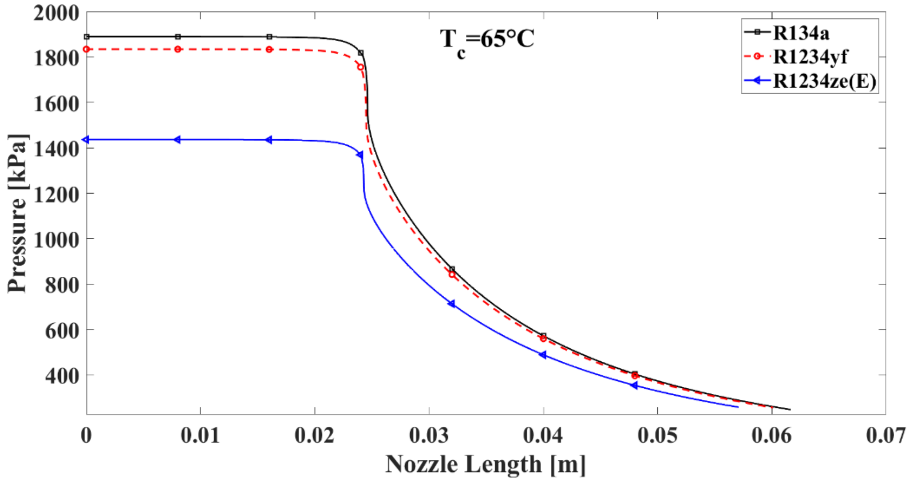


**(c)**

Figure 6.11 continues

Figure 6.12 (a), (b), and (c) shows the variations of the throat diameter, motive nozzle outlet velocity, and outlet Mach number with reference to the condenser temperature. When condenser temperature is increased, throat diameter decreases. Throat diameters are closer to each other for R134a and R1234yf based on the inlet pressure as shown in Figure 6.12 (a). However, R1234ze(E) has the highest throat diameter when compared to the others at the same inlet pressures.

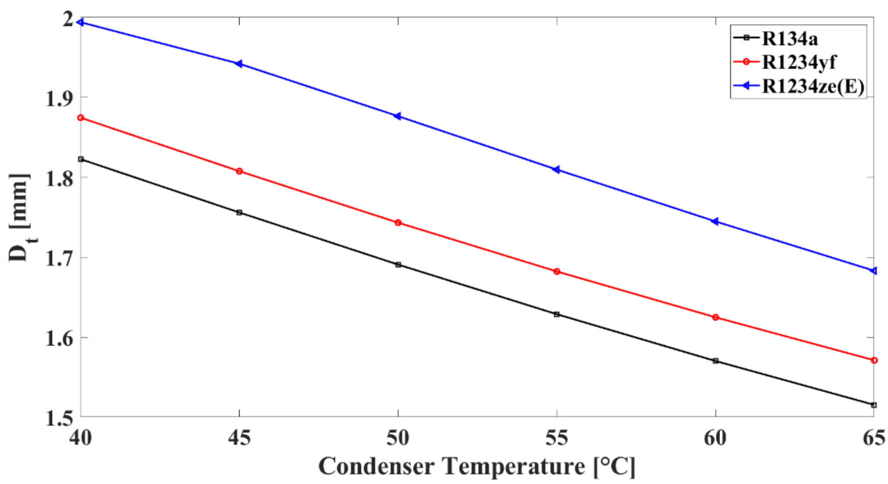


**(a)**

Figure 6.12 Variations of (a) the throat diameter, (b) the motive nozzle outlet velocity, and (c) the Mach number at the motive nozzle outlet for R134a, R1234yf, and R1234ze(E) according to condensation temperature

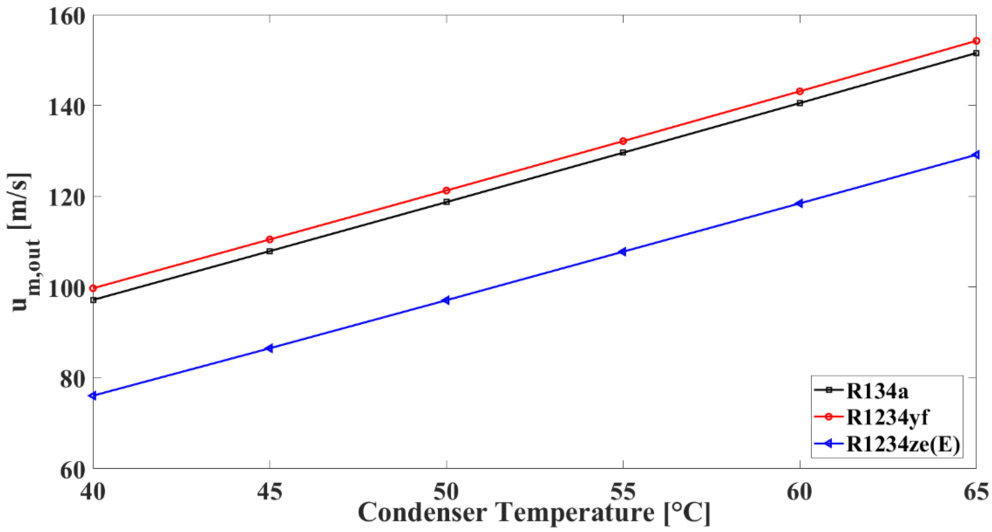


(b)

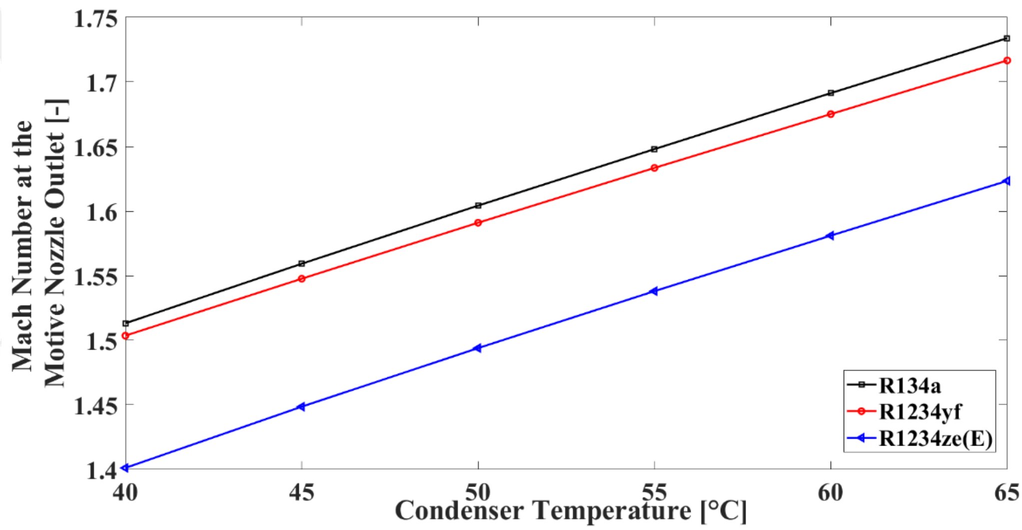


(c)

Figure 6.12 continues

Opposed to the throat diameter, motive nozzle outlet velocity increases while the inlet pressure is increased as shown in Figure 6.12 (b). Similar to variations in the throat diameter, the outlet velocity of R134a and R1234yf is very close to each other. R1234ze(E) has the lowest velocity when compared to these two refrigerants within the investigated range. Increased outlet velocity is concerned with the increased quality of the refrigerant at that point. R1234ze(E) has the lowest outlet quality and R1234yf has the highest outlet quality. Highest outlet Mach numbers are calculated for R134a and R1234ze(E) yields the lowest values. The trend of the outlet Mach numbers according to the inlet pressures is very similar to each other for R134a and R1234yf.

In conclusion, 1D model of the motive nozzle which is the essential part of the two-phase ejector is established under steady-state, equilibrium, and adiabatic flow conditions. The converging and diverging parts of the motive nozzle are divided into infinitesimally small computational grids. For each computational grid, the total derivatives of the density, velocity, enthalpy, and pressure are calculated implicitly. Hence, outlet values of these parameters could be calculated for each computational grid. The motive flow directly comes from the condenser in the EERC configuration. Therefore, the refrigerant is expected to be in compressed liquid state at the inlet of the nozzle.

1D model presented in this study is validated both experimentally and numerically with reference to previous studies provided in the literature. The verifications are made through the $CO_2$ nozzles. However, the investigated refrigerants are R134a, R1234yf, and R1234ze(E). The agreement between the experimental data obtained from the literature and the numerical results of the present model is found satisfactory. Therefore, 1D model under the above-given assumptions could be used to investigate subcooling temperature difference, mass flow rate, motive nozzle outlet diameter, and motive nozzle inlet pressure (saturation pressure corresponding to the condenser temperature) parametrically.

Subcooling temperature slightly affects the throat diameter. The outlet pressure and the nozzle efficiency as well is not influenced by the same parameter. This parameter mostly affects the distance between the throat and the point where two-phase flow formation starts. At higher subcooling temperatures, these two points are nearly the same. At lower subcooling temperatures, the distance under discussion increases. In other words, the refrigerant starts phase change before the throat. Outlet velocity slightly decreases when the subcooling temperature is increased due to the minute decrease in the quality at the outlet. The refrigerant stays in liquid phase from beginning to approximately the end of the converging section. The phase change starts around the throat. Hence, velocity profiles of the converging and diverging sections are completely different from each other.

When the mass flow rate is increased, the outlet pressure, motive nozzle efficiency, and the throat diameter increase. On the other hand, outlet velocity and Mach number decrease for these three refrigerants due to the decrease in the outlet quality of the two-phase fluid. Throat diameter is not affected by the motive nozzle outlet diameter as expected. To decrease the outlet pressure, motive nozzle outlet diameter is to be increased. Nozzle efficiency also decreases when the outlet diameter of the nozzle is increased. Outlet velocity and Mach number increase corresponding to the increase in the outlet diameter owing to the increased quality.

With reference to the investigated ranges of the condensation temperature, i.e. inlet pressure and the mass flow rate, the latter operating parameter has more influence on the throat diameter. Throat diameter decreases approximately 15-17% according to the increased inlet pressure for the investigated refrigerants. However, throat diameter increases more than 85% in accordance with the increased mass flow rate for the same three refrigerants. Outlet pressure is affected mainly by the outlet diameter and mass flow rate. Effect of the subcooling temperature difference and condenser temperature (inlet pressure) on the outlet pressure is ignored. Similarly, nozzle efficiency is affected by the mass flow rate and outlet diameter. Condenser temperature and subcooling temperature difference negligibly affects the nozzle efficiency.

To sum up, estimation of the direct location for the beginning of the phase change is a critical issue, hence it is to be determined based on the thermodynamic properties of the refrigerant throughout the nozzle. The results presented in this section enlighten the variations of some of the design aspects, i.e., motive nozzle throat and outlet diameter. Moreover, the influence of the operating parameters such as subcooling temperature difference, mass flow rate, and motive nozzle inlet pressure are discussed in terms of the outlet velocity, quality, pressure, and Mach number in addition to nozzle efficiency. Hence, the established results are beneficial for the preliminary experimental and numerical EERC studies including R134a, R1234yf, and

R1234ze(E). For further research, 1D motive nozzle model would be implemented into the 0D thermodynamic analyses in order to calculate more realistic performance evaluations.

# CHAPTER SEVEN
# SEMI-1D MODEL OF THE EJECTOR EXPANSION REFRIGERATION CYCLE

Semi-1D model is the combination of the 0D thermodynamic model and 1D motive nozzle model. The thermodynamic models of the two-phase ejector are made more comprehensive with the addition of 1D model of the motive nozzle since the exact suction nozzle pressure is calculated based on the actual operating conditions and nozzle design. The sucked flow which is mainly responsible for the cycle refrigeration capacity is determined properly with respect to the motive nozzle design and the operating conditions. With this semi-1D model, one of the most crucial assumptions, suction nozzle pressure is calculated and used in the overall performance evaluation of the cycle.

So far, it is proved from the thermodynamic analyses that not only ejector components, but the external components such as liquid-vapor separator as well has influence on both the design of the ejector and cycle performance. Previous thermodynamic analyses show that liquid-vapor separator efficiency is to be added to the models in addition to the efficiency of all ejector components to yield more realistic performance investigations. The thermodynamic investigations in the previous chapters emphasize also the importance of the ejector design rather than the operating conditions.

Therefore, thermodynamic modelling equations in the semi-1D model include the efficiency of the mixing section and liquid-vapor separator in addition to other ejector components to calculate the design and performance parameters more accurately. The analyses presented in this section has two objectives as follows; (i) presenting a preliminary design of the ejector and (ii) evaluating the ejector design and cycle performance according to the mixing section efficiency and different condensation temperatures. Proposed ejector design with respect to the outcomes of the semi-1D model is given in *Appendix*-1 in detail. Later on, these dimensions are used to manufacture the ejector to be used in the experimental analyses of R134a in the EERC.

The reason for choosing the mixing section efficiency for the investigations is the critical importance of this ejector component on the overall performance improvement of the EERC according to thermodynamic analyses conducted under CPM assumption (Atmaca et al., 2019a). Only condensation temperature is chosen since in terms of the motive nozzle 1D modelling, it is a more critical parameter than the evaporator temperature (Atmaca et al., 2020a). Moreover, Lawrence (2012) as well made the parametric operating condition analyses only with respect to the condensation temperatures. Effect of the evaporating temperature would be investigated as the further research. Within the content of this thesis, only effect of the condensation temperature is analyzed to combine the parametric investigations of the motive nozzle with the thermodynamic modelling approach.

R134a and R1234yf are the working fluids chosen for the investigations. R1234ze(E) is omitted since the evaporation pressure defined as the saturation pressure at the selected evaporation temperature is lower than the calculated outlet pressure of the reference nozzle and operating conditions for R1234ze(E). Hence, for the reference nozzle and operating conditions, it is not possible for R1234ze(E) to be sucked into the ejector. As a result, this semi-1D model is a quick and practical tool to propose preliminary designs and performance evaluations. One of the biggest literature contribution of this thesis is the semi-1D model.

### 7.1 Inputs and Outputs of the Semi-1D Model

Only motive nozzle model is 1D in the semi-1D modelling approach. The mixing process of the motive and suction fluids is modelled with the thermodynamic modelling equations. CAM ejector theory is chosen in the design concepts of the most of the EERC applications. Hence the mixing assumption in the semi-1D model is chosen as the CAM approach. CPM ejector is not a constant shape ejector since the outlet diameter of the mixing section is to be changed in accordance with the variations in the operating conditions.

The inputs are arranged for the preliminary design calculations with respect to the initial experiments of the EERC. Inputs of the semi-1D model is comprised of the inputs of the EERC thermodynamic model such as evaporator temperature, condenser temperature, evaporator superheat temperature difference, condenser subcooling temperature difference, compressor efficiency, working fluid selection, efficiencies of the suction nozzle, mixing section, diffuser, and liquid-vapor separator; inputs of the motive nozzle 1D model, i.e. motive nozzle inlet diameter, mass flow rate of the primary fluid, convergence angle, divergence angle, motive nozzle outlet diameter, estimated throat diameter, and computational grid length; and some more additional design parameters as wall thickness (*wt*) of the motive nozzle at the outlet which could be determined with respect to the selected material, suction nozzle angle, diffuser angle, and minimum required spacing (*mrs*) for the secondary flow in the suction nozzle where the outlet of the motive nozzle is located.

Motive nozzle efficiency is the output of 1D motive nozzle model, hence it is not given among the inputs. It is calculated according to nozzle design and operating conditions. Inputs of the thermodynamic models and 1D model of the motive nozzle are discussed in Chapter Four and Chapter Six, respectively. However, the additional geometrical inputs are clarified as given in Figure 7.1. Therefore, it is easier to present the link between the proposed geometrical inputs and target outputs.

The target outputs are performance improvement ratio, entrainment ratio, and pressure lift ratio for the actual pressure drop rather than the assumed or optimum pressure drop, area ratio for the given motive nozzle outlet cross-sectional area and calculated mixing section cross-sectional area, cooling capacity, secondary fluid mass flow rate, total ejector mass flow rate, mixing section diameter, suction nozzle diameter at the outlet of the motive nozzle, resultant pre-mixing section length or pre-mixing section length with respect to the minimum required space as a design constraint, mixing section length, diffuser outlet diameter, and diffuser length with reference to diffuser angle stated by ESDU (1992) with reference to Rusly et al. (2005).

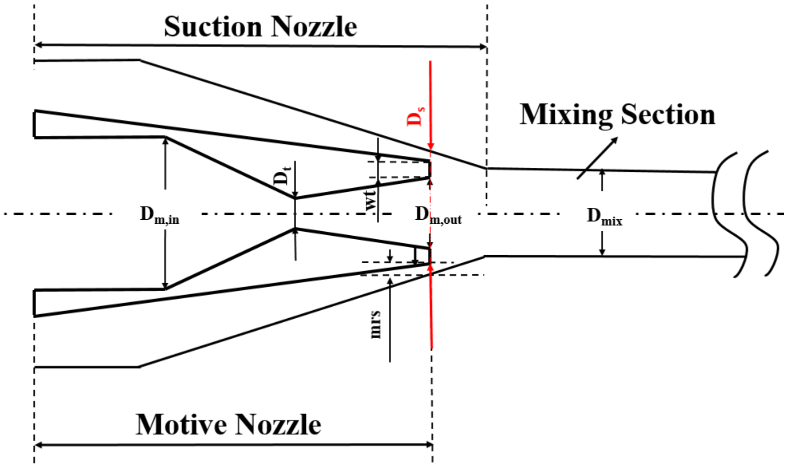


Figure 7.1 Representation of the wall thickness of the motive nozzle at the outlet and minimum required space in addition to some of other design parameters

Suction nozzle diameter is given for the point where motive nozzle outlet is located and both primary and secondary fluid streams meet as seen in Figure 7.1. Calculated suction nozzle diameter may be different than the modified suction nozzle diameter when the minimum required space (mrs) as well added to the diameter. In the ejector designs of this thesis, minimum required space is chosen as 1 mm by default if the calculated space according to motive nozzle outlet diameter, wall thickness, and calculated suction nozzle diameter is less than 1 mm. If it is larger than 1 mm, it stays as is.

## 7.2 Modified Thermodynamic Equations of the Semi-1D Model

In the semi-1D modelling approach, one of the assumptions regarding the motive nozzle outlet pressure is eliminated and the motive nozzle outlet velocity, pressure, and enthalpy, and nozzle efficiency are calculated directly with respect to the actual nozzle geometry and operating conditions as discussed in Chapter 6. Therefore, suction nozzle pressure is determined based on an actual nozzle. To sum up, the thermodynamic modelling equations are replaced with the 1D modelling equations of the motive nozzle in the semi-1D model. For the secondary flow analyses, equation set stays the same. However, the outlet enthalpy and velocity is determined according to the calculated motive nozzle outlet pressure.

Equations of the mixing section for the constant area mixing assumption are given only since the equations of the diffuser as well are not changed. The CAM ejector equations are different from the previous constant area mixing modelling equations for pure thermodynamic modelling approach presented in Chapter 4. The following equation set includes the mixing section and liquid-separator efficiency as well. Equations of the mixing section for the conservation of mass, momentum, and energy are as follows;

$$\begin{aligned} u_{mix,out} &= \lfloor P_s(a_{m,out} + a_{s,out})C \rfloor - \lfloor P_{mix,out}(a_{m,out} + a_{s,out})C \rfloor \\ &+ \left[ \eta_{mix} u_{m,out}(r_{d,out}\eta_{vap} + (1 - r_{d,out})(1 - \eta_{liq})) \right] \\ &+ \left[ \eta_{mix} u_{s,out}(r_{d,out}(1 - \eta_{vap}) + (1 - r_{d,out})\eta_{liq}) \right] \end{aligned} \tag{7.1}$$

$$\begin{aligned} h_{mix,out} &= (r_{d,out}\eta_{vap} + (1 - r_{d,out})(1 - \eta_{liq}))h_{m,in} \\ &+ (r_{d,out}(1 - \eta_{vap}) + (1 - r_{d,out})\eta_{liq})h_{s,in} - \frac{u_{mix,out}^2}{2} \end{aligned} \tag{7.2}$$

$$(a_{m,out} + a_{s,out})C\rho_{mix,out}u_{mix,out} = 1 \tag{7.3}$$

The mixing section efficiency is added to the conservation of momentum equation with reference to the final report of Liu & Groll (2008). Mixing section equations presented by Liu & Groll (2008) include the pressure, velocity, and cross-sectional areas of both streams and total flow in addition to mixing section efficiency. The motive nozzle of Liu & Groll (2008) is converging only. In the modelling equation presented in this section, not only outlet pressure, but the mixing section cross-sectional area is to be calculated as well. Actually, the conservation of momentum equation presented in this section is the simplified version of Liu and Groll (2008). However, the modelling equation presented here takes the liquid-vapor separator efficiency into account as well. Hence, the mixing section equations are the first modelling equations considering both the mixing section efficiency and liquid-vapor separator efficiency for the constant area mixing approach when compared to the available CAM modelling equations of the literature.

### 7.3 Requirement of the Area Increment Factor, *C* for the Modelling of the Constant Area Mixing Section

The mixing section efficiency is easily added to the equation of the constant pressure mixing equation since there is not any cross-sectional area requirement regarding with this assumption. Therefore, the mixing section efficiency definition was firstly introduced for the constant pressure mixing ejector by Eames et al. (1995). However, addition of the mixing section efficiency to the constant area mixing section equation for the conservation of momentum declared by Equation 4.10 results in a convergence problem for the iterations of the constant area mixing modelling equations. It could be concluded that for the thermodynamic models including no geometrical inputs where cross-sectional areas are defined as the area per unit total ejector flow, addition of the mixing section efficiency results in the convergence problem.

For example, Ersoy & Bilir (2010) investigated the effects of the ejector component efficiencies. They only considered the motive nozzle, suction nozzle, and the diffuser. Because of this convergence problem, the mixing section efficiency could not be implemented into the thermodynamic models easily. On the other hand, mixing section efficiency is the most important component and the models must include the efficiency of this section as a result of the previous thermodynamic analyses.

Addition of the mixing section efficiency into the equations of the constant pressure mixing section does not cause a problem since there are not any design constraints with respect to this assumption. According to the mixing assumption, the pressure stays the same throughout the mixing process. It is assumed that the mixing chamber of the ejector has a kind of geometry enabling constant pressure mixing process. As a result, there is no geometrical constraint for constant pressure mixing assumption.

However, for the thermodynamic modelling approach including no geometrical inputs, addition of the mixing section efficiency with reference to Liu and Groll (2008) results in the decrease in the mixing section outlet velocity. According to the constant area mixing assumption, the area of the mixing section stays the same and this area is the total of the occupied areas of the primary and secondary fluid streams per unit total ejector mass flow rate in the pure thermodynamic modelling approach. It should be reminded that pure thermodynamic modelling approach is not capable of calculating the mass flow rates of the primary and secondary fluid streams due to the lack of the geometrical inputs, hence the cross-sectional areas are calculated in terms of the area per unit total ejector mass flow rate. When two fluid streams meet at the mixing section inlet, their flow rates are calculated as follows;

$$\dot{m}_m = A_m \rho_m u_m \tag{7.4}$$

$$\dot{m}_s = A_s \rho_s u_s \tag{7.5}$$

If there is an inefficiency in the mixing process, the outlet velocity decreases as declared by the definition of the mixing section efficiency with Equation 4.26 and the outlet density is negligibly affected by the change in the mixing section efficiency. Hence, if the cross-sectional area stays the same as the area of 100% efficient mixing process case, there would be a continuity problem since mass conservation is not established. For the 100% efficient mixing process, the total mass flow rate is given as

$$\dot{m}_t = (A_m + A_s) \rho_{mix} u_{mix} \tag{7.6}$$

When mixing process efficiency decreases, the proposed mixing cross-sectional area is to be higher than the calculated cross-sectional areas of the primary and secondary fluid flows. In other words, proposed cross-sectional area of the mixing section is required to be increased to satisfy the mass conservation since the outlet velocity decreases as a result of inefficient mixing process. To sum up, if the mixing section efficiency is introduced into the model, an area increment factor, $C$ as well is to be added to the model. The total mass flow rate is defined by the following equation with the area increment factor to compensate for the decrease in the outlet velocity as a result of the inefficient mixing process.

$$\dot{m}_t = (A_m + A_s)C\rho_{mix}u_{mix} \tag{7.7}$$

Geometrical representations are shown in Figure 7.2 (a) and (b) for the pure thermodynamic modelling approach including no geometrical inputs and semi-1D modelling approach including motive nozzle outlet diameter and wall thickness of the motive nozzle among the inputs, respectively. $a_{m,out}$ and $a_{s,out}$ are just occupied areas calculated for the specified conditions.

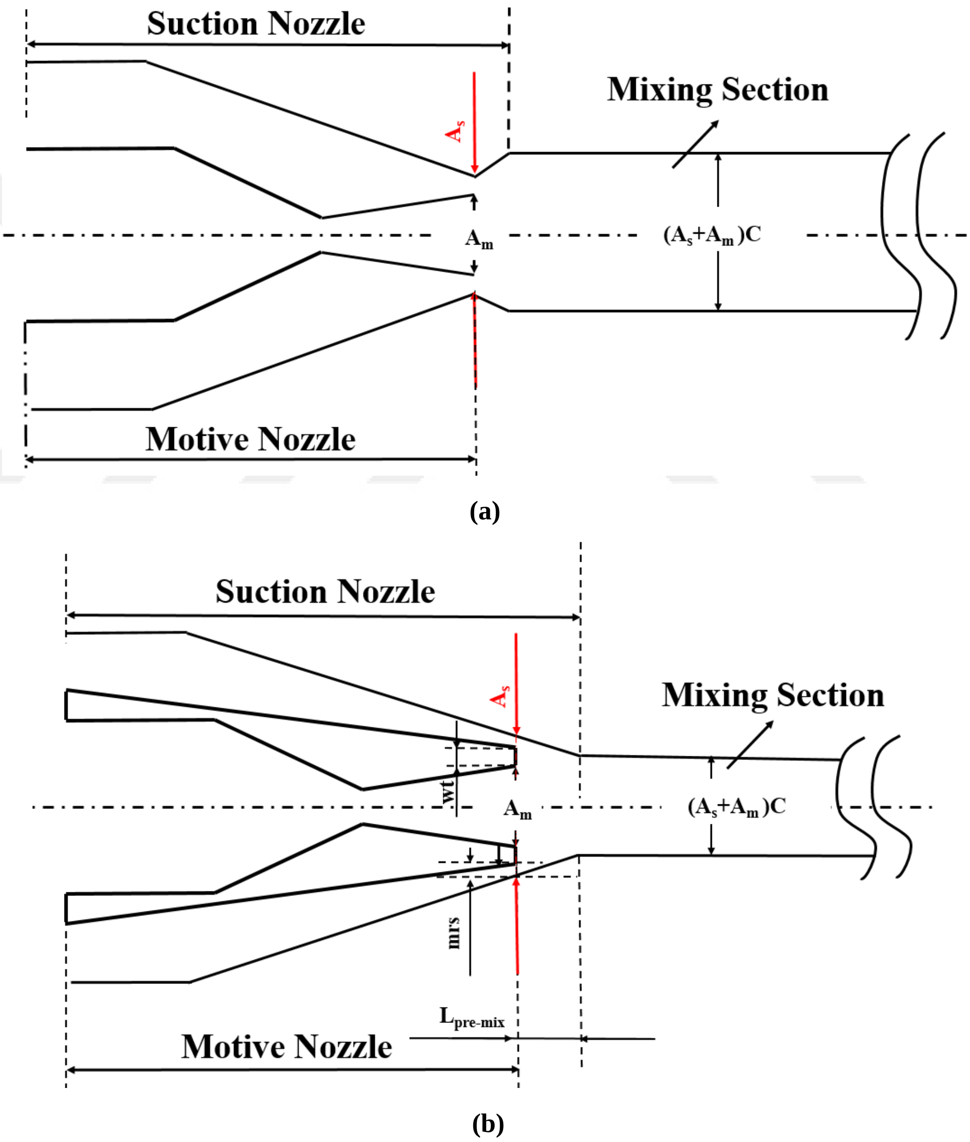


Figure 7.2 Schematic display of the increased mixing chamber cross-sectional area as a result of the inefficient mixing for (a) pure thermodynamic approach including no geometrical inputs and (b) semi-1D modelling approach taking wall thickness and motive nozzle outlet diameter into consideration

Any increment factor could be proposed and they could be rearranged with respect to other geometrical constraints. In the following section, for example, suction nozzle diameter is formulated taking the wall thickness of the motive nozzle at its outlet into consideration. Because of this reason, the increased diameter calculated for the inefficient mixing process case is lower than the suction nozzle diameter as seen from the schematic representation of ejector components in Figure 7.2 (b). Hence, a pre-mixing chamber length arises as some part of the suction nozzle.

Moreover, it could be modified if the remaining space between the suction nozzle and motive nozzle outlet is needed to be increased. However, for the pure thermodynamic modelling approach, there are not any constraints about the wall thickness and minimum required space. Therefore, the proposed mixing section diameter is larger than the suction nozzle diameter and an enlargement is declared at the mixing section inlet. To sum up, area increment factor is defined as $1/\eta_{mix}$ in the analyses of the initial ejector design which is for the manufacture of the ejector to be used in the preliminary experiments. Rest of the parametric investigations of the semi-1D model, area increment factor is chosen as *1.25*. As stated previously, any increment factor could be chosen. It should be stated that the performance and design parameters are obtained with respect to that specified area increment factor.

### 7.4 Geometrical and Performance Parameter Calculations from the Semi-1D Model

The solution algorithm is the combination of the 1D model of the motive nozzle and the thermodynamic models. Firstly, 1D modelling equations are solved for the motive nozzle as expressed in Chapter 6 in detail. Secondly, the 0D thermodynamic modelling equations are solved with reference to the constant area mixing assumption as discussed in Chapter 4. For constant area mixing approach, two iterations are required in order to calculate the entrainment ratio and mixing chamber outlet pressure.

Under the semi-1D modelling approach, primary fluid mass flow rate is assumed to be known and entrainment ratio is calculated iteratively. Hence, the mass flow rate of the secondary fluid and total ejector fluid are calculated accordingly. A similar approach is presented for the ejector design given in Chapter 5. However, according to the design methodology displayed in Chapter 5, cooling capacity is assumed to be known and the proposed design is based on the optimum operating conditions (optimum suction nozzle pressure). With respect to this semi-1D modelling approach, only primary fluid mass flow rate is known and the cooling capacity is calculated in accordance with the sucked flow.

$$\dot{m}_s = w\dot{m}_m \tag{7.8}$$

$$\dot{m}_t = \dot{m}_m(1+w) \tag{7.9}$$

$$\dot{Q}_e = \dot{m}_s(h_{e,out} - h_{e,in}) \tag{7.10}$$

Area ratio according to the semi-1D modelling approach is different than the previously stated area ratio given in the thermodynamic modelling approach since the mixing section cross-sectional area is increased to solve the continuity problem. It is defined as the ratio of the cross-sectional area of the mixing chamber to that of motive nozzle as follows;

$$\phi = \frac{A_{mix,cs}}{A_{m,out,cs}} \tag{7.11}$$

Finally, mixing section and suction nozzle diameters which are the critical design parameters are defined as

$$D_{mix} = \sqrt{\frac{4\dot{m}_m(1+w)}{\pi\rho_{mix}u_{mix}}} \tag{7.12}$$

$$D_s = \sqrt{\frac{4}{\pi}\left[\frac{\dot{m}_s}{\rho_s u_s} + \frac{\pi(D_{m,out} + 2wt)^2}{4}\right]} \tag{7.13}$$

## 7.5 Derivation of the Other Geometrical Parameters from the Critical Design Parameters

When the critical design parameters, i.e. mixing section diameter and suction nozzle diameter, are calculated, the premixing length could be calculated with reference to suction nozzle angle stated by ESDU (1992). Minimum required space as well could be considered as a design constraint at this point to change the suction nozzle diameter and pre-mixing length. Actually, the performance and design parameters such as performance improvement ratio, entrainment ratio, area ratio, pressure lift ratio, secondary fluid mass flow rate, total mass flow rate, cooling capacity, mixing section diameter, suction nozzle diameter at which two fluid streams meet are the target outputs and calculated as a result of the calculation routine.

Premixing section length, mixing section length, diffuser length, and diffuser outlet diameter could also be defined under this modelling approach. However, they are not determined based on the 1D mixing modelling of the primary and secondary fluid streams. They are determined combining the calculated mixing section diameter and the design suggestions of ESDU (1992) and Keenan, Neumann, & Lustwerk (1950). Suction nozzle converging angle and diffuser diverging angle is given as 10° and 3.5° (half angle) by ESDU (1992) as stated by Rusly et al. (2005).

Till this point, premixing length is calculated with the collected design knowledge from the literature. Moreover, Rusly et al. (2005) used the relation of $(L_{mix}+L_{pre\text{-}mix})/D_{mix}$ and $P_m/P_s$ presented by Keenan et al. (1950) to define the constant area mixing section length. The original plot showing the relationship between $(L_{mix}+L_{pre\text{-}mix})/D_{mix}$ and $P_m/P_s$ is given in Figure 7.3 with reference to Keenan et al. (1950). The same plot is given in Figure 7.4 as well more clearly collecting the data from the original plot.

The same plot is rearranged in Figure 7.4 collecting the data from the original plot given in Figure 7.3. $P_i$ and $P_o$ represent the inlet pressures of motive and suction fluids, respectively. $L$ is the constant area mixing section length and $y$ is the pre-mixing section length in Figure 7.3. Lastly, $D$ in the same figure is the minimum mixing chamber diameter. So far, mixing section length is also calculated after mixing section diameter is specified.

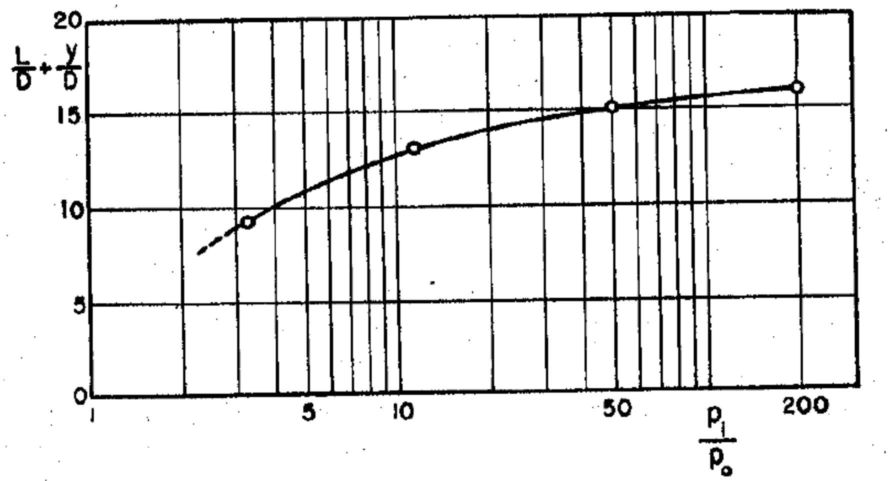


Figure 7.3 Optimum length from the primary nozzle exit to the diffuser entrance given as a function of the pressure ratio of the motive fluid to suction fluid (Keenan et al., 1950)

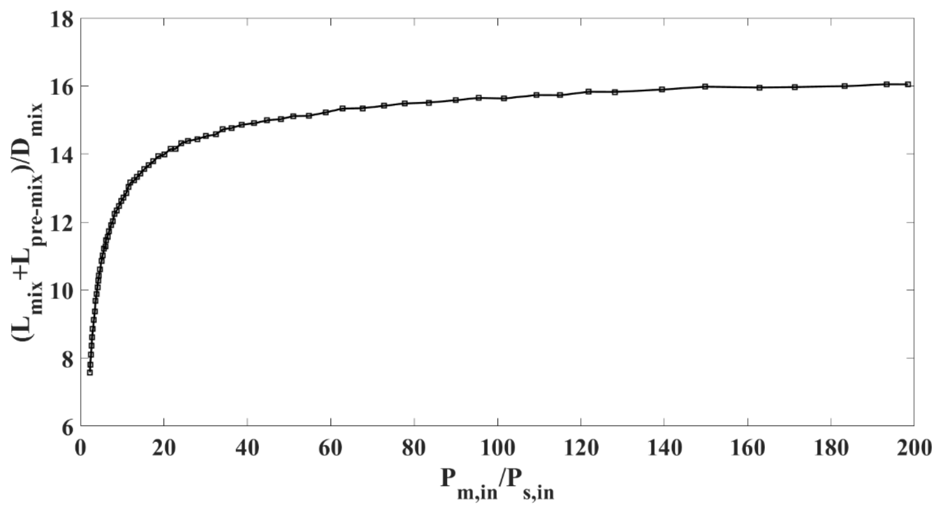


Figure 7.4 Display of the optimum length from the primary nozzle exit to the diffuser entrance according to pressure ratio of the motive fluid to suction fluid collecting the data from the original plot (Keenan et al., 1950)

Mixing section diameter is critical design parameter affecting most of the other design parameters. Rusly et al. (2005) stated that diffuser length is recommended to be 8 times of the constant area mixing chamber diameter with reference to Al-Khalidy and Zayonia (1995) and Henzler (1983). Finally, diffuser outlet diameter is calculated using the diffuser length, constant area mixing chamber diameter, and diffuser angle suggested by ESDU (1992).

To sum up, after calculating the mixing chamber diameter, the other dimensions covering the mixing section length are determined for the preliminary ejector design. However, this kind of preliminary design is not enough. The whole mixing process is to be modelled in order to show that the proposed design is working properly. Moreover, for the initial design of the ejector to be used in the preliminary testing, this kind of geometrical specifications are very beneficial.

For more comprehensive design comments, comprehensive CFD analyses are required. It should be emphasized one more time that the geometrical design specifications concerned with the mixing section length and the diffuser is just for the initial CFD analyses, rough designs or preliminary testing. For more elaborate design comments, detailed CFD analyses or experimental works are required. As in the 1D modelling approach of motive nozzle, the proposed geometry is to be checked according to the actual flow characteristics. Correlations and relations are used just for design proposals. Hence, parametric analyses are conducted for only basic design parameters such as constant area mixing section diameter and performance analyses under semi-1D modelling approach. Rest of the dimensions obtained from the design relations of the literature are only used for the rough design specifications. In other words, they are just used for the initial dimension definitions.

In the design procedure of this thesis, firstly the ejector given in Ersoy & Sag (2014) is manufactured and experimental boundary conditions for the motive nozzle analyses and thermodynamic analyses are collected for the initial ejector design. It is important to discover the system characteristics for the constructed experimental set-up. Later on, a new design is proposed according to the collected experimental boundary conditions. The initial design determined in this way is aimed to be manufactured and used in the preliminary testing. The design to be used in the preliminary EERC tests is explained clearly in the next section.

## 7.6 Results of the Semi-1D Model

In this section, two kinds of results are declared. Firstly, the initial design analyses are expressed. Secondly, the effects of the mixing section efficiency on the performance parameters are displayed and the effects of the operating conditions on the performance and design parameters are discussed making use of semi-1D modelling approach.

### *7.6.1 Initial Design*

Initial design is specified according to the experimental boundary conditions. First of all, a reference ejector mostly according to the design of Ersoy & Sag (2014) is manufactured and a test is conducted. The throat diameter of the motive nozzle is decreased to 1.4 mm and outlet diameter is increased to 3 mm in the current design after the improper results obtained from the experiments with the original motive nozzle of Ersoy & Sag (2014). The converging and diverging lengths are 15.2 mm and 20.2 mm, respectively.

At the beginning, the cause of the improper results is thought to be the design of the motive nozzle proposed by Ersoy & Sag (2014). Hence, it is changed with reference to outcomes of the flow analyses making use of 1D motive nozzle model. However, it is later discovered that the manufacture of the nozzle is not appropriate. The biggest problems concerned with the manufacture of the motive nozzle is that the converging length of the nozzle is very short. In this way, the inlet conditions occurred in the presently established experimental set-up are obtained. The design proposal is made based on the main operating conditions collected from the experimental set-up and reference operating conditions used in the thermodynamic models.

Average gage pressures for the condenser and evaporator are 15.36 bar and 1.76 bar, respectively. They are directly measured from the experiments. They are the high and low pressures which are typically formed in the system. Superheat and subcooling temperature differences used from the experiments are 22.7 K and 1.8 K, respectively. Compressor isentropic efficiency is calculated as 0.6 from the experimental data. Refrigerant is R134a. Mass flow rate of the primary fluid is calculated from the measured data as 0.019 kg/s.

For the new ejector design proposal, the inlet diameter is 12 mm according to 1D analyses of the motive nozzle in the semi-1D model. Converging and diverging lengths are 25.2 mm and 17. 2 mm, respectively. Outlet diameter of the motive nozzle is 2.5 mm. Wall thickness of the motive nozzle at the outlet is assumed to be 1.5 mm. Converging suction nozzle angle and diverging diffuser angle is 15° and 3.5°, respectively.

Minimum required space for the suction nozzle diameter calculation is taken as 1 mm. Efficiency of the motive nozzle is calculated under 1D modelling approach. The efficiencies for the suction nozzle, mixing section, diffuser are 0.9, 0.95, and 0.8, respectively. As for the liquid-vapor separator, vapor separation efficiency and liquid separation efficiency are assumed to be 0.95 and 0.9 in the respective order. The technical drawings of the proposed design are given in Appendix-1.

The full assembly proposed under these operating conditions and assumptions is shown in Figure 7.5. In terms of the experimental conditions, it is important to observe the high and low pressures that could be occurred in the system in addition to the primary fluid mass flow rate, superheating and subcooling temperature differences. Calculated design and performance parameters are given in Table 7.1.

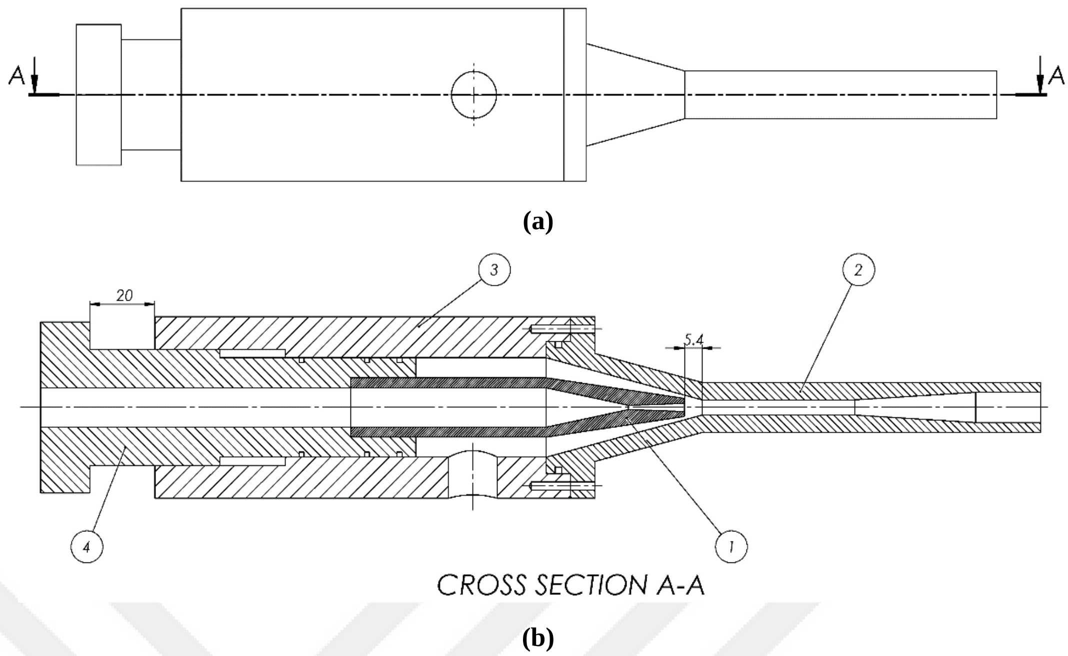


Figure 7.5 Technical drawing of the ejector assembly displaying the ejector sub-sections as follows; (1) Motive nozzle, (2) Suction (Secondary) nozzle-Mixing section (chamber)-Diffuser, (3) Secondary flow inlet section (chamber), and (4) Motive nozzle holder: (a) top view and (b) cross-sectional view from A-A section

The velocities of the primary and secondary fluid streams are calculated as 148.4 m/s and 98.4 m/s, respectively, for the design case according to the measured and specified operating conditions. In the analyses, it should be always checked that the velocity of the secondary fluid stream is required to be lower than that of the primary fluid stream for a two-phase ejector operating properly. In Appendix-1, the technical drawings of the planned ejector are provided. However, the manufactured ejector is different than the proposed ejector. The reason for the improper manufacture is bad machining processes and deviations from the proposed design degrades the performance. For example, the proposed nozzle in the new design is replaced with the previous nozzle having throat diameter of 1.4 mm due to the manufacture problems. Due to the lack of the dimensional checks that could made by the coordinate measuring machine (CMM), most of the dimensions could not be checked. As a result, the dimensions of the tested ejector have deviations from the proposed dimensions because of the bad machining processes and lack of the measurement checks.

Table 7.1 Calculated performance and design parameters of the ejector for the initial ejector testing

| **Output parameters** | **Values** |
|---|---|
| Performance improvement ratio | 1.14 |
| Entrainment ratio | 0.5613 |
| Area ratio | 3.43 |
| Pressure lift ratio | 1.30 |
| Secondary fluid mass flow rate | 0.0107 kg/s |
| Total ejector mass flow rate | 0.0297 kg/s |
| Cooling capacity | 2055.88 W |
| Suction nozzle pressure | 216.91 kPa |
| Pressure drop between the suction nozzle and its inlet | 59.09 kPa |
| Converging angle of the motive nozzle (full angle) | 24 ° |
| Diverging angle of the motive nozzle (full angle) | 4° |
| Motive nozzle efficiency | 0.9640 |
| Motive nozzle throat diameter | 1.29 mm |
| Mixing section diameter | 4.63 mm |
| Suction nozzle diameter (without mrs) | 6.66 mm |
| Suction nozzle diameter (with mrs) | 7.5 mm |
| Pre-mixing length | 5.35 mm |
| Mixing section length | 46.86 mm |
| Diffuser outlet diameter | 9.16 mm |
| Diffuser length | 37.04 mm |

So far, with reference to semi-1D modelling approach, critical dimensions, i.e. constant area mixing section diameter and suction nozzle diameter are calculated based on the operating conditions and assumptions. Moreover, suction nozzle pressure, which is the most important assumption in the thermodynamic modelling approach, could definitely be calculated with this modelling approach. Using the relations between the geometrical dimensions of the ejector, other dimensions of the ejector could be roughly estimated. A design is proposed in this way in this thesis although there are some problems concerned with the manufacture and the dimensional control of the ejector components.

To sum up, all details regarding the technical drawings are provided in Appendix-1. The proposed ejector with the motive nozzle of 1.4 mm throat diameter is used in the experiments. The experimental EERC results are obtained only for R134a. Experimental data is also used to validate the numerical results of the semi-1D model through medium of the estimated efficiency values of the ejector components and liquid-vapor separator. Ersoy & Sag (2014) as well checked the reliability of their model with reference to various efficiency case combinations of the motive nozzle, suction nozzle, and diffuser.

Final ejector used in the experiments is the total of the firstly used motive nozzle with 1.4 throat diameter and the proposed design given in Appendix-1. With reference to deviations from the actual proposed design, manufactured ejector has certainly some inefficiencies. Moreover, the liquid-vapor separator has separation inefficiencies resulting from the separator design. All these issues would be discussed in the next chapter in detail. It is just aimed to be emphasized at this point that the applicability of the semi-1D model could be discussed from the viewpoint of the efficiency estimations of the ejector component, liquid and vapor separation efficiencies.

### *7.6.2 Parametric Analyses*

Three result groups are presented in this section making use of semi-1D modelling approach as follows; (i) Effect of the mixing section efficiency on the area ratio, entrainment ratio, performance improvement ratio, secondary fluid mass flow rate, and cooling capacity at two different condensation temperatures, i.e. 40 °C and 65 °C for R134a and R1234yf, (ii) Comparison of the purely thermodynamic modelling approach and semi-1D modelling approach according to performance improvement ratio, entrainment ratio, the area ratio, pressure drop, section nozzle pressure, and pressure lift ratio for R134a and R1234yf with respect to condensation temperature, and (iii) Comparison of cooling capacity, secondary fluid mass flow rate, mixing section and suction nozzle diameters with respect to the condensation temperature for R134a and R1234yf.

The basic design parameters for the motive nozzle of the semi-1D model are given in Table 7.2. The throat diameter and efficiency of the motive nozzle are calculated as the outputs. Mass flow rate and condenser outlet subcooling temperature difference are fixed as 0.03 kg/s and 2 K under the specified operating conditions. The condenser temperature is 40 °C and 65 °C for the mixing section efficiency investigations. However, it is varied between 40 °C-65 °C when the effect of the condensation temperature is analyzed. 0 °C is chosen as the evaporation temperature and 5 K is used as the evaporator superheat temperature difference. Suction nozzle and diffuser efficiencies are *0.8* and *0.75*, respectively, with reference to Lawrence (2012). In the first result group, the mixing section efficiency is varied between 0.70-0.95 since it is the main issue to be investigated. However, for the condensation temperature investigations, it is selected as 0.90 in the rest of the results according to reference value given by Liu, Groll et al. (2012). Vapor and liquid separation efficiencies are used in the analyses according to efficiency ranges given by Elbel et al., 2012 and Lawrence, 2012. The motive nozzle efficiency is calculated between 96-94% for R134a and R1234yf under the investigated conditions.

Table 7.2 Main geometrical parameters of the motive nozzle to be used in the analyses

| | |
|---|---|
| Motive nozzle inlet diameter | 12 mm |
| Motive nozzle outlet diameter | 3 mm |
| Converging angle (half angle) | 12° |
| Diverging angle (half angle) | 1.15° |

R1234ze(E) is omitted from the analyses since evaporation pressure is to be higher than the suction nozzle pressure. The outlet pressure, velocity, and density are displayed with respect to condensation temperatures in Table 7.3 for R134a, R1234yf, and R1234ze(E). Furthermore, the evaporation pressures for R134a, R1234yf, and R1234ze(E) are given in Table 7.4 for two alternative evaporation temperatures as 0 °C and 5 °C that could be investigated. As seen from the comparisons between the evaporation pressures and motive nozzle outlet pressures, R1234ze(E) has lower evaporation pressure for 0 °C evaporation temperature than the nozzle outlet pressure and nearly the same pressure as the nozzle outlet pressure for 5 °C evaporation temperature. Hence, for R1234ze(E) investigations, different flow conditions or motive nozzle design are required to be proposed.

Table 7.3 Calculated outlet pressure, velocity, and density of the motive nozzle for R134a, R1234yf, and R1234ze(E)

| R134a | | | R1234yf | | | R1234ze(E) | | |
|---|---|---|---|---|---|---|---|---|
| $P_{m,out}$ | $u_{m,out}$ | $\rho_{m,out}$ | $P_{m,out}$ | $u_{m,out}$ | $\rho_{m,out}$ | $P_{m,out}$ | $u_{m,out}$ | $\rho_{m,out}$ |
| 246.26 | 97.18 | 43.66 | 254.96 | 99.75 | 42.54 | 255.5913 | 76.0863 | 55.77929 |
| 246.61 | 107.92 | 39.31 | 255.07 | 110.5 | 38.4 | 257.0897 | 86.52582 | 49.03517 |
| 246.84 | 118.72 | 35.74 | 255.48 | 121.27 | 34.99 | 257.4347 | 97.11103 | 43.687 |
| 246.62 | 129.61 | 32.74 | 255.46 | 132.16 | 32.11 | 257.0704 | 107.8038 | 39.35923 |
| 246.88 | 140.54 | 30.19 | 255.45 | 143.13 | 29.65 | 257.1996 | 118.4487 | 35.8219 |
| 247.05 | 151.58 | 27.99 | 255.53 | 154.26 | 27.51 | 257.3119 | 129.161 | 32.8504 |

Table 7.4 Evaporation pressures corresponding two different evaporation temperature for R134a, R1234yf, and R1234ze(E)

| | R134a | R1234yf | R1234ze(E) |
|---|---|---|---|
| $P_{evap}$ (0 °C) | 292.80 kPa | 315.82 kPa | 216.55 kPa |
| $P_{evap}$ (5 °C) | 349.66 kPa | 372.92 kPa | 259.34 kPa |

Condensation temperature is analyzed according to 0 °C evaporation temperature and efficiency of the ejector components are selected according to Lawrence (2012) since the flow conditions inside the ejector must be arranged in a way that the velocity of the secondary flow is lower than that of the primary fluid as shown in Table 7.5. This condition is certainly required to be checked for all of the analyses. If this condition is not satisfied, motive nozzle geometry or operating conditions is to be revised.

For the second target of this section which is making comparison between the results of the semi-1D model and the purely thermodynamic model, the inputs of the thermodynamic analyses are presented in Table 7.6. As seen from this table, the inputs are partially compatible with the inputs of the semi-1D model. However, efficiency of the mixing section and liquid-vapor separator is not added to the thermodynamic model analyses. This thesis shows the effects of all efficiencies on the critical performance parameters gradually, hence it is important to emphasize the huge difference between the performance curves of the firstly established thermodynamic model and the lastly constructed comprehensive model. Since semi-1D model is built based on the CAM approach, the thermodynamic model analyses are presented with respect to the same mixing theory.

Table 7.5 Comparison of two different evaporation temperatures according to the velocity of the primary and secondary fluid streams

| R134a | | | |
|---|---|---|---|
| $T_e$=5 °C, $\eta_s$=0.9, $\eta_{mix}$=0.9, $\eta_d$=0.8 &$T_c$=40 °C | | $T_e$=0 °C, $\eta_s$=0.8, $\eta_{mix}$=0.9, $\eta_d$=0.75&$T_c$=40 °C | |
| $u_{m,out}$ (m/s) | $u_{s,out}$ (m/s) | $u_{m,out}$ (m/s) | $u_{s,out}$ (m/s) |
| 97.18 | 114.3839 | 97.18 | 75.7216 |

Table 7.6 Operating conditions for the thermodynamic analyses

| **Parameters** | **Values** |
|---|---|
| Evaporator temperature ($T_e$) | 0 ˚C |
| Evaporator outlet superheat temperature difference ($\Delta T_{sh}$) | 5 K |
| Condenser Temperature ($T_c$) | 40 - 65 ˚C |
| Condenser outlet subcooling temperature difference ($\Delta T_{sc}$) | 2 K |
| Compressor efficiency ($\eta_{comp}$) | 0.75 |
| Primary nozzle efficiency ($\eta_m$) | 0.95 |
| Suction nozzle efficiency ($\eta_s$) | 0.8 |
| Diffusor efficiency ($\eta_d$) | 0.75 |

Primary nozzle efficiency is the calculated efficiency value in the motive nozzle analyses.  Other common parameters are directly from the semi-1D model analyses in order to create a comparative base. Semi-1D model takes the mixing section efficiency and liquid-vapor separator efficiency as well into account and calculates the motive nozzle outlet pressure directly under the actual design and operating conditions. However, the performance parameters are presented with respect to the optimum suction nozzle pressure yielding the highest performance parameters. Figure 7.6 (a), (b), (c), (d), and (e) shows the effect of the mixing section efficiency on the performance improvement ratio, entrainment ratio, area ratio, secondary fluid mass flow rate, and cooling capacity, respectively, at two different condensation temperatures for R1234yf and R134a. When mixing section efficiency is increased, the performance improvement ratio and entrainment ratio increase as seen from Figure 7.6 (a) and (b).

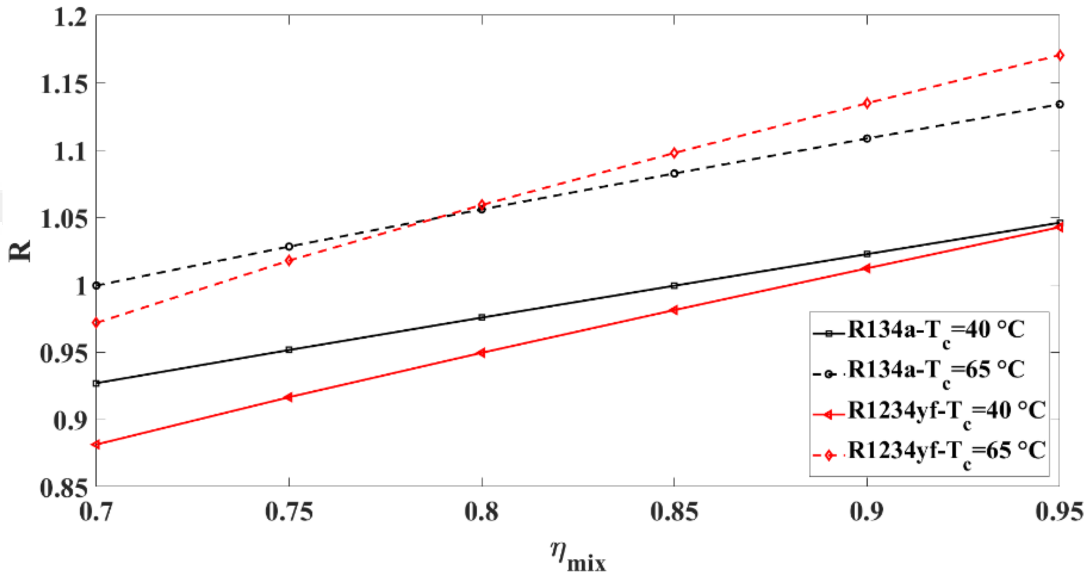


**(a)**

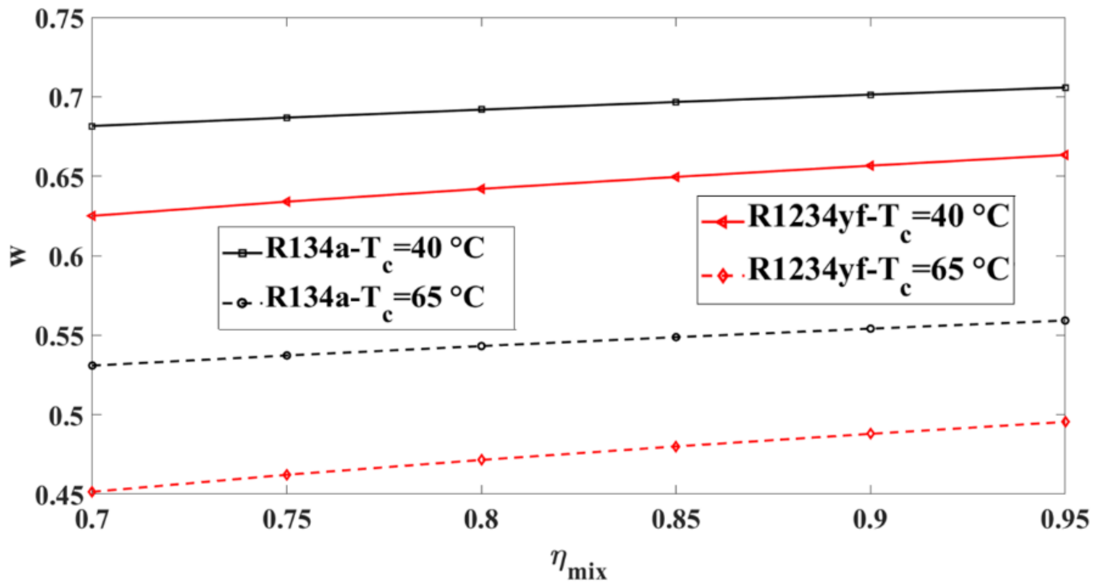


**(b)**

Figure 7.6 Effect of the mixing section efficiency on the (a) performance improvement ratio, (b) entrainment ratio, (c) area ratio, (d) secondary fluid mass flow rate, and (e) cooling capacity

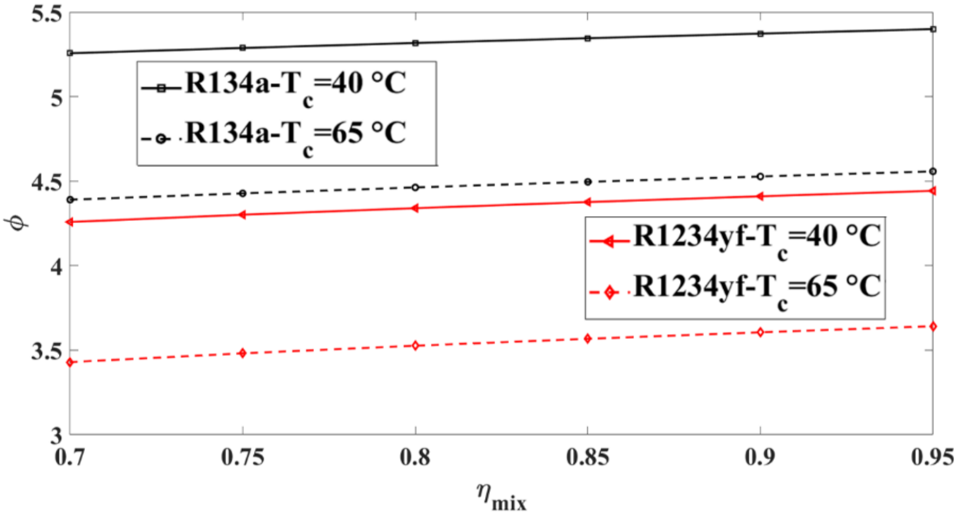


**(c)**

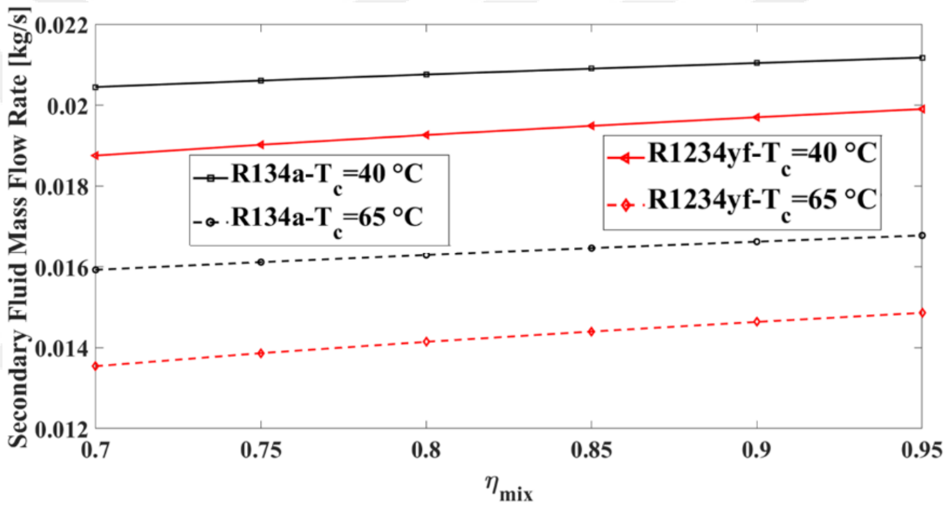


**(d)**

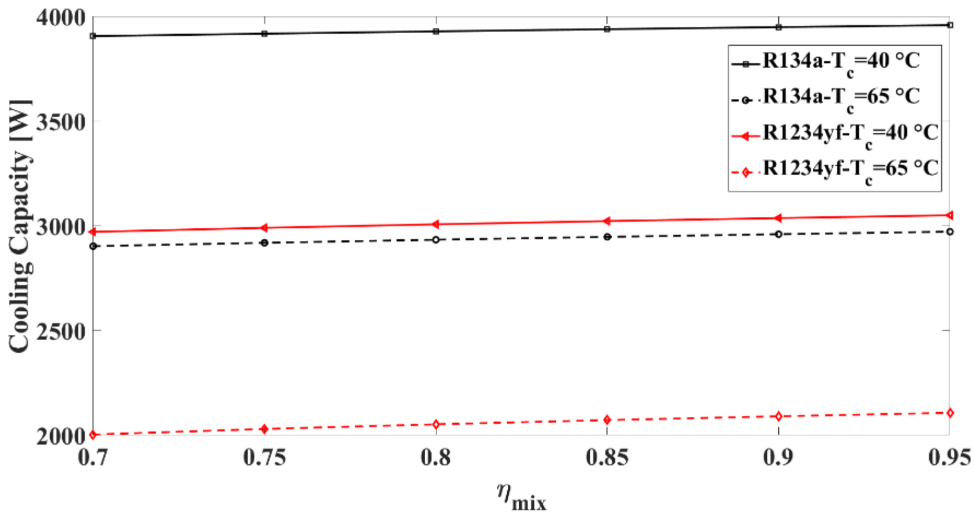


**(e)**

Figure 7.6 continues

Performance improvement ratio changes more in comparison with the entrainment ratio for both of the refrigerants and operating conditions. Moreover, similar to previous findings, R1234yf reacts more to the variations in the mixing section efficiency when compared with R134a. Change in the area ratio is very little as given in Figure 7.6 (c). Motive nozzle outlet diameter is kept constant throughout the analyses. The effect of the mixing section efficiency on the mixing section diameter is directly related to the changes in the total flow.

The effect of the mixing section efficiency on the suction fluid mass flow rate has similar trend to the variations of the entrainment ratio as displayed in Figure 7.6 (d). However, the total flow is negligibly affected under the investigated conditions. Therefore, mixing section diameter is negligibly affected with respect to the variations in the mixing section efficiency. Such being the case, the influence of the mixing section efficiency on the area ratio is very little. Cooling capacity nearly stays constant for R134a when mixing section efficiency increases as seen Figure 7.6. (e). The effect is more visible for R1234yf, even at the higher condensation temperature of 65 °C. The change in the cooling capacity is more than 5% for R1234yf at this temperature. Cooling capacity is visibly affected by the operating conditions, i.e. condensation temperature as discussed in the following figures in detail.

To sum up, all these parameters in Figure 7.6 increases when the mixing section efficiency is increased. The effect of the mixing section efficiency is more influential at the highest condensation temperature. It could be stated that the most effected parameter is the performance improvement ratio and the less effected one is total mass flow rate and mixing section diameter. Performance improvement ratio is increased due to the increase in the pressure lift ratio when mixing efficiency is improved. Suction fluid mass flow rate and the cooling capacity are affected less by the mixing section efficiency improvement, hence their effect on the overall performance improvement is less.

These general comments obtained from the analyses of the semi-1D model are not sufficient to evaluate the effects of the mixing section on most of the design and performance parameters. These explanations only establish the links between the variations of the parameters derived from the results of the model. As stated previously, mixing section efficiency is the most important parameter in comparison with the other components and elaborate CFD analyses are required. Figure 7.7 (a), (b), (c), (d), (e), and (f) compares the 0D thermodynamic modelling approach and the semi-1D modelling approach in terms of the performance improvement ratio, entrainment ratio, pressure lift ratio, area ratio, suction nozzle pressure, and pressure drop with respect to condensation temperature for R134a and R1234yf.

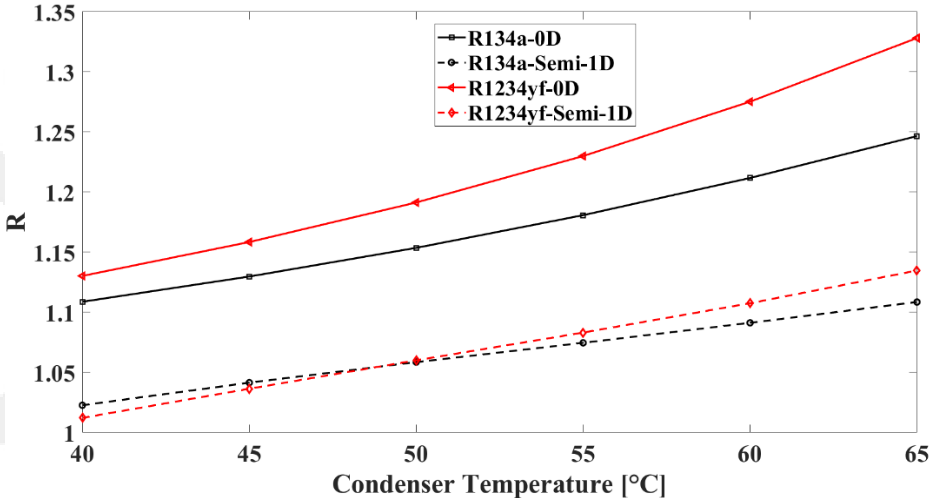


(a)

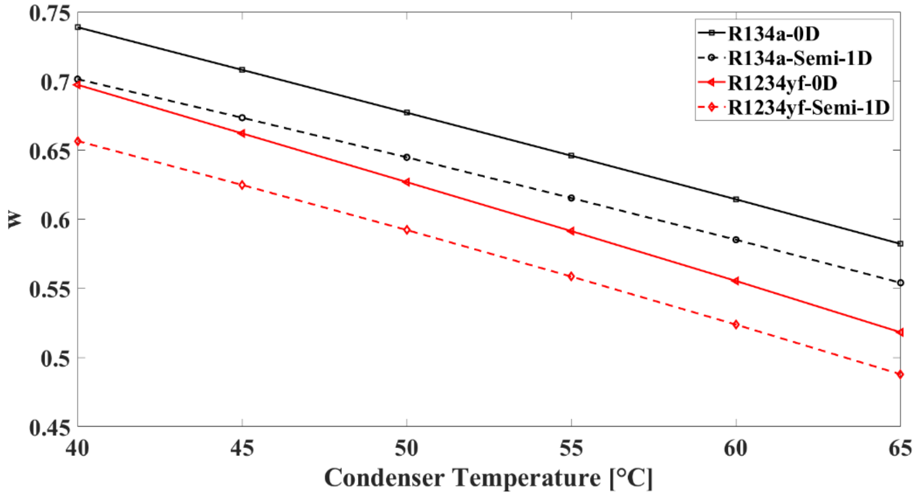


(b)

Figure 7.7 Effect of the condensation temperature on the (a) performance improvement ratio, (b) entrainment ratio, (c) pressure lift ratio, (d) area ratio, (e) suction nozzle pressure, and (f) pressure drop for R134a and R1234yf according to 0D thermodynamic modelling and semi-1D modelling approaches

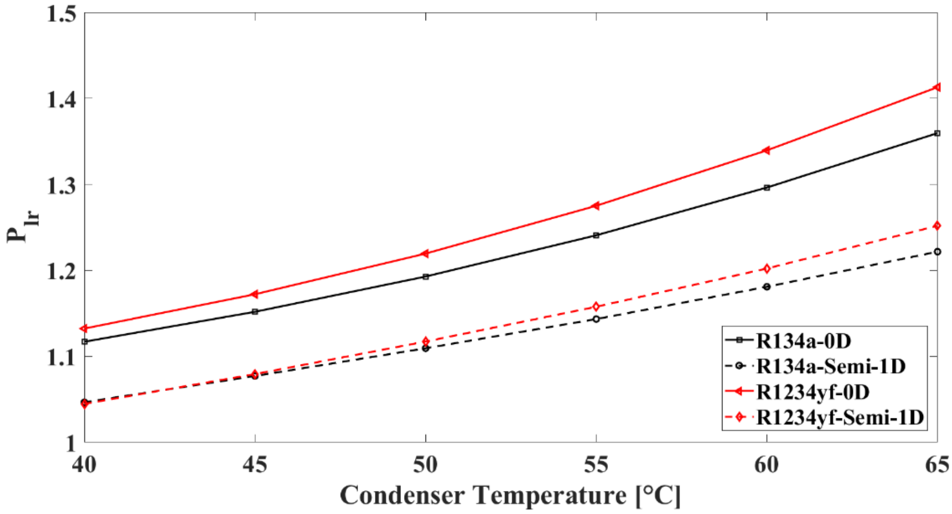


(c)

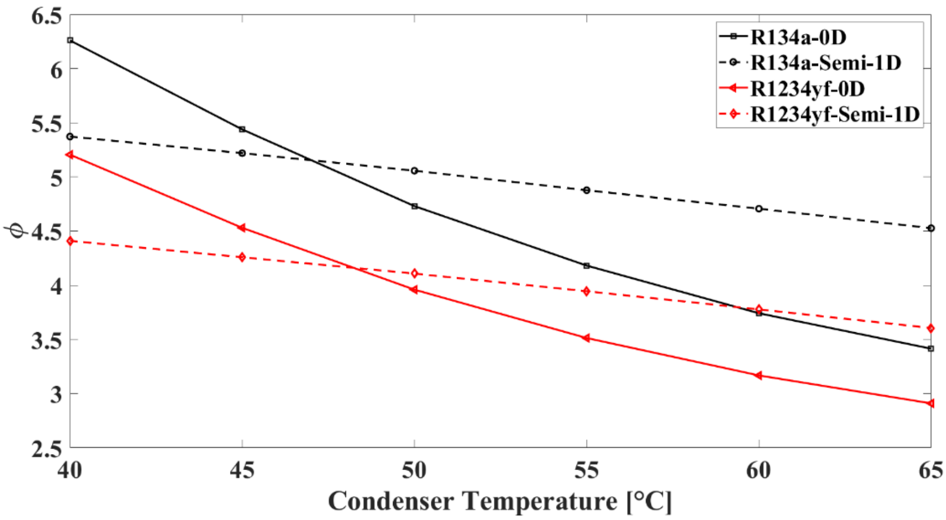


(d)

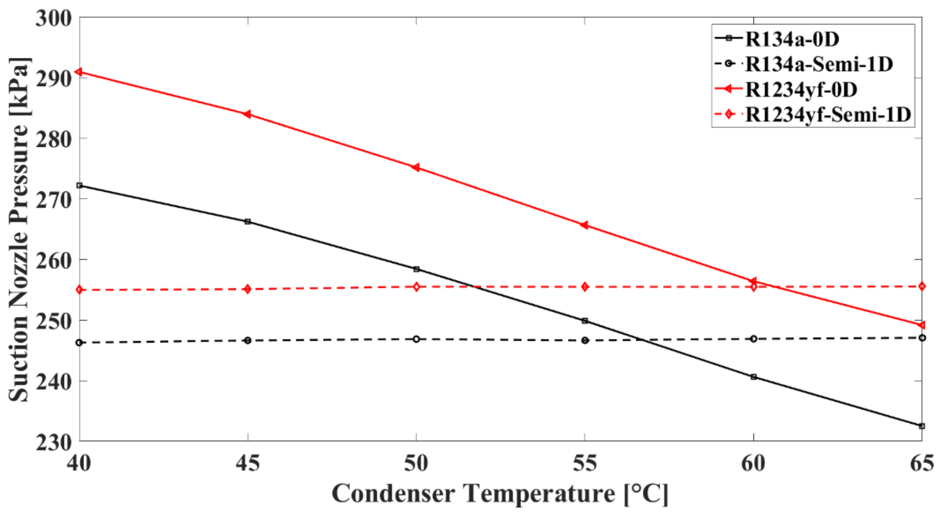


(e)

Figure 7.7 continues

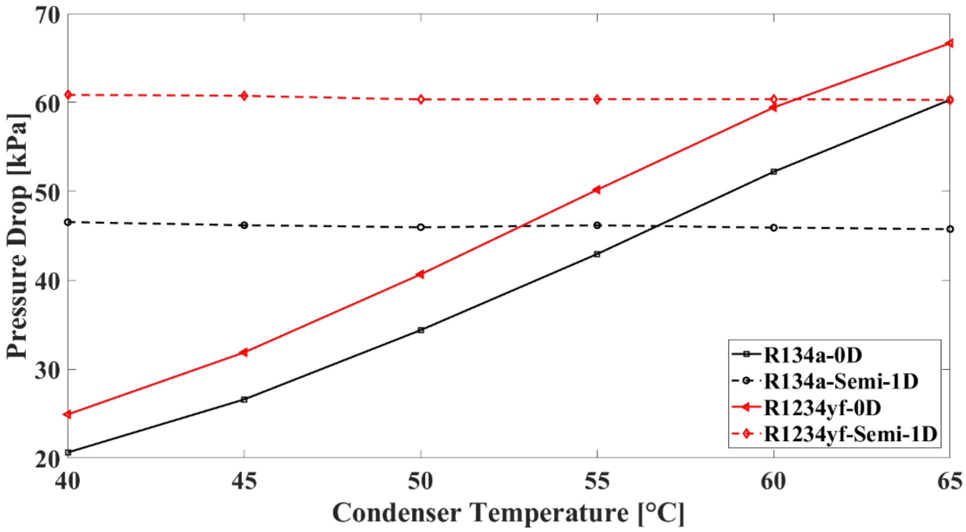


**(f)**

Figure 7.7 continues

As seen from Figure 7.7 (a), performance improvement is around 2% and 1% for R134a and R1234yf, respectively, at 40 °C condensation temperature according to the semi-1D model. However, under the thermodynamic modelling assumptions, the performance improvement is 11% and 13% for R134a and R1234yf, respectively for the same condensation temperature. For the highest investigated condensation temperature, the performance improvement is around 11% and 13% for R134a and R1234yf, respectively, based on the semi-1D model; whereas R134a displays approximately 25% performance improvement and R1234yf has performance improvement around 33% according to pure thermodynamic model. It shows that thermodynamic modelling approach yields higher performance evaluations than the expected values with respect to the actual operating conditions and designs. Semi-1D model results in more realistic performance evaluations since it evaluates all ejector component efficiencies, liquid-vapor separator efficiency, and the exact suction nozzle pressure.

With reference to thermodynamic modelling approach, R1234yf yields better performance improvement all over the condensation temperature range. However, in semi-1D modelling approach, the superiority of these two refrigerants may vary since the motive nozzle flow is analyzed according to operating conditions and actual nozzle design. Semi-1D model shows that R134a and R1234yf performances are very close to each other at the analyzed conditions. Performance improvement profile curves of R134a and R1234yf are nearly the same especially at low condensation temperatures. The highest difference between the performance of these two refrigerants is more than 8% at the highest investigated condensation temperature under thermodynamic modelling approach; whereas it is around 2.5% according to semi-1D modelling.

Similar to performance improvement ratio, entrainment ratio and pressure lift ratio are calculated higher under thermodynamic modelling approach as seen from Figure 7.7 (b) and (c). Pressure lift ratio is nearly identical at the lower condensation temperatures for R134a and R1234yf. The gap between the pressure lift ratio curves of R134a and R1234yf is displayed larger under the thermodynamic modelling approach. The variation of the area ratio is less according to the semi-1D model as declared in Figure 7.7 (d) due to the constant suction nozzle pressures calculated according to the actual nozzle geometry and constant motive nozzle outlet diameter.

Optimum suction nozzle pressure decreases when condensation temperature is increased according to thermodynamic modelling approach as given in Figure 7.7 (e). However, the actual pressure calculated for the specified nozzle geometry slightly increases at the investigated operating conditions with respect to the semi-1D modelling approach. Hence, optimum suction nozzle pressure drop increases for both of the refrigerants according to increased condensation temperature as given in Figure 7.7 (f). However, in semi-1D modelling approach, the motive nozzle geometry is kept constant and the variation of the outlet pressure to the condensation temperature is negligible. Therefore, the suction nozzle pressure and pressure drop stay nearly the same throughout all condensation temperature range as shown in Figure 7.7 (e) and (f). Variations of the optimum suction nozzle pressure with respect to both evaporation and condensation temperatures are discussed elaborately in Chapter 4.

Dependency of the secondary fluid mass flow rate and cooling capacity on the condensation temperature is displayed in Figure 7.8 (a) and (b), respectively for R134a and R1234yf. Secondary fluid mass flow rate decreases 21% and 26% for R134a and

R1234yf when condensation temperature is increased as given in Figure 7.8 (a). As a result, cooling capacity of the EERC decreases 25% and 31% for R134a and R1234yf, respectively. Figure 7.9 shows the variation of the mixing section and suction nozzle diameters according to condensation temperature for R134a and R1234yf. Suction nozzle diameter is calculated at the point where motive nozzle outlet is located. The given diameter in Figure 7.9 is the directly calculated suction nozzle diameter without considering the minimum required space added to the model just for design considerations. As for the calculated dimensions, the change in the mixing section diameter is less than 10% and the variation of the suction nozzle diameter is around 5% for both of the refrigerants with respect to the condensation temperature.

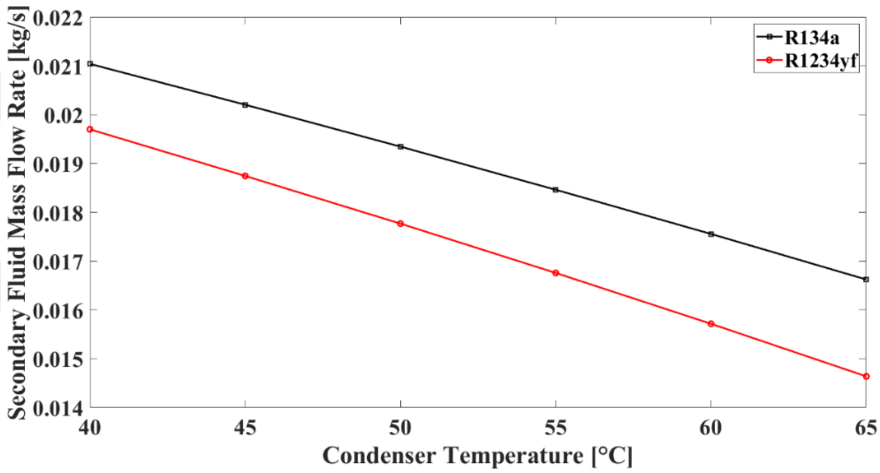


(a)

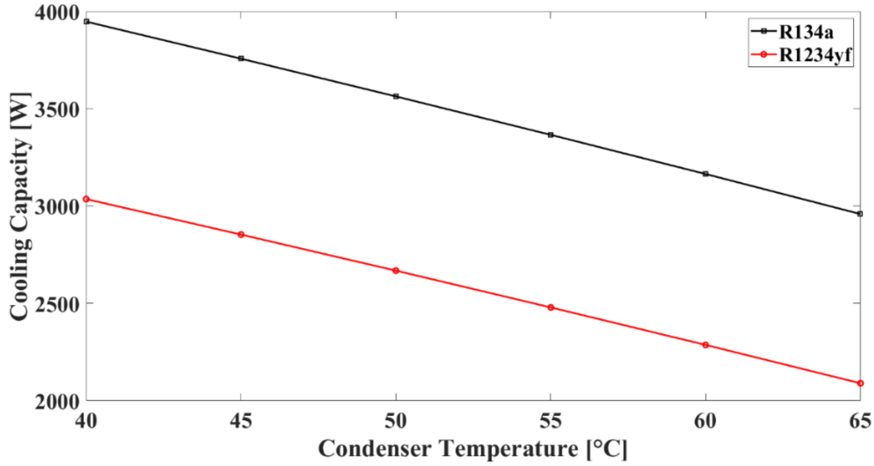


(b)

Figure 7.8 Variation of (a) the secondary fluid mass flow rate and (b) cooling capacity with respect to condensation temperature for R134a and R1234yf

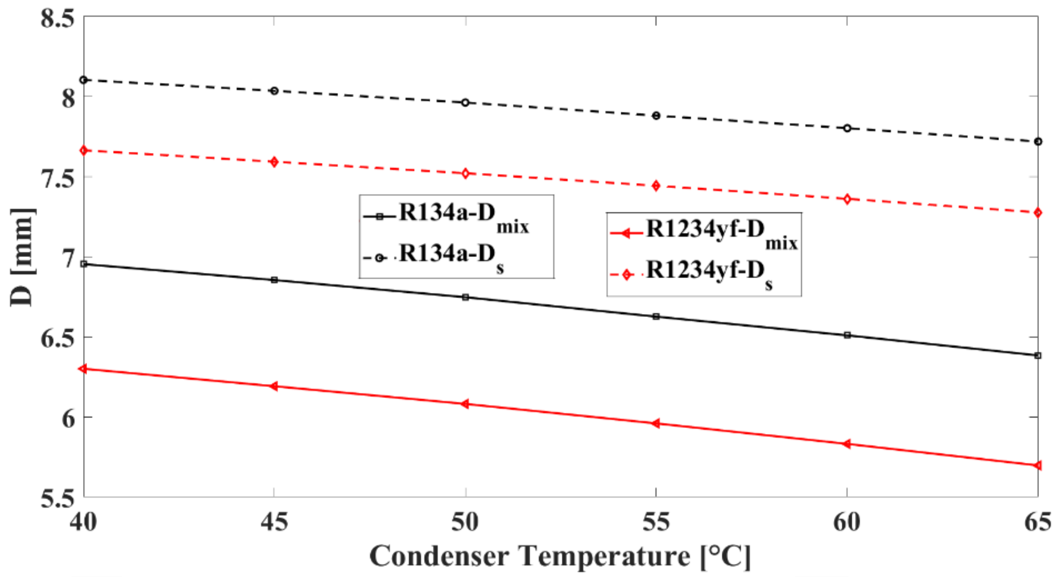


Figure 7.9 Dependency of the mixing section diameter and suction nozzle diameter on the condenser temperature for R134a and R1234yf

### 7.7 Comments on the Semi-1D Modelling Approach

The design approach concerned with the mixing section diameter and suction nozzle diameter lacks the details of flow characteristics and dynamics. Hence, the design comments derived from the present investigations are to be checked with the computational fluid dynamics analyses. However, this semi-1D model shows general trends of the parameters, i.e. performance improvement ratio, entrainment ratio, pressure lift ratio, area ratio, suction nozzle mass flow rate, cooling capacity according to various motive nozzle designs and operating conditions. For the preliminary designs and experiments as the starting points of the tests and analyses, the geometrical definition of the ejector could be made with reference to this established semi-1D model, but further investigations must be accompanied by CFD analyses.

To sum up, thermodynamic modelling approach yields higher performance evaluations than the expected values in the actual operating conditions and designs. Semi-1D model yields more realistic evaluations since it considers all ejector component efficiencies, liquid-vapor separator efficiency, and the exact suction nozzle pressure.

# CHAPTER EIGHT
# EXPERIMENTAL INVESTIGATIONS ON THE VAPOR COMPRESSION REFRIGERATION CYCLE AND EJECTOR EXPANSION REFRIGERATION CYCLE

In this section experimental works are presented. The construction of the experimental set-up is displayed. Equipment to be used in the system is introduced. The test rig is capable of operating in two different working mode as VCRC and EERC. The refrigerants tested in this section is R134a and R1234yf. Calibration process of the temperature measurement devices is expressed. Repeatability of the experimental set-up is analyzed. Next, based on the accuracy of the measurement devices, uncertainty in COP is calculated. Equations for the analyses of the measured data are presented.

The performance of the refrigerants is investigated and compared in the VCRC mode. After presenting basic performance values of these two refrigerants in the VCRC concept, the performance of R134a is investigated in the EERC operating mode. The design specification of the manufactured ejector is presented in the previous section. The EERC tests of R134a are used to validate the numerical results calculated from the semi-1D model of the cycle. The EERC tests are used as well to define the critical performance parameters based on the experimental data. The term "external operating conditions" represents the operating conditions concerned with the temperature and flow rate of the secondary heat transfer fluid (SHTF) and compressor frequency. However, the "internal operating conditions" expresses the operating conditions regarding the refrigerant side.

## 8.1 Experimental Set-up

Experimental set-up is composed of two cycles for performance tests of VCRC and EERC. Main measurements taken from the system are temperature, pressure, power, and flow rate. Actually, flow meters are attached at the condenser outlet and at the liquid outlet of the liquid-vapor separator where the refrigerant is expected to be fully in liquid state. However, test results show that the measured refrigerant flow rates are not reliable when compared to the calculated flow rates. Therefore, the flow rate measurements are omitted although they are shown schematically in the schematic view given in Figure 8.1.

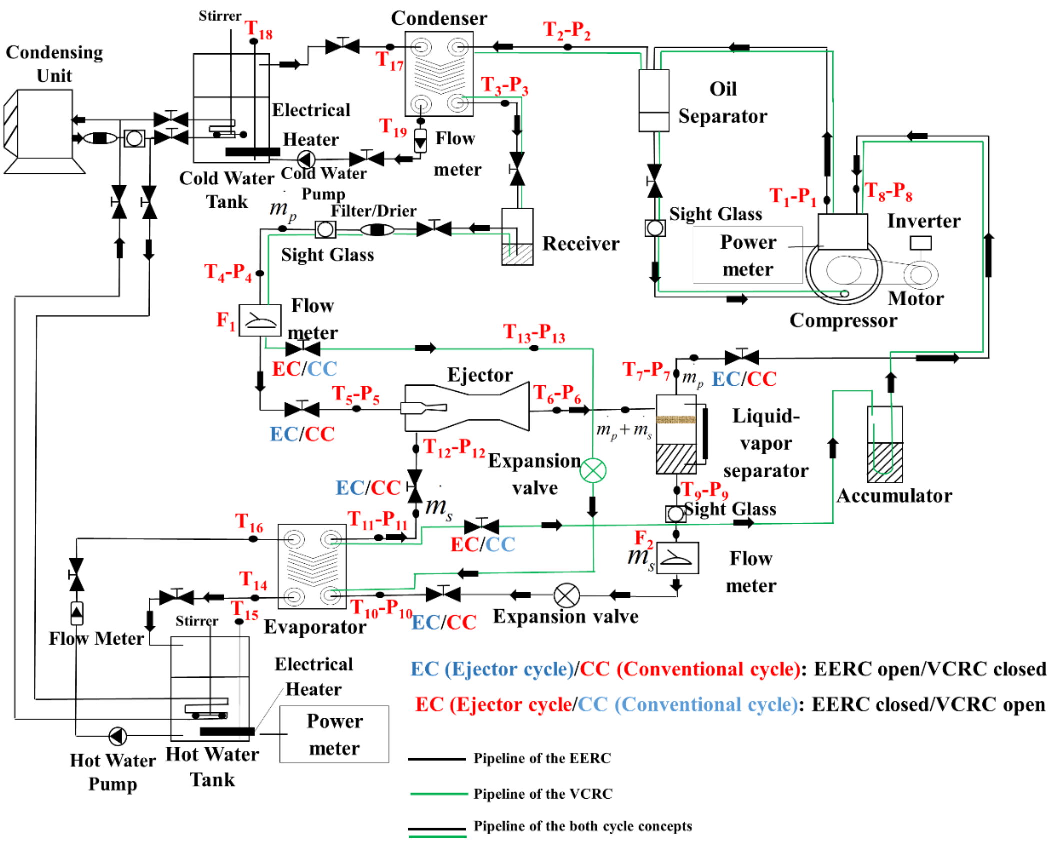


Figure 8.1 Schematic view of the experimental test rig operating in both EERC and VCRC modes (Disawas & Wongwises, 2004; Ersoy & Sag, 2014)

The temperature and pressure measurements are used to define the states of the refrigerants. Power measurements are taken from the energy analyzers attached to compressor and the heater in the evaporator water tank. SHTF of the evaporator and condenser are water. In the conventional cycle, an accumulator to prevent the flow of the liquid refrigerant through the compressor and a receiver to prevent the vapor refrigerant passing through the expansion valve are used. In the EERC, a liquid-vapor separator and an ejector is used additionally. Ejector is used instead of the expansion valve. However, as shown from the schematic view in Figure 8.1, an additional small-scale expansion valve is used in the system to balance the pressure difference between the liquid port of the separator and the evaporator. Moreover, in the circuit of the EERC, a check valve is used in the suction line of the ejector to prevent the flow of the secondary fluid in the reverse direction. The test rig shown in Figure 8.1 is designed according to two reference studies in the literature, i.e. Disawas & Wongwises (2004) and Ersoy & Sag (2014). All specifications concerned with the test rig is shown in Figure 8.1 and the general view of the manufactured test rig is shown in Figure 8.2.

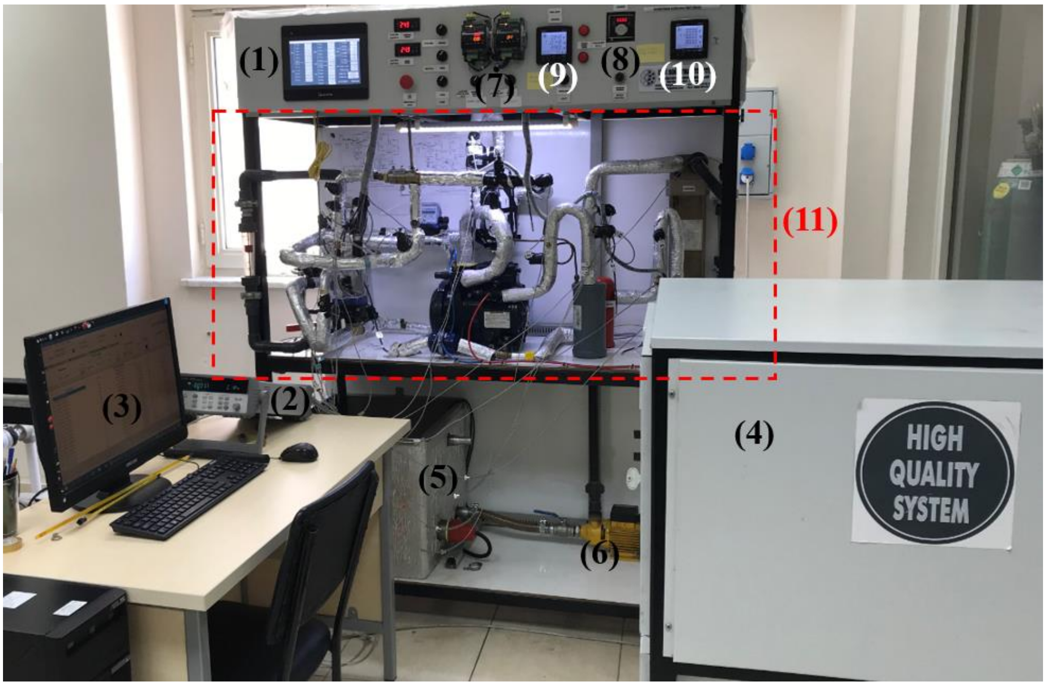


Figure 8.2 General view of the VCRC/EERC experimental test rig (Personal archive, 2020)

The general descriptions of the test rig is made on Figure 8.2 as follows; (1) Control screen, (2) Data logger for temperature measurements with thermocouples, (3) Computer for the temperature records, (4) Condensing unit and cold water tank for the condenser water, (5) Hot water tank including electrical heater inside, (6) Hot water pump, (7) Controllers of the expansion valves of the EERC and conventional cycle, (8) Inverter, (9) Energy analyzer of the compressor, (10) Energy analyzer of the evaporator electrical heater, and (11) Main refrigeration cycle circuits of the EERC and VCRC. As seen from the schematic view, temperature and pressure is collected from 19 and 13 points, respectively. Thermocouples and pressure transmitters are used in the system for the measurements. Tip of the thermocouples are inserted into the system with special connections since the system operates at high pressures. The other ends of the thermocouples are attached to the channels of the data logger; hence the temperatures at the critical points of the test rig are measured. For the temperature records during the operation, the data logger is connected to a computer. Temperature measurements are made externally independent of the test rig. However, pressure values are displayed on the screen of the test rig. Due to this control screen, measurement and calibration adjustments could be made.

Main components of both refrigeration cycle concepts are shown as a separate focusing points by the dashed red lines in Figure 8.2. This section is displayed and introduced in detail with front, left, and right side views as seen from Figure 8.3 (a), (b), and (c), respectively. In other words, main and auxiliary refrigeration system components are displayed in Figure 8.3.

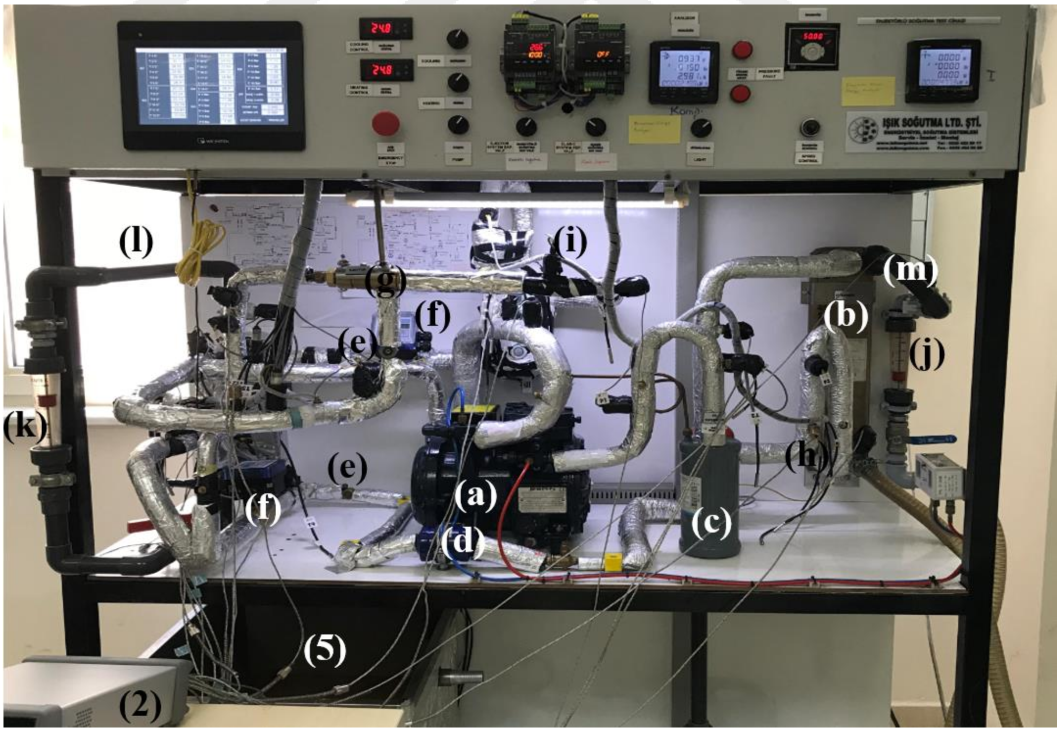


**(a)**

Figure 8.3 Elaborately extended (a) front, (b) left, and (c) right views of the test rig (Personal archive, 2020)

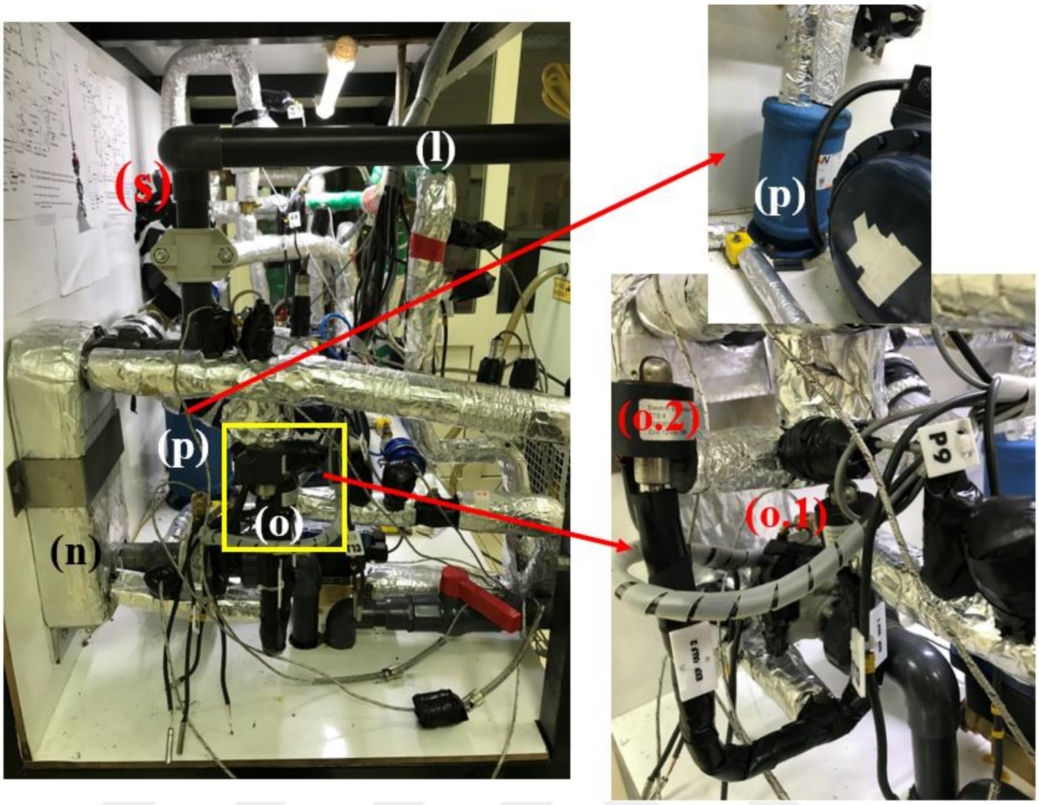


**(b)**

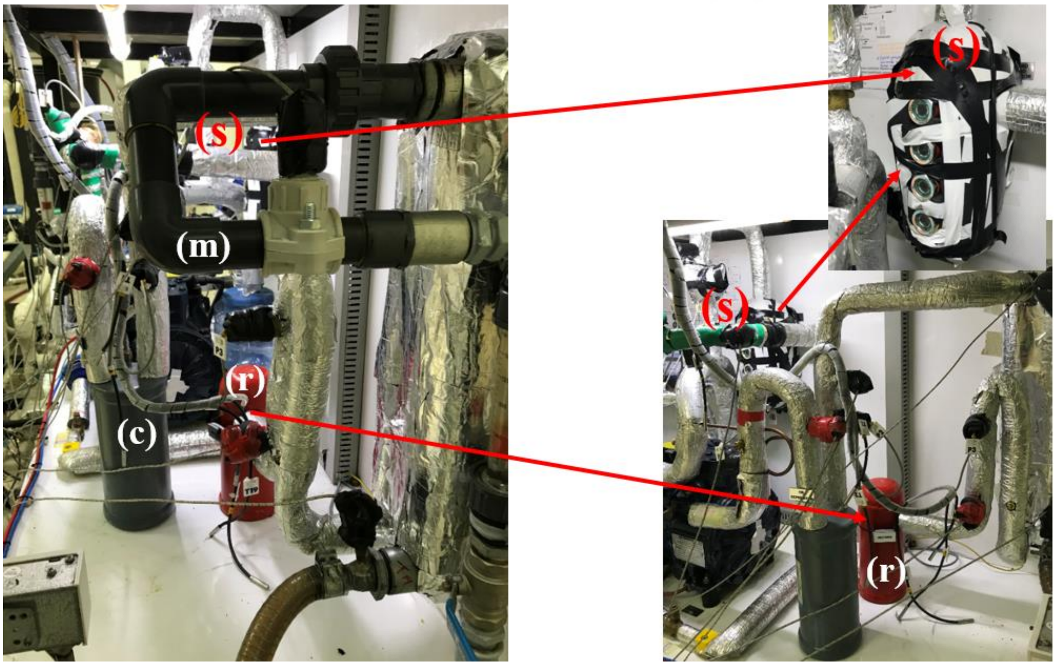


**(c)**

Figure 8.3 continues

The components shown in Figure 8.3 are as follows; (a) Compressor, (b) Condenser, (c) Oil separator, (d) Filter drier, (e) Sight glass, (f) Flowmeters for the measurements of the main refrigerant flow of the VCRC or primary fluid of the EERC at the condenser outlet, and the measurement of the secondary fluid of the EERC at the liquid port outlet of the separator, (g) Two-phase ejector, (h) One of the thermocouples attached to the system, (i) One of the pressure transmitters inserted into the system, (j) Rotameter for the volumetric flow rate measurement of the condenser water, (k) Rotameter for the volumetric flow rate measurement of the evaporator water, (l) Water pipeline between the hot water tank and evaporator, (m) Water pipeline between the cold water tank and the condenser, (n) Evaporator, (o) Expansion valves, (p) Accumulator, (r) Receiver, and (s) Liquid-vapor separator.

As mentioned previously, flow meters for the direct flow rate measurements of the refrigerants are not used. The flow rates of the refrigerant are calculated from the other recorded measurements, i.e. energy consumption of the compressor per second with the temperature and pressure of the refrigerants at the inlet and outlet of the compressor. There are other alternatives to calculate the flow rate of the refrigerant. These calculations are explained in detail in the subsequent sections.

There are two expansion valves in the experimental system as the large-scale expansion valve shown with the symbol “o.1” and attached in the VCRC circuit and the small-scale expansion valve displayed by the symbol “o.2” and used in the EERC. The large-scale expansion valve is used to decrease the refrigerant pressure from condenser pressure to the evaporator pressure; whereas the small-scale expansion valve is used to decrease the pressure of the secondary fluid (in the EERC concept) from liquid port outlet pressure of the separator to the evaporator pressure.

Two most important components are the ejector and liquid-vapor separator for the EERC. The exploded view of the two-phase ejector shown with the symbol “g” is displayed in Figure 8.4. As previously discussed in detail, ejector is manufactured module by module. All design aspects concerned with the manufactured ejector is discussed formerly and the dimensional details are presented in Appendix-1.

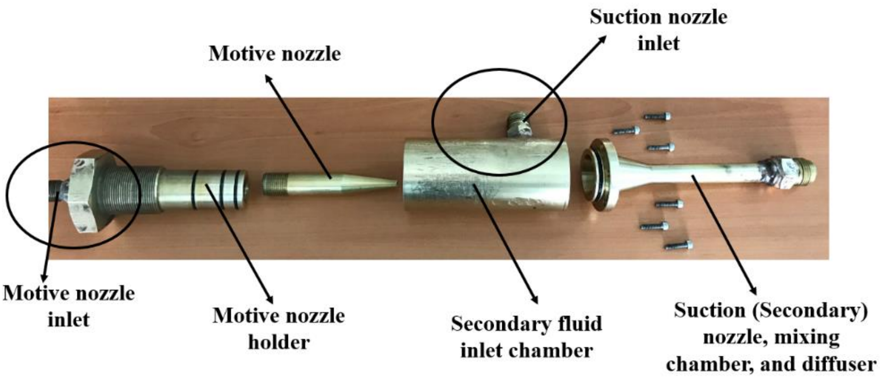


Figure 8.4 Exploded view of the manufactured ejector (Personal archive, 2020)

The inlet and outlets of the isolated liquid-vapor separator is shown in Figure 8.5. Two-phase refrigerant coming from the diffuser outlet enters into the separator. The vapor and liquid portions of the two-phase refrigerant are separated inside this component. Vapor refrigerant is sucked by the compressor and liquid refrigerant is sent to the evaporator. The design of the separator is of critical importance for the overall performance improvement. The sight glasses show the level of the collected liquid refrigerant inside the separator. The separator is manufactured without a special design in this test rig. Hence, the effects of the poor separation as well are discussed while evaluating the results.


Figure 8.5 Inlet and outlets of the insulated liquid-vapor separator used in the EERC (Personal archive, 2020)

One of the biggest problem regarding this separator is the locations of the refrigerant inlet and vapor port of the separator. The distance between these critical points is to be determined with the proper design calculations. Hence, the distance of the vapor port and separator inlet is to be arranged in a way that suction of the compressor is not affected by the separation process. Properties of the main components used in the experimental set-up and accuracy of the measurement equipment are displayed in Table 8.1 and Table 8.2, respectively.

Table 8.1 Properties of the main components used in the test rig

| Main Components | Type | Brand/Model |
|---|---|---|
| Compressor | Semi hermetic,<br>Reciprocating,<br>Variable speed | Dorin<br>Series: HI<br>Range: HI11<br>Model: HI241CC |
| Condenser | Plate heat exchanger<br>Brazed-plate type | WTK (14 plate) |
| Evaporator | Plate heat exchanger<br>Brazed-plate type | WTK (10 plate) |
| Expansion valves | Electrically operated | Danfoss/ETS 6 |

Table 8.2 Accuracy of the measurement devices in the experimental set-up

| Measurement device | Measurement Range | Accuracy |
|---|---|---|
| Rotameter<br>(Variable area flow-meter)<br>(GENTEK)<br>Condenser water | 160-1600 L/h | 1%<br>(Full scale) |
| Rotameter<br>(Variable area flow-meter)<br>(GENTEK)<br>Evaporator water | 160-1600 L/h | 1%<br>(Full scale) |
| Power meter<br>(ENTES-MPR-45S) | 0…9999 MW | 1%<br>(Exact scale) |
| Thermocouple (J type) | -210-760 °C | Standard:<br>+/- 2.2°C or +/- 0.75%<br>Special Limits of Error: +/- 1.1°C or 0.4%<br>(Exact scale) |
| Pressure Transmitter<br>(WIKA) | 0-1000 kPa (Low pressure)<br>0-3000 kPa (High pressure) | 0.25%<br>(Exact scale) |

Meanwhile, some of the thermocouple connections are changed because of the low durability of the thermocouple connections on the system. They could not cope with the high pressure; hence thermal well type insertion is used. A thermal well is inserted into the pipe and welded. A thermal paste is inserted into those thermal wells and the thermocouples are placed into those welded closed plugs. It is a safer implementation method for these kinds of highly pressurized systems. Lastly, insulation of these connections are very important for the safe measurements.

### 8.2 Calibration of the Thermocouples

J-type thermocouples are used in the experimental set-up. Before starting the experiments, the thermocouples are calibrated and calibration lines are obtained for each thermocouple. Example calibration curves are displayed in Appendix-2. Moreover, coefficients of the linearly fitted calibration curves for all thermocouples are given in Appendix-2 as well. All thermocouples are inserted into constant-temperature bath for the calibration process as shown in Figure 8.6.

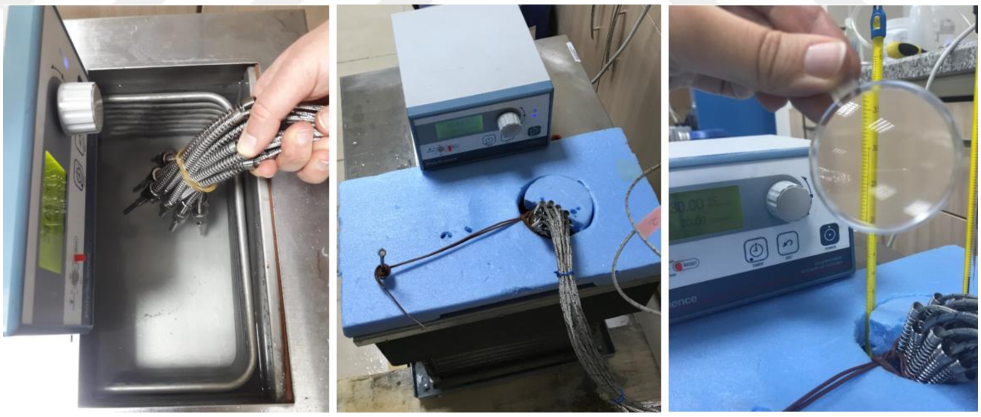

Figure 8.6 Calibration process of the thermocouples to be used in the experimental set-up (Personal archive, 2020)

For the calibration process, the temperature measurement range is defined between -5 °C-70 °C. A very sensitive constant temperature bath is required to calibrate the thermocouples accurately. Furthermore, the temperature of the bath should be checked by a mercury glass thermometer at the same time. Firstly, a temperature value between the specified temperature range is adjusted for the constant temperature bath and after reaching steady-state, the measured values of the thermocouples are recorded for a time interval. Using the average of these temperature measurements over the time intervals and the exact temperature values, the calibration lines are obtained for the thermocouples.

Whole measurements are repeated two times and the measured value is the average of these two repetitions for each thermocouple when compared to the exact value. Hence, linearly fitted calibration curves are obtained for each thermocouple as exemplified in Appendix-2. These curves are inserted into the data logger and each measured value are corrected with respect to these curves.

### 8.3 Repeatability of the Experiments

Performance evaluations are made based on the single experiment for each case. At the beginning, the reliability is to be investigated to make sure that single experiment is sufficient. For this reason, repeatability of three experiments are checked for a specific operating condition. The selected operating condition is given in Table 8.3.

Table 8.3 Operating condition for the repeatability tests

| **Parameters** | **Values** |
|---|---|
| $T_{c,sec,fl(w)}$ (°C) | 35 |
| $T_{e,sec,fl(w)}$ (°C) | 20 |
| Volumetric flow rate of condenser water (l/h) | 400 |
| Volumetric flow rate of evaporator water (l/h) | 1200 |
| Compressor frequency (Hz) | 50 |

All details concerned with the repeatability tests are provided in Appendix-3. The given measurements are roughly the average of the 3-hour record after the system reaches steady-state. The system is assumed to reach the steady-state conditions after operating approximately two hours. The maximum temperature and pressure difference among the repeated experiments for the specific measurement points is around 1K and 0.1 bar, respectively. The maximum difference is around 30 W for the compressor power input which is approximately 3% of the measured power which is averagely 1218 W. With reference to cooling capacity, maximum difference is about 100 W, and similarly compressor power input, this difference is also 4% of the full capacity calculated averagely as 2997 W. The cooling capacity is determined based on the heat transfer from the evaporator SHTF.

The equations used to analyze the experimental data would be discussed in the following sections. However, some information concerned with the COP and mass flow rate calculations is to be provided briefly. COP is calculated based on two evaporation capacity calculation alternatives, i.e. evaporation capacity based on the evaporator electrical heater power consumption and evaporation capacity defined as the heat transfer from the evaporator SHTF. Compressor power is determined with reference to energy analyzer data (power consumption) only. COP with reference to evaporator electrical heater power consumption is averagely 2.65 and the maximum difference among the experiments is approximately 2% of the average COP; whereas average COP according to the heat transfer from the evaporator SHTF is 2.46 and the maximum difference is about 1% of the reference average COP. COP calculated with respect to the heat transfer from the evaporator SHTF is assumed to be the most accurate since there is unavoidable heat exchange between the system and the surroundings.

Lastly, mass flow rate is calculated based on the experimental measurements rather than the direct flow measurements. Mass flow rate is calculated according to the established energy balance for the evaporator, condenser, and compressor. The average mass flow rates according to the compressor, evaporator, and condenser are 0.0235 kg/s, 0.0228 kg/s, 0.0258kg/s, respectively for the three repeated experiments. Maximum differences of the mass flow rates among these repeated experiments are around 2%, 4%, and 3% of the average mass flow rates calculated from the energy balances established throughout the compressor, evaporator, and condenser, respectively. As a result, making only single experiment is acceptable to make performance evaluation of any operating conditions. Next, uncertainty analysis is made with reference to these repeatability tests.

### 8.4 Uncertainty Analyses

The uncertainty method proposed by Kline and McClintock in 1953 is used to calculate the uncertainty of COP obtained from the experimental data. In this thesis, the uncertainty analyses are conducted based on the repeatability experiments for only the most critical performance parameter, i.e. COP values similar to Sağ (2015) with reference to Genceli (2008). According to this method, the total uncertainty error of the parameter, $Y$ obtained from the experimental measurements is calculated as follows;

$$\omega_Y = \left[ \left( \frac{\partial Y}{\partial x_1} \right)^2 \omega_1^2 + \left( \frac{\partial Y}{\partial x_2} \right)^2 \omega_2^2 + ... + \left( \frac{\partial Y}{\partial x_n} \right)^2 \omega_n^2 \right]^{1/2} \tag{8.1}$$

$x_1$, $x_2$, …, $x_n$ are the independent variables having influence on the physical parameter, $Y$. The error of each independent variable is $\omega_1$, $\omega_2$, …, $\omega_n$. The errors of the measurement equipment in the test rig are provided in Table 8.2. In this thesis, only uncertainty of COP is formulated and calculated. COP is calculated in two different ways as calculating the evaporation capacity according to the power consumption of the evaporator electrical heater and the heat transfer from the evaporator SHTF. As stated previously, COP calculation using the evaporation capacity with respect to the heat transfer from the SHTF is chosen as the most accurate way since there are unavoidable losses/gains within the system. COP calculated from the experimental data is formulated as given below

$$COP = \frac{\dot{Q}_{e,\sec,fl(w)}}{\dot{W}_{comp,in}} \tag{8.2}$$

COP calculation formula could be extended in terms of the directly measured parameters from the system with reference to aforecited COP declaration as

$$COP = \frac{(\rho \dot{V} c_p (T_{in} - T_{out}))_{e,\sec,fl(w)}}{\dot{W}_{comp,in}} \tag{8.3}$$

Therefore, the independent variables in terms of the measurements in order to calculate the uncertainty in the COP are formulated as below

$$COP = COP(\dot{V}, T_{in}, T_{out}, \dot{W}_{comp,in}) \tag{8.4}$$

The derivatives required to calculate the error in COP are given as follows;

$$\frac{\partial COP}{\partial \dot{V}} = \frac{(\rho c_p (T_{in} - T_{out}))_{e,\sec,\,fl(w)}}{\dot{W}_{comp,in}} \tag{8.5}$$

$$\frac{\partial COP}{\partial T_{in}} = \frac{(\rho \dot{V} c_p)_{e,\sec,\,fl(w)}}{\dot{W}_{comp,in}} \tag{8.6}$$

$$\frac{\partial COP}{\partial T_{out}} = \frac{(-\rho \dot{V} c_p)_{e,\sec,\,fl(w)}}{\dot{W}_{comp,in}} \tag{8.7}$$

$$\frac{\partial COP}{\partial \dot{W}_{comp,in}} = \frac{(-\rho \dot{V} c_p (T_{in} - T_{out}))_{e,\sec,\,fl(w)}}{(\dot{W}_{comp,in})^2} \tag{8.8}$$

Therefore, the total error in COP and error ratio of COP is calculated with reference to the following equations

$$\omega_{COP} = \left[ \left( \frac{\partial COP}{\partial \dot{V}} \right)^2 \omega_{\dot{V}}^2 + \left( \frac{\partial COP}{\partial T_{in}} \right)^2 \omega_{T_{in}}^2 + \left( \frac{\partial COP}{\partial T_{out}} \right)^2 \omega_{T_{out}}^2 + \left( \frac{\partial COP}{\partial \dot{W}_{comp,in}} \right)^2 \omega_{\dot{W}_{comp,in}}^2 \right]^{1/2} \tag{8.9}$$

$$\frac{\omega_{COP}}{COP} = \left[ \left( \frac{\omega_{\dot{V}}}{\dot{V}} \right)^2 + \left( \frac{\omega_{T_{in}}}{T_{in} - T_{out}} \right)^2 + \left( - \frac{\omega_{T_{out}}}{T_{in} - T_{out}} \right)^2 + \left( - \frac{\omega_{\dot{W}_{comp,in}}}{\dot{W}_{comp,in}} \right)^2 \right]^{1/2} \tag{8.10}$$

With reference to the declared uncertainties and errors in Table 8.2, the error of the rotameter is defined as ± 14.4 l/h. The errors of the J-type thermocouples are taken as ± 1.1 °C with reference to special limits of error. Lastly, the error is defined for the power meter according to the exact measured value. The total error ratios in COP and the uncertainties in COP are given in Table 8.4 for the three repeated experiments. The average uncertainty in COP is calculated as 72.3%. This uncertainty is actually very high. Uncertainty analyses show the accuracy of the derived parameters from the set-up. Another benefit of the uncertainty analyses is that it shows the parameter having the highest contribution to the error. In other words, uncertainty analysis shows the variable causing the highest error. Hence, the uncertainty analyses highlight the focusing point to decrease the total error (Deneysel Çalışmalarda Hata ve Belirsizlik Analizi, n.d.).

Table 8.4 Total error ratio of COP and the uncertainty in COP according to the repeatability experiments

| **Experiment No** | **Total Error Ratio of COP (-)** | **Uncertainty in COP (%)** |
|---|---|---|
| **Experiment # 1** | 0.7211 | 72.1144 |
| **Experiment # 2** | 0.7108 | 71.0838 |
| **Experiment # 3** | 0.7377 | 73.7698 |
| **Average** | 0.7232 | 72.3227 |

If the accuracy of the temperature measurement device is ± 0.1 °C, the total error ratio, and hence the uncertainty decreases dramatically as shown in Table 8.5 with reference to the previous experimental data. This time the average uncertainty decreases from 72.3% to the 6.8%. It could be understood from the comparison of Table 8.4 and Table 8.5 that low accuracy of the thermocouples has the highest contribution of the uncertainty in COP. However, the uncertainty shows the maximum experimental error in COP. Since all thermocouples of the test rig is calibrated before the experiments, the potential error is expected to be much more less than the calculated uncertainty values in COP.

Table 8.5 Resultant total error ratio of COP and uncertainty in COP when the temperature accuracy is increased for the same repeatability experiment set

| Experiment No | Total Error Ratio of COP (-) | Uncertainty in COP (%) |
|---|---|---|
| **Experiment # 1** | 0.0674 | 6.7379 |
| **Experiment # 2** | 0.0665 | 6.6468 |
| **Experiment # 3** | 0.0688 | 6.8844 |
| **Average** | 0.0676 | 6.7563 |

Meanwhile, the temperature difference of the evaporator SHTF between the inlet and outlet of the evaporator is very close to the error in the temperature measurement. It is another factor increasing the uncertainty in COP. The improvement potentials in the experimental set-up would be discussed in Chapter 9 in detail. J-type thermocouples are required to be changed with the more accurate temperature measurement devices such as PT100 sensors to achieve high accuracy in COP. As for the future study, flow rate of the SHTF would be decreased to create a larger temperature difference and to reduce the uncertainty in COP for the proposed experiments.

### 8.5 Equations to Analyze the Experimental Data

There are two equation sets for analyzing the experimental data. First group is for the investigations on the VCRC; whereas the second group is for the EERC. Thermodynamic properties are obtained using REFPROP version 10.0 (Lemmon et al., 2018).

#### *8.5.1 Equations of the VCRC*

Thermodynamic functions used in the state definitions are presented below with reference to specific measurement points in the test rig. The states of the refrigerants at each measurement point are checked with respect to the saturation conditions. The enthalpies of the refrigerants at the inlets and outlets of each component are expressed as

$$h_{comp,in} = h(T_{comp,in}, P_{comp,in}) \quad (8.11)$$

$$h_{comp,out} = h(T_{comp,out}, P_{comp,out}) \tag{8.12}$$

$$h_{c,in} = h(T_{c,in}, P_{c,in}) \tag{8.13}$$

$$h_{c,out} = h(T_{c,out}, P_{c,out}) \tag{8.14}$$

$$h_{\exp v,in} = h(T_{\exp v,in}, P_{\exp v,in}) \tag{8.15}$$

$$h_{\exp v,out(e,in)} = h_{\exp v,in} \tag{8.16}$$

$$h_{e,out} = h(P_{e,out}, T_{e,out}) \tag{8.17}$$

Subcooling temperature difference at the outlet of the condenser is calculated according to the saturation temperature at the outlet pressure as follows;

$$\Delta T_{sc} = T_{c,out,sat} - T_{c,out} \tag{8.18}$$

$$T_{c,out,sat} = T_{sat}(P_{c,out}) \tag{8.19}$$

$\Delta P_{\mathrm{check,expv,out(check,e,in)}}$ and $\Delta T_{\mathrm{check,expv,out(check,e,in)}}$ must be close to zero as most as possible. This control is required to show that the refrigerant is in two-phase region at the outlet of the expansion valve. The quality of the refrigerant at the evaporator inlet (expansion valve outlet) is determined with reference to the independent parameter couples comprised of enthalpy and pressure or enthalpy and temperature.

$$\Delta P_{check,\exp v,out(check,e,in)} = P_{\exp v,out,sat(e,in,sat)} - P_{\exp v,out(e,in)} \tag{8.20}$$

$$\Delta T_{check,\exp v,out(check,e,in)} = T_{\exp v,out,sat(e,in,sat)} - T_{\exp v,out(e,in)} \tag{8.21}$$

$$r_{\exp v,out(e,in)(P)} = r(P_{\exp v,out(e,in)}, h_{\exp v,out(e,in)}) \tag{8.22}$$

$$r_{\exp v,out(e,in)(T)} = r(T_{\exp v,out(e,in)}, h_{\exp v,out(e,in)}) \tag{8.23}$$

As it is seen from the Equation (8.22) and Equation (8.23), the quality of the refrigerant is defined according to the pressure and temperature in addition to the enthalpy at the same point, respectively for checking the reliability of the results. They yield nearly the same quality values. Superheat temperature difference at the outlet of the evaporator is determined as below

$$T_{e,out,sat} = T_{sat}(P_{e,out}) \tag{8.24}$$

$$\Delta T_{sh} = T_{e,out} - T_{e,out,sat} \tag{8.25}$$

Next, compressor isentropic efficiency is calculated as follows;

$$s_{comp,in} = s(T_{comp,in}, P_{comp,in}) \tag{8.26}$$

$$h_{comp,out,isen} = h(P_{comp,out}, s_{comp,in}) \tag{8.27}$$

$$\eta_{comp,isen} = \frac{h_{comp,out,isen} - h_{comp,in}}{h_{comp,out} - h_{comp,in}} \tag{8.28}$$

Heat loss from the compressor as well is taken into account and added to the rest of the calculations. Compressor is thought to be a cylindrical object having approximately 10 cm diameter and 30 cm length. Average surface temperature of the compressor is measured and defined as 46.74 °C. Environment temperature is measured as 29 °C at the time of a typical experiment. All properties of the air are evaluated at the film temperature. The correlation of Churchill & Chu (1975) is used with reference to Incropera, Dewitt, Bergman, & Lavine (2007) for the long horizontal cylinder. The correlation of Churchill & Chu (1975) recommended for a wide Rayleigh number range ($Ra_D \leq 10^{12}$) is given as

$$\overline{Nu_D} = \left\{ 0.60 + \frac{0.387 Ra_D^{1/6}}{\left[1 + (0.559/\Pr)^{9/16}\right]^{8/27}} \right\}^2 \tag{8.29}$$

The heat transfer coefficient for the free convection based on the aforecited correlation is calculated as 4.32 W/m$^2$K and the magnitude of the heat losses from the compressor is 8.54 W. Refrigerant mass flow rate is calculated in three different ways from the experimental measurements. All must be close to each other as most as possible. First one is from the compressor power which is obtained from the energy analyzer.

$$\dot{m}_{ref,comp,en-analyzer} = \frac{\dot{W}_{comp,in} - \dot{Q}_{comp,loss}}{h_{comp,out} - h_{comp,in}} \tag{8.30}$$

The heat transfer rates from refrigerant to the condenser SHTF (water) and from evaporator secondary fluid (water) to the refrigerant are used to calculate the refrigerant mass flow rate.

$$\dot{Q}_{c,\sec,fl(w)} = (\dot{m} c_p (T_{out} - T_{in}))_{c,\sec,fl(w)} \tag{8.31}$$

$$\dot{Q}_{e,\sec,fl(w)} = (\dot{m} c_p (T_{out} - T_{in}))_{e,\sec,fl(w)} \tag{8.32}$$

$$\dot{m}_{ref,c,\sec,fl(w),} = \frac{\dot{Q}_{c,\sec,fl(w)}}{h_{c,in} - h_{c,out}} \tag{8.33}$$

$$\dot{m}_{ref,e,\sec,fl(w)} = \frac{\dot{Q}_{e,\sec,fl(w)}}{h_{e,out} - h_{e,in}} \tag{8.34}$$

Mass flow rate from the compressor energy balance is assumed to be the most accurate since heat loss from the compressor as well is taken into account. For example, according to the outcomes of the repeated experiments, when the mass flow rate calculated from the compressor's energy balance is assumed to be the most accurate, the percentage error is approximately 3% and 10% in comparison with the mass flow rates calculated from the energy balances of the evaporator and condenser, respectively. The percentage error between the mass flow rates calculated from the energy balance of the condenser and evaporator is around 13% when the mass flow rate calculation from the evaporator's energy balance is assumed more accurate. As discussed previously, COP determined in two different ways are formulated as follows;

$$COP_1 = \frac{\dot{Q}_{e,en-analyzer}}{\dot{W}_{comp,in}} \tag{8.35}$$

$$COP_2 = \frac{\dot{Q}_{e,sc,fl(w)}}{\dot{W}_{comp,in}} \tag{8.36}$$

To sum up, the exact heat transfer from the SHTF in the evaporator is assumed to be more correct for the evaporation capacity used in the COP declarations. For the mass flow rate calculation, the energy consumption of the compressor is used mainly to establish the energy balance. Lastly, the conservation of the energy throughout the cycle is given for the repeated experiments based on the following equation.

$$\Delta \dot{E}_{cons} = \dot{W}_{comp,in} + \dot{Q}_{e,\sec,fl(w)} - \dot{Q}_{c,\sec,fl(w)} - \dot{Q}_{comp,loss} \tag{8.37}$$

### *8.5.2 Equations of the EERC*

Evaluation of the properties at the inlet and outlet of the main components are the same as the VCRC. Moreover, heat removal and rejection from/to the SHTFs of the evaporator and condenser, respectively, and COP are calculated in the same way. All differences are described with the following equations. The enthalpy of the refrigerants at the motive and suction nozzle inlets are given as

$$h_{m,in} = h(T_{m,in}, P_{m,in}) \tag{8.38}$$

$$h_{s,in} = h(T_{s,in}, P_{s,in}) \tag{8.39}$$

Experimental analyses include various checks concerned with the states of the refrigerants at various locations. Refrigerant is in two-phase state at the outlet of the ejector. It is checked whether the pressure and temperature of the refrigerant at the diffuser outlet correspond to the saturation conditions.

$$P_{ej,out,sat} = P_{sat}(T_{ej,out}) \tag{8.40}$$

$$\Delta P_{check,ej,out} = P_{ej,out,sat} - P_{ej,out} \tag{8.41}$$

$$T_{ej,out,sat} = T_{sat}(P_{ej,out}) \tag{8.42}$$

$$\Delta T_{check,ej,out} = T_{ej,out,sat} - T_{ej,out} \tag{8.43}$$

$\Delta P_{check,ej,out}$ and $\Delta T_{check,ej,out}$ must be close to “0” as most as possible. The enthalpy of the total refrigerant flow could be calculated from the energy balance after defining the mass flow rates of the primary and secondary fluids of the ejector. This equation is provided after the mass flow rate calculations of the primary and secondary fluids. Enthalpy and pressure of the total flow are two independent properties; hence the quality of the refrigerant is defined at the ejector outlet. Diffuser outlet quality cannot be determined with only primary and secondary fluid mass flow rates since the separation efficiencies of the liquid-vapor separator are not known.

$T_{ej,out,sat}$ is slightly higher than $T_{ej,out}$; hence compressed liquid assumption is as well valid at this point. However, because of the cycle’s nature, it is known that the refrigerant is in two-phase state at this point. Making use of the energy balance of the ejector, it could be proved later that the refrigerant has a quality value at this point. Therefore, it is important to know the details of the cycle to determine the phases of the critical points. The measurement devices of the temperature and pressure have uncertainties and it is impossible to measure directly corresponding saturation pressure for a temperature or corresponding saturation temperature for a pressure. To be sure that the refrigerant at the separator vapor port is saturated vapor and the refrigerant at the separator liquid port is saturated liquid, the following parameters (differences) are controlled.

$$P_{rsvp,out,sat} = P_{sat}(T_{rsvp,out}) \tag{8.44}$$

$$\Delta P_{check,rsvp,out} = P_{rsvp,out,sat} - P_{rsvp,out} \tag{8.45}$$

$$T_{rsvp,out,sat} = T_{sat}(P_{rsvp,out}) \tag{8.46}$$

$$\Delta T_{check,rsvp,out} = T_{rsvp,out,sat} - T_{rsvp,out} \tag{8.47}$$

$$h_{rsvp,out(P)} = h(P_{rsvp,out}, r_{rsvp,out} = 1) \tag{8.48}$$

$$h_{rsvp,out(T)} = h(T_{rsvp,out}, r_{rsvp,out} = 1) \tag{8.49}$$

$$\Delta h_{check,rsvp,out} = h_{rsvp,out(P)} - h_{rsvp,out(T)} \tag{8.50}$$

$$P_{rslp,out,sat} = P_{sat}(T_{rslp,out}) \tag{8.51}$$

$$\Delta P_{check,rslp,out} = P_{rslp,out,sat} - P_{rslp,out} \tag{8.52}$$

$$T_{rslp,out,sat} = T_{sat}(P_{rslp,out}) \tag{8.53}$$

$$\Delta T_{check,rslp,out} = T_{rslp,out,sat} - T_{rslp,out} \tag{8.54}$$

$$h_{rslp,out(P)} = h(P_{rslp,out}, r_{rslp,out} = 0) \tag{8.55}$$

$$h_{rslp,out(T)} = h(T_{rslp,out}, r_{rslp,out} = 0) \tag{8.56}$$

$$\Delta h_{check,rslp,out} = h_{rslp,out(P)} - h_{rslp,out(T)} \tag{8.57}$$

Hence, it could be understood from the values of the controlled differences ($\Delta P_{check,rsvp,out}$, $\Delta T_{check,rsvp,out}$, $\Delta h_{check,rsvp,out}$, $\Delta P_{check,rslp,out}$, $\Delta T_{check,rslp,out}$, and $\Delta h_{check,rslp,out}$), the refrigerant flows leaving the separator vapor port and liquid port are in saturated vapor and saturated liquid states, respectively. The separation efficiencies are not known although it is observed that the system includes inefficient separation.

Hence, the refrigerants at the vapor port and liquid port are assumed to be in saturated vapor and saturated liquid states, respectively while determining the diffuser outlet enthalpy. Next, primary refrigerant fluid mass flow rate could be determined in two different ways, i.e. compressor power consumption and heat rejection to the SHTF of the condenser as

$$\dot{m}_{ref,comp,pf} = \frac{\dot{W}_{comp,in} - \dot{Q}_{comp,loss}}{h_{comp,out} - h_{comp,in}} \tag{8.58}$$

$$\dot{m}_{ref,c,\sec,fl(w),pf} = \frac{\dot{Q}_{c,\sec,fl(w)}}{h_{c,in} - h_{c,out}} \tag{8.59}$$

Mass flow rate of the secondary (suction) fluid is calculated according to the heat gain from the SHTF of the evaporator.

$$\dot{m}_{ref,e,\sec,fl(w),sf} = \frac{\dot{Q}_{e,\sec,fl(w)}}{h_{e,out} - h_{e,in}} \tag{8.60}$$

With the known mass flows, the enthalpy of the two-phase refrigerant at the diffuser outlet could be calculated from the energy balance assuming that the velocity of the refrigerant flows at the inlets and outlet of the ejector is equal to zero. Two independent properties, i.e. enthalpy and pressure of the refrigerant at the ejector outlet is enough to define the quality at this point.

$$h_{ej,out} = \frac{\dot{m}_{ref,comp,pf}\, h_{m,in} + \dot{m}_{ref,e,\sec,fl(w),sf}\, h_{s,in}}{(\dot{m}_{ref,comp,pf} + \dot{m}_{ref,e,\sec,fl(w),sf})} \tag{8.61}$$

$$r_{ej,out} = r(P_{ej,out}, h_{ej,out}) \tag{8.62}$$

## 8.6 Experimental Results

Experimental results are categorized into four groups as follows;

- Performance analyses of R134a in the conventional cycle at three different compressor frequency values,
- Parametric performance analyses of R134a according to various operating conditions,
- Performance analyses of the R1234yf in the conventional VCRC,
- Performance analyses of R134a in the EERC at three different compressor frequency values.

### *8.6.1 Performance Analyses of R134a in the VCRC according to Compressor Frequency*

First result group is presented for R134a in the conventional VCRC at different compressor frequencies, i.e. 50 Hz, 45 Hz, and 40 Hz. The specifications concerned with the operating condition are given in Table 8.6. The performance evaluation for the compressor frequency of 50 Hz is given as the average of the repeatability experiments.

Table 8.6 External operating conditions for the compressor frequency analyses of VCRC

| **Parameters** | **Values** |
|---|---|
| $T_{c,sec,fl(w)}$ (°C) | 35 |
| $T_{e,sec,fl(w)}$ (°C) | 20 |
| Volumetric flow rate of condenser water (l/h) | 400 |
| Volumetric flow rate of evaporator water (l/h) | 1200 |
| Compressor frequency (Hz) | 50-45-40 |

Temperature and pressure variations at the compressor outlet are shown in Figure 8.7 (a) and (b) with respect to variations in the compressor frequency. Only compressor outlet pressures and temperatures are plotted with respect to the variations in the compressor frequency as the example declarations. The temperature at the compressor outlet gives an instantaneous reflect to the change in the frequency. However, the temperature profiles are stabilized around the same temperature in a very short time as shown in Figure 8.7 (a). Moreover, compressor outlet pressure decreases slightly when the compressor frequency is decreased as shown in Figure 8.7 (b).

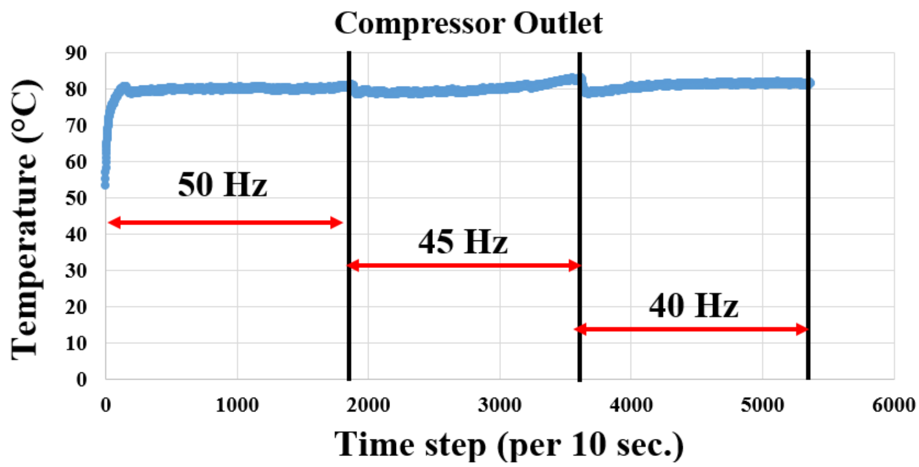


(a)

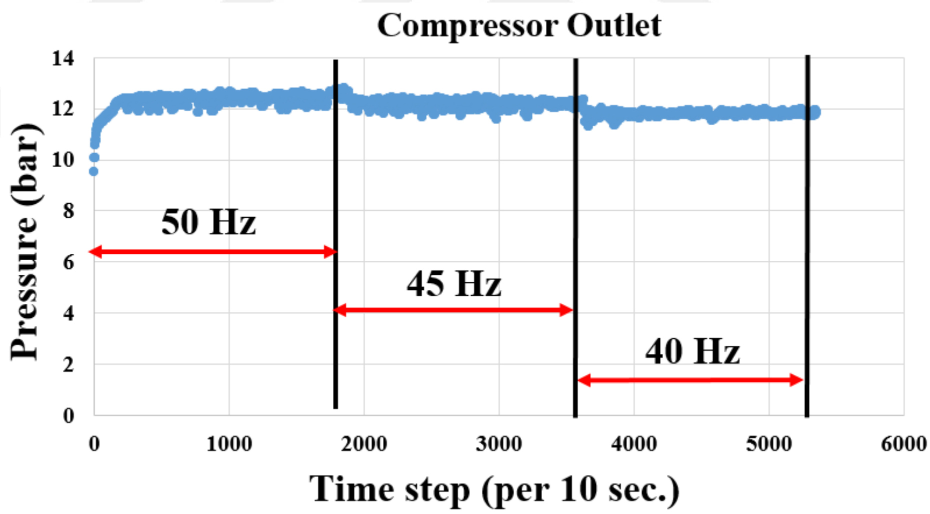


(b)

Figure 8.7 Variations of (a) the temperature and (b) the pressure (gage) profiles at the compressor outlet with respect to variations in the compressor frequency

Table 8.7 shows the pressure difference between the compressor inlet and outlet, evaporation capacity, compressor work input, COP, and refrigerant mass flow rate with respect to the variations in the compressor frequency. As stated previously, heat transfer from the evaporator SHTF is considered in the COP calculations as the evaporation capacity and mass flow rate of the refrigerant is determined based on the compressor work input obtained from the energy analyzer.

Table 8.7 Performance values of R134a in the VCRC according to compressor frequency

| **Compressor frequency (Hz)** | **Inlet and outlet gage pressures of the compressor (kPa)** | **Evaporation capacity (W)** | **Compressor work input (W)** | **COP (-)** | **Refrigerant mass flow rate (kg/s)** |
|---|---|---|---|---|---|
| **50** | 234.05 -1243.42 | 2997.02 | 1217.78 | 2.46 | 0.0235 |
| **45** | 238.62 -1218.06 | 2735.18 | 1100.00 | 2.49 | 0.0217 |
| **40** | 247.28 -1180.46 | 2603.95 | 971.43 | 2.68 | 0.0194 |

As seen from Table 8.7, when the compressor frequency is decreased, the operating pressure range of the compressor decreases as well. Both evaporation capacity and compressor work decrease in accordance with the reduction in the compressor frequency. Moreover, percentage decrease is higher in the compressor work input in comparison with the evaporation capacity. Hence, there is a slight increase in COP with respect to the decrease in the compressor frequency. Mass flow rate of the refrigerant decreases as well when the compressor frequency is decreased as expected.

### *8.6.2 Parametric Performance Analyses of R134a in the VCRC under Various Operating Conditions*

This parametric investigation is required to evaluate the performance improvement in the EERC. The main aim of these parametric analyses is displaying the performance curves of R134a according to operating pressures. They are not direct comparison experiments for the corresponding tests of EERC. All these experiments conducted under the research scope of this thesis are for the investigation of the cycle characteristics. It is satisfactory to give a COP range with reference to operating pressure ranges. Operating conditions are changed by adjusting the temperature of the SHTF at the evaporator and/or condenser. The summary of the parametric operating conditions is given in Table 8.8.

Table 8.8 External operating conditions for the parametric analyses of VCRC

| **Parameters** | **Values** |
|---|---|
| $T_{c,sec,fl(w)}$ (°C) | 30-35-40-45 |
| $T_{e,sec,fl(w)}$ (°C) | 10-15-20-25 |
| Volumetric flow rate of condenser water (l/h) | 400 |
| Volumetric flow rate of evaporator water (l/h) | 1200 |
| Compressor frequency (Hz) | 50 |

As seen from Table 8.8, the temperature range for the condenser SHTF is between 30 °C-45 °C and this range is between 10 °C-25 °C for the evaporator SHTF. While varying the temperature of the evaporator SHTF, the temperature of the condenser SHTF is kept constant as 35 °C. Similarly, for the temperature variations of the condenser SHTF, the temperature of the evaporator SHTF is kept at 20 °C. For the case of the evaporator SHTF temperature of 20 °C and condenser SHTF temperature of 35 °C, the average performance values of the repeatability experiments are used. The results of the parametric analyzes are given in Table 8.9 and Table 8.10 according to variations of the evaporator and condenser SHTF temperatures, respectively.

Table 8.9 Performance of R134a in the VCRC at various evaporator SHTF temperatures

| **$T_{e,sec,fl(w)}$ (°C)** | **Inlet and outlet gage pressures of the compressor (kPa)** | **Evaporation capacity (W)** | **Compressor work input (W)** | **COP (-)** | **Refrigerant mass flow rate (kg/s)** |
|---|---|---|---|---|---|
| **10** | 138.88 -1115.41 | 1550.20 | 988.24 | 1.57 | 0.0168 |
| **15** | 179.99 -1186.15 | 2235.23 | 1100.00 | 2.03 | 0.0194 |
| **20** | 234.05 -1243.42 | 2997.02 | 1217.78 | 2.46 | 0.0235 |
| **25** | 266.51 -1323.35 | 3618.16 | 1315.38 | 2.75 | 0.0263 |

Variations of the condenser and evaporator SHTF temperatures result in the various operating conditions in terms of the condenser and evaporator pressures, respectively. Actually, when the condensation pressure is changed, the evaporation pressure is affected as well as being different from the ideal numerical operating conditions. The following plots based on the aforecited experimental performance values presented in Table 8.9 and Table 8.10, are given with reference to condenser and evaporator inlet pressures as the condensation and evaporation pressures. Actual pressures at the inlet and outlet of the compressor is given in both of the tables.

Table 8.10 Performance of R134a in the VCRC at various condenser SHTF temperatures

| $T_{c,sec,fl(w)}$ (°C) | Inlet and outlet gage pressures of the compressor (kPa) | Evaporation capacity (W) | Compressor work input (W) | COP (-) | Refrigerant mass flow rate (kg/s) |
|---|---|---|---|---|---|
| **30** | 212.85 -1104.60 | 3030.38 | 1136.84 | 2.67 | 0.0228 |
| **35** | 234.05 -1243.42 | 2997.02 | 1217.78 | 2.46 | 0.0235 |
| **40** | 253.89 -1447.97 | 2847.92 | 1366.67 | 2.08 | 0.0250 |
| **45** | 269.92 -1569.03 | 2678.83 | 1440.68 | 1.86 | 0.0252 |

As seen from this pressure range, when the temperature of the evaporator SHTF is changed while keeping the temperature of the condenser SHTF constant, the evaporator pressure is affected mostly rather than the condenser pressure. Similarly, when the temperature of the condenser SHTF is varied while keeping the temperature of the evaporator SHTF constant, the SHTF temperature of the condenser has the main influence on the condenser pressure when compared to the corresponding changes in the evaporator pressure. Effects of the condenser and evaporator pressure are displayed in Figure 8.8 (a) and (b). Generally speaking, COP decreases when the condenser pressure is increased; whereas COP increases when the evaporator pressure is increased.

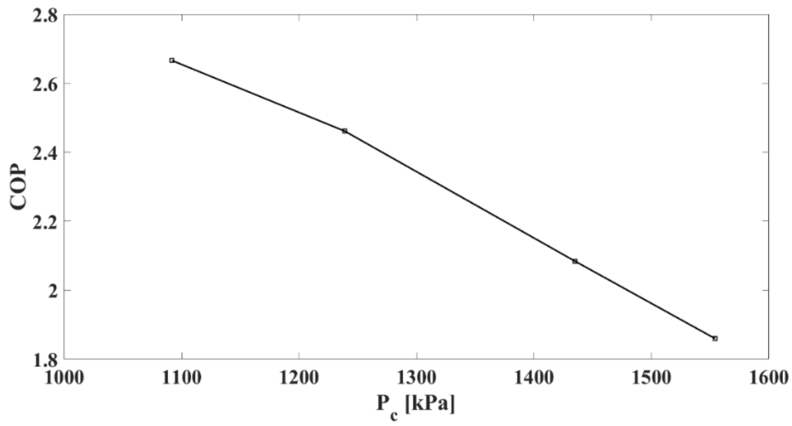


**(a)**

Figure 8.8 Effect of (a) the condenser and (b) the evaporator pressures (gage) on experimental COP

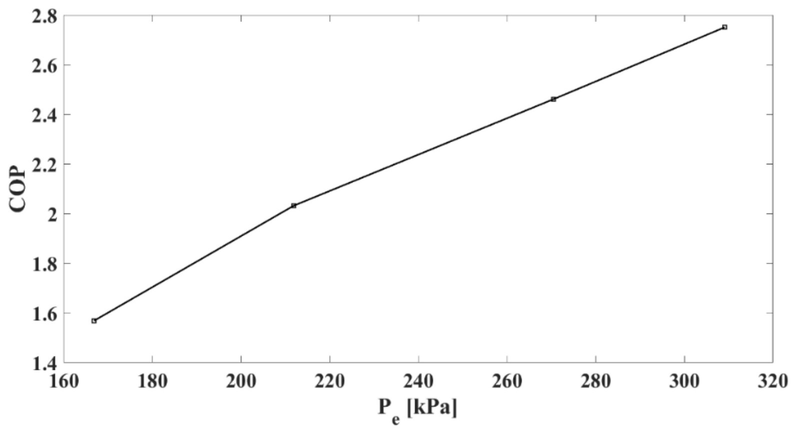


**(b)**

Figure 8.8 continues

The corresponding evaporation capacity and compressor work input according to variations in the condenser and evaporator pressures are declared in Figure 8.9 (a) and (b), respectively. Increase in the condenser pressure yields decrease in the evaporation capacity and increase in the compressor work input as shown in Figure 8.9 (a). Hence, COP decreases as a result of this double effect. By the way, percentage increase in the compressor work input is two times higher than the percentage decrease in the cooling capacity according to investigated operating conditions.

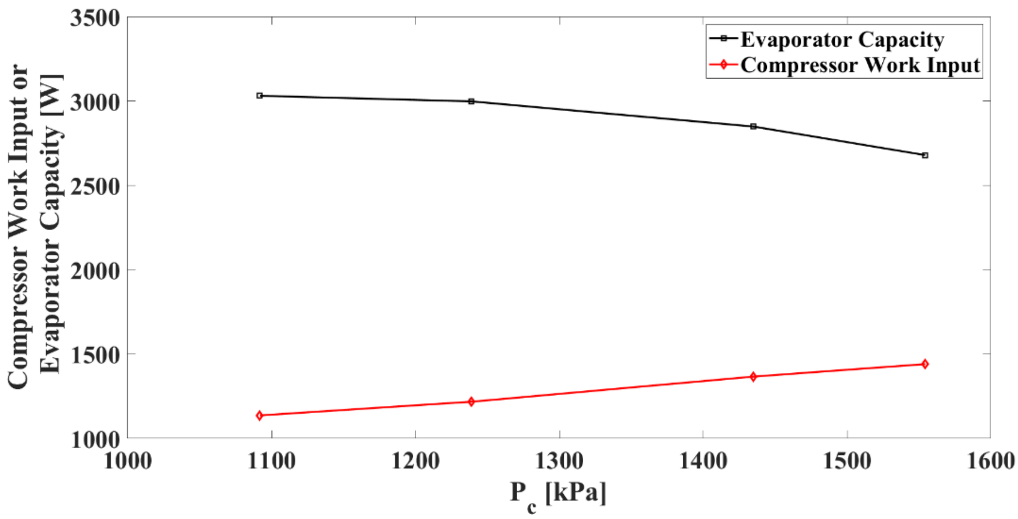


**(a)**

Figure 8.9 Variations of the experimental evaporator capacity and compressor work input according to operating conditions: (a) condenser pressure (gage) and (b) evaporator pressure (gage)

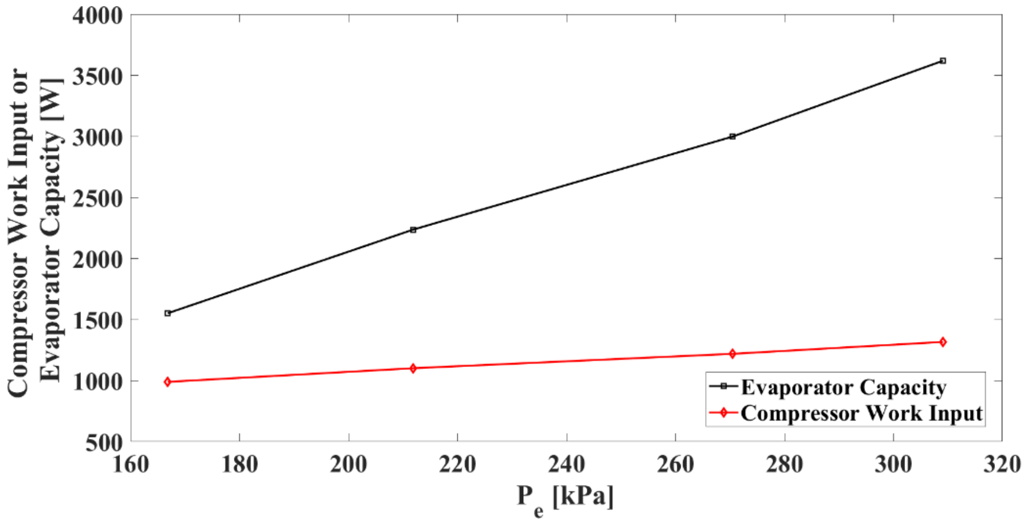


**(b)**

Figure 8.9 continues

When the evaporator pressure is increased, both evaporation capacity and compressor work input increases as shown in Figure 8.9 (b). However, percentage increase in the evaporator capacity is much higher than the percentage increase in the compressor work input causing increase in COP at the higher evaporator pressures. Finally, mass flow rate of the refrigerant increases when both the evaporator and condenser pressures are increased. However, evaporation capacity affects more the refrigerant mass flow rate when compared to the condenser pressure.

### *8.6.3 Performance Investigation of R1234yf in the VCRC*

The performance of R1234yf is investigated in the VCRC to compare its performance with R134a. Three experimental case is presented to analyze the performance of R1234yf. The operating conditions are given in Table 8.11. According to the operating conditions given in Table 8.11, the performance parameters are given in Table 8.12. External conditions and valve openings are adjusted to create typically the same internal conditions of R1234yf experiments as R134a experiments. The external operating conditions given in Table 8.11 for R1234yf correspond to the operating condition of R134a having 40 °C and 20 °C condenser and evaporator SHTF temperatures, respectively.

Table 8.11 External operating conditions for the analyses of R1234yf in the VCRC: Case #1

| Parameters | Values |
|---|---|
| $T_{c,sec,fl(w)}$ (°C) | 45 |
| $T_{e,sec,fl(w)}$ (°C) | 20 |
| Volumetric flow rate of condenser water (l/h) | 350 |
| Volumetric flow rate of evaporator water (l/h) | 800 |
| Compressor frequency (Hz) | 40 |

Table 8.12 Performance evaluation of R1234yf for the external conditions given in Table 8.11.

| Performance Parameters | Values |
|---|---|
| Inlet and outlet gage pressures of the compressor (kPa) | 295.06 -1444.88 |
| Evaporation capacity from the SHTF (W) | 2261.54 |
| Evaporation capacity from the energy analyzer (W) | 2215.38 |
| Compressor work input (W) | 1138.46 |
| $COP_1$ (-) | 1.95 |
| $COP_2$ (-) | 1.99 |
| Refrigerant mass flow rate (kg/s) | 0.0252 |
| Condenser outlet subcooling temperature difference (K) | 0.17 |
| Evaporator outlet superheat temperature difference (K) | 10.19 |

R134a has 1194 kPa pressure difference between the inlet and outlet of the compressor for 1448 kPa compressor outlet gage pressure. The evaporator inlet gage pressure of R134a for this case is 296 kPa. However, R1234yf displays the pressure difference of 1150 kPa between the inlet and outlet of the compressor for 1445 kPa compressor outlet gage pressure and this pressure difference is less than that of R134a. By the way, the evaporator inlet gage pressure of R1234yf for the same case is 334 kPa. Although the operating range is lower for R1234yf at nearly the same compressor outlet pressure, the COP is lower in comparison with R134a as obvious from the Table 8.10 and Table 8.12.

R1234yf yields 6.3% lower COP value at this operating condition with respect to evaporation capacity from the energy analyzer when compared to the COP of R134a. However, R1234yf displays 4% lower COP in comparison with R134a with reference to evaporation capacity from the evaporator SHTF side. For the parametric analyses of R134a, evaporation capacity from the SHTF side is used which is more correct since eliminates the energy losses/gains throughout the system. Actually, in this case evaporation capacities are closer to each other from both of the approaches, i.e. energy analyzer and SHTF. It is expected that R1234yf performance is lower than that of R134a at the nearly same operating conditions.

On the other hand, for some cases, volumetric flow rate of the evaporator SHTF is adjusted very low just to configure the internal operating conditions of R1234yf similar to one of the parametric operating condition of R134a. Therefore, a comparative base is created and the superheat temperature difference is kept below 10 K at the evaporator outlet. As a result of the lower flow rate of evaporator SHTF, the thermocouple has the sensing problem inside the pipe. This situation creates such a condition that the SHTF leaves the evaporator with a higher temperature when compared to the inlet temperature. It is well known from the energy analyzer that there is cooling throughout the evaporator. Therefore, COP value with reference to the evaporation capacity obtained from the energy analyzer is the reference value for the parametric analyses of R1234yf.

Both of the evaporation capacities are provided if the data is available with respect to the external operating conditions. However, for the external operating conditions including lower evaporator SHTF volume flow rate, performance parameters evaluated with respect to only evaporation capacity from the energy analyzer are provided. Table 8.13 shows the second experimental analysis case for R1234yf and Table 8.14 gives the corresponding performance values.

The second parametric case for R1234yf yields similar internal conditions of R134a operating at the condenser SHTF temperature of 35 °C and the evaporator SHTF temperature of 20 °C. The pressure difference between the compressor inlet and outlet is 1018 kPa for R1234yf and 1009 kPa for R134a. The compressor outlet gage pressure is 1274.6 kPa for R1234yf and 1243.42 kPa for R134a. Evaporator inlet gage pressures as well 305.2 kPa and 270.5 kPa for R1234yf and R134a, respectively. Hence, it is concluded that both cases having nearly the same internal conditions could be compared in terms of performance.

Table 8.13 External operating conditions for the analyses of R1234yf in the VCRC: Case #2

| **Parameters** | **Values** |
|---|---|
| $T_{c,sec,fl(w)}$ (°C) | 40 |
| $T_{e,sec,fl(w)}$ (°C) | 20 |
| Volumetric flow rate of condenser water (l/h) | 350 |
| Volumetric flow rate of evaporator water (l/h) | 300 |
| Compressor frequency (Hz) | 40 |

Table 8.14 Performance evaluation of R1234yf for the external conditions given in Table 8.13

| **Performance Parameters** | **Values** |
|---|---|
| Inlet and outlet gage pressures of the compressor (kPa) | 256.58 -1274.55 |
| Evaporation capacity from the SHTF (W) | - |
| Evaporation capacity from the energy analyzer (W) | 2100 |
| Compressor work input (W) | 1033.33 |
| $COP_1$ (-) | 2.03 |
| $COP_2$ (-) | - |
| Refrigerant mass flow rate (kg/s) | 0.0236 |
| Condenser outlet subcooling temperature difference (K) | 0.20 |
| Evaporator outlet superheat temperature difference (K) | 4.05 |

As seen from Table 8.10 and Table 8.14, R1234yf displays nearly 17.5% lower COP in comparison with R134a. The declared COP value for R134a in Table 8.10 is 2.46 and it is determined with respect to the evaporation capacity from the SHTF side. However, if the COP is determined with reference to evaporation capacity from the energy analyzer of the evaporator, it is calculated as 2.65 which is higher than the COP defined with respect to evaporation capacity from the SHTF side. This time according to COP comparison with reference to the same evaporation capacity calculation approach, R1234yf has 23.4% lower COP in comparison with R134a. The external operating conditions and performance evaluation are presented in Table 8.15 and Table 8.16, respectively for the last case.

Table 8.15 External operating conditions for the analyses of R1234yf in the VCRC: Case #3

| **Parameters** | **Values** |
|---|---|
| $T_{c,sec,fl(w)}$ (°C) | 35 |
| $T_{e,sec,fl(w)}$ (°C) | 20 |
| Volumetric flow rate of condenser water (l/h) | 350 |
| Volumetric flow rate of evaporator water (l/h) | 250 |
| Compressor frequency (Hz) | 40 |

Performance evaluation of the third case for R1234yf given in Table 8.16 corresponds to the performance evaluation of R134a at the external conditions of 30 °C and 20 °C condenser and evaporator SHTF temperatures, respectively. The pressure difference between the inlet and outlet of the compressor is 892 kPa for R134a; whereas the corresponding difference is 911 kPa for R1234yf. The compressor outlet gage pressures are 1135.44 kPa and 1104.60 kPa for R1234yf and R134a, respectively. Evaporator inlet gage pressure is 269 kPa for R1234yf and 249 kPa for R134a. Hence, the internal operating conditions of both refrigerants under the given external conditions could be compared.

Since the evaporator SHTF volume flow rate is lower, the same temperature sensing problem is again occurred. Therefore, COP is calculated with respect to the power consumption of the evaporator heater. According to the evaporation capacity obtained from the energy analyzer, R1234yf performs 12.4% less COP when compared to the COP of R134a at the very similar internal operating conditions. However, if COP of R134a as well is determined according to the evaporation capacity from the energy analyzer, COP is calculated as 2.89 and the percentage decrease is defined as 19% when R1234yf is used.

Table 8.16 Performance evaluation of R1234yf for the external conditions given in Table 8.15

| Performance Parameters | Values |
|---|---|
| Inlet and outlet gage pressures of the compressor (kPa) | 224.30 - 1135.44 |
| Evaporation capacity from the SHTF (W) | - |
| Evaporation capacity from the energy analyzer (W) | 2142.86 |
| Compressor work input (W) | 914.29 |
| $COP_1$ (-) | 2.34 |
| $COP_2$ (-) | - |
| Refrigerant mass flow rate (kg/s) | 0.0210 |
| Condenser outlet subcooling temperature difference (K) | 0.06 |
| Evaporator outlet superheat temperature difference (K) | 4.07 |

To sum up, at the all investigating cases, R1234yf performs less in comparison with R134a at the similar internal operating conditions. Condenser outlet subcooling temperature difference shows that the refrigerant may be at the saturation conditions. Superheat temperature difference at the evaporator outlet is less for R134a which is around 2 K. Pressure nearly stays the same throughout the condenser during the operations; whereas pressure drop of the evaporator is around 15-25 kPa for both of the refrigerants. Lastly, mass flow rates of these two refrigerants operating under similar internal conditions are very close to each other for the first and second cases. The third case results in a lower mass flow rate for R1234yf when compared to R134a at the similar internal conditions.

### *8.6.4 Performance Analyses of R134a in the EERC*

EERC tests are conducted mainly according to compressor frequency. This analyses do not correspond to parametric analyses of the EERC. They are just useful to investigate the EERC performance in terms of the system parameters. Three compressor frequency are chosen as 40 Hz, 38 Hz, and 36 Hz. All details concerned with the operating conditions are given in Table 8.17. All state checks are made with reference to Equation 8.20, Equation 8.21, Equation 8.41, Equation 8.43, Equation 8.45, Equation 8.47, Equation 8.50, Equation 8.52, Equation 8.54, Equation 8.57 for the critical points of the cycle, i.e. ejector outlet, expansion valve outlet, liquid-vapor separator outlets.

Table 8.17 External operating conditions for EERC tests of R134a

| **Parameters** | **Values** |
|---|---|
| $T_{c,sec,fl(w)}$ (°C) | 45 |
| $T_{e,sec,fl(w)}$ (°C) | 20 |
| Volumetric flow rate of condenser water (l/h) | 200 (EERC Exp. #1 & 2) and 225 (EERC Exp. #3) |
| Volumetric flow rate of evaporator water (l/h) | 800 |
| Compressor frequency (Hz) | 40 (EERC Exp. #1)<br>38 (EERC Exp. #2)<br>36 (EERC Exp. #3) |

All experimental performance evaluations are given in Table 8.18. Experimental performance evaluations show that the best efficient case is obtained for 38 Hz compressor frequency. Increase in the superheat temperature difference at the evaporator shows that COP of the cycle decreases. Hence, COP obtained for 38 Hz compressor frequency is the case having the lowest superheat temperature difference at the evaporator outlet. The highest pressure difference between the inlet and outlet of the compressor is obtained at the second experimental case as well. Moreover, the outlet pressure of the compressor is the highest for the same case. As seen from Table 8.18, evaporator operating pressure is higher for the second and third experiments in comparison with the first case. The reason for this situation is the manual adjustment of the valve at the compressor inlet. Therefore, the mass flow rate of the primary fluid is decreased while closing the valve at the compressor inlet as seen in Figure 8.10.

Table 8.18 Performance comparison of the EERC tests for R134a with reference to compressor frequency

| **Performance Parameters** | **EERC Exp. #1** | **EERC Exp. #2** | **EERC Exp. #3** |
|---|---|---|---|
| | **Values** | **Values** | **Values** |
| Inlet and outlet gage pressures of the compressor (kPa) | 179.09 - 1487.92 | 224.94 - 1542.52 | 222.90 - 1468.16 |
| Inlet and outlet gage pressures of the evaporator (kPa) | 183.71 - 180.84 | 326.82 - 330.46 | 298.77 - 300.12 |
| Evaporation capacity from the SHTF (W) | 1154.10 | 1681.58 | 1311.58 |
| Evaporation capacity from the energy analyzer (W) | 1100 | 1313.43 | 1266.67 |
| Compressor work input (W) | 933.33 | 1014.93 | 966.67 |
| $COP_1$ (-) | 1.18 | 1.29 | 1.31 |
| $COP_2$ (-) | 1.24 | 1.66 | 1.36 |
| Primary (Motive) fluid mass flow rate (kg/s) | 0.0141 | 0.0156 | 0.0153 |
| Secondary (suction) fluid mass flow rate (kg/s) | 0.0053 | 0.0087 | 0.0066 |
| Entrainment ratio (-) | 0.3765 | 0.5536 | 0.4306 |
| Diffuser outlet pressure (kPa) | 196.04 | 333.22 | 307.36 |
| Quality at the diffuser outlet (-) | 0.5988 | 0.6020 | 0.5663 |
| Condenser outlet subcooling temperature difference (K) | 0.51 | 0.57 | 0.55 |
| Evaporator outlet superheat temperature difference (K) | 22.03 | 5.44 | 9.82 |
| Pressure drop throughout the evaporator (kPa) | 2.87 | - | - |
| Compressor isentropic efficiency (-) | 0.5560 | 0.5425 | 0.5400 |

(a) (b)

Figure 8.10 Position of the valve at the compressor inlet after the separator vapor port: (a) fully open case for the 40 Hz compressor frequency test and (b) partially open case for the 38 and 36 Hz compressor frequency cases (Personal archive, 2020)

For the first experiment, the valve at the vapor port outlet (compressor inlet) is fully open as seen in Figure 8.10 (a). When it is seen that the entrainment ratio is very low at 40 Hz compressor frequency experiment, evaporator pressure is increased to create a higher secondary fluid mass flow rate. Therefore, the rest of the experiments are made with the valve position given in Figure 8.10 (b). Suction performance of the ejector is also dependent on the primary fluid mass flow rate. Since the designed motive nozzle could not be used in the ejector, the motive fluid mass flow rate is varied to obtain the highest COP. If the proposed motive nozzle could be manufactured and used in the ejector, the motive nozzle flow rate may again be required to be adjusted in the actual operating conditions. It is a well-known fact that suction nozzle pressure drop is an issue required to be optimized. Therefore, motive fluid mass flow rate is varied with the valve position and compressor frequency.

It is shown in Table 8.7 that the refrigerant mass flow rate decreases when the compressor frequency is decreased. In the EERC configuration, the motive nozzle mass flow rate is not only affected by the compressor frequency, but the motive nozzle design as well. A nozzle could be operated within a specific operating band. With the combined effect of the motive nozzle inlet pressure, the highest motive and suction nozzle mass flow rates are obtained for 38 Hz compressor frequency. Moreover, this operating case yields the highest entrainment ratio as expected. It is seen that when the valve opening or compressor frequency is changed, the dynamic system behavior is changed from various aspects, i.e. evaporator pressure, motive nozzle inlet pressure, motive nozzle mass flow rate. Within the content of this thesis, the effects are discussed based on the global performance parameters such as COP and entrainment ratio.

All experimental evaluations are made according to 100% efficient separator assumption. However, it is observed that the vapor and liquid separation processes have inefficiencies as seen from Figure 8.11. The design of the liquid-vapor separator has a very high importance on the EERC overall performance evaluation. From the previous numerical analyses, it is proved that although it is an external component, it has influence even on the ejector design. The liquid refrigerant and oil is accumulated in the liquid-vapor separator as seen in Figure 8.11 due to the poor suction. Hence, the refrigerant and oil mixture reaches nearly to the separator inlet. The space left for the refrigerant separation process deceases as a result.

Figure 8.11 Liquid refrigerant and oil accumulation in the liquid-vapor separator (Personal archive, 2020)

By the way, vapor port of the separator and two-phase refrigerant inlet of the separator are close to each other. The high-quality refrigerant is flowing through the compressor affecting the overall cycle performance. To sum up, separator inefficiency affects the performance adversely.

With reference to internal operating conditions, the third experiment of the EERC corresponds to VCRC experiment of R134a at the external condition of 40 °C condenser SHTF temperature and 20 °C evaporator SHTF temperature. For this case the performance improvement ratio is calculated as 0.65. The second experiment of EERC for 38 Hz compressor frequency is the counterpart of the VCRC experiment including 45 °C and 20 °C condenser and evaporator SHTF temperatures, respectively. For this case the performance improvement is calculated as 0.9. In the second case the EERC could be operated more appropriately with respect to the critical operating conditions such as motive nozzle inlet pressure, motive nozzle mass flow rate, and evaporation pressure.

Moreover, the performance improvement coefficient is always expected to be higher at the elevated condensation temperatures. Actually, these comparisons are made roughly. All internal operating conditions are to be identical for a safe comparison between the EERC and VCRC. These comparisons given in this thesis are only with respect to the similarity of the pressure differences between the compressor inlet and outlet and the compressor outlet pressures of the VCRC and EERC tests.

### 8.7 Experimental Validation of the Semi-1D Model

Experiments of R134a in the EERC are used in order to validate the semi-1D model with reference to assumed ejector component and liquid-vapor separator efficiencies. Motive nozzle efficiency is not necessary for semi-1D modelling approach since motive nozzle outlet pressure, velocity, and density is determined with respect to actual flow analyses. The suction nozzle efficiency is assumed to accomplish that the secondary fluid sucked into the ejector has a lower velocity than the velocity of the motive fluid. Critical operating and design parameters and their values implemented into the semi-1D model are presented in Table 8.19 for the three validation case. These validation cases are EERC tests of R134a in the previous section. The corresponding experimental conventional cycle COP values are estimated with respect to performance curves displayed in Figure 8.8. Motive nozzle geometry is defined with reference to the mounted nozzle inside the ejector. It is previously known that the throat diameter is calculated in the model according to operating conditions and other design parameters. Hence, although the throat diameter is fixed as 1.4 mm, the calculated throat diameters are presented for each validation case.

Table 8.19 Summary of the operating and design parameters for the validation cases

| **Parameters** | **Values** | | |
|---|---|---|---|
| | **Case #1 (for EERC Exp. #1)** | **Case #2 (for EERC Exp. #2)** | **Case #3 (for EERC Exp. #3)** |
| Refrigerant | R134a | R134a | R134a |
| Motive nozzle inlet diameter (mm) | 12 | 12 | 12 |
| Motive nozzle throat diameter (mm) | 1.1 | 1.2 | 1.2 |
| Converging angle (°) (half angle) | 19.2 | 19.2 | 19.2 |
| Length of the computational grid (mm) | 0.00004 | 0.00004 | 0.00004 |
| Primary fluid mass flow rate (kg/s) | 0.0141 | 0.0156 | 0.0153 |
| Diverging angle (°) (half angle) | 2.3 | 2.3 | 2.3 |
| Motive nozzle outlet diameter (kg/s) | 3 | 3 | 3 |
| Motive nozzle inlet temperature (°C) | 56.6 | 58.15 | 56.17 |
| Condenser outlet subcooling temperature difference (K) | 0.51 | 0.57 | 0.55 |
| Evaporator inlet temperature (°C) | -0.64 | 10.98 | 9.09 |
| Evaporator outlet superheat temperature difference (K) | 22.03 | 5.44 | 9.82 |
| Compressor isentropic efficiency (-) | 0.556 | 0.5425 | 0.54 |

Length of the computational grid is the same for each motive nozzle analysis in the previous chapter. For the condenser pressure, the saturation pressure corresponding to motive nozzle inlet temperature is used since the experimental temperature measurements are very close to each other for the condenser outlet and motive nozzle inlet. Since the pressure distribution is obtained according to the motive nozzle inlet conditions, the condenser pressure is determined with respect to the same conditions in the modelling approach just for the simplification. The subcooling temperature difference is very low for the validation cases. Hence, using the motive nozzle inlet temperature instead of the condenser temperature would not create a big difference. The inputs are used as the same inputs as the semi-1D model while evaluating the validation cases for a practical approach. However, if there is a higher subcooling temperature difference at the condenser outlet, this simplification may be misleading.

The condenser pressure is again could be defined in the same way, but the motive nozzle inlet temperature would be lower than the actual case. In semi-1D model, the condenser outlet and motive nozzle inlet temperatures are the same. However, there is a slight difference in terms of the experimental measurements. Evaporator pressure as well is determined with respect to the saturation pressure corresponding to the evaporator inlet temperature.

The efficiency combinations for each validation case are presented in Table 8.20. The suction nozzle efficiency is assumed to yield less secondary fluid velocity in comparison with the velocity of the primary fluid as given in Table 8.21. Mixing section and diffuser efficiencies are implemented into the model as high values to catch the experimental COP values. Liquid and vapor separation efficiencies are determined according to the relationship between the ejector outlet quality and entrainment ratio.

It is previously discussed under the literature findings that the vapor separation efficiency is generally high and liquid separation efficiency may have lower values. Hence, reasonable assumptions are made for these two efficiencies. It is already estimated that some portion of the liquid is sent to the compressor due to the inappropriate separator design resulting in lower performance than the conventional cycle. As a result of these discussions, the separator design is the crucial aspect preventing the higher COP targets of the EERC when compared to VCRC.

Table 8.20 Reasonable efficiency combinations for the experimental validation cases based on the estimations to catch the numerical performance values

| Case Number | Efficiency combinations | | | | |
|---|---|---|---|---|---|
| | $\eta_s$ | $\eta_{mix}$ | $\eta_d$ | $\eta_{vap}$ | $\eta_{liq}$ |
| Case #1 | 0.5 | 0.95 | 0.9 | 0.9 | 0.53 |
| Case #2 | 0.5 | 0.95 | 0.95 | 0.95 | 0.82 |
| Case #3 | 0.5 | 0.95 | 0.9 | 0.9 | 0.56 |

Table 8.21 Outlet conditions of the primary and secondary fluids and the resultant pressure drop in the suction nozzle with reference to evaporator pressure

| Case Number | $P_{m,out}$ (kPa) | $\rho_{m,out}$ (kg/m³) | $u_{m,out}$ (m/s) | $u_{s,out}$ (m/s) | $P_{drop}$ (kPa) |
|---|---|---|---|---|---|
| Case #1 | 98.24 | 10.89 | 183.09 | 151.93 | 187.76 |
| Case #2 | 110.22 | 12.17 | 181.20 | 165.80 | 318.13 |
| Case #3 | 108.35 | 12.17 | 177.79 | 164.57 | 293.80 |

Experimental validations are made for the COP of the EERC as given in Table 8.22 and for the secondary fluid mass flow rate and entrainment ratio as displayed in Table 8.23.

Table 8.22 Performance comparison of the EERC according to experimental measurements and semi-1D modelling approach

| Experiment Number | $COP_{EERC,exp}$ | $COP_{EERC,Semi\text{-}1D}$ |
|---|---|---|
| EERC Exp. #1 | 1.24 | 1.31 |
| EERC Exp. #2 | 1.66 | 1.56 |
| EERC Exp. #3 | 1.36 | 1.43 |

The percentage differences for the presented values of Table 8.22 and Table 8.23 show that semi-1D modelling approach yields a good agreement for the performance parameters of the EERC concept. All percentage differences for the COP of the EERC, secondary fluid mass flow rate, and entrainment ratio are displayed in Table 8.24.

Table 8.23 Comparison of the experimental measurements and semi-1D modelling approach for the secondary fluid mass flow rate and entrainment ratio

| **Experiment Number** | **Secondary fluid mass flow rate (kg/s) (Experimental)** | $\mathbf{w_{exp}}$ | **Secondary fluid mass flow rate (kg/s) (Semi-1D Model)** | $\mathbf{w_{semi\text{-}1D}}$ |
|---|---|---|---|---|
| EERC Exp. #1 | 0.0053 | 0.3765 | 0.0051 | 0.3611 |
| EERC Exp. #2 | 0.0087 | 0.5536 | 0.0076 | 0.4875 |
| EERC Exp. #3 | 0.0066 | 0.4306 | 0.0060 | 0.3927 |

Table 8.24 Percentage differences between the experimental data and numerical results obtained from the semi-1D modelling approach

| **Experiment Number** | $\mathbf{COP_{EERC}}$ **(%)** | **Secondary fluid mass flow rate (%)** | **w (%)** |
|---|---|---|---|
| EERC Exp. #1 | 5.49 | 3.92 | 4.08 |
| EERC Exp. #2 | 5.99 | 12.58 | 11.93 |
| EERC Exp. #3 | 4.86 | 8.95 | 8.79 |

Maximum percentage difference is around 6% for the COP of the EERC concept with the proper ejector component and liquid-vapor separator efficiency definitions. The secondary fluid mass flow rate is another critical issue in terms of the performance since they affect directly the evaporation capacity. It could be estimated via the semi-1D modelling approach with a maximum 13% error between the experimental and numerical results with reference to investigated three validation cases. Lastly, the maximum error for the entrainment ratio is around 12%. For more precise conclusions about the sensitivity of the model, range of the operating conditions is necessary to be widened. Up to now, outcomes of the semi-1D model could be used for the preliminary performance and design calculations instead of the thermodynamic modelling approach.

### 8.8 Comments on the Experimental Results

Four types of experiments are conducted under these thesis as follows; (i) VCRC experiments of R134a at various compressor frequencies, (ii) Parametric analyses of R134a in the VCRC, (iii) Performance analyses of R1234yf in the VCRC, and (iv)

Performance investigation of R134a in the EERC. For COP calculations, evaporation capacity is defined according to the heat removal from the evaporator SHTF by the refrigerant. Only for two performance tests of R1234yf, the evaporation capacity from the energy analyzer is used due to the temperature sensing problem of the thermocouple inside the pipe at lower volumetric flow rates of the evaporator SHTF. All these two performance comparisons of R1234yf are made according to COP of R134a from the evaporation capacity defined with respect to the energy analyzer as well in the corresponding operating range.

Condenser outlet subcooling temperature difference is less than 1K with respect to saturation temperature of the condenser outlet pressure. It is concluded that the refrigerant is in saturated liquid or still in two-phase regrion rather than being in compressed liquid state. However, it is assumed in the compressed liquid state according to calculated temperature difference.

Compressor frequency affects both cycle operating range and refrigerant mass flow rate. The operating range of the compressor and the refrigerant mass flow rate decreases with the decreased frequency. However, the cycle performance increases with respect to the decrease in the frequency. When evaporation pressure is increased at the same condenser SHTF temperature, COP as well increases. Although the condenser SHTF temperature is kept constant, condenser pressure increases due to the increase in the evaporator pressure. Therefore, both compression work and and evaporation capacity increases. However, the evaporation capacity increases more than the compressor work and the resultant effect is COP increase.

Similarly, when the condenser pressure is increased at the same evaporator SHTF temperature, evaporation capacity is also affected. Evaporation capacity decreases and compression work increases as a result of the increase in the condenser pressure thereby decreasing COP. With respect to the performance comparison of R1234yf and R134a, it is certainly be concluded that R1234yf always performs less than R134a. Hence, for R134a replacement, the cycle proposed to be operated with R1234yf needs performance improvement.

The experimental investigation of EERC with R134a shows the sensitivity of the ejector design with respect to the operating conditions. Ejector design as well has a very critical effect on the overall performance improvement. The biggest cause of the performance failure of the ejector is the sensitivity of the ejector design according the operating conditions. Secondly, even at very higher condenser temperatures at which ejector shows its performance improvement potential better, the EERC performs worse than the classical cycle due to the inefficiencies of the ejector components.

Lastly, as discussed numerically in the previous sections, liquid-vapor separator inefficiency decreases the performance. The required EERC modifications to obtain proper performance improvements are discussed in the next chapter. The states of the refrigerants at the separator vapor and liquid ports are assumed to be saturated vapor and saturated liquid, respectively. Hence, the enthalpy of the refrigerants is determined based on this state assumption. However, it is obvious that there are inefficiencies in the vapor and liquid separation processes. Since the quality of the refrigerant flowing through the vapor port is very high, the enthalpy of the actual high-quality refrigerant is close to the saturated vapor enthalpy defined at the separator pressure. Similarly, the refrigerant flowing through the liquid port has a very low quality whose enthalpy is very close to the enthalpy of the saturated liquid.

Therefore, the enthalpy definitions according to saturated vapor and liquid conditions are reasonable assumptions. The quality of the refrigerant at the ejector outlet is determined based on the enthalpy of the primary and secondary fluid mixture and ejector outlet pressure. Calculated mass flow rates of the primary and secondary fluids are required as well in order to obtain diffuser outlet enthalpy. The relationship between the ejector outlet quality and entrainment ratio is not established for a 100% efficient separator for these experiments. Hence, it could be understood that vapor and liquid separation inefficiencies occur after the two-phase refrigerant mixture enters into the separator.

For the conventional cycle tests evaporation capacity from the SHTF is less than the evaporation capacity from the energy analyzer (power consumption of the electrical heater placed inside the evaporator SHTF tank). There is always 200-300 W difference between these two evaporation capacities for the current investigations. By the way the volumetric flow rate of the evaporator SHTF is high, i.e.1200 l/h. It is observed that when the volumetric flow rate of the evaporator SHTF is high around 1200 l/h, the evaporation capacity from the SHTF is lower than the evaporation capacity from the energy analyzer of the evaporator heater.

Only possible heat transfer during the experiments are from environment to the system if it is assumed that the environment is around 27 °C and the maximum evaporator SHTF temperature is 25 °C. Regional heat transfer from the evaporator tank to the environment could occur around the evaporator heater located inside the evaporator tank. However, for lower evaporator SHTF flow rates around 800 l/h, evaporator capacity from the SHTF is higher than the evaporation capacity from the energy analyzer. As stated previously, 200-300 W difference is again observed between the evaporation capacities from the SHTF and energy analyzer of the evaporator heater when the evaporator capacity from the SHTF is higher.

It is reasonable that the evaporation capacity from the SHTF side is expected to be higher in comparison with the evaporation capacity according to the energy analyzer since energy could be transferred from environment to the system. However, it is known that the locations/insertions of the thermocouples at the inlet and outlet of the evaporator SHTF are not appropriate. The uncertainty is high for the temperature measurements; hence the accuracy of the thermocouples is required to be improved.

The degree of the difference between two evaporation capacities is the dependency of the temperature measurement accuracy on the volume flow rate of the SHTF. Temperature measurement accuracy of the constructed test rig is dependent on the volume flow rate of the evaporator SHTF since volume flow rate affects the temperature difference. Moreover, sensing capability is affected by the insertion and all attachments must be uniform. If there is a sensing problem regarding with the insertions, another cause of the uncertainty arises. Lastly, although attached thermocouples are calibrated, their accuracy is low thereby increasing the uncertainty in COP. To sum up, solving for the problem of the difference between the evaporation capacities, not only the accuracy of the thermocouples is required to be improved, but the insertions of the thermocouples are to be checked at the inlets and outlets of the evaporator SHTF as well.

# CHAPTER NINE
# CONCLUSIONS

The basic objective of this thesis is making numerical and experimental investigations on the EERC. Around this main research target, thermodynamic analyses are conducted for both the VCRC and EERC. The validity of the assumptions is discussed in the EERC models. The effects of the ejector components and liquid-vapor separator efficiencies on the overall performance are investigated. Hence, thermodynamic models are improved to yield more realistic performance evaluations and to estimate the critical design parameters. Semi-1D model of the EERC is introduced. Moreover, EERC is modelled under reversible ejector assumption to emphasize the highest improvement potential of the cycle. Experimental analyses are provided for both of the cycle configurations. The motivating aspect of the EERC analyses is proved experimentally by showing that R1234yf performs lower than R134a in the conventional cycle. Experimental investigations of EERC for R134a highlights importance of the ejector design sensitivity according to operating conditions and the effect of the liquid and vapor separation efficiencies. Experimental data is used also to validate the semi-1D model of the EERC.

## 9.1 Novelty of the Principal Findings

The novelties of this thesis are displayed with reference to the following outcomes:

- Thermodynamic models are firstly established for the conventional VCRC. Hence, the new generation refrigerants compatible with the GWP requirements of the environmental legislation are investigated. They are inspected with respect to not only COP values, but also the throttling losses caused by expansion valve. Hence, a group of environmentally-friendly refrigerants are specified to be analyzed in the EERC.
- Various refrigerants are investigated in the thermodynamic analyses of this thesis since ejectors display typical behaviors under the ejector mixing theories. However, the actual performance values vary from refrigerant to refrigerant. As

a result, under the typical behaviors of the ejectors, various refrigerant alternatives are evaluated. Therefore, the content of the thesis is widened. Transcritical EERC as well is investigated for the three high-pressure refrigerants. Although, the target refrigerants are R1234yf and R134a, R1234ze(E), R290, R600a, R744, R170, and R41 as well are analyzed in the thesis for the performance evaluations.

- The most significant conclusion to be derived from the thermodynamic analyses is that although they are simple and quick, they include very critical assumptions affecting the overall performance improvement. It is possible to increase the reliability of these models according to investigations made on the ejector components and auxiliary equipment of the cycle. All component efficiencies of the ejector and liquid and vapor separation efficiencies are required to be implemented into the model.
- Suction nozzle pressure is to be determined based on the actual calculations rather than assumed pressure drops since this pressure drop is highly dependent upon the motive flow operating conditions, motive nozzle design, and selected working fluid.
- For the calculation of the actual nozzle pressure drop, 1D model of the motive nozzle is established and inserted into the thermodynamic models. Therefore, the semi-1D model is constructed to calculated more realistic performance improvement ratios and determine the critical ejector design parameters, i.e. ejector mixing section diameter and suction nozzle diameter at the point where the primary and secondary refrigerant flows meet. Experimentally validated semi-1D model is beneficial for the initial ejector designs.
- Proposing the aforecited critical design parameters are of vital importance for the initial ejector designs and preliminary ejector testing. Although, at the beginning various refrigerants are analyzed for the performance investigations making use of the thermodynamic modelling approach, this thesis specifically focuses on R134a and R1234yf. They are typically similar refrigerants. All these critical results in terms of the modelling comparisons and geometrical parameters are given for these two refrigerants.

- EERC experimental set-up is established under the work plan of this thesis. The test rig is also capable of the performance evaluations of the VCRC. R134a is tested in both cycle concepts. The performance evaluation of the R1234yf is presented only for the VCRC concept. Performance of the R134a in the EERC concept is analyzed at three different operating conditions. The experimental EERC investigations show that the effect of the liquid-vapor separator efficiency for the overall performance improvement is as important as the ejector design.

## 9.2 Summary of the Results

The overview of the results is expressed as

- According to the thermodynamic analyses of the conventional cycle, R134a, R1234yf, R1234ze(E), R600a, and R290 are found to be the most appropriate refrigerants to be evaluated in the EERC in terms of the high expansion losses. R1234yf has nearly the lowest COP among the investigated refrigerant alternatives according to thermodynamic analyses of VCRC.
- Percentage expansion loss of R1234yf is calculated around 40% at the highest investigated condenser temperature. The corresponding percentage expansion loss is around 35% for R1234ze(E). Hence, these two refrigerants have higher performance improvement potential in the EERC among the other investigated environmentally-friendly refrigerant alternatives.
- Thermodynamic analyses of EERC are presented under both CAM and CPM ejector theories. Two suction nozzle pressure drop assumptions as well are used in the models, i.e. constant suction nozzle pressure drop assumption and optimum suction nozzle pressure drop assumption.
- Optimum suction nozzle pressure drop nearly stays the same under CPM assumption according to evaporation temperature. However, optimum pressure drop reacts more to the changes in the evaporation temperature under CAM approach.

- At lower evaporator and higher condenser temperatures, performance improvements at design and off-design conditions are very similar to each other.
- There is a wide range that CAM approach offers similar results under both suction nozzle pressure drop assumptions at higher condenser temperatures.
- Under CAM assumption, the agreement between the constant pressure and the optimum pressure assumptions for the suction nozzle are better when compared to CPM approach according to investigated ranges.
- Maximum difference between the optimum performance improvement percentages with reference to CAM and CPM assumption is 2.78% for R1234yf. Therefore, both of the assumptions could be used in the thermodynamic modelling.
- Smaller area ratio is calculated for the CAM assumption in comparison with CPM approach. The velocity ratio of the secondary fluid to the primary fluid is calculated higher for the CAM approach. Density ratio of the secondary fluid to the primary fluid is the determining factor on the variation of the area ratio with respect to the operating conditions.
- R744 and R170 experiencing very high expansion losses around 30-40% and R41 having around 23-25%expansion losses according to the investigated ranges are the potential refrigerant alternatives to be investigated in the transcritical EERC.
- The effect of the compressor isentropic efficiency on the overall performance improvement ratio is negligible and hence, variable or constant isentropic efficiency of the compressor could be used in the thermodynamic models.
- Mixing section efficiency is the most important parameter among the efficiencies of the other ejector components.
- Liquid-vapor separator efficiency affects the overall performance improvement ratio, area ratio, and entrainment ratio.
- For R1234yf, the performance improvement potential may be calculated as low as 8% at the highest investigated condenser temperature with the addition of the mixing section efficiency and the difference is more than 12% with the implementation of both the mixing section and liquid-vapor separator efficiency

when compared to base model considering only the efficiency of the motive nozzle, suction nozzle, and diffuser.

- Each ejector theory displays a typical behavior with respect to the parametric suction nozzle pressure defined based on the evaporation temperature.
- The performance improvement ratio difference between the actual and reversible EERC is around 20% at the lowest investigated evaporator temperature and 35% at the highest investigated condenser temperature for R1234yf.
- If the ejector design is not appropriate, the ejector would not operate efficiently even in the operating conditions at which ejector has the highest improvement potential.
- A preliminary design model is established based on the optimum operating conditions obtained from the thermodynamic models for CAM ejector.
- 1D model of the motive nozzle is validated with a maximum 6% error for the pressure drop throughout the nozzle using the experimental data from the literature.
- Motive nozzle outlet pressure is affected by the outlet diameter and mass flow rate. Effect of the subcooling temperature difference and condenser temperature on the outlet pressure is negligible.
- Motive nozzle efficiency is affected by the mass flow rate and the outlet diameter. Influence of the condenser temperature and subcooling temperature difference on the motive nozzle efficiency is ignored.
- Subcooling temperature difference is the most critical parameter affecting the location of the phase-change formation.
- Throat diameter is affected by the inlet pressure and the mass flow rate.
- Performance analyses are conducted as well under semi-1D modelling approach combining 0D thermodynamic models and 1D motive nozzle model. Therefore, suction nozzle pressure is calculated according to actual operating conditions and motive nozzle design rather than the assumptions.
- At the highest investigated condensation temperature, the performance improvement is approximately 11% for R134a and 13% for R1234yf according to the semi-1D modelling approach. However, the corresponding percentage

performance improvement is 25% and 33% for R134a and R1234yf, respectively based on the thermodynamic modelling approach.

- Semi-1D model including all ejector component efficiencies, liquid-vapor separator efficiency, and exactly calculated suction nozzle pressure drop yields more realistic performance evaluation when compared to pure thermodynamic models.
- The highest contribution to the uncertainty of COP is from the J-type thermocouples.
- It is experimentally shown that R1234yf has lower performance than R134a. Typical performance values of these two refrigerants are compared.
- The experimental analyses of R134a in the EERC show the importance of the sensitive ejector design based on the operating conditions and efficient liquid-vapor separation processes in the system.
- Semi-1D model is validated using the experimental results of R134a in the EERC under the assumed ejector component and liquid-vapor separator efficiencies. The agreement between the numerical results and experimental data is found satisfactory for the COP of the EERC, secondary fluid mass flow rate, and entrainment ratio.

### 9.3 Literature Contribution of the Thesis

The following papers are published under this thesis:

- Atmaca, A.U., Erek, A., & Ekren, O. (2017). Investigation of new generation refrigerants under two different ejector mixing theories. *Energy Procedia (4. International Conference on Energy and Environment Research (ICEER 2017)), 136*, 394-401.
- Atmaca, A.U., Erek, A., & Ekren, O. (2018). Performance evaluations of the constant area and constant pressure mixing ejector models. *Engineer and Machinery, 59* (690), 89-118.
- Atmaca, A.U., Erek, A., Ekren, O., Çoban, M.T. (2018). Thermodynamic performance of the transcritical refrigeration cycle with ejector expansion for

R744, R170, and R41. *Isı Bilimi ve Tekniği Dergisi (Journal of Thermal Science and Technology), 38* (2), 111-127.

- Atmaca, A.U., Erek, A., Ekren, O. (2019). Impact of the mixing theories on the performance of ejector expansion refrigeration cycles for environmentally-friendly refrigerants. International Journal of Refrigeration, 97, 211-225.
- Atmaca, A.U., Erek, A., & Ekren, O. (2020). Investigation of the liquid–vapor separator efficiency on the performance of the ejector used as an expansion device in the vapor-compression refrigeration cycle. *Journal of Energy Resources Technology, 142* (1), 012003 (12 pages).
- Atmaca, A.U., Erek, A., & Ekren, O. (2019). Preliminary Design of the Two-Phase Ejector under Constant Area Mixing Assumption for 5 kW Experimental System, *E3S Web of Conferences (4. International Conference on Advances on Clean Energy Research (ICACER 2019)), 103*, 01002.

The following conference proceeding are presented and published as full texts.

- Atmaca, A.U., Erek, A., & Ekren, O. (2016). Performance analyses of environmentally friendly low-GWP refrigerants. *International Conference on Thermophysical and Mechanical Properties of Advanced Materials (THERMAM 2016)*, 133-144.
- Atmaca, A.U., Erek, A., & Ekren. O. (2017). Investigating the effects of the ejector section efficiencies on the overall cycle performance. *21. National Congress of Thermal Sciences and Technology*, 1209-1222.
- Atmaca, A.U., Erek, A., Çoban, M.T., & Ekren, O. (2018). Parametric investigation of supercritical refrigeration cycle for R744 and R170. *7th Global Conference on Global Warming (GCGW-2018)*, 612-617.
- Atmaca, A.U., Erek, A., & Ekren, O. (2018). Thermodynamic assessment of ejector expansion refrigeration cycle under reversible ejector assumption. *7th Global Conference on Global Warming (GCGW-2018)*, 618-624.
- Atmaca, A.U., Erek, A., & Ekren, O. (2018). Comprehensive Performance Comparison of R290 and R600a in an ejector expansion refrigeration cycle. *4th*

*Anatolian Energy Symposium with International Participation (4. Uluslararası Katılımlı Anadolu Enerji Sempozyumu)*, 888-899.

- Atmaca, A.U., Erek, A., & Ekren, O. (2019). (Theoretical investigation of the vapor-liquid separator efficiency in the ejector expansion refrigeration cycle for R134a, R1234yf, and R1234ze(E) under various operating conditions (Ejektör genleştiricili soğutma çevriminde sıvı-buhar ayırıcı verimliliğinin R134a, R1234yf ve R1234ze(E) soğutkanları için farklı çalışma koşullarında teorik olarak incelenmesi). *14. Ulusal Tesisat Mühendisliği Kongresi (TESKON 2019)*, 383-398.
- Atmaca, A.U., Erek, A., Ekren, O., & Çoban M.T. (2019). Investigating the effects of the ejector section efficiencies on the ejector expansion transcritical $CO_2$ refrigeration cycle with respect to gas cooler pressure and outlet temperature (Ejektör kısım verimliliklerinin ejektör genleştiricili transkritik $CO_2$ soğutma çevrimi üzerindeki etkilerinin farklı çalışma koşullarında incelenmesi).*14. Ulusal Tesisat Mühendisliği Kongresi (TESKON 2019)*, 399-415.

## 9.4 Future Works

Although the future research targets are mentioned throughout the thesis, they are summarized in this section. Design and performance analyses are planned to be conducted for the CAM and CPM ejectors at the optimum suction nozzle pressure under thermodynamic modelling approach with the addition of the all ejector components and liquid-vapor separator efficiencies. Similar results are presented in Chapter Five based on the optimum operating conditions for 5 kW experimental system with a thermodynamic model including only the efficiency of the motive nozzle, suction nozzle, and diffuser. However, as for the future work, similar approach would be developed with the implementation of the mixing section and liquid-vapor separator efficiencies. Critical diameters would be calculated for both of CAM and CPM assumptions.

Comprehensive analyses would be made under semi-1D modelling approach according to different motive nozzle geometries and operating conditions in future studies. Furthermore, experimental validation ranges of the semi-1D model according to the estimated ejector component and liquid-vapor separator efficiencies would be widened.

As for the experimental set-up, the whole system is to be modified. The uncertainty in COP is to be decreased at least to 5%. Hence, the accuracy of the temperature measurement devices is required to be increased. The temperature measurement points would be completely made thermal well type insertion. All thermocouple insertions would be checked at the SHTF sides that the temperature measurements would not be affected by the flow rates of the evaporator and condenser SHTF. The dimensional checks of the ejector are to be made with coordinate measurement machine for the rest of the ejector designs. Separator design is to be changed, hence it is proposed to be larger and the height of the separator is aimed to be increased. As a result, the performance improvement of the EERC is naturally higher than the conventional cycle.

The following papers are under preparation or review as the potential future publications:

- Atmaca, A.U., Erek, A., Ekren, O. (2020). Analysis of the motive nozzle for the two-phase ejector: Effect of the operating and design parameters. *Applied Thermal Engineering*, under review.
- Atmaca, A.U., Erek, A., & Ekren, O. (2020-2021). Performance and design comparison of the ejector mixing theories according to the efficiency of the separator and ejector components (under preparation).
- Atmaca, A.U., Erek, A., Ekren, O. (2020-2021). Development of a semi-1D model for the ejector performance and design (under preparation).

## REFERENCES


*Alarko Carrier, Technical Bulletin*, No:4, April 2005. Retrieved July 06, 2016, from http://www.alarko-carrier.com.tr/eBulten/TekBulten/images_4/e_tekbulten4_print.pdf.

AL-Khalidy, N., & Zayonia, A. (1995). Design and experimental investigation of an ejector in an air-conditioning and refrigeration system. *ASHRAE Transactions*, 383–391.

Angielczyk, W., Bartosiewicz, Y., Butrymowicz, D., & Seynhaeve, J.M. (2010). 1-D modeling of supersonic carbon dioxide two-phase flow through ejector motive nozzle. *International Refrigeration and Air Conditioning Conference*, 1102.

ANSI/ASHRAE Standard 34-2010 ASHRAE (2010). Designation and Safety Classification of Refrigerants. American Society of Heating, Refrigerating, and Air-Conditioning Engineers, Inc.,Atlanta, GA.

Aprea, C., Greco, A., Maiorino, A. (2016). An experimental investigation on the substitution of HFC134a with HFO1234YF in a domestic refrigerator. *Applied Thermal Engineering*, *106*, 959–967.

Atmaca, A.U., Erek, A., & Ekren, O. (2016). Performance analyses of environmentally friendly low-GWP refrigerants. *International Conference on Thermophysical and Mechanical Properties of Advanced Materials (THERMAM 2016)*, 133-144.

Atmaca, A.U., Erek, A., & Ekren, O. (2017a). Investigation of new generation refrigerants under two different ejector mixing theories. *Energy Procedia (4th International Conference on Energy and Environment Research (ICEER 2017))*, *136*, 394-401.

Atmaca, A.U., Erek, A., & Ekren. O. (2017b). Investigating the effects of the ejector section efficiencies on the overall cycle performance. *21. National Congress of Thermal Sciences and Technology*, 1209-1222.

Atmaca, A.U., Erek, A., Çoban, M.T., & Ekren, O. (2018). Parametric investigation of supercritical refrigeration cycle for R744 and R170. *7th Global Conference on Global Warming (GCGW-2018)*, 612-617.

Atmaca, A.U., Erek, A., Ekren, O., Çoban, M.T. (2018). Thermodynamic performance of the transcritical refrigeration cycle with ejector expansion for R744, R170, and R41. *Isı Bilimi ve Tekniği Dergisi (Journal of Thermal Sciences and Technology), 38* (2), 111-127.

Atmaca, A.U., Erek, A., & Ekren, O. (2018a). Performance evaluations of the constant area and constant pressure mixing ejector models. *Engineer and Machinery, 59* (690), 89-118.

Atmaca, A.U., Erek, A., & Ekren, O. (2018b). Thermodynamic assessment of ejector expansion refrigeration cycle under reversible ejector assumption. *7$^{th}$ Global Conference on Global Warming (GCGW-2018)*, 618-624.

Atmaca, A.U., Erek, A., & Ekren, O. (2018c). Comprehensive Performance Comparison of R290 and R600a in an ejector expansion refrigeration cycle. *4$^{th}$ Anatolian Energy Symposium with International Participation (4. Uluslararası Katılımlı Anadolu Enerji Sempozyumu)*, 888-899.

Atmaca, A.U., Erek, A., Ekren, O., & Çoban M.T. (2019). Investigating the effects of the ejector section efficiencies on the ejector expansion transcritical $CO_2$ refrigeration cycle with respect to gas cooler pressure and outlet temperature (Ejektör kısım verimliliklerinin ejektör genleştiricili transkritik $CO_2$ soğutma çevrimi üzerindeki etkilerinin farklı çalışma koşullarında incelenmesi). *14. Ulusal Tesisat Mühendisliği Kongresi (TESKON 2019)*, 399-415.

Atmaca, A.U., Erek, A., Ekren, O. (2019a). Impact of the mixing theories on the performance of ejector expansion refrigeration cycles for environmentally-friendly refrigerants. *International Journal of Refrigeration*, *97*, 211-225.

Atmaca, A.U., Erek, A., & Ekren, O. (2019b). (Theoretical investigation of the vapor-liquid separator efficiency in the ejector expansion refrigeration cycle for R134a, R1234yf, and R1234ze(E) under various operating conditions (Ejektör genleştiricili soğutma çevriminde sıvı-buhar ayırıcı verimliliğinin R134a, R1234yf ve R1234ze(E) soğutkanları için farklı çalışma koşullarında teorik olarak incelenmesi). *14. Ulusal Tesisat Mühendisliği Kongresi (TESKON 2019)*, 383-398.

Atmaca, A.U., Erek, A., & Ekren, O. (2019c). Preliminary Design of the Two-Phase Ejector under Constant Area Mixing Assumption for 5 kW Experimental System, *E3S Web of Conferences* (*4. International Conference on Advances on Clean Energy Research (ICACER 2019), 103,* 01002.

Atmaca, A.U., Erek, A., & Ekren, O. (2020a). Investigation of the liquid–vapor separator efficiency on the performance of the ejector used as an expansion device in the vapor-compression refrigeration cycle. *Journal of Energy Resources Technology*, *142* (1), 012003.

Atmaca, A.U., Erek, A., Ekren, O. (2020b). Analysis of the motive nozzle for the two-phase ejector: Effect of the operating and design parameters. *Applied Thermal Engineering* (under review).

Awad, M.M., Muzychka, Y.S. (2008). Effective property models for homogeneous two-phase flows. *Experimental Thermal and Fluid Science*, *33*,106-113.

Bai, T., Yu, J., & Yan, G. (2016). Advanced exergy analyses of an ejector expansion transcritical $CO_2$ refrigeration system. *Energy Conversion and Management*, *126*, 850-861.

Balamurugan, S., Gaikar, V.G., & Patwardhan, A.W. (2006). Hydrodynamic characteristics of gas–liquid ejectors. *Chemical Engineering Research and Design, 84* (A12), 1166–1179.

Banasiak, K., & Hafner, A. (2011). 1D Computational model of a two-phase R744 ejector for expansion work recovery. *International Journal of Thermal Sciences, 50,* 2235-2247.

Bilir, N., & Ersoy, H.K. (2009). Performance improvement of the vapor compression refrigeration cycle by a two-phase constant area ejector. *International Jornal of Energy Research, 33,* 469-480.

Bivens, D.B., & Minor, BH. (1998). Fluoroethers and other next generation fluids. *International Journal of Refrigeration, 21,* 567–576.

Brunin, O., Feidt, M., & Hivet, B. (1997). Comparison of the working domains of some compression heat pumps and a compression-absorption heat pump. *International Journal of Refrigeration, 20,* 308-318.

Burk, R., Dürr, G., Feuerecker, G., Kohl, M., Manski, R., Strauß, T. (2006). *Vorrichtung zur Luftkonditionerung für ein Kraftfahrzeug.* D.E. Patent 10 2005 021 396 A1.

Calm, J.M. (2008). The next generation of refrigerants - Historical review, considerations, and outlook. *International Journal of Refrigeration, 31*, 1123-1133.

Calm, J.M. (2012). Refrigerant transitions...again. *ASHRAE/NIST Refrigerants Conference*. ASHRAE, Inc, Gaithersburg, MD, 1-16.

Çengel, Y.A., & Boles, M.A. (2007). *Thermodynamics: An Engineering Approach*, (6th ed.). USA: The McGraw-Hill Companies, Inc.

Chaiwongsa, P., & Wongwises, S. (2007). Effect of throat diameters of the ejector on the performance of the refrigeration cycle using a two-phase ejector as an expansion device. *International Journal of Refrigeration*, *30,* 601-608.

Chaiwongsa, P., & Wongwises, S. (2008). Experimental study on R-134a refrigeration system using a two-phase ejector as an expansion device. *Applied Thermal Engineering*, *28*, 467–477.

Chen, J., Havtun, H., & Palm, B. (2015). Conventional and advanced exergy analysis of an ejector refrigeration system. *Applied Energy*, *144*, 139-151.

Chunnanond, K., Aphornratana, S. (2004). Ejectors: applications in refrigeration technology. *Renewable and Sustainable Energy Reviews, 8*, 129-155.

Churchill, S.W. (1977). Friction factor equation spans all fluid flow regimes. *Chemical Engineering*, *84*, 91-92.

Churchill, S.W., & Chu, H.H.S. (1975). Correlating Equations for Laminar and Turbulent Free Convection from a Horizontal Cylinder. *International Journal of Heat and Mass Transfer, 18,* 1049-1053.

Cox, N., Mazur, V., & Colbourne, D. (2008). New High Pressure Low-GWP Azeotropic and Near-Azeotropic Refrigerant Blends. *International Refrigeration and Air Conditioning Conference*, 987.

Dai, B., Dang, C., Li, M., Tian, H., & Ma, Y. (2015). Thermodynamic performance assessment of carbon dioxide blends with low-global warming potential (GWP) working fluids for a heat pump water heater. *International journal of Refrigeration, 56*, 1-14.

*Deneysel Çalışmalarda Hata ve Belirsizlik Analizi, (n.d.).* Retrieved on February 5, 2020, from http://cdn.hitit.edu.tr/mf/files/66164_2047113654.pdf.

Deng, J.Q., Jiang, P.X., Lu, T., & Lu, W. (2007). Particular characteristics of transcritical $CO_2$ refrigeration cycle with an ejector. *Applied Thermal Engineering, 27*, 381–388.

Dinçer, İ., & Kanoğlu, M. (2010). *Refrigeration Systems and Applications*, (2nd ed.). USA: John Wiley & Sons, Ltd.

Directive 2006/40/EC of the European Parliament and of the Council of 17 May 2006 relating to emissions from air-conditioning systems in motor vehicles and amending Council Directive 70/156/EEC. *Official Journal of the European Union*, 2006.

Disawas, S., & Wongwises, S. (2004). Experimental investigation on the performance of the refrigeration cycle using a two-phase ejector as an expansion device. *International Journal of Refrigeration, 27*, 587–594.

Dixon, S.L. (1998). *Fluid Mechanics, Thermodynamics of Turbomachinery*, (4th ed.). Butterworth-Heinemann: A division of Reed Educational and Professional Publishing Ltd..

Eames, I.W., Aphornratana, S., & Haider H. (1995). A theoretical and experimental study of a small-scale steam jet refrigerator. *International Journal of Refrigeration, 18,* 378-386.

Elbel, S. (2011). Historical and present developments of ejector refrigeration systems with emphasis on transcritical carbondioxide air-conditioning applications. *International Journal of Refrigeration, 34,* 1545–1561.

Elbel, S., & Hrnjak, P. (2008a). Ejector Refrigeration: An Overview of Historical and Present Developments with an Emphasis on Air-Conditioning Applications. *International Refrigeration and Air Conditioning Conference*, 884.

Elbel, S., & Hrnjak, P. (2008b). Experimental validation of a prototype ejector designed to reduce throttling losses encountered in transcritical R744 system operation. *International Journal of Refrigeration, 31*, 411–422.

Elbel, S., & Lawrence, N. (2016). Review of recent developments in advanced ejector technology. *International Journal of Refrigeration, 62*, 1-18.

Elbel, S., Reichle, M., Bowers, C., & Hrnjak, P. (2012). Integration of a two-phase ejector into a compact, lightweight unitary-type air-conditioner using R744 for energy efficient operation in hot climates. *10th IIR Gustav Lorentzen Conference on Natural Refrigerants,* 180.

Ersoy, H.K. & Sag, N.B. (2014). Preliminary experimental results on the R134a refrigeration system using a two-phase ejector as an expander. *International Journal of Refrigeration, 43,* 97-110.

Ersoy, H.K., & Bilir, N. (2010). The influence of ejector component efficiencies on performance of ejector expander refrigeration cycle and exergy analyses. *International Journal of Exergy, 7,* 425-438.

ESDU (1992). *Ejectors and jet pumps, data item: 92042*. London, UK: ESDU International Ltd.

Gay, N.H. (1931). *Refrigerating system*. US Patent 1,836,318.

Genceli, O.F. (2008). *Ölçme Tekniği Boyut, Basınç, Akış ve Sıcaklık Ölçmeleri*. İstanbul: Birsen Yayınevi.

Geng, L., Liu, H., & Wei, X. (2019). CFD analysis of the flashing flow characteristics of subcritical refrigerant R134a through converging-diverging nozzles. *International Journal of Thermal Sciences, 137*, 438–445.

Hassanain, M., Elgendy, E., & Fatouh, M. (2015). Ejector expansion refrigeration system: Ejector design and performance evaluation. *International Journal of Refrigeration, 58*, 1-13.

Henry, R.E., & Fauske, H.K. (1971). The two-phase critical flow of one-component mixtures in nozzles, orifices, and short tubes. *Journal of Heat Transfer, 93(2)*, 179-187.

Henzler, H.J. (1983). Design of ejectors for single-phase material systems. *German Chemical Engineering, 6*, 292–300.

*Honeywell International Inc. (n.d.).* Retrieved on July 18, 2017, from http://honeywell-refrigerants.com/.

Incropera, F.P., Dewitt, D.P., Bergman, T.L., & Lavine, A.S. (2007). *Fundamentals of Heat and Mass Transfer*, sixth ed., John Wiley & Sons, Inc., USA.

Jarall, S. (2012). Study of refrigeration system with HFO-1234yf as a working fluid. *International Journal of Refrigeration, 35*, 1668-1677.

Keenan, J.H., Neumann, E.P., & Lustwerk, F. (1950). An investigation of ejector design by analysis and experiment. *Journal of Applied Mechanics*, 299–309.

Kemper, C.A., Harper, G.F., & Brown, G.A. (1966). *Multiple-phase ejector refrigeration system*. US Patent Number 3,277,660, assigned to Joseph Kaye & Co., Inc., Cambridge, Mass., a corporation of Massachusetts.

*Kigali Amendment Enters into Force, Bringing Promise of Reduced Global Warming (n.d.).* Retrieved on November 04, 2019, from https://sdg.iisd.org/news/kigali-amendment-enters-into-force-bringing-promise-of-reduced-global-warming/.

Klein, S.A. (2017). *Engineering Equation Solver (EES)*, Academic Professional V10.294, F-Chart Software, Madison, WI, USA.

Klein, S.A. (2019). *Engineering Equation Solver (EES)*, Academic Professional V10.294, F-Chart Software, Madison, WI, USA.

Kong, N., Qi, Z. (2018). Influence of speed of sound in two-phase region on 1-D ejector performance modelling. *Applied Thermal Engineering*, *139*, 352–355.

Kornhauser, A. A. (1990). The use of an ejector as a refrigerant expander. *International Refrigeration and Air Conditioning Conference*, 82.

Lawrence, N. (2012). *Analytical and experimental investigation of two-phase ejector cycles using low-pressure refrigerants*. Mechanical Engineering, Master of Science Thesis. University of Illinois at Urbana-Champaign, Urbana, Illinois.

Lawrence, N., & Elbel, S. (2012). Experimental and analytical investigation of automotive ejector air-conditioning cycles using low-pressure refrigerants. *International Refrigeration and Air Conditioning Conference*, 1169.

Lawrence, N., & Elbel, S. (2013). Theoretical and practical comparison of two-phase ejector refrigeration cycles including First and Second Law analysis. *International Journal of Refrigeration, 36,* 1220-1232.

Lawrence, N., & Elbel, S. (2014). Experimental investigation of a two-phase ejector cycle suitable for use with low-pressure refrigerants R134a and R1234yf. *International Journal of Refrigeration, 38,* 310-322.

Lawrence, N., & Elbel, S. (2015). Analyses of two-phase ejector performance metrics and comparison of R134a and $CO_2$ ejector performance. *Science and Technology for the Built Environment*, *21*, 515-525.

Lemmon, E.W., Bell, I.H., Huber, M.L., & McLinden, M.O. (2018). NIST Standard Reference Database 23: Reference Fluid Thermodynamic and Transport Properties-REFPROP, Version 10.0, National Institute of Standards and Technology, Standard Reference Data Program, Gaithersburg, 2018.

Lemmon, E.W., Huber, M.L., & McLinden, M.O. (2013). NIST Standard Reference Database 23: Reference Fluid Thermodynamic and Transport Properties-REFPROP, Version 9.1, National Institute of Standards and Technology. Standard Reference Data Program, Gaithersburg.

Li, D.Q., & Groll, E.A. (2005). Transcritical $CO_2$ refrigeration cycle with ejector-expansion device. *International Journal of Refrigeration*, *28*, 766-773.

Li, H., Cao, F., Bu, X., Wang, L., & Wang, X. (2014). Performance characteristics of R1234yf ejector-expansion refrigeration cycle. *Applied Energy*, *121*, 96-103.

Li, Y., & Yu, J. (2019). The effects of ejector geometry parameter and refrigerant charge amount on an ejector-expansion refrigeration system. *Applied Thermal Engineering, 152*, 402–408.

Lin, C., Xu, C., Yue, B., Jiang, C., Omori, H., & Deng, J. (2019). Experimental study on the separator in ejector-expansion refrigeration system. *International Journal of Refrigeration, 100,* 307–314.

Liu, F. (2014). Review on ejector efficiencies in various ejector systems. *International Refrigeration and Air Conditioning Conference*, 1533.

Liu, F., & Groll, E.A. (2008). Recovery of throttling losses by a two-phase ejector in a vapor compression cycle. *ARTI Report No. 10110-01*, Final report.

Liu, F., Groll, E.A., & Li, D. (2012). Investigation on performance of variable geometry ejectors for $CO_2$ refrigeration cycles. *Energy*, *45*, 829-839.

Liu, F., Groll, E.A., Ren, J. (2016). Comprehensive experimental performance analyses of an ejector expansion transcritical $CO_2$ system. *Applied Thermal Engineering, 98,* 1061–1069.

Liu, F., Li, Y., & Groll, E.A. (2012). Performance enhancement of $CO_2$ air conditioner with a controllable ejector. *International Journal of Refrigeration, 35,* 1604-1616.

Lorentzen, G. (1995). The use of natural refrigerants: a complete solution to the CFC/HCFC predicament. *International Journal of Refrigeration, 18,* 190-197.

Ma, Z., Bao, H., & Roskilly, A.P. (2017). Thermodynamic modelling and parameter determination of ejector for ejection refrigeration systems. *International Journal of Refrigeration, 75,* 117–128.

McGovern, R.K., Narayan, G.P., & Lienhard V, J.H. (2012). Analysis of reversible ejectors and definition of an ejector efficiency. *International Journal of Thermal Sciences, 54,* 153-166.

McLinden, M.O., Kazakov, A.F., Brown, J.S., Domanski, P.A. (2014). A thermodynamic analysis of refrigerants: Possibilities and tradeoffs for low-GWP refrigerants. *International Journal of Refrigeration, 38,* 80-92.

Metin, C., Gök, O., Atmaca, A.U., & Erek, A. (2019). Numerical investigation of the flow structures inside mixing section of the ejector. *Energy, 166,* 1216-1228.

Minnaert, M. XVI. (1933). On musical air-bubbles and sounds of running water. *Philosophical Magazine, 16,* 235–248.

Molés, F., Navarro-Esbrí, J., Peris, B., Mota-Babiloni, A., & Barragán-Cervera, A. (2014). Theoretical energy performance evaluation of different single stage vapour compression refrigeration configurations using R1234yf and R1234ze(E) as working fluids. *International Journal of Refrigeration, 44,* 141-150.

Mota-Babiloni, A., Navarro-Esbrí, J., Barragán, A., Molés, F., & Peris, B. (2014). Drop-in energy performance evaluation of R1234yf and R1234ze(E) in a vapor compression system as R134a replacements. *Applied Thermal Engineering, 71,* 259-265.

Mota-Babiloni, A., Navarro-Esbrí, J., Barragán-Cervera, A., Molés, F., & Peris, B. (2015). Analysis based on EU Regulation No 517/2014 of new HFC/HFO mixtures as alternatives of high GWP refrigerants in refrigeration and HVAC systems. *International Journal of Refrigeration, 52,* 21-31.

Mota-Babiloni, A., Navarro-Esbrí, J., Molés, F., Barragán-Cervera, A., Peris, B., & Verdú, G. (2016). A review of refrigerant R1234ze(E) recent investigations. *International Journal of Refrigeration, 95,* 211-222.

Motta, S.F.Y., Bercerra, E.D.V., Spatz, M.W. (2010). Analysis of LGWP alternatives for small refrigeration (Plugin) applications. *International Refrigeration and Air Conditioning Conference*, 1149.

Musser, A., & Hrnjak, P.S. (2014). Mobile heat pump exploration using R445A and R744. *International Refrigeration and Air Conditioning Conference*, 1514.

Nakagawa, M., Berana, M., S., & Kishine, A. (2009). Supersonic two-phase flow of $CO_2$ through converging–diverging nozzles for the ejector refrigeration cycle. *International Journal of Refrigeration, 32,* 1195-1202.

Nakagawa, M., Marasigan, A.R., & Matsukawa, T. (2011). Experimental analysis on the effect of internal heat exchanger in transcritical $CO_2$ refrigeration cycle with two-phase ejector. *International Journal of Refrigeration, 34*, 1577-1586.

Navarro-Esbrí, J., Mendoza-Miranda, J.M., Mota-Babiloni, A., Barragán-Cervera, A., & Belman-Flores, J.M. (2013). Experimental analysis of R1234yf as a drop-in replacement for R134a in a vapor compression system. *International Journal of Refrigeration, 36,* 870-880.

Nehdi, E., Kairouani, L., & Bouzaina, M. (2007). Performance analysis of the vapor compression cycle using ejector as an expander. *International Journal of Energy Research, 31,* 364-375.

Newton, A.B. (1972a). *Capacity control for multiple-phase ejector refrigeration systems*. US Patent Number 3,670,519, assigned to Borg-Warner Corporation, Chicago, IL.

Newton, A.B. (1972b). *Controls for multiple-phase ejector refrigeration systems.* US Patent Number 3,701,264, assigned to Borg-Warner Corporation, Chicago, IL.

Oshitani, H., Yamanaka, Y., Takeuchi, H., Kusano, K., Ikegami, M., Takano, Y., Ishizaka, N., Sugiura, T. (2005). Vapor compression cycle having ejector, U.S. Patent Application Publication US 2005/0268644 A1.

Ouzzane, M., & Aidoun, Z. (2003). Model development and numerical procedure for detailed ejector analysis and design. *Applied Thermal Engineering, 23*, 2337–2351.

Palacz, M., Smolka, J., Kus, W., Fic, A., Bulinski, Z., Nowak, A.J., Banasiak, K., & Hafner, A. (2016). CFD-based shape optimisation of a $CO_2$ two-phase ejector mixing section. *Applied Thermal Engineering, 95,* 62–69.

Palacz, M., Smolka, J., Nowak, A.J., Banasiak, K., & Hafner, A. (2017). Shape optimisation of a two-phase ejector for $CO_2$ refrigeration systems. *International Journal of Refrigeration, 74,* 212-223.

Paris Agreement - UNFCCC (2015). Retrieved Mach 23, 2020, from https://unfccc.int/sites/default/files/english_paris_agreement.pdf.

Pham, H.M. & Rajendran, R. (2012). R32 and HFOs as low-GWP refrigerants for air conditioning. *International Refrigeration and Air Conditioning Conference*, 1235.

Pigani, L., Boscolo, M., & Pagan, N. (2016). Marine refrigeration plants for passenger ships: Low-GWP refrigerants and strategies to reduce environmental impact. *International Journal of Refrigeration, 64*, 80-92.

Regulation (EU) No 517/2014 of the European Parliament and of the Council of 16 April 2014 on fluorinated greenhouse gases and repealing Regulation (EC) No 842/2006. Off. *Official Journal of the European Union*, 2014.

Ruangtrakoon, N., Thongtip, T., Aphornratana, S., & Sriveerakul, T. (2013). CFD simulation on the effect of primary nozzle geometries for a steam ejector in refrigeration cycle. *International Journal of Thermal Sciences, 63*, 133-145.

Rusly, E., Aye, L., Charters, W.W.S., and Ooi, A. (2005). CFD analysis of ejector in a combined ejector cooling system. *International Journal of Refrigeration, 28*, 1092–1101.

Sag, N.B., & Ersoy, H.K. (2016). Experimental investigation on motive nozzle throat diameter for an ejector expansion refrigeration system. *Energy Conversion and Management, 124*, 1–12.

Sağ, N.B. (2015). *Experimental investigation of usability of ejector for expansion work recovery in refrigeration cycle.* Mechanical Engineering, PhD Thesis. Selçuk University, Konya, Turkey.

Sarkar, J. (2012). Ejector enhanced vapor compression refrigeration and heat pump systems-A review. *Renewable and Sustainable Energy Reviews, 16*, 6647–6659.

Seckin, C. (2017). Parametric analysis and comparison of ejector expansion refrigeration cycles with constant area and constant pressure ejectors. *Journal of Energy Resources Technology, 139* (4), 042006.

Sherif, S.A., Lear, W.E., Steadham, J.M., Hunt, P.L., & Holladay, J.B. (2000). Analysis and modeling of a two-phase jet pump of a thermal management system for aerospace applications. *International Journal of Mechanical Sciences, 42*,185-198.

Smith, S.L. (1969). Void fractions in two-phase flow: a correlation based upon an equal velocity head model. *Proceedings of the Institution of Mechanical Engineers, 184*, 647–664.

Smolka, J., Bulinski, Z., Fic, A., Nowak, A.J., Banasiak, K., & Hafner, A. (2013). A computational model of a transcritical R744 ejector based on a homogeneous real fluid approach. *Applied Mathematical Modelling, 37*, 1208–1224.

Steadtke, H. (2006). *Gasdynamic aspects of two-phase flow*. Weinheim: WILEY-VCH Verlag GmbH & Co. KGaA.

Sumeru, K., Nasution, H., Ani, F.N. (2012). A review on two-phase ejector as an expansion device in vapor compression refrigeration cycle. *Renewable & Sustainable Energy Reviews, 16*, 4927-4937.

Sun, D. W., & Eames, I.W. (1996). Performance characteristics of HCFC-123 ejector refrigeration cycles. *International Journal of Energy Research, 20*, 871-885.

Tashtoush, B.M., Al-Nimr, M.A., & Khasawneh, M.A. (2019). A comprehensive review of ejector design, performance, and applications. *Applied Energy, 240,* 138–172.

*The Chemours Company (n.d.).* Retrieved on July 18, 2017, from https://www.chemours.com/Refrigerants/en_US/.

The Kigali Amendment to the Montreal Protocol: HFC Phase-down, UNEP, 28th meeting of Montreal Protocol, 10-14 October 2016, Kigali, Rwanda.

*The Linde Group (n.d.).* Retrieved on July 18, 2017, from http://www.linde-gas.com/tr/products_and_supply/refrigerants/index.html.

*The Linde Group (n.d.).* Retrieved on July 25, 2018, from http://www.linde-gas.com/en/products_and_supply/refrigerants/index.html.

Thongtip, T., & Aphornratana, S. (2017). An experimental analysis of the impact of primary nozzle geometries on the ejector performance used in R141b ejector refrigerator. *Applied Thermal Engineering, 110,* 89–101.

Tsuru, W., Ueno, S., Kinoue, Y., & Shiomi, N. (2014). Comparison of one-dimensional analysis with experiment for $CO_2$ two-phase nozzle flow. *Open Journal of Fluid Dynamics, 4,* 415-424.

*Türkiye Cumhuriyeti Çevre ve Şehircilik Bakanlığı, Sözleşme ve Protololler, Montreal Protokolü* (*n.d.).* Retrieved November 02, 2019, from https://iklim.csb.gov.tr/montreal-protokolu-i-4364.

Wang, D., Lu, Y., & Tao, L. (2017). Thermodynamic analysis of $CO_2$ blends with R41 as an azeotropy refrigerant applied in small refrigerated cabinet and heat pump water heater. *Applied Thermal Engineering, 125,* 1490–1500.

Wang, F., Li, D.Y., & Zhou, Y. (2016). Analysis for the ejector used as expansion valve in vapor compression refrigeration cycle. *Applied Thermal Engineering, 96,* 576-582.

Wang, L., Yan, J., Wang, C., & Li, X. (2017). Numerical study on optimization of ejector primary nozzle geometries. *International Journal of Refrigeration, 76,* 219–229.

Wongwises, S., & Disawas, S. (2005). Performance of the two-phase ejector expansion refrigeration cycle. Technical note. *International Journal of Heat and Mass Transfer, 48,* 4282–4286.

Wu, Y., Liang, X., Tu, X., Zhuang, R. (2012). Study of R161 refrigerant for residential air-conditioning applications. *International Refrigeration and Air Conditioning Conference,* 1189.

Yapıcı, R., & Ersoy, H.K. (2005). Performance characteristics of the ejector refrigeration system based on the constant area ejector flow model. *Energy Conversion and Management, 46,* 3117–3135.

Yataganbaba, A., Kilicarslan, A., and Kurtbaş, İ. (2015). Exergy analysis of R1234yf and R1234ze as R134a replacements in a two evaporator vapour compression refrigeration system. *International Journal of Refrigeration, 60,* 26-37.

Yu, J., Ren, Y., Chen, H., & Li, Y. (2007). Applying mechanical subcooling to ejector refrigeration cycle for improving the coefficient of performance. *Energy Conversion and Management, 48,* 1193–1199.

Zilio, C., Brown, J.S., Schiochet, G., & Cavallini, A. (2011). The refrigerant R1234yf in air conditioning systems. *Energy, 36,* 6110-6120.

**APPENDICES**

**APPENDIX-1: Technical Drawings of the Ejector Assembly and Ejector Components**

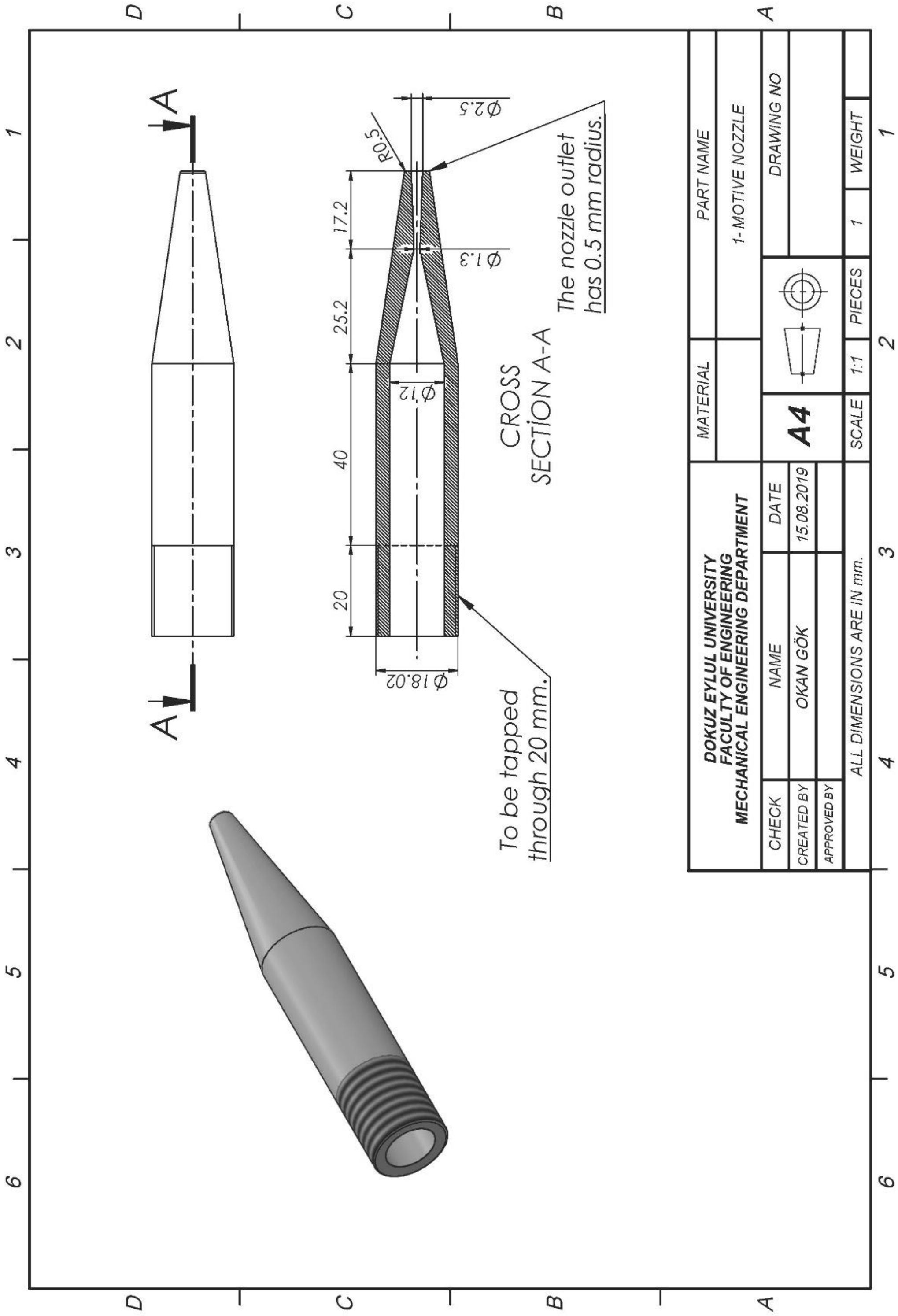

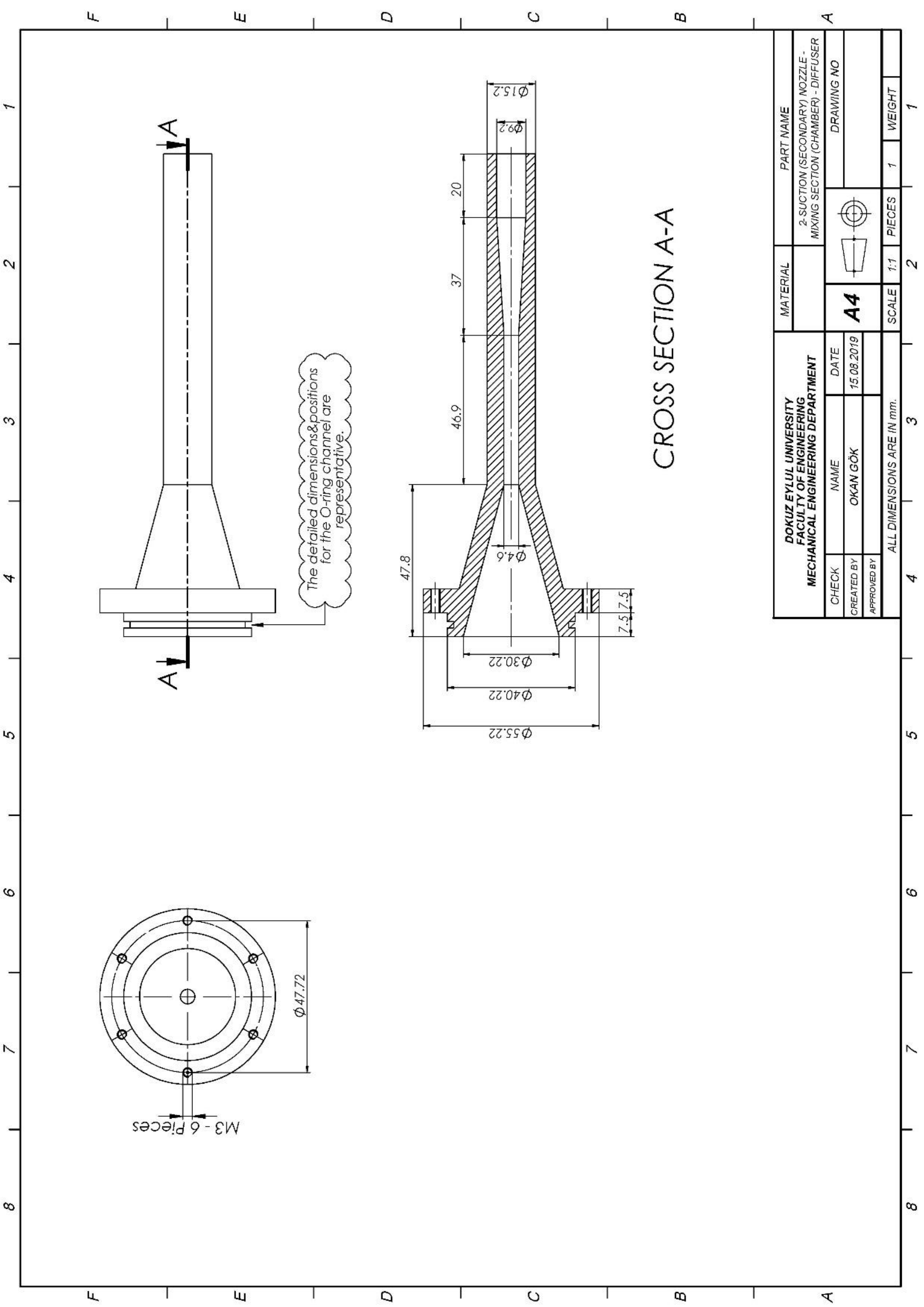

CROSS SECTION A-A
A
A
The detailed dimensions&positions for the O-ring channel are representative.
Ø15.2
Ø9.2
20
37
46.9
47.8
Ø4.6
7.5
7.5
Ø30.22
Ø40.22
Ø55.22
Ø47.72
M3 - 6 Pieces
DOKUZ EYLUL UNIVERSITY
FACULTY OF ENGINEERING
MECHANICAL ENGINEERING DEPARTMENT
CHECK
NAME
DATE
CREATED BY
OKAN GÖK
15.08.2019
APPROVED BY
ALL DIMENSIONS ARE IN mm.
MATERIAL
PART NAME
2- SUCTION (SECONDARY) NOZZLE - MIXING SECTION (CHAMBER) - DIFFUSER
DRAWING NO
A4
SCALE
1:1
PIECES
1
WEIGHT

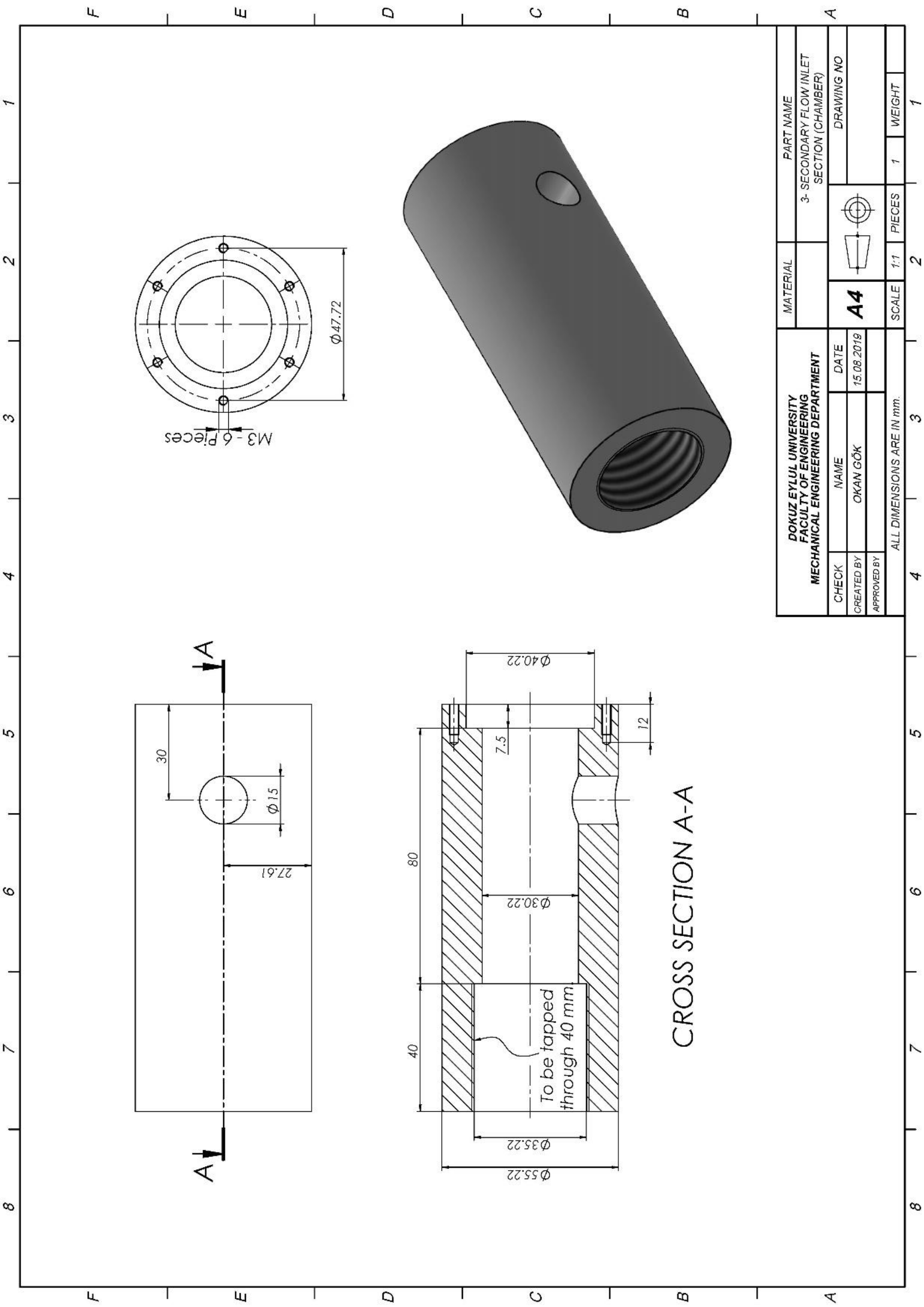

PART NAME
3- SECONDARY FLOW INLET SECTION (CHAMBER)
DRAWING NO
MATERIAL
DOKUZ EYLUL UNIVERSITY
FACULTY OF ENGINEERING
MECHANICAL ENGINEERING DEPARTMENT
CHECK
NAME
DATE
CREATED BY
OKAN GÖK
15.08.2019
APPROVED BY
A4
ALL DIMENSIONS ARE IN mm.
SCALE
1:1
PIECES
1
WEIGHT
M3 - 6 Pieces
Ø47.72
Ø40.22
7.5
12
30
Ø15
27.61
80
Ø30.22
40
To be tapped through 40 mm
Ø35.22
Ø55.22
CROSS SECTION A-A
A
A

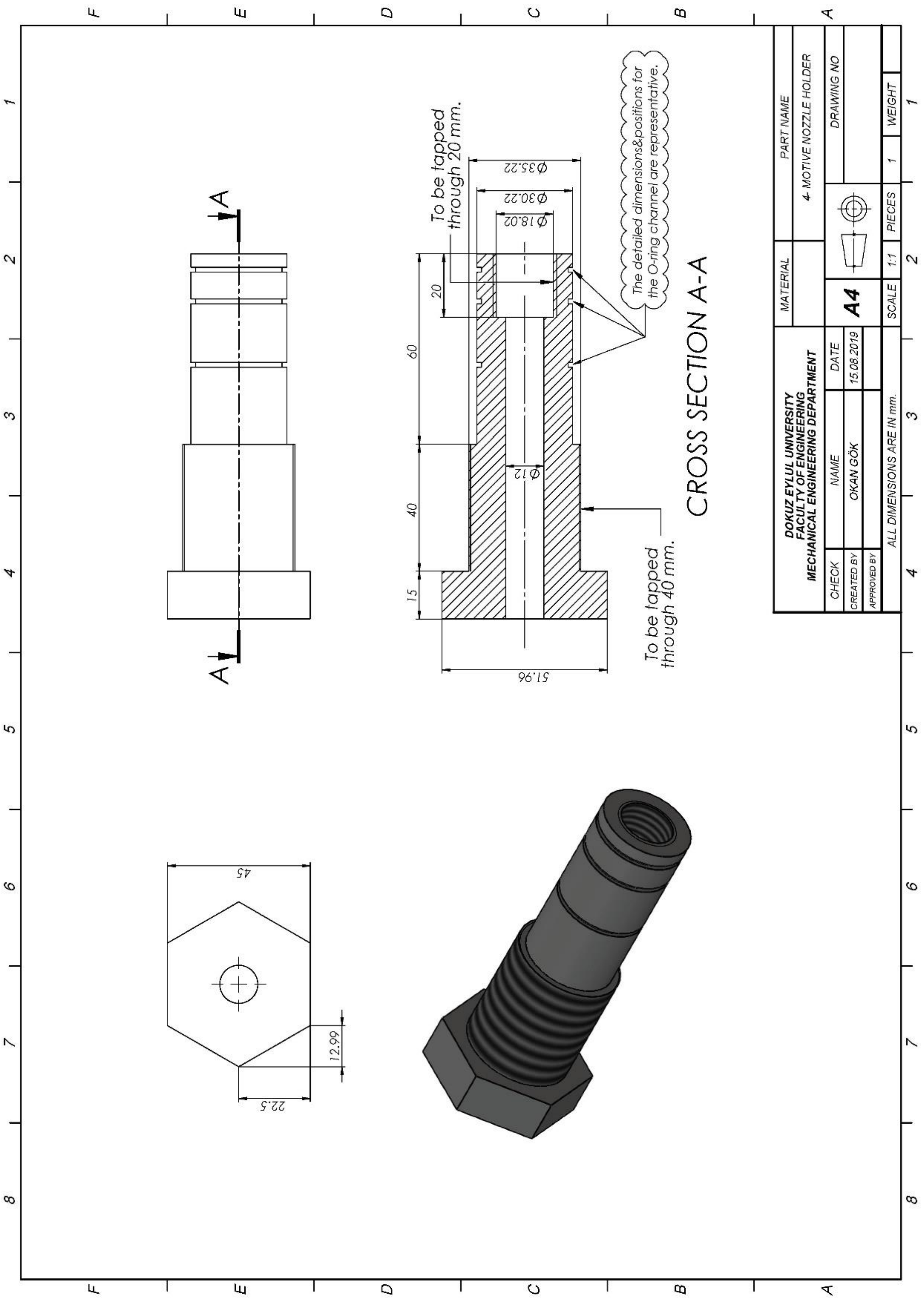
A
A
To be tapped through 20 mm.
The detailed dimensions&positions for the O-ring channel are representative.
Ø35.22
Ø30.22
Ø18.02
Ø12
20
60
40
15
51.96
CROSS SECTION A-A
To be tapped through 40 mm.
45
12.99
22.5
DOKUZ EYLUL UNIVERSITY
FACULTY OF ENGINEERING
MECHANICAL ENGINEERING DEPARTMENT
MATERIAL
PART NAME
4- MOTIVE NOZZLE HOLDER
DRAWING NO
CHECK
NAME
DATE
CREATED BY
OKAN GÖK
15.08.2019
APPROVED BY
A4
SCALE
1:1
PIECES
1
WEIGHT
ALL DIMENSIONS ARE IN mm.

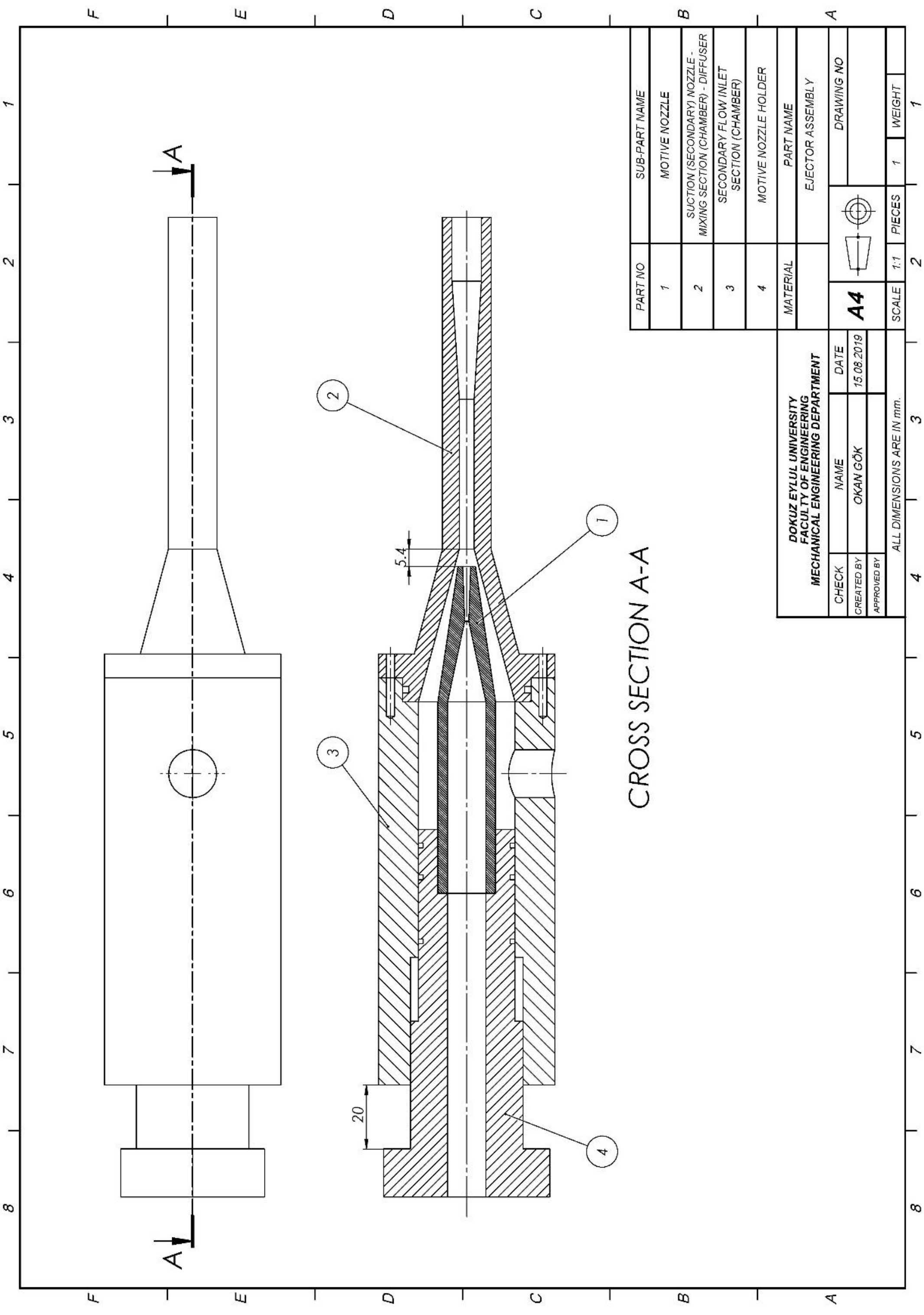

CROSS SECTION A-A
SUB-PART NAME
PART NO
MOTIVE NOZZLE
SUCTION (SECONDARY) NOZZLE - MIXING SECTION (CHAMBER) - DIFFUSER
SECONDARY FLOW INLET SECTION (CHAMBER)
MOTIVE NOZZLE HOLDER
PART NAME
MATERIAL
EJECTOR ASSEMBLY
DRAWING NO
A4
SCALE
1:1
PIECES
1
WEIGHT
DOKUZ EYLUL UNIVERSITY
FACULTY OF ENGINEERING
MECHANICAL ENGINEERING DEPARTMENT
CHECK
NAME
DATE
CREATED BY
OKAN GÖK
15.08.2019
APPROVED BY
ALL DIMENSIONS ARE IN mm.
5.4
20

## APPENDIX-2: Example Calibration Curves of the J-type Thermocouples

Calibration curves of the thermocouple measuring the refrigerant temperature at the compressor outlet, ejector outlet, evaporator inlet, and compressor inlet are presented in Figure A2.1, Figure A2.2, Figure A2.3, and Figure A2.4, respectively.

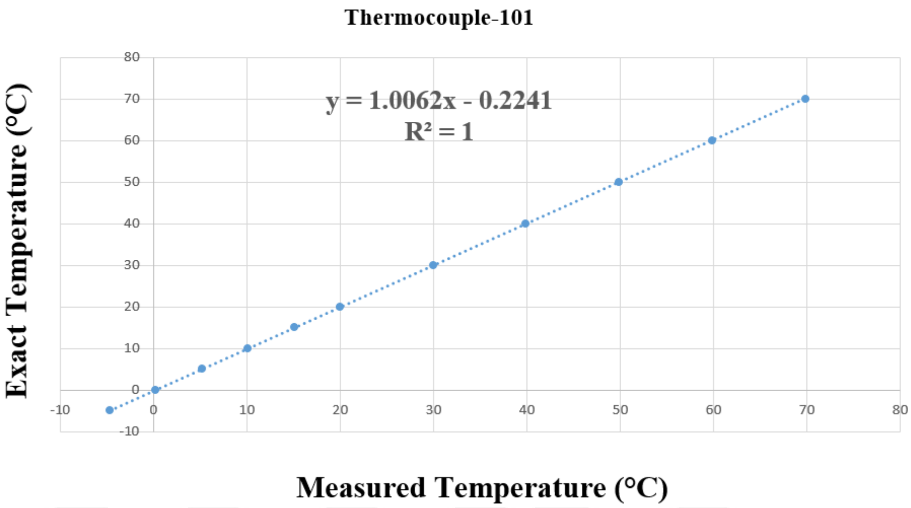


Figure A2.1 Calibration curve of the thermocouple connected to channel 101

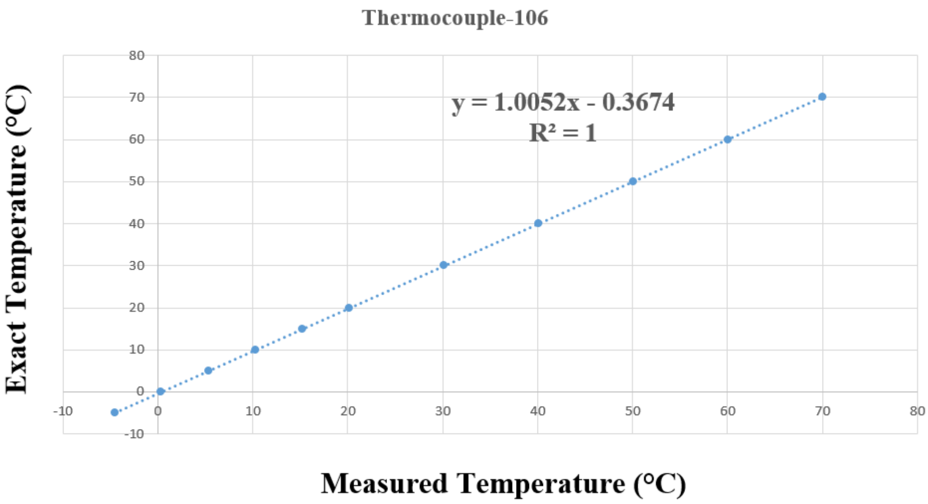


Figure A2.2 Calibration curve of the thermocouple connected to channel 106

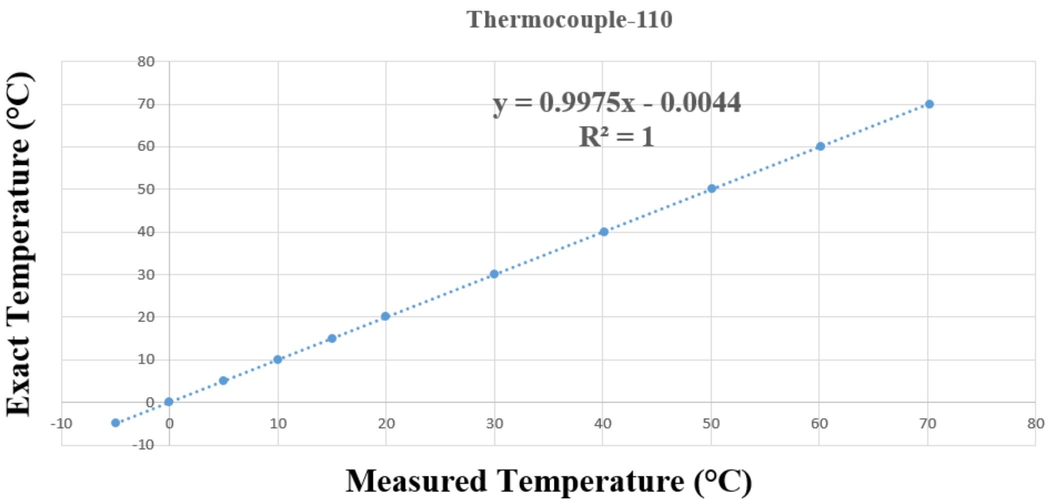


Figure A2.3 Calibration curve of the thermocouple connected to channel 110

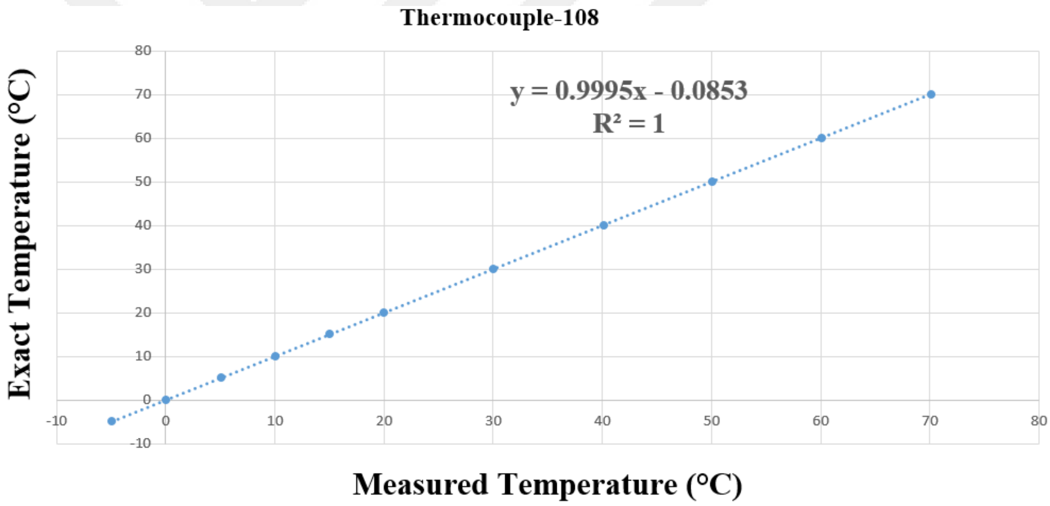


Figure A2.4 Calibration curve of the thermocouple connected to channel 108

Table A2. 1 Coefficients of the linearly fitted calibration curves for all thermocouples attached to the experimental set-up

| Thermocouple No | M(x) | B |
|---|---|---|
| **101** | 1.0062 | -0.2241 |
| **102** | 1.0059 | -0.271 |
| **103** | 1 | -0.0778 |
| **104** | 0.9918 | 0.1064 |
| **105** | 0.9977 | -0.0859 |
| **106** | 1.0052 | -0.3674 |
| **107** | 0.9989 | -0.0735 |
| **108** | 0.9995 | -0.0853 |
| **109** | 1.0017 | -0.1472 |
| **110** | 0.9975 | -0.0044 |
| **111** | 0.9962 | 0.0208 |
| **112** | 1.0011 | -0.1268 |
| **113** | 1.0004 | -0.0789 |
| **114** | 0.9941 | 0.1528 |
| **115** | 0.9987 | -0.0104 |
| **116** | 1.0022 | -0.0372 |
| **117** | 1.0056 | -0.1225 |
| **119** | 1.0064 | -0.1405 |

## APPENDIX-3: Repeatability of the Experiments

Table A3.1 Operating conditions of the repeatability experiments

| **Date of experiment** | **06.11.2019** | **07.11.2019** | **08.11.2019** |
|---|---|---|---|
| Test start time | 9:30 | 8:45 | 13:55 |
| Target of the experiment | Repeatability Experiment # 1 | Repeatability Experiment # 2 | Repeatability Experiment # 3 |
| Ambient Temperature (°C) | 25.5 | 25.5 | 26 |
| $T_{c,sec,fl(w)}$ (°C) | 35 | 35 | 35 |
| $T_{e,sec,fl(w)}$ (°C) | 20 | 20 | 20 |
| Volumetric flow rate of condenser water (l/h) | 400 | 400 | 400 |
| Volumetric flow rate of evaporator water (l/h) | 1200 | 1200 | 1200 |
| Compressor frequency (Hz) | 50 | 50 | 50 |

Table A3.2 Temperature and pressure measurements from the specific points of the test rig for the first repeatability experiment

| **Repeatability Experiment # 1** | | |
|---|---|---|
| **System points** | **Temperature (°C)** | **Gage Pressure (bar)** |
| Compressor inlet (8) | 9.94 | 2.34 |
| Compressor outlet (1) | 80.15 | 12.43 |
| Condenser inlet (2) | 78.30 | 12.34 |
| Condenser outlet (3) | 50.02 | 12.33 |
| Mass flow rate inlet (4) | 49.99 | 12.32 |
| Expansion valve inlet (13) | 49.94 | 12.28 |
| Expansion valve outlet or Evaporator inlet (10) | 6.25 | 2.72 |
| Evaporator outlet (11) | 6.87 | 2.47 |
| Condenser inlet (SHTF) (17) | 36.36 | - |
| Condenser outlet (SHTF) (19) | 46.66 | - |
| Evaporator outlet (SHTF) (14) | 17.92 | - |
| Evaporator inlet (SHTF) (16) | 20.08 | - |

Table A3.3 Temperature and pressure measurements from the specific points of the test rig for the second repeatability experiment

| Repeatability Experiment # 2 | | |
|---|---|---|
| **System points** | **Temperature (°C)** | **Gage Pressure (bar)** |
| Compressor inlet (8) | 9.28 | 2.30 |
| Compressor outlet (1) | 81.16 | 12.55 |
| Condenser inlet (2) | 78.47 | 12.44 |
| Condenser outlet (3) | 50.39 | 12.43 |
| Mass flow rate inlet (4) | 50.30 | 12.40 |
| Expansion valve inlet (13) | 50.25 | 12.37 |
| Expansion valve outlet or Evaporator inlet (10) | 6.09 | 2.69 |
| Evaporator outlet (11) | 6.39 | 2.46 |
| Condenser inlet (SHTF) (17) | 36.77 | - |
| Condenser outlet (SHTF) (19) | 46.90 | - |
| Evaporator outlet (SHTF) (14) | 17.95 | - |
| Evaporator inlet (SHTF) (16) | 20.14 | - |

Table A3.4 Temperature and pressure measurements from the specific points of the test rig for the third repeatability experiment

| Repeatability Experiment # 3 | | |
|---|---|---|
| **System points** | **Temperature (°C)** | **Gage Pressure (bar)** |
| Compressor inlet (8) | 10.12 | 2.31 |
| Compressor outlet (1) | 79.96 | 12.51 |
| Condenser inlet (2) | 78.56 | 12.38 |
| Condenser outlet (3) | 50.20 | 12.34 |
| Mass flow rate inlet (4) | 50.09 | 12.33 |
| Expansion valve inlet (13) | 50.01 | 12.32 |
| Expansion valve outlet or Evaporator inlet (10) | 6.30 | 2.71 |
| Evaporator outlet (11) | 6.91 | 2.46 |
| Condenser inlet (SHTF) (17) | 36.41 | - |
| Condenser outlet (SHTF) (19) | 46.87 | - |
| Evaporator outlet (SHTF) (14) | 18.02 | - |
| Evaporator inlet (SHTF) (16) | 20.13 | - |

Table A3.5 Comparison of the performance evaluation with respect to the repeatability experiments

| Parameters | Repeatability Experiment # 1 | Repeatability Experiment # 2 | Repeatability Experiment # 3 |
|---|---|---|---|
| | Values | Values | Values |
| Compressor power consumption (W) | 1220 | 1233.33 | 1200 |
| Evaporator electrical heater power consumption (W) | 3260 | 3233.33 | 3200 |
| Heat absorbed from the evaporator SHTF (W) | 3005.02 | 3048.56 | 2937.47 |
| Heat gain of the condenser SHTF (W) | 4745.84 | 4665.86 | 4815.86 |
| $COP_1$ (Compressor power consumption & Evaporator electrical heater power consumption) (-) | 2.67 | 2.62 | 2.67 |
| $COP_2$ (Compressor power consumption & Heat absorbed from the evaporator SHTF) (-) | 2.46 | 2.47 | 2.45 |
| Mass flow rate of the refrigerant from the compressor power consumption (kg/s) | 0.0237 | 0.0233 | 0.0236 |
| Mass flow rate of the refrigerant from the heat absorbed from the evaporator SHTF (kg/s) | 0.0228 | 0.0233 | 0.0223 |
| Mass flow rate of the refrigerant from the heat gain of the condenser SHTF (kg/s) | 0.0258 | 0.0254 | 0.0262 |
| Subcooling temperature difference at the outlet of the condenser (K) | 0.44 | 0.38 | 0.29 |
| Superheat temperature difference at the evaporator outlet (K) | 2.08 | 1.69 | 2.22 |
| Compressor isentropic efficiency (-) | 0.59 | 0.58 | 0.60 |
| Quality of the refrigerant at the evaporator inlet (-) | 0.33 | 0.33 | 0.33 |
| Result of the total energy conservation (W) | -529.36 | -392.51 | -686.93 |

## APPENDIX-4: Nomenclature

| | |
|---|---|
| 1,2,…,10 | Operational steps of the EERC |
| a,b,c,d | Operational steps of the VCRC |
| $a$ | Area per unit total ejector mass flow rate [$m^2s/kg$] |
| A | Area [$m^2$] |
| c | Speed of sound [m/s] |
| $c_p$ | Specific heat at constant pressure [kJ/kgK] |
| C | Area increment factor for the mixing section equations presented under semi-1D modelling approach for constant area mixing assumption |
| COP | Coefficient of performance [-] |
| D | Diameter [m] |
| dx | Length of the computational grid (cell) [m] |
| $f$ | Friction factor [-] |
| h | Enthalpy [kJ/kg] |
| L | Length [L] |
| $\dot{m}$ | Mass flow rate [kg/s] |
| mrs | Minimum required space [mm] |
| N | Total number of the calculation grids [-] |
| $\overline{Nu_D}$ | Nusselt number based on the cylinder diameter [-] |
| P | Pressure [kPa] |
| $P_s$ | Suction chamber pressure (also known as the pressure of the primary and the secondary fluids at the mixing chamber inlet or the mixing pressure for the constant pressure mixing ejector) [kPa] |
| Pr | Prandtl Number [-] |
| q | Heat transfer on a unit-mass basis [kJ/kg] |
| $\dot{Q}$ | Heat transfer rate [kW] |
| r ($X_m$) | Quality or dry mass fraction [-] |
| R | Performance improvement ratio or coefficient [-] |
| $Ra_D$ | Rayleigh number based on the cylinder diameter |
| Re | Reynolds Number [-] |

| | |
|---|---|
| Ref | Refrigerant (working fluid) type |
| s | Entropy [kJ/kgK] |
| T | Temperature [K] |
| u | Velocity [m/s] |
| $v$ | Specific volume [m$^3$/kg] |
| $\dot{V}$ | Volume flow rate [m$^3$/s] |
| VCC | Volumetric cooling capacity [kJ/m$^3$] |
| w | Entrainment ratio [-] |
| $w_{in}$ | Work input to the compressor [kJ/kg] |
| $w_{net}$ | Net work transfer to/from the system [kJ/kg] |
| $\dot{W}_{net}(\dot{W})$ | Net work transfer rate to/from the system [kW] |
| wt | Wall thickness |
| x | Exergy on a unit-mass basis [kJ/kg] |
| $\dot{X}$ | The rate of exergy [kW] |
| Y | A physical quantity (parameter) obtained from the experimental measurements |

**Subscripts**

| | |
|---|---|
| 0 | Dead state |
| abs | Absolute value |
| act | Actual |
| as | Assumed |
| b | Base cycle (VCRC) |
| c | Condenser |
| calc | Calculated |
| Carnot | Carnot refrigeration cycle |
| check | State check or control |
| comp | Compressor |
| cons | Conservation |
| const | Constant |

| | |
|---|---|
| conv | Converging |
| cs | Cross-sectional |
| d | Diffuser |
| dest | Destruction |
| div | Diverging |
| drop | Pressure drop |
| e | Evaporator |
| ej | Ejector |
| en-analyzer | Energy analyzer |
| est | Estimated |
| exp | Experimental |
| expv | Expansion valve |
| g | Gas/vapor phase |
| gc | Gas cooler |
| H | High temperature environment |
| imp | Improvement |
| in | Inlet |
| isen | Isentropic |
| k | Location (boundary) |
| l | Liquid phase, liquid port or liquid portion of the total two-phase flow entering the separator |
| L | Low temperature environment |
| liq | Liquid separation |
| loss | Losses |
| lr | Lift ratio |
| lslp | Liquid portion of the refrigerant at the separator liquid port |
| lt | Lateral |
| m | Primary (motive) nozzle/flow |
| mix | Mixing chamber |
| n | Number of the independent variables affecting the physical quantity, Y obtained from the experimental measurements |
| opt | Optimum (yielding maximum COP) |

| | |
|---|---|
| out (o) | Outlet |
| P | Saturation property definition with respect to the pressure |
| Pre-mix | Pre-mixing section |
| pf | Primary/motive fluid (ejector refrigerant side) |
| rev | Reversible |
| rslp | Refrigerant at the separator liquid port |
| rsvp | Refrigerant at the separator vapor port |
| s | Suction (secondary) nozzle/flow |
| sat | Saturation point |
| sc | Subcooling |
| sep | Separator |
| sec-fl(w) | Secondary heat transfer fluid (water) of the evaporator or the condenser |
| semi-1D | Semi-1D modelling approach |
| sf | Secondary/suction fluid (ejector refrigerant side) |
| sh | Superheating |
| t | Throat or total |
| T | Saturation property definition with respect to the temperature |
| tp,mix | Two-phase mixture |
| turb | Turbine |
| v | Vapor port or vapor portion of the total two-phase flow entering the separator |
| vap | Vapor separation |
| var | Variable |
| vsvp | Vapor portion of the refrigerant at the separator vapor port |

**Greek letters**

| | |
|---|---|
| $\alpha$ | Angle [°] or void fraction [-] |
| $\Delta$ | Difference |
| $\varepsilon$ | Roughness [m] or error between the calculated and assumed values [-] |
| $\eta$ | Efficiency [-] |
| $\eta_{II}$ | Second-law (exergy) efficiency [-] |

| | |
|---|---|
| $\mu$ | Dynamic viscosity [Pas] |
| $\rho$ | Density [kg/m$^3$] |
| $\tau$ | Pressure ratio ($P_{high}/P_{low}$) |
| $\phi$ | Area ratio [-] |
| $\psi$ | Flow (or stream) exergy [kJ/kg] |
| $\omega$ | Error in a physical quantity (parameter) measured/obtained from the set-up |

**Abbreviations**

| | |
|---|---|
| 0D | Zero-dimensional |
| 1D | One-dimensional |
| AHRI | Air-Conditioning, Heating, and Refrigeration Institute |
| CAM | Constant area mixing |
| CFCs | Chlorofluorocarbons |
| CFD | Computational Fluid Dynamics |
| CG | Computational grid |
| CM | Coefficient matrix |
| COP | Coefficient of performance |
| COS | Condenser outlet split |
| CPM | Constant pressure mixing |
| DEM | Delayed equilibrium model |
| DOS | Diffuser outlet split |
| EERC | Ejector expansion refrigeration cycle |
| GHGs | Greenhouse gases |
| GWP | Global warming potential, normally and herein relative to carbon dioxide ($CO_2$) for the duration of 100 years (McLinden et al. (2014), Calm (2012)) |
| HCFCs | Hydrochlorofluorocarbons |
| HEM | Homogeneous equilibrium model |
| HFCs | Hydrofluorocarbons |

| | |
|---|---|
| HFOs | Hydrofluoroolefins |
| HRM | Homogeneous relaxation model |
| IHE | Isentropic Homogeneous Equilibrium |
| LCCP | Life-cycle climate performance |
| NBP | Normal boiling point |
| NWI | Net warming impact |
| ODP | Ozone depletion potential |
| PF | Primary fluid |
| RHSV | Right-hand side vector |
| SF | Secondary fluid |
| SHTF | Secondary heat transfer fluid |
| SV | Solution vector |
| TEWI | Total equivalent warming impact |
| VCC | Volumetric cooling capacity |
| VCRC | Vapor-compression refrigeration cycle |